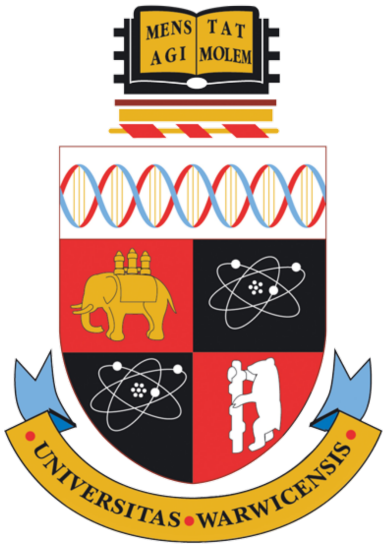

Detection of Stellar Flares and a Transiting Brown Dwarf with the Next Generation Transit Survey

by

James Arthur George Jackman

Thesis

Submitted to the University of Warwick

for the degree of

Doctor of Philosophy

Department of Physics

June 2020

Contents

List of Tables

List of Figures

Acknowledgments

First and foremost, I would like to thank my family for all their love and support during my PhD. Without them always being there for me, this certainly would have been a much harder endeavour than it already was. This thanks of course extends to my cat Sam who, despite his screaming, has always been a joy to see.

Next, I'd like to thank my supervisor Prof. Peter Wheatley. This thesis would not have been possible without his guidance, encouragement and refusal to let me cut corners. Without him, I wouldn't have decided to focus on the stars rather than the planets around them. He has my sincerest gratitude for all his help.

I of course need to thank all those within the Warwick astronomy and CFSA groups for their help. Whether it was an astrophysical issue, or that we'd run out of coffee beans, their help has been much appreciated. I'd especially like to acknowledge the PhD students and postdocs. Thanks to everyone for the long lunches, pub quizzes (and spicy bean burgers), the curries, pub sessions, postgraduate seminars and film screenings (both good and bad). I'd like to thank them for putting up with my endless references to memes, The Simpsons, and puns (sometimes all at the same time). The building may have been awful, but you lot certainly made it worth coming back to each day.

On a similar note, I'd also like to thank my Sunday Phoenix pub quiz team. We may not have gotten the quickest answers (or even the correct ones), but we certainly gave it a good go anyway.

I'd also like to thank the NGTS consortium for all their help and insights as well. The experience of presenting my work at NGTS meetings is one I won't soon forget.

Finally, the opportunity to study and contribute to such an exciting field of research has been one I'll forever be thankful for. My PhD may not have ended quite the way I expected it to, but I still had a good time along the way.

Declarations

I submit this thesis to the University of Warwick graduate school for the degree of Doctor of Philosophy. This thesis has been composed by myself and has not been submitted for a degree at another University.

This thesis includes material previously published in/submitted to journals, as follows:

- Jackman et al. (2018), MNRAS 477, 4655, *"Ground-based detection of G star superflares with NGTS"*. Material from this paper is used in Chapter 3.
- Jackman et al. (2019a), MNRAS 482, 5553, *"Detection of a giant flare displaying quasi-periodic pulsations from a pre-main-sequence M star by the Next Generation Transit Survey"*. Material from this paper is used in Chapter 4.
- Jackman et al. (2019b), MNRAS Letters, 485, L136 *"Detection of a giant white-light flare on an L2.5 dwarf with the Next Generation Transit Survey"*. Material from this letter is used in Chapter 5.
- Jackman et al. (2019c), MNRAS 489, 5146, *"NGTS-7Ab: an ultrashort-period brown dwarf transiting a tidally locked and active M dwarf"*. Material from this paper is used in Chapter 6.
- Jackman et al. (2020), MNRAS under review, *"White-light flares detected from Orion"*. Material from this paper is used in Chapter 7.

Chapters 1 and 2 make use of material from these works also. I also acknowledge the following contributions:

- For Chapter 4, SED fitting was performed by Grant Kennedy.
- For Chapter 4, material in the introduction regarding the physical mechanisms behind quasi-periodic pulsations (QPPs) was written by Chloe Pugh.
- For Chapter 4, spectroscopic observations were taken by Simon Murphy.
- For Chapter 4, the X-ray analysis Sect. 4.2.3 was performed by Peter J. Wheatley.
- For Chapter 4, the Fourier analysis of the QPPs was performed by Chloe Pugh.
- For Chapter 4, the EMD analysis of the QPPs was performed by Dmitrii Kolotkov.
- For Chapter 4, the wavelet analysis of the QPPs was performed by Anne-Marie Broomhall.
- For Chapter 4, Chloe Pugh, Dimtrii Kolotkov and Anne-Marie Broomhall contributed significantly to the analysis of the QPPs, in particular the analysis of the MHD modes.
- The research contained within Chapter 6 features measurements and observations taken by several members of the NGTS consortium. These are as follows: (i) SAAO lightcurves were taken by Matt Burleigh. (ii) EulerCam lightcurves were taken by Oliver Turner. (iii) *TESS* full frame images were reduced by Sam Gill. (iv) HARPS spectroscopy was obtained by Tom Louden. (v) HARPS spectra were reduced in several different masks by Louise Neilsen. (vi) SAAO spectra were taken by Ian Braker. (vii) Analysis of the Gaia photometry and astrometry was performed by myself with aid from Simon Hodgkin. (viii) Analysis of the HARPS CCF spectra was performed by myself with aid from Dan Bayliss and Didier Queloz. (ix) X-ray analysis was performed by myself with aid from Peter J. Wheatley and Katja Poppenhaeger. (x) David Brown helped the analysis of the future evolution of NGTS-7Ab.

Abstract

Stellar flares are explosive phenomena caused by reconnection events in the magnetic fields of stars. They emit across a wide range of wavelengths but notably in the optical, UV and in X-rays. They are some of the highest energy events seen from other stars and they regularly dwarf those seen from the Sun. They are regularly seen on low mass stars and provide a way of studying the magnetic activity of these systems. Their role in exoplanet habitability (in particular for low mass stars) has become increasingly relevant in recent years, necessitating studies of their energies and occurrence rates.

In this thesis I present observations and analysis of stellar flares detected with the Next Generation Transit Survey (NGTS). These flares come from stars ranging from G to L spectral type. I also present the detection and analysis of the transiting brown dwarf NGTS-7Ab, discovered in part because of the multiple flares detected from the M dwarf host star.

These flare detections include the first ground-based CCD detections of superflares from a G-type star, NGTS J030834.9-211322. I used the high cadence NGTS observations to apply a Solar inspired empirical flare model, one which does not require arbitrary break points between the flare rise and decay.

I also present the detection of a giant flare from a pre-main sequence M star. This flare was one of the most energetic detected from an M star and displayed quasi-periodic pulsations in the flare peak. I apply solar techniques to analyse these oscillations and identify their cause.

I present the first detection of a white-light flare from an L2.5 dwarf. This is the coolest star to ever show a white-light flare to date and shows strong tran-

sient magnetic activity can persist to the brown dwarf boundary. I also show how full frame images in wide-field exoplanet surveys, provided they are a high enough cadence, can be used to detect flares from the faintest and coolest stars.

I present the detection of NGTS-7Ab, an ultra-short period brown dwarf around a tidally locked and active M star. I analyse the entire system, showing through a kinematic and photometric analysis that it is likely a hierarchical triple system formed of two active M stars (NGTS-7A and NGTS-7B) and a transiting brown dwarf (NGTS-7Ab). This is the shortest period transiting brown dwarf discovered to date and it has spun up and tidally locked its host star, placing the system in a state of spin-orbit synchronisation.

Finally, I discuss the detection of white-light flares from pre-main sequence stars associated with the Orion complex. These stars have an average age of 4 Myr. I measure the average flare occurrence rate for M0-M3 stars, finding a non-linear relationship between flare occurrence rate and cluster age.

My work shows how the ground-based NGTS observations can rival those available from space for high energy white-light flare events. Throughout this work I also discuss the possible effects flares may have on nearby exoplanets, along with how the detected flare events relate to other signs of magnetic activity such as starspots.

Abbreviations

CME Coronal Mass Ejection

HXR Hard X-ray

NGTS Next Generation Transit Survey

NIR Near Infrared

QPP Quasi-periodic Pulsation

SED Spectral Energy Distribution

TESS *Transiting Exoplanet Survey Satellite*

XUV X-ray and Extreme Ultraviolet

AU Astronomical Unit, 1.496×10^8 km

M_J Jupiter Mass, 1.898×10^{27} kg

R_J Jupiter Radius, 71492 km

$M_\odot$ Solar Mass, 1.988×10^{30} kg

$R_\odot$ Solar Radius, 695700 km

1 erg $= 10^{-7}$ W

Chapter 1

Introduction

Stellar activity - who flares wins?

1.1 The Sun, Other Stars, And Their Activity

For half the time, our sky is dominated by our nearest star, the Sun. It is the centre of our solar system and comprises roughly 99.9% of the mass within it. For the other half we are able to see a vast array of stars in the sky, which have a wide variety of masses, radii and ages. Depending on the type of star, some of these have different internal structures than that of the Sun. In this section I will discuss the types of stars which can be observed in the sky, along with their internal and external structure. I will focus specifically on solar and lower mass stars, right down to the brown dwarf boundary. I will discuss how we classify these stars based on their surface properties, along with their surface activity.

1.1.1 Stellar Masses and Spectral Types

In order to classify stars we use the Harvard classifciation scheme (Cannon and Pickering, 1901; Payne, 1925). This scheme is based on the relative strength of absorption lines within spectra. The hottest stars generally only feature hydrogen and helium lines. As we go to cooler stars, more complex molecules form within stellar photospheres. The overall shape of the spectra themselves changes with temperature, making both the presence of absorption features and the spectral shape itself good classifiers for temperatures and masses. A type stars show strong Balmer absorption lines, whereas M star spectra are marked by the presence of strong TiO and VO absorption features (e.g. Allard and Hauschildt, 1995), along with SEDs

peaking at longer wavelengths. The list of spectral types and the masses, radii and temperatures they correspond to are given in Tab. 1.1. The stars I will be discussing in this thesis are those from G to L spectral types.

The changing temperatures and luminosities of stars with spectral type means these parameters can be used for comparisons. The method for this is through the use of a *Hertzsprung-Russell* (HR) diagram (Hertzsprung, 1911; Russell, 1914). An example of such a diagram is shown in Fig. 1.1. On the HR diagram the horizontal axis signifies decreasing temperature, while the vertical axis is increasing luminosity. More luminous stars reside towards the top of the diagram and cooler stars reside towards the right hand side. Often observable signatures such as colour and absolute magnitude (if the distance to the star is known) are used in place of the physical parameters.

While all stars have roughly the same shape (a sphere approximately, depending on their speed of rotation or the presence of companions), they have a wide range of masses and radii. The lower end of the stellar mass regime is marked by the brown dwarf boundary (75-80 Jupiter masses; Halbwachs et al., 2000) and is where stars never begin to fuse hydrogen in their cores. The upper end of the mass regime is more ambiguous and depends on your chosen theoretical limit (accretion, Eddington) or even the amount of mass present to form your star in the first place. Either way, I do not consider this regime in this thesis. In between these limits reside stars of various masses and luminosities, which reside in different locations, also depending on their age, on the HR diagram. Three can be seen in Fig. 1.1, the *main sequence*, *giant branch* and *white dwarfs*. We can use the luminosity classes to denote different types of star which may have the same temperatures. The Yerkes spectral classification scheme is given in Tab. 1.2, with each type used as a suffix to the Harvard classification unless noted otherwise (Morgan et al., 1943). For reference, the Sun is a main sequence G2 star, so has a spectral type of G2V.

The main sequence of a star is the period in its life where it fuses hydrogen within its core to form helium. During the main sequence, the star remains in a state of hydrostatic equilibrium, where the inwards force of gravity is balanced by the outwards gas and radiation pressure (for a detailed explanation, see Kippenhahn et al., 1990). All main sequence stars fuse hydrogen within their cores at a mass-dependent rate. More massive stars have greater internal pressures and temperatures, so fuse hydrogen faster than their lower mass counterparts. The relation between the luminosity of a star on the main sequence and its mass is

$$L \propto M^{\alpha} \tag{1.1}$$

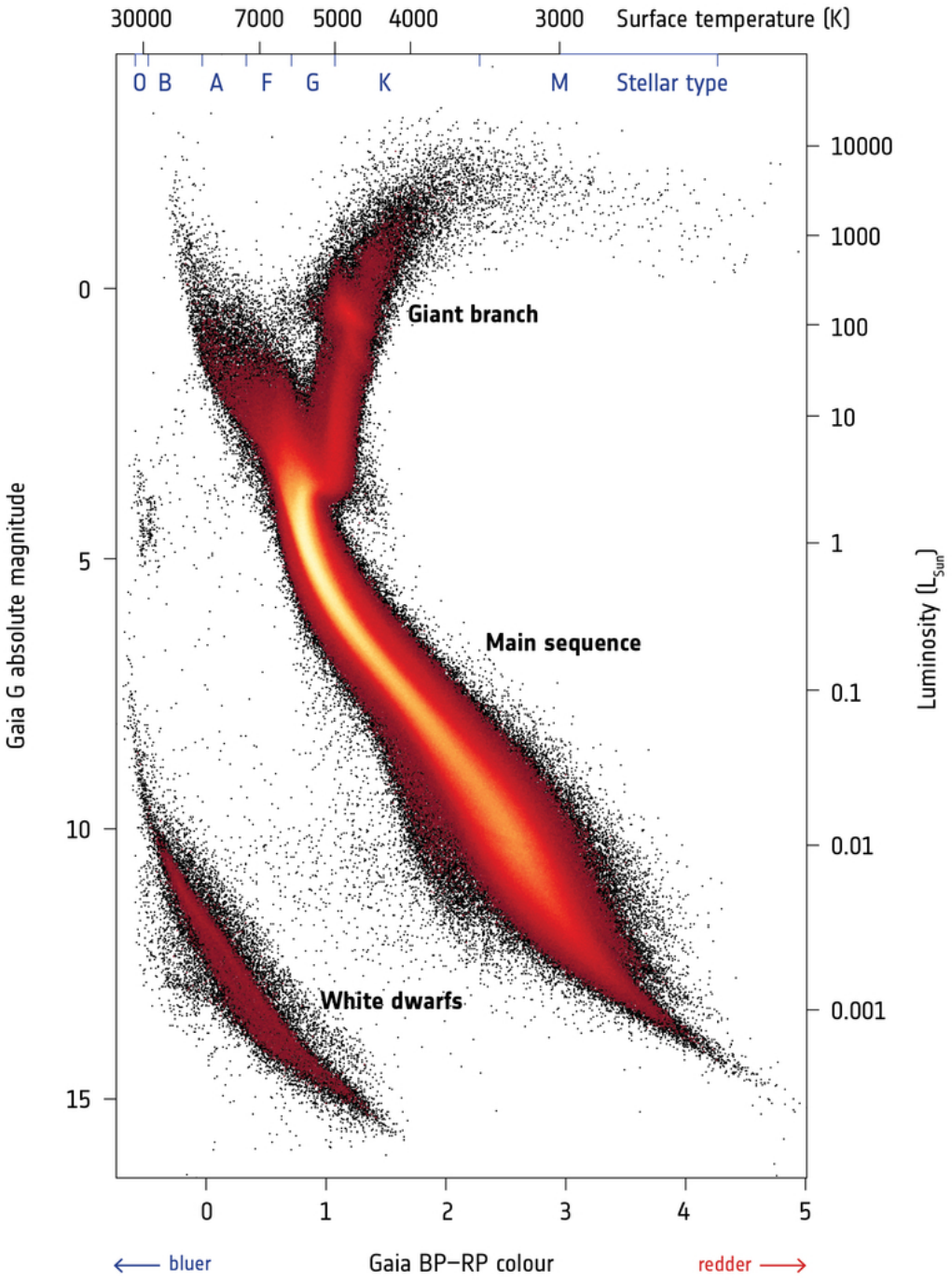

Figure 1.1: Example of a Hertzsprung-Russell diagram, showing the changing position in both temperature-luminosity space and colour-magnitude space. Taken and adapted from Gaia Collaboration et al. (2018a). *Acknowledgement: Gaia Data Processing and Analysis Consortium (DPAC); Carine Babusiaux, IPAG Universit Grenoble Alpes, GEPI Observatoire de Paris, France.*

Spectral Type	Mass ($M_\odot$)	Radius ($R_\odot$)	Temperature (K)
O	>17.5	>7.53	>31500
B	2.30-17.5	2.09-7.53	9700-31500
A	1.59-2.30	1.79-2.09	7220-9700
F	1.08-1.59	1.12-1.79	5920-7220
G	0.87-1.08	0.82-1.12	5280-5920
K	0.55-0.87	0.56-0.82	3870-5280
M	0.08-0.55	0.11-0.56	2250-3870

Table 1.1: Spectral types and their main sequence stellar properties. We have left out the L spectral type, which is mainly brown dwarfs.Values taken from Pecaut and Mamajek (2013) and associated online table[1].

with the power exponent α depending on the stellar mass. For stars up to 2 solar masses it varies between around 2.3 and 4 (e.g. Hansen and Kawaler, 1994; Salaris and Cassisi, 2005), depending on whether the star is partially or fully convective (see below). Higher mass stars are more luminous than lower mass stars and fuse hydrogen at a higher rate to offset gravitational collapse. Since $\alpha > 1$, these higher mass stars have shorter lifetimes than their lower mass counterparts, despite their larger "fuel" supply. For example, the expected main sequence lifetime for the Sun (G2V spectral type) is roughly 10 billion years (Kippenhahn et al., 1990). However, a low mass (and luminosity) M star is expected to be on the main sequence for hundreds of times the solar lifetime. The lower luminosity of low mass stars manifests itself in two properties - their radius and their temperature. Lower mass stars are smaller and cooler than high mass stars. Therefore, if we were able to observe a set of stars formed at the same time evolve, we would see the highest mass stars burn bright, blue and quickly along their main sequence while the low mass stars would be faint, red and last a long time in the main sequence. However, as we only see individual stars at a snapshot of their lives, we are unable to see this full evolution and instead classify stars based on their observable features, as discussed above.

1.1.2 The Carrington Event

The first detection of a *solar flare* was the detection of the famous "Carrington event" on September 1st, 1859 (Carrington, 1859; Hodgson, 1859). The Carrington event was first detected by Carrington and Hodgson when performing routine imaging of the solar disc to measure sunspot shapes and sizes. Carrington (1859) reported that the "brilliancy was fully equal to that of direct sun-light", however

[1]https://www.pas.rochester.edu/∼emamajek/EEM_dwarf_UBVIJHK_colors_Teff.txt

Luminosity class	Type
I	Supergiants
II	Bright giants
III	Giants
IV	Subgiants
V	Main sequence stars
sd (prefix)	subdwarfs
D (prefix)	white dwarfs

Table 1.2: Yerkes spectral classification.

after 60 seconds (the time taken to call someone to witness the flare) the event had risen and then become "much changed and enfeebled". The event was independently observed by Hodgson (1859), confirming this indeed was a real solar flare. Further confirmation came one day later when the world experienced a solar storm arguably not seen in such intensity since. This was due to the flare-associated *Coronal Mass Ejection* (CME) which bombarded the Earth with a stream of charged particles. This buffeting of the Earth with charged particles caused a series of phenomena, such as aurora (caused by the solar wind being channelled to the poles by the Earth's magnetic field) being visible as far south as Cuba. The storm also had a notable impact on electrical systems at the time, as changing magnetic fields from the storm induced electric currents in telegraph systems. Interestingly, in the cases where telegraph cables hadn't shorted out entirely, systems could send and receive messages even while disconnected from their main power supplies. As Prescott (1860) reports, "such was the state of the line on the 2nd of September, 1859, when for more than an hour they hold communication over the wire with the aid of the celestial batteries alone". While this may sound exciting, it has a dark undertone. The energy of the Carrington event has been estimated at 10^{32} erg (Tsurutani et al., 2003) and is taken as the benchmark figure of the most energetic observed solar flare (at least post-1800). Recent studies have shown that if a Carrington-like flare were to occur today, the associated storm would shut down entire electrical grids and cause the US economy losses of between $6 Bn and $42 Bn per day, with up to a further $7 Bn per day lost globally through damage to supply chains (Oughton et al., 2017). In fact, a smaller scale version of this occurred in March 1989, when an extreme solar storm knocked out the Quebec electrical grid, which was estimated by Lloyd's of London as causing C$13.2Bn worth of damage (Lloyd's, 2013). This 1989 storm is believed to be associated with two X4.5 and M7.3 flares (roughly 10^{31} and 10^{30} erg respectively; Maehara et al., 2015, and described in Sect. 1.2) that occurred a few days before (Boteler, 2019). For these reasons along with reasons of scientific

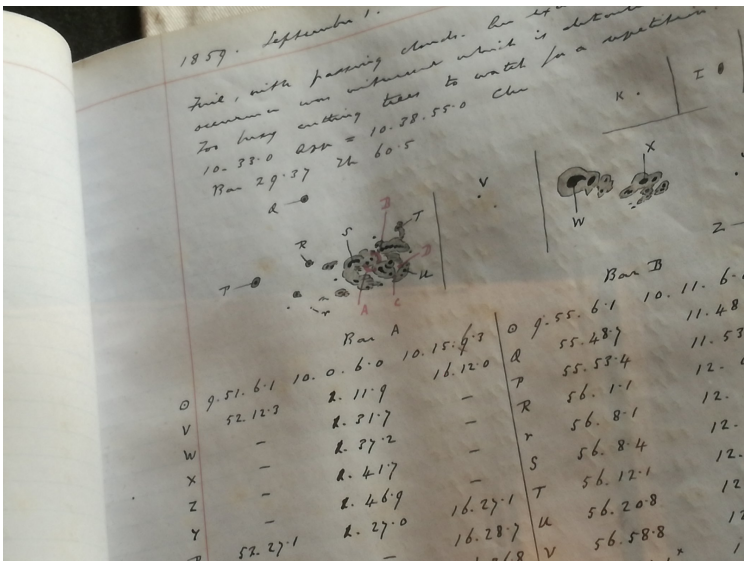

Figure 1.2: Hand drawings of the Carrington flare (A, B, C, D) and associated sunspot groups. Photo taken in the Burlington library by James A. G. Jackman.

curiosity, flares have been a subject of research since 1859.

1.1.3 Stellar Activity Across The HR Diagram

Across the HR diagram we observe a wide range of signals that are related to the magnetic field of the star and are collectively termed *stellar activity*. Many of these behaviours are due to stellar magnetic fields (resulting in the term *magnetic activity* also being used). On the Sun, commonly observed forms of magnetic activity associated with the visible surface (the *photosphere*), and discussed in this thesis, are *flares* and *sunspots*. Flares are sudden outbursts of energy caused by magnetic field reconnection events in the outer solar atmosphere (see Benz and Güdel, 2010, and references therein). In solar white-light observations they are seen as a sudden brightening in an isolated region on the solar surface. The highest energy flares on the Sun are often associated with Coronal Mass Ejections, outbursts of magnetised plasma and energy away from the Sun. These charged particles can impact the geomagnetic field, inducing electric currents. As described above, this was the case for the Carrington event. On the Sun, flares are also often associated with sunspots. Again, this was the case for the Carrington event, as depicted in Fig. 1.2. Sunspots are dark regions on the photosphere where energy transport from the lower regions of the Sun has been suppressed by the magnetic field (see Thomas and Weiss, 2008, and references therein). An example of sunspots is shown in Fig. 1.3. These two forms of magnetic activity are commonly seen on other stars as well, from F down to M and

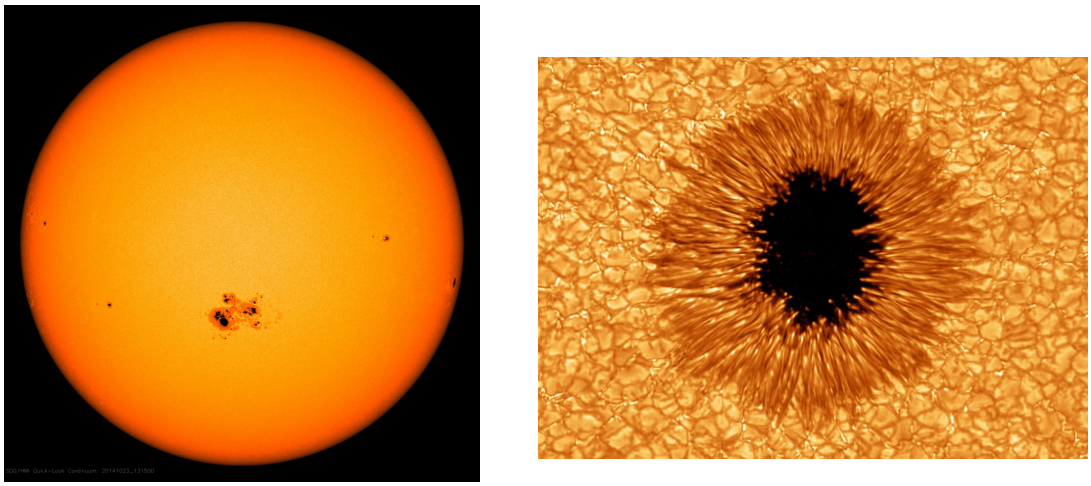

Figure 1.3: Left: SDO/HMI of the solar photosphere from October 2014, showing a large sunspot region associated with active region 12192. Image credit: NASA/SDO. Right: An zoomed in example of a sunspot, observed with the New Solar Telescope at the Big Bear Solar Observatory in July 2010. Note the central dark region where convection and energy transport has been suppressed. Around the spot solar granulation can be seen. Image courtesy of BBSO/ NJIT.

even L spectral types (e.g. Balona, 2012; Gizis et al., 2015). In stellar *photometric* observations, where we measure the total stellar brightness as a function of time, flares appear as sudden spikes in flux followed by an exponential decay. Sunspots, now termed *starspots*, result in periodic modulation of the observed brightness as they move across the visible disc of the star. If we observe multiple cycles of this periodicity we can use starspots to measure the rotation periods of other stars. Another form of magnetic activity seen in both the Sun and stars is the presence of X-rays from the corona, something I will discuss in Sect. 1.1.5. It is understood that in both the Sun and other stars the magnetic field (and associated activity) is driven by the *stellar dynamo*, which converts rotational energy to magnetic energy (e.g. Charbonneau, 2010). By observing magnetic activity on both the Sun and other stars we can improve our understanding of this mechanism, along with the environments both inside and outside the star.

1.1.4 Internal Structure and the Dynamo

It isn't only the surface of the star that changes with stellar mass, the interior structure changes also. For stars with $0.35 M_{\odot} <$ M $< 1.5 M_{\odot}$ the stellar interior is formed of the core, the radiative zone and the convective zone. Nuclear fusion of hydrogen occurs in the core. Above the core is the radiative zone. In the radiative zone energy is transferred by radiative diffusion and thermal conduction, as photons

are absorbed and scattered by electrons (see Kippenhahn et al., 2012, for a detailed explanation). Above the radiative zone is the convective zone, where convection is the dominant method of transporting energy (e.g. Severino, 2017).

For a region to be stable against convection, it needs to have a high enough density gradient such that perturbed parcels of plasma will return to equilibrium (e.g. Maciel, 2015). If the density gradient is too low, then the parcel will be unstable to convection. This instability requirement can be achieved by a high temperature gradient or by high opacities, neither of which are achieved in the hot solar radiative zone. At cooler temperatures further from the centre, opacity increases due to recombination and ionisation of hydrogen and helium, along with trace amounts of heavier elements. For a solar type star, this causes a large enough temperature gradient to result in an outer convective zone. Lower mass (cooler) stars achieve this transition closer and closer to the core, eventually reaching a point where the entire interior is dominated by convection. When this occurs, stars are referred to as *fully convective*. This occurs at M=$0.35M_{\odot}$, or M3-M4 spectral type (Chabrier and Baraffe, 1997).

Between the radiative and convective zones of partially convective stars there is a boundary layer called the *tachocline* (Spiegel and Zahn, 1992). The radiative zone rotates as a solid body with all latitudes moving with the same angular frequency. However, the convective zone undergoes latitudinal differential rotation. For instance, on the Sun the surface rotation period of the equator is around 24 days (e.g. Newton and Nunn, 1951; Balthasar and Woehl, 1980) and gets longer closer to the poles. The tachocline connects the radiative and convective zones together and in turn acts as an intense shearing layer. Fully convective stars would lack a tachocline. The presence of the tachocline is believed to be linked to the dynamo mechanism in partially convective stars.

The Dynamo Mechanism

The dynamo is the physical mechanism within stars that is responsible for the generation of magnetic fields, converting rotational energy to magnetic energy. For partially-convective stars (M>$0.35M_{\odot}$) the mechanism is referred to as a $\alpha - \Omega$ dynamo, or an interface dynamo (for a review, see Charbonneau, 2010, and references therein). In the $\alpha - \Omega$ dynamo, initially poloidal field lines are wound out by differential rotation into a toroidal field (Ω mechanism). The Ω mechanism requires a strong shearing force to stretch out the poloidal field lines, which for partially convective stars is available at the tachocline. This toroidal field can stretch around the entire star and, once formed, parts of the field will rise upwards through the con-

vective zone via magnetic buoyancy. These buoyant regions are twisted as they rise and upon reaching the surface can form magnetic loops anchored in the photosphere but stretching out into the corona (discussed in Sect. 1.1.5). The α mechanism of the $\alpha - \Omega$ dynamo refers to the generation of poloidal fields from the toroidal field. Rising plasma within a convection cell is subject to cyclonic (or helical) twisting, which in turn twists the toroidal field lines. This twisting was initially proposed by Parker (1955) as due to the Coriolis force acting on rising parcels. This twisting, if it occurs over many convection cells can then convert a large scale toroidal field back into a poloidal one, from which the $\alpha - \Omega$ dynamo process can repeat.

The $\alpha - \Omega$ dynamo process requires the presence of a strong shearing layer, provided by the tachocline. So what happens when the tachocline is not present, such as for fully convective stars? As mentioned in Sect. 1.1.3, stars down to L spectral type are known to exhibit signs of magnetic activity such as starspots, X-ray luminosity and flares (e.g. Giles et al., 2017; Wright et al., 2018; Osten et al., 2010). Fully convective stars can be more magnetically active than their higher mass counterparts as well, with West et al. (2015) finding greater proportions of fully convective stars to show signs of chromospheric activity. Polarimetry has found fully convective stars to have strong average surface magnetic fields, with strengths in the kilogauss regime (e.g. Shulyak et al., 2017, 2019). For reference, the average surface magnetic field strength of the quiet Sun is a few Gauss (Solanki, 2009). Clearly, fully convective stars are able to generate intense magnetic fields, despite lacking the tachocline required for the $\alpha - \Omega$ mechanism. One suggested alternative form is the α^2 mechanism (e.g. Chabrier and Küker, 2006). In this scenario, turbulent motions within the convective zone are able to generate and sustain a large scale magnetic field within the stellar interior. Another is the $\alpha^2 - \Omega$ mechanism, in which the convective zone takes a more dominant role in the dynamo (e.g. Houdebine et al., 2017). This mechanism has also been suggested for the Sun's large-scale field (e.g. Racine et al., 2011). However, the exact form of the fully convective dynamo is still a matter of debate.

1.1.5 Outer Structure

Above the convective zone are a series of layers understood to be the external regions of a star. At the base of these layers is the photosphere. The photosphere is what we perceive as the visual surface of a star, as below this layer the star is opaque to visual light. All lightcurves presented in this thesis are observations of stellar photospheres. The photosphere is host to various transient signatures. One example of this is stellar granulation, where convection of cells can be observed (e.g. Müller

et al., 2001). One significant photospheric feature for this thesis are starspots. As described in Sect. 1.1.3, starspots are dark regions where a magnetic field loop has broken through the photosphere (Babcock, 1961) and visually mark the presence of strong *active regions*, regions of enhanced magnetic field. An example of how starspots look on the Sun is shown in Fig. 1.3. The concentrated magnetic flux at the loop footpoints suppresses convection, reducing the energy transferred from the stellar interior (e.g. Zwaan, 1978) to this local region. These regions become cooler and less luminous than their surroundings, resulting in the observed darker spots on the stellar surface. On the Sun, spots occur in pairs (where the loop footpoints are) with opposite polarities (Hale et al., 1919). On other stars spots have been invoked as an explanation for periodic modulation often seen in optical lightcurves (e.g. Zeilik et al., 1990; Bonomo and Lanza, 2012). As the star rotates and the spot passes in and out of view the overall flux received from the stellar surface decreases and then increases, resulting in a periodic signature. Starspots have been observed on spectral types from F down to late M and possibly even early L stars (Balona, 2019; Howard et al., 2019b; Gizis et al., 2013).

Above the photosphere is the chromosphere. The temperature and density of the chromosphere vary as a function of height, with the solar chromosphere becoming hotter and less dense with increasing height. The lower layers have temperatures matching that of the photosphere, roughly 5800 K for the Sun. In the upper layers this reaches up to ∼10,000 K (for a review see Foukal, 2007, and references therein). The spectrum of the chromosphere is therefore awash in ultraviolet and optical emission lines, some of which can be used as indicators of magnetic activity. This is in contrast to the photosphere where the majority of cooling is via continuum emission (in particular from H^-). Chromospheric features commonly used as magnetic activity indicators include the Balmer series, the Ca II H&K lines and He I lines (e.g. Ayres, 2019). On the Sun each line probes a different depth of the chromosphere (e.g. Ca II H&K probes the lower chromosphere/upper photosphere Ayres, 2019), a result of the changing chromospheric temperature. In regions of strong magnetic activity (e.g. plages associated with active regions) these spectral lines go from absorption into emission. In some cases there can be an emission reversal, from absorption and scattering in upper layers of the chromosphere (e.g. Fontenla et al., 2016). The presence of veiling or emission in these lines is taken as signs a star is magnetically active. I use all these lines as indicators of chromospheric activity in Chapters 4, 5 and 6.

Above the chromosphere is the *transition region*, which separates the chromosphere from the corona. The corona is the outermost layer of a star and for the

Sun is comprised of tenuous plasma with a temperature of $\sim 10^6$ K (see Aschwanden, 2006, and references therein). Magnetic field loops which have penetrated the photosphere have their tops in the corona. The corona is the dominant source of solar and stellar X-ray emission, which for the Sun is believed to be dominated by line emission, although there is a continuum component present also. For all late type stars it is believed that the corona is the source of the quiescent X-ray emission. The exact heating mechanism of the corona is still a mystery, as energy must be delivered from the interior to the corona without heating the layers in between. This mystery has its own name - *the coronal heating problem* (Klimchuk, 2006). One suggested solution is the presence of nano- or microflares which occur extremely frequently, delivering energy to the corona and driving its intense temperatures (Parker, 1988; Parnell and Jupp, 2000; Ishikawa et al., 2017; Li et al., 2018).

1.1.6 Stellar Evolution

As mentioned in Sect. 1.1.1, stars have a mass-dependent lifetime. During this lifetime, stars go through a series of stages. The most active stage of a stars life is arguably the pre-main sequence stage. The pre-main sequence stage, which occurs after a star has formed out the molecular gas cloud, but before it reaches the zero-age main sequence (ZAMS) and begins to fuse hydrogen within its core. Pre-main sequence stars start off as luminous fully convective T-Tauri stars. As they age, they undergo gravitational contraction (which is the main source of their heating) and they move along what is termed the *Hayashi track* in temperature-luminosity space (also on the Hertzsprung-Russell diagram) (Hayashi, 1961). As they move along this track they stay at approximately the same temperature while decreasing in radius and luminosity. For stars with masses above $0.35 M_{\odot}$ eventually a radiative zone will form within the stellar interior, after which they move along the *Henyey track* (Henyey et al., 1955) until hydrogen fusion begins.

Pre-main sequence stars can identified in a number of ways. Firstly, the increased luminosity of pre-main sequence stars compared to main sequence stars of the same temperature results in an elevated position on the HR diagram. Secondly, their spectra can be checked for the presence of lithium absorption at a wavelength of 6708Å. Stars form with a finite amount of lithium from their molecular cloud. However, lithium is destroyed at temperatures of around 2.5×10^6 K (Jeffries, 2014). Convective motions transport lithium to hotter regions within the interior where it is destroyed. For fully convective stars below $0.35\, M_{\odot}$lithium burning happens rapidly and photospheric lithium is quickly depleted. For higher mass stars depletion of photospheric lithium is halted by the formation of the radiative zone, which stops

convection of lithium to high temperature regions where it can be depleted. In very young groups of stars there also exists a *lithium depletion boundary*, a mass below which the core temperature isn't hot enough to burn lithium, so lithium reappears in the spectrum (e.g. Basri et al., 1996; Jeffries and Oliveira, 2005). Therefore, the presence of lithium within a spectrum is a sign of youth for stars. I use these two methods to confirm the star in Chapter 4 is a pre-main sequence source. A third method of checking whether a star is pre-main sequence is to check whether it is a known member of a young association or an open cluster. Star forming regions result in many stars, which remain localised for a certain time after formation. Open clusters are good examples of this, as they are collections of stars of the same (or very similar) age within a close region of space (e.g. Janes and Adler, 1982). As the clusters get older they disperse. If a star is a known member of a young open cluster then it will be young also. I use this method in Chapter 7 to find pre-main sequence stars associated with the Orion complex. Another option is to look for signs of a circumstellar disc, which is evidence that the star is young.

1.2 Solar and Stellar Flares

Flares are high energy phenomena caused by reconnection events in the magnetic fields of stars. These reconnection events release energy and accelerate charged particles from the corona down towards the chromosphere and photosphere. Flares can be detected in astronomical surveys via their sudden outbursts of electromagnetic radiation, in particular in optical, ultraviolet and X-ray wavelengths. In this section I discuss solar and stellar flares and the mechanisms which give rise to them. I will initially describe the first observations of solar and stellar flares and how we classify them based on their energies. I will discuss what we learnt from these observations. I will then discuss the process of magnetic reconnection and give an overview of the full standard flare model, focusing on specifically on those detected in optical wavelengths, *white-light flares*.

Flare Energy Scales - GOES and Ergs

After the Carrington event, more and more solar flares and storms were observed. These observations initially focused on the Hα line, which originates in the chromosphere and is sensitive to flares (Benz and Güdel, 2010). In the 1940s the Sun was first observed at radio wavelengths, then in the 1950s rockets and balloons began hard X-ray observations of flares (e.g. Chubb et al., 1957; Peterson and Winckler, 1959). Since the 1970s space telescopes have been observing the Sun in the UV and

X-ray wavelengths. One particular telescope (or rather, a series of telescopes) of note for solar flare studies has been the GOES satellites.

The GOES satellite program is a series of geostationary satellites designed for meteorological and solar observations. Solar observations are performed using onboard X-ray sensors, which obtain Sun-as-a-star observations in two wavebands. These are 1–8Å and 0.5–4Å (Hanser and Sellers, 1996). Observations in these two wavebands have been made by GOES since 1986 and their precursor NOAA SMS satellites since 1974 (Garcia, 1994). Therefore they provide a large and relatively homogenous catalogue of flares, which has made the GOES soft X-rays the go to for solar flare classification. Solar flares are classified by their peak intensity in the 1–8Å band. Five different logarithmic bands are used for classification. These are A, B, C, M and X. A is the weakest, with intensities below $10^{-7}\,\mathrm{Wm}^{-2}$, while X is the strongest with intensities above $10^{-4}\,\mathrm{Wm}^{-2}$. As these bands are logarithmic, an M5 flare is 5 times more energetic than an M1, while an X1 is 10 times more energetic than an M1. Consequently, it can be seen that the X4.5 and M7.3 flares associated with the 1989 solar storm had an energy ratio of 6.16.

Observations of stellar flares are taken using much broader filters than those used in solar observations. Along with this, white-light flares are observed in broad optical filters and often with much longer exposure times than those used for solar flares. Therefore we cannot directly apply the GOES classification scheme for soft X-ray luminosity. Instead, the integrated energies of stellar flares are reported in the cgs unit of *ergs*. An erg is equal to 10^{-7} J. Depending on the study, filter-specific energies or *bolometric* energies can be reported. Bolometric energies are calculated by assuming some shape for the flare spectrum, in order to calculate the energy over all wavelengths. As I will mention in Sect. 1.3 and discuss in detail in Sect. 1.3.2 this is usually a 9000 K blackbody spectrum. The Carrington event, as mentioned above, is estimated to have had a bolometric energy of 10^{32} erg (Tsurutani et al., 2003).

In order to estimate the GOES classification of stellar flares, previous studies have used solar flares observed simultaneously with GOES and other instruments (e.g. *RHESSI* and *SOHO*; Emslie et al., 2012). Emslie et al. (2012) found that approximately one-fifth of the estimated total energy radiated by a solar flare is in the soft X-rays. They found that the emission detected in the GOES 1–8Å band is a good tracer of the total energy. Following this work, Maehara et al. (2015) estimated that 10^{32} ergs (Carrington-energy) is equivalent to an X10 flare, 10^{33} is X100 and so on.

1.2.1 The First Ground Based Stellar Flare Studies

Eventually the study of flares turned to other stars. Namely, could we even detect flares from other stars and what kind of energies would they have? The answers to these questions would be provided in the 1970s when ground based studies began to target nearby active M dwarfs with high cadence electronic detectors. These studies typically observed in the U band filter in order to maximise the flux received during the flare relative to the red photosphere of these low mass stars. Examples of nearby active stars targeted include AD Leo, EV Lac and UV Ceti (Moffett, 1974; Lacy et al., 1976). These studies found that not only could we detect flares from other stars, their energies were approaching or equal to that of the Carrington event. Interestingly as well, these studies showed that these high energy flares could occur regularly, with Carrington energy flares occurring anywhere between 1-50 days from the Lacy et al. (1976) sample. The occurrence rates of these high energy flare events on active M stars were measured and found to be well-characterised by a power law in energy, something I discuss further in Sect. 1.2.4. These power laws meant predictions of even higher energy flares could be made and compared to the Sun. Later surveys carried on this work, moving from individual M dwarfs to larger sets of active and inactive M dwarfs and those of different spectral types. An example of such a survey is that from Hilton (2011), who observed active and inactive M0-M9 stars. These studies confirmed the expectation that active M dwarfs (those with Hα in emission, a sign of magnetic activity) on average flared more often than inactive M dwarfs of the same spectral types. The occurrence rates from these studies could then be used to predict the number of flaring stars in future surveys such as the Legacy Survey of Space and Time (formerly the Large Synoptic Sky Telescope; LSST). Later studies also made use of large scale photometric surveys such as 2MASS (Skrutskie et al., 2006) and the Sloan Digital Sky Survey (York et al., 2000, SDSS;) to detect flares. Repeated visits of these surveys to individual stars meant sparse lightcurves could be constructed and in the case of more focused regions (e.g. SDSS Stripe 82), flare surveys on thousands of M dwarfs could be performed (Kowalski et al., 2009; Davenport et al., 2012). These surveys confirmed the findings of earlier dedicated surveys of M dwarfs and obtained multi-wavelength observations of flares, showing them to be much brighter at bluer wavelengths as expected.

As time went on, targeted studies of M dwarf flares progressed from single filter observations to those in multiple filters. As I will discuss in Sect. 1.3.2 (and is shown in Fig. 1.9), initial broadband photometry of white-light flares suggested that their emission could be modelled with a 9000 - 10,000 K blackbody

(Hawley and Fisher, 1992). However, later high cadence observations of flares in multiple filters (e.g. using ULTRACAM; Kowalski et al., 2011) charted how the colours of single flares changed with time, showing impulsive blue emission giving way to redder fluxes, suggesting a changing flare temperature, instead of a single blackbody feature. Along with this, targeted spectroscopic observations were also being made to constrain the flare spectrum. As I will discuss in Sect. 1.3.2, these observations showed that the white-light spectrum is not strictly a blackbody, but rather a "blackbody-like" feature which could be approximated to a 9000 K blackbody. This "blackbody-like" feature was also found to have changing temperatures throughout the impulsive and decay phase (Kowalski et al., 2013). The "blackbody-like" spectrum showed the presence of absorption and emission features, suggesting multithermal flare emission and hydrogen recombination at work.

It should also be noted that along with targeted observations, more serendipitous flare detections were happening as well. Several serendipitous flare detections from F and G stars in the literature were compiled by Schaefer (1989) and Schaefer et al. (2000). The earliest case was in 1899, when observers were checking the position of a comet using nearby bright stars. During these observations, the G1V type star S Fornacis flared and is reported to have become three magnitudes brighter than usual - something which complicated comparisons to starcharts. Other examples of detections include when a comparison star flared (HD 137050; Olson, 1980) and while searching for meteors in Canada (β Cam; Wdowiak and Clifton, 1985). These flares were the first seen from G type stars other than the Sun. These events also had very high energies (which allowed them to be seen), showing that superflares from stars not dissimilar from the Sun were possible.

1.2.2 Going into space with Kepler

The studies mentioned so far had their limitations. Targets had to be active enough to flare on average once per night and be bright enough so that high signal to noise photometry and spectroscopy could be performed with short exposure times. This resulted in low target numbers (coupled with limited observing time), so while detailed photometric and spectroscopic observations of flares could be obtained, it was difficult to scale these up to larger sample sizes. Along with this, measurements of flare behaviours (e.g. occurrence rates) were biased to the more active stars. The surveys that did exist from the large scale photometric surveys suffered from the opposite problem, in that they had many stars but sparse lightcurves. In order to scale up the flare studies to larger sample sizes, a way of observing thousands of stars with continuous photometry was required.

Wide-field exoplanet surveys provided a way to perform these observations. The principal aim of these exoplanet surveys is to find exoplanets via the *transit method*, the dip in light caused when a planet passes in front of their host star, something I discuss further in Sect. 1.5.1. However, due to the high inclinations required, the chance of a given exoplanet transiting is low. To try and maximise the chance of finding exoplanets, these surveys use wide fields of view to observe many thousands of stars at any one time. To further maximise the chance of detecting an exoplanet and measuring its orbital period, these surveys also monitor single fields for long periods of time (at least months). Consequently, transiting exoplanet surveys provide thousands (if not more) of lightcurves which cover long durations. In the case of space-based missions, these lightcurves are continuous also. As one may have realised, these datasets are also excellent for stellar flare surveys. Thus a new form of flare studies came into being.

The wide-field exoplanet survey to really change things was the *Kepler* mission. The aim of the *Kepler* mission was to "determine the frequency of Earth-size and larger planets in the habitable zone of solar-like stars" (Borucki et al., 2009). It launched in 2009 and observed the same set of hundreds of thousands stars for roughly four years, providing effectively uninterrupted photometry for that period. The homogeneous dataset of lightcurves provided by *Kepler* changed stellar flare studies. Suddenly large scale studies could be performed like never before, to study how flare properties changed across not just across the M spectral type, but others as well. The exquisite precision of *Kepler* meant it could be used to search for flares from K, G and even F stars.

Some active M dwarfs within the *Kepler* field of view were observed in the 1-minute short cadence mode, allowing for studies analogous to those originally performed from the ground. Not only did these studies characterise the occurrence rates of more individual active M dwarfs, they also studied the flares themselves and how they related to other signs of magnetic activity. Davenport et al. (2014) used the 1-minute cadence observations of 885 flares from GJ 1243 to generate an empirical flare model, which is now often used for flare fitting and injection tests (e.g. Gizis et al., 2017b; Ilin et al., 2019). For individual M stars the relation between starspot phase and flare occurrence was investigated (e.g. Hawley et al., 2014), finding no relation between the two. This was in contrast to solar observations, where flares are observed to occur at active regions, where starspots are located (as discussed in Sect. 1.3.)

Along with observing individual stars for longer periods of time than ever before, large scale studies of M dwarf flares were also performed using *Kepler* data.

These used both the 1-minute and 30-minute cadence modes of *Kepler* to study how flare energies, amplitudes and durations varied across K and early M stars. An example of a result from these studies was that the maximum observed flare energy decreases with stellar effective temperature, although early M stars could still flare with energies thousands of times the Carrington event (e.g. Davenport, 2016). The large sample size of flaring and non-flaring stars also allowed for studies of the fraction of flaring M stars. Yang et al. (2017) found from their sample of M stars an increasing fraction of flaring stars for later spectral types, up to almost 50 per cent for M4-M5 stars. One possibility is that these stars remain active for longer periods of their lives than higher mass stars, meaning a random selection of field stars is likely to have a higher fraction of more active stars. Studies of the activity of stars with known ages (such as in Chap. 7) can help constrain this.

It was not just K and M stars that benefited from the arrival of *Kepler*. For G stars, the *Kepler* mission brought a revolution in itself. No longer were serendipitous observations from a collection of surveys with varying methods and equipment required to study these events. Long and short cadence observations from *Kepler* revealed the presence of hundreds of flaring G stars, some with properties similar to the Sun. The initial study of Maehara et al. (2012) found 365 flares from 148 G-type stars and later studies by Shibayama et al. (2013) and Maehara et al. (2015) expanded upon this to discover upwards of 1600 more flares. These studies found the occurrence rates of G star flares to have power laws similar to solar flares ($\alpha \approx 1.75$ Crosby et al., 1993; Aschwanden et al., 2000). This is shown in Fig. 1.4. Shibayama et al. (2013) also found the exact occurrence rate was dependent on rotation, with faster spinning stars showing more flares on average. Other studies took the energy questions a different way and asked whether the energies of these flares went upwards for ever with ever decreasing occurrence rates, or did they saturate at some value? Wu et al. (2015) identified a saturation value of around 2×10^{37} erg for G stars, using the sample of Maehara et al. (2012) that displayed periodic modulation. However, for other spectral types this saturation level hasn't been well constrained.

1.2.3 Stellar Flare Morphology

The ground-based and *Kepler* observations of white-light flares showed that they have a distinctive shape. It can be characterised as an impulsive rise, up to a peak, followed by a gradual decay (e.g. Davenport et al., 2014). An example of a stellar flare is shown in Fig. 1.5. The impulsive rise is the same as the one mentioned in Sect. 1.3.2 which can be characterised with ∼10,000 K "blackbody-like" emission

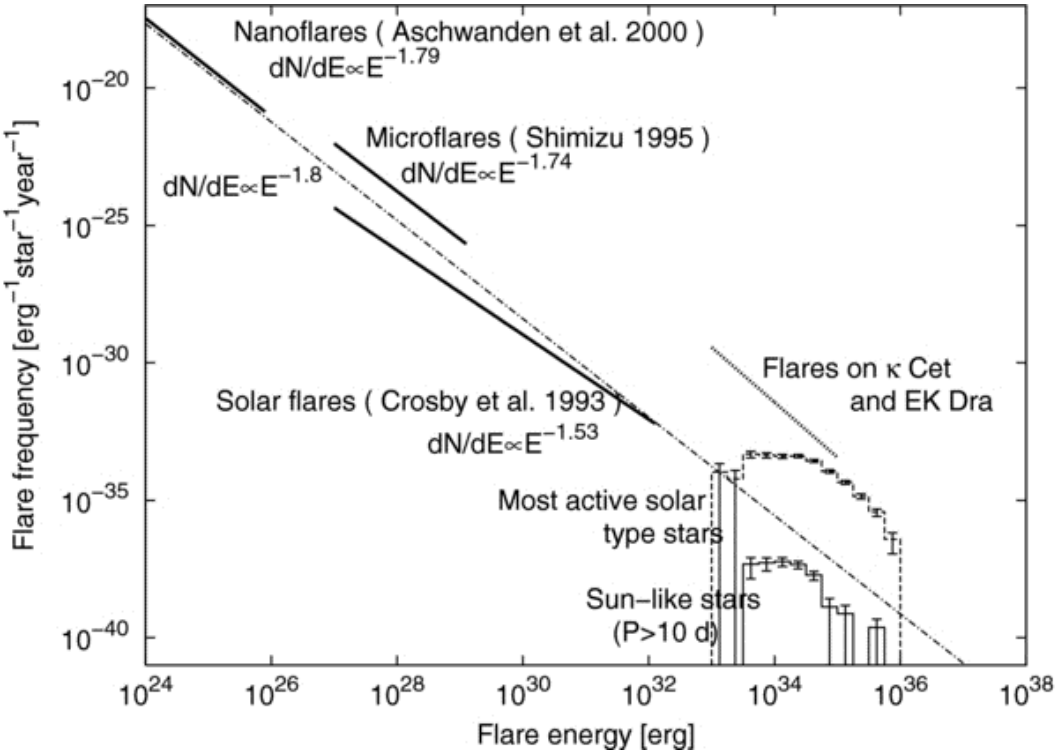

Figure 1.4: Comparison of solar flare and G star white-light superflare occurrence rates observed with *Kepler*. Taken from Shibayama et al. (2013).

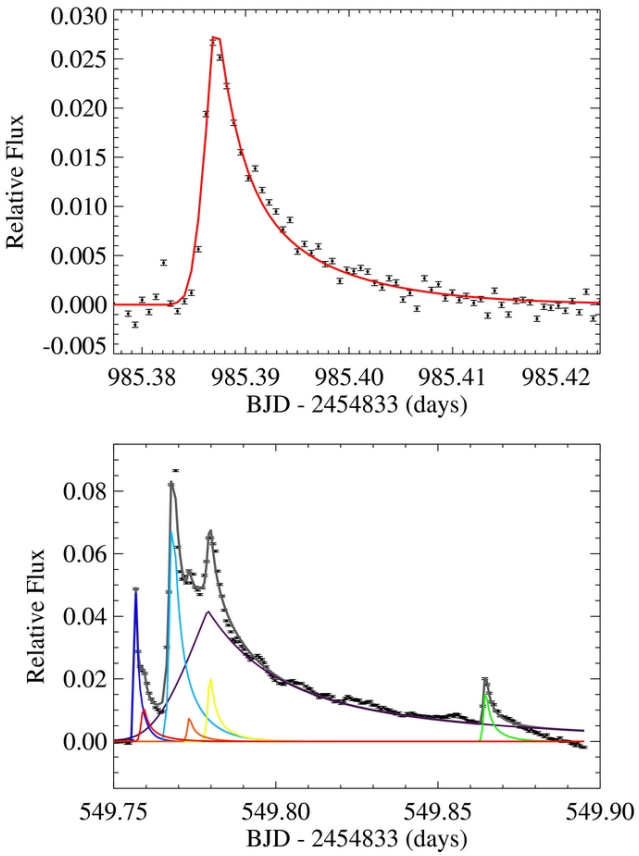

Figure 1.5: Examples of simple (top panel) and complex (bottom panel) flares observed with *Kepler*. The complex flare (in black) has been fit as a series of simple flares, using the Davenport et al. (2014) empirical flare model. Figure taken from Davenport et al. (2014).

(and some absorption). After the impulsive rise is the peak. In many photometric studies the peak appears as a sharp boundary between the rise and the decay. High cadence observations (such as those presented in Chapter 3) have shown instead that it appears more as a rollover and a gradual transition, marking where the cooling of the $\sim$10,000 K blackbody-like feature starts to dominate. The decay of a stellar flare is typically assumed to be an exponential, however many studies have shown it is better fit with two exponential decay components. The initial decay is believed to be dominated by the cooling of the blackbody-like emission (Hawley and Fisher, 1992; Kowalski et al., 2013). The second, typically longer, decay component has been attributed to cooling from the Balmer and other chromospheric emission (Kowalski et al., 2013).

The described features (rise, peak, decays) model single flare events such as the one seen in Fig. 1.5 particularly well. Previous works have been able to incorporate these components into models that are commonly used (e.g. Davenport et al., 2014). These flares are typically called "simple" flares. However, lightcurves often show flares which feature substructure deviating from the simple model. These flares are called "complex". Complex flares usually have multiple flare peaks, such as can be seen in Fig. 1.5. Hawley et al. (2014) and Davenport et al. (2014) found that complex flares generally have higher energies and longer durations than their simple counterparts. These complex flares can sometimes be fitted with multiple single flare events, suggesting they may be a composite feature formed of several simple flares. One possibility is that the multiple flare events have overlapped in time in a random fashion. Moon et al. (2002) found for solar flares this random overlap to be statistically unlikely (from an excess of flares at short waiting times compared to a stochastic process), suggesting "sympathetic flaring" as an alternative mechanism. In this process one reconnection event can trigger others in nearby active regions, resulting in repeated flaring behaviour at short waiting times. On the Sun, flares can be both temporally and spatially resolved to test for correlations between active regions, or large-scale structures linking them together (e.g. Török et al., 2011). However, we are unable to spatially resolve the active regions related to stellar flares. This means that while it is likely very closely spaced flares are related, it is very difficult to confirm whether sympathetic flaring is the cause.

Sometimes stellar flares will also feature more complex substructure. The primary example of this are oscillations of flare intensity with time, called "quasi-periodic pulsations", or QPPs. QPPs are regularly detected in solar flares, however still have relatively low detected numbers from stellar flares. In stellar flares they have been observed in multiple wavelength regimes, including the white-light (e.g.

Balona et al., 2015; Cho et al., 2016; Doyle et al., 2018). The exact cause of these oscillations is still unknown. Multiple mechanisms for their generation have been proposed, such as periodic modulation of plasma heating by MHD oscillations (e.g. Zaitsev and Stepanov, 1982) and periodic reconnection events (e.g. Foullon et al., 2005).

1.2.4 Occurrence Rates

The first targeted studies of flares from nearby active M dwarfs showed that stellar flares occur according to a power law distribution in energy (Lacy et al., 1976). This is typically written as

$$dN(E) \propto E^{-\alpha} dE \tag{1.2}$$

where $dN(E)$ is the number of flares (per unit time) with an energy in the interval from E to dE, E is the flare energy and α is the power law index. From this, a linear relation for the cumulative flare frequency distribution (CFFD) can be written as

$$\log \nu = C + \beta \log E \tag{1.3}$$

where ν is the cumulative flare frequency, C is a normalisation constant and $\beta = 1-\alpha$ (Hawley et al., 2014). The value of α dictates how often high energy flares occur relative to those of lower energy and has been observed to vary across different spectral types. As mentioned in Sect. 1.2.2, the Sun has $\alpha \approx 1.75$ (e.g. Crosby et al., 1993; Shimizu, 1995; Aschwanden et al., 2000). For comparison, M and L dwarfs have had measured α values from 1.4 to 2 (e.g. Paudel et al., 2018b). Examples of observed flare energy distributions and fitted occurrence rates are shown in Fig. 1.6. The value of α also has implications for the environment of the stellar corona. A value of α greater than 2 implies that there is effectively a limitless number of low energy flares that can occur. This is because if write Eq. 1.2 as

$$\frac{dN(E)}{dE} = kE^{-\alpha} \tag{1.4}$$

where k is a constant of proportionality, then the total energy released in some interval is

$$E_{tot} = \int_{E_{min}}^{E_{max}} \frac{dN(E)}{dE} E dE \approx \frac{k}{\alpha - 2} E_{min}^{-(\alpha-2)} \tag{1.5}$$

As E_{min} approaches 0 the total energy release diverges, allowing any power release at small energies, something which does not occur for $\alpha < 2$ (Güdel et al., 2003).

As mentioned in Sect. 1.1.5, if this is the case then these very low energy

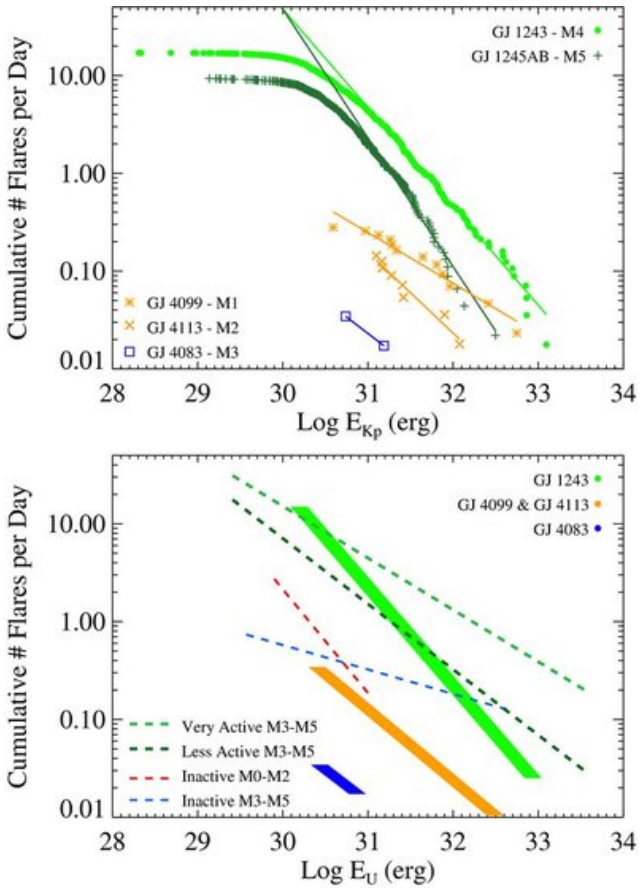

Figure 1.6: Flare occurrence rates for individual active M stars, measured by Hawley et al. (2014) using *Kepler* short cadence observations. Taken from Hawley et al. (2014).

flares (e.g. nanoflares) may be responsible for the quiescent heating and X-ray environment of the stellar corona (Güdel et al., 2003). The value of the normalisation constant C dictates how often flares of a given energy occur. Measuring C means power laws can be anchored to realistic values, making them of use to studies of exoplanet habitability (see Sect. 1.4.2).

Measuring both C and α requires fitting Eq. 1.3 to a measured population of flares. This is either done by fitting Eq. 1.3 directly to measured data, or by first converting to log-log space and then fitting a linear function. Measurements of the flare occurrence rate have been done for a variety of individual stars (e.g. Moffett, 1974; Lacy et al., 1976; Hawley et al., 2014) and for larger samples (e.g. Hilton, 2011; Lin et al., 2019). Studies of flare occurrence rates often note two features which require careful treatment, both of which can be seen in Fig. 1.6.

The first of these features is at low energies and is due to the limiting sensi-

tivity of flare detection. At the highest energies, flares will always be seen in a given dataset — their amplitudes are large enough to trigger any detection algorithm, whether it be automated or by eye. However, as one goes to lower energies fewer flares have an amplitude large enough to trigger detection. Eventually the lowest energy flares will be lost in the noise, cutting off the measured sample. The effect of this is a *turn-over* at lower energies where the observed distribution no longer fits a power law. The lowest energies are usually masked during fitting, with an energy cut-off selected to include the most data but not deviate from an expected power law distribution (e.g. Lin et al., 2019).

The second feature is a break in the observed power law at the highest energies (e.g. Chang et al., 2015). This apparent break has been attributed to both systematic and physical effects. One reason for it being a systematic effect is that the parameter space for highest energy flares has not been fully sampled. This would result in an apparent drop if the observation length covered a flare and most of the time between its predecessor and successor. An alternative theory is that if the highest energy flares are complex flares formed of several single events then these flares would not follow the distribution followed by the lower energy single events (e.g. Davenport et al., 2014). Or it may just be that the highest energy flares are simply intrinsically rarer, possibly due to more complex magnetic configurations being required.

Flare occurrence rates and power laws have been measured for both individual stars and for larger samples. When measuring α and C over large samples the completeness of the sample must be considered. Stars of different magnitudes will have different flare sensitivities, meaning the same energy flare would not be detected on all stars. Different studies account for this by using flare injection and recovery (often using an empirical flare model, e.g. Davenport et al., 2014) or an energy-magnitude consideration using their detected flares. This then allows studies to constrain their analysis to parameter spaces considered statistically complete.

1.3 The Standard Flare Model

In this section I will discuss in detail the mechanisms that give rise to solar and stellar flares. In particular I will elaborate on processes and mechanisms already mentioned in previous sections, such as magnetic reconnection and the generation of white-light flares.

Magnetic Reconnection

Stellar flares are believed to be analogous to those on the Sun and so the same model is applied. This model is called the "standard flare model", or the "CSHKP model" after the major contributors (Carmichael, 1964; Sturrock, 1966; Hirayama, 1974; Kopp and Pneuman, 1976). In this model, depicted in Fig. 1.8, a flare is a series of emission mechanisms caused by an initial magnetic reconnection event. Magnetic reconnection occurs when oppositely directed magnetic field lines within a plasma come together. In the ideal MHD regime, magnetic field lines are frozen into the surrounding plasma, so share its motion. As plasma regions move about, oppositely directed field lines can come together. When this happens, (and lines go into the so-called "diffusion region"; Gonzalez and Parker, 2016), non-ideal MHD effects cause reconnection to occur. The immediate aftermath of reconnection is a change in the overall system topology with new field lines formed. A 2D example is shown in Fig. 1.7, where the existing magnetic field lines travel inwards, reconnect and then new field lines travel outwards. The reconnection event results in the new field lines existing at a lower energy state, with the excess energy being released into the surrounding plasma (with the majority being converted into kinetic energy). Of course, it should be remembered that reconnection is a three-dimensional problem and often is not limited to a single site as is suggested by the 2D example in Fig. 1.7. Instead of occurring at the "X-point" where the field is neutral, reconnection in a 3D body occurs for multiple field lines near-simultaneously in rapid succession wherever a magnetically neutral flux region occurs. It should also be noted that magnetic reconnection isn't just limited to solar and stellar flare events. Field lines in the Earth's magnetosphere undergo magnetic reconnection on both the dayside (magnetopause) and nightside (magnetotail) (e.g. Cassak and Shay, 2007). Reconnection also occurs in laboratory experiments and can be a problem for tokamak fusion reactors, where reconnection events can lead to "sawtooth crashes" and instabilities.

High Energy Emission

According to the standard flare model, magnetic reconnection occurs in the corona. When a reconnection event occurs it kicks off a chain reaction, resulting in emission from radio wavelengths all the way up to hard X-ray and in the most energetic cases, gamma rays. The flux received at different wavelengths allows us to probe different areas of the standard flare model. The energy from the initial reconnection event is released as thermal and kinetic energy, accelerating charged particles

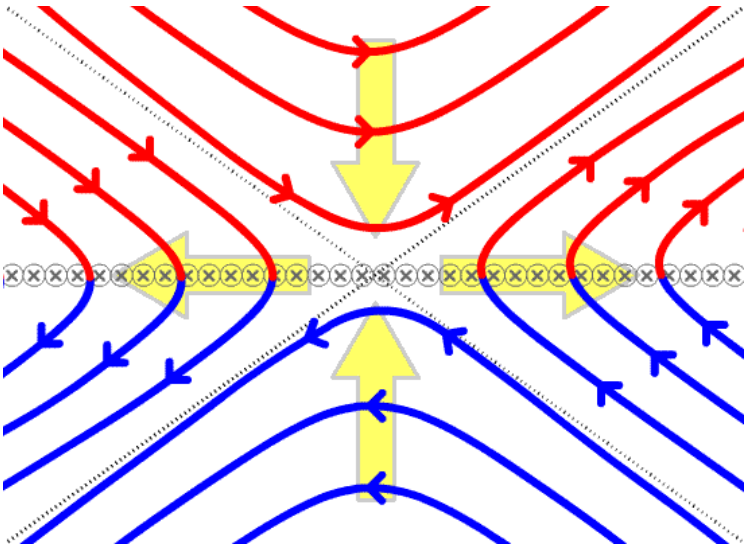

Figure 1.7: Magnetic reconnection in a 2D plane. The red and blue lines indicate magnetic field lines and the yellow arrows indicate the direction of plasma flow. Oppositely moving field lines move with their plasma towards the reconnection site in the centre of the image. There, the field lines connect and proceed to move outwards. During this process the magnetic field lines change their topology and release energy into the surrounding plasma.

in the surrounding plasma downwards towards the chromosphere and photosphere. These non-thermal particles spiral along the newly reconnected magnetic field lines. As they do so, these particles emit non-thermal microwave radiation via the gyrosynchrotron mechanism (Peterson and Winckler, 1958; Kundu, 1961; White et al., 2011).

The accelerated particles then reach the denser plasma of the upper chromosphere and impact this atmospheric layer. As they impact this region they are rapidly decelerated. This deceleration occurs via the bremsstrahlung process, where charged particles slowing down in an external electromagnetic field release radiation. This process heats the surrounding plasma to $\sim 10^6$ K, evaporating it to form a *chromospheric evaporation* (Antonucci and Dennis, 1983; Mason et al., 1986). The plasma is also ionised by the same heating and collisions with non-thermal electrons. At the same time as the chromospheric evaporation, to conserve momentum, heated chromospheric plasma forms a *chromospheric condensation* which is a compression pushing down towards the lower chromosphere (e.g. Canfield et al., 1987; Fisher, 1989). The chromospheric evaporation rises and fills the newly reconnected magnetic field lines, creating what are called *hot flare loops*, or in the past these have been termed *post-flare loops*. These coronal loops are anchored into

the dense plasma at the points of impact, called *flare footpoints*. At the flare footpoints the bremsstrahlung process emits significantly in hard X-rays, while the hot plasma within the loops emits most strongly in the ultraviolet and via soft X-rays. After some amount of time, the hot plasma within the flare loops cools down and condenses back at the flare footpoints.

Solar flares are observed to occur close to or at active regions, where the magnetic field is perturbed. It is thought that active regions provide the magnetic energy required for the particle acceleration and plasma heating. Solar flares are associated with sunspots (e.g. Zirin and Liggett, 1987; Jiang et al., 2012), something that was seen in the first solar flare observations (see Fig. 1.2). Some studies have suggested that reconnection events are driven in part by the twisting of field lines by sunspot rotation. This can be exacerbated by multiple spots in sunspot groups, where the shearing between spots provides energy for the reconnection events (Yan et al., 2018).

Solar flares are sometimes associated with Coronal Mass Ejections (CMEs). CMEs are outbursts of dense magnetised plasma and energy away from the Sun. Flares which are accompanied by CMEs are termed "eruptive" flares, while those which do not are called "confined" flares (Svestka and Cliver, 1992). High energy solar flares (e.g. X class) have been observed to be more likely to have an accompanying CME event than low energy flares (e.g. Yashiro and Gopalswamy, 2009). If particles from the CME outburst reach the Earth, they collide with the magnetosphere, exerting a pressure as they do so. They then travel along the geomagnetic field lines towards the poles, where they reach the atmosphere. The changing currents in the Earth's magnetic field caused by CMEs can induce electric fields on Earth (see Sect. 1.2 for historical examples).

1.3.1 Solar White-light Flares

White-light flares are the component of flares that are visible at optical wavelengths, with optical continuum emission in excess of the quiescent photosphere. Observations have shown solar white-light flares to comprise of continuum emission which can be modelled as blackbody with temperatures ranging between ∼5000 to 10,000 K (Watanabe et al., 2013; Kretzschmar, 2011). This photospheric continuum emission is often interpreted as due to either H^- continuum emission, hydrogen recombination emission (Balmer/Paschen), or some combination of both (Heinzel et al., 2017). The low contrast between the white-light flare optical emission and the quiescent solar photosphere makes the detection of solar white-light flares a difficult task. For this reason, detections are often limited to the highest energy X class flares. How-

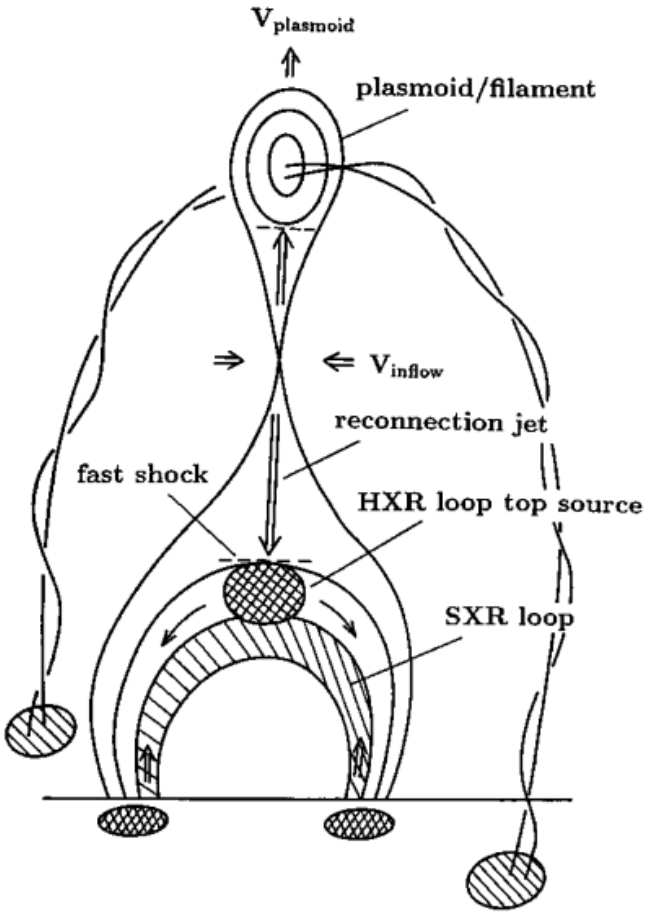

Figure 1.8: An illustrated depiction of the standard CSHKP flare model. Taken from Shibata et al. (1995).

ever, lower energy flares have also been observed to exhibit white-light emission also (C class flares; Hudson et al., 2006), suggesting a common mechanism across a wide range of flare energies.

Unfortunately, the exact emission mechanism of solar white-light flares is currently unknown and there exist many different models and explanations. The white-light continuum emission is typically attributed to emission from the middle/upper photosphere or the lower chromosphere. The majority of solar white-light flares (so called *Type-I*) exhibit a Balmer/Paschen jump in the continuum emission. These flares are well correlated both spatially and temporally with HXR emission, suggesting the accelerated electron jet has a role in the production of the white-light emission (e.g. Xu et al., 2014). This is typically attributed to the ionisation of hydrogen in the chromosphere via an increase in plasma temperature and collisions with non-thermal electrons. However, despite the apparent spatial HXR correlation the source height of the white-light emission remains a matter of debate. Some observations have found the white-light emission to originate lower down than the HXR emission (Watanabe et al., 2010). Other observations have shown the white-light and HXR emission heights to overlap remarkably well (possibly through an optically thin, directly heated, layer; Kerr and Fletcher, 2014), although the apparent emitting volumes have been linked to both the chromosphere (Krucker et al., 2015) and the photosphere (Martínez Oliveros et al., 2012). Observations linking white-light emission to the photosphere then run into problems regarding energy transport (see below).

The other form of white-light flares observed from the Sun are *Type-II* white-light flares, which either show only weak Balmer emission lines or lack them entirely. The continuum emission from these flares appears more consistent with photospheric H^-. The lack of chromospheric emission may point instead to direct heating in the photosphere. Models that require direct heating of the photosphere run into problems regarding the strength of the accelerated electron jet. Solar electron jets are typically not believed to be strong enough to penetrate through the upper chromosphere to directly heat lower layers of both the chromosphere and photosphere. However, observations currently require some method of heating the photosphere to give rise to H^- continuum emission and match observed low emission heights (Watanabe et al., 2010; Martínez Oliveros et al., 2012). Suggestions for such indirect heating include backwarming by Balmer emission or XUV emission from hot flare loops (e.g. Hawley and Fisher, 1992), Alfven waves dissipating energy (e.g. Fletcher and Hudson, 2008), or energy transport by the chromospheric condensations (e.g. Kowalski et al., 2017).

1.3.2 Stellar white-light flares

Stellar flares are energetic events believed to be analogous to solar flares observed on other stars. These events have been observed to occur on a wide range of stars, from F (e.g. Balona, 2015) down to L spectral types (e.g. Gizis et al., 2017a) and with some possibly even occurring on A type stars (Van Doorsselaere et al., 2017). The energies of stellar white-light flares can be orders of magnitude greater in energy than those seen on the Sun, causing some to question whether the stellar flare heating and cooling mechanisms are exactly the same as for the Sun (e.g. Namekata et al., 2017; Heinzel and Shibata, 2018). In this section I will discuss some of the observations of white-light flare behaviour from other stars and outline how these findings are used in my work.

Firstly, it is worth highlighting some of the differences between stellar and solar observations. We are unable to spatially resolve the surfaces of stars (other than the Sun) in our observations. Consequently, we observe the summed flux from the visible disc of the star at any one time. Individual flare events cannot be linked to specific active regions on the stellar surface, nor can we be entirely certain that what we have observed is a single large flare event, or some composition of several smaller events. We are also not able to measure the altitude of emission in the stellar atmosphere. However, observations of stellar flares do have some benefits over their solar cousins. The majority of stars observed in stellar flare studies are more magnetically active than the Sun and have lower effective temperatures (i.e. K and M stars). This means that many low mass stars show high energy flares (relative to the Sun) on a regular basis. Secondly it means that when these high energy flares do occur they appear larger than they would on the Sun, due to the greater contrast between the flare spectrum and the quiescent (cool) photosphere. Spectroscopy of stellar flares also benefit from broadband observations, allowing several emission lines and continua to be observed simultaneously in a single filter.

Similar to their solar counterparts, the exact mechanisms driving stellar flares are currently a subject of debate. Studies of flares using broadband photometry found that white-light flares can be modelled with a $\sim$9000 K blackbody (Hawley and Fisher, 1992), which was interpreted as evidence of photospheric emission, requiring deep heating possibly provided by soft X-ray emission from the hot flare loop. An example of such photometry and the associated flare model is shown in Fig. 1.9. Later simulations of white-light flares by Allred et al. (2006) found that this XUV flux could not adequately heat the photosphere and suggested that the 9000 K blackbody in UBVR photometry could be explained instead by enhanced Balmer and Paschen emission, originating from the heated chromospheric plasma.

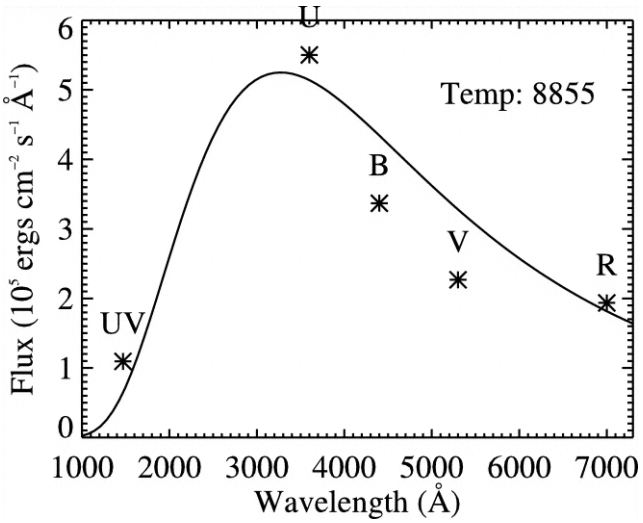

Figure 1.9: UV and UBVR photometry of a flare-only spectrum. Note the appearance of a ≈9000 K blackbody. Taken from Allred et al. (2006).

More recent studies (Kowalski et al., 2013, 2015, 2018) have found white-light stellar flares are better characterised as having ∼10,000 K "blackbody-like" emission. Spectroscopy of M dwarf flares by Kowalski et al. (2013) showed that the impulsive rise of flares exhibited both a ∼9000-14,000 K blackbody-like component (typically attributed to the lower chromosphere/photosphere) and varying strengths of Balmer emission lines (typically attributed to the upper chromosphere). The presence of Balmer emission also results in a Balmer jump above the blackbody feature which can be fit to the continuum. All of these features can be seen in Fig. 1.10. When isolated, the hot blackbody showed signs of absorption (hence "blackbody-like") and appeared similar to the spectrum of an A type star (Vega in particular). The Balmer emission lines also exhibited wing absorption, which Kowalski et al. (2013) took as a sign of chromospheric layers of different temperatures.

Observations show that the blackbody and emission components persist into the decay (shown in Fig. 1.11), although the overall optical emission becomes redder (e.g. Hawley and Fisher, 1992; Kowalski et al., 2016). This was partially due to a cooling of the hot blackbody component (down to ∼8000 K), as seen in Fig. 1.11, but also due to the formation of a secondary redder blackbody continuum (∼ 6000 K), the origin of which is not yet fully understood. One possibility is emission from the heated photosphere (e.g. from Balmer continuum backwarming). Other possibilities include multithermal flare emission and higher order hydrogen continua (e.g. Paschen from recombining chromospheric hydrogen).

Explanations for these stellar flare observations differ from their solar coun-

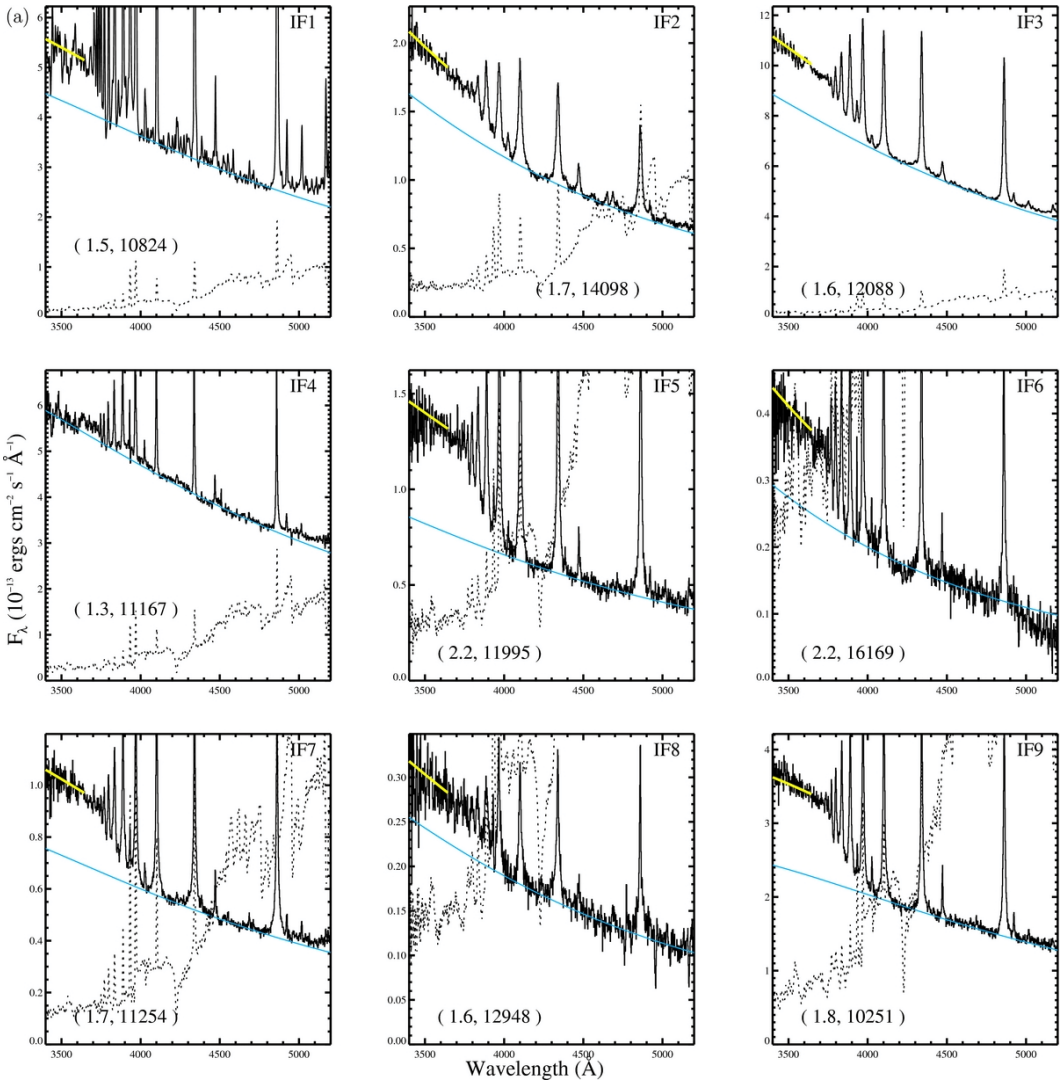

Figure 1.10: Example M dwarf flare spectra at maximum emission, taken from Kowalski et al. (2013). The solid line is the flare spectrum, the dashed is the quiescent M dwarf spectrum. The blue line on each indicates the best fitting Planck function, from fitting to the blue optical emission. The yellow line is a fit to the Balmer continuum emission alone. The χ^2 and temperature for each are shown in brackets. Note the Balmer jump in each.

terparts, in that they are primarily chromospheric rather than invoking photospheric emission. Kowalski et al. (2015) has proposed the $\sim 10,000$ K blackbody-like emission is due to chromospheric condensations. As condensations travel downwards they cool from T$\sim 10^6$ K, reaching T$\sim$10,000 K. Radiative hydrodynamical simulations have been able to model this and generate both blackbody and Balmer and Paschen continuum emission. These simulations can therefore match the observed "blackbody-like" component and Balmer jump, however they currently do not match other signatures such as observed Balmer line broadening. These simulations also currently require electron jets with extremely high densities which may not be available for all flare energies. It has been pointed out that models that focus only on chromospheric condensation emission ignore the effect of the chromospheric evaporation, the plasma of which fills the hot flare loops (Heinzel and Shibata, 2018). Solar coronal loops are long but very narrow features (e.g. Jing et al., 2016), which are usually deemed to contribute negligible amounts of white-light flux. However, the strong magnetic fields (kG; Shulyak et al., 2017) on M dwarfs could result in much larger coronal loops with greater surface areas than their solar counterparts. Heinzel and Shibata (2018) found that these large flare loops could contribute non-negligible amounts of optically thin emission for superflares from active stars. Heinzel and Shibata (2018) argue this will be a mixture of Paschen or free-free emission, with free-free dominating at high temperatures (10^6 K). Again, high flare plasma electron densities for the flare loops are required in this model (10^{13} cm^{-3}), above those seen on the Sun ($10^{11} - - - 10^{12}$ cm^{-3}) but at levels expected from superflares. For comparison, the Kowalski et al. (2015) simulations produce beam electron densities of 10^{15} cm^{-3}. High energy stellar flares may then be a combination of footpoint and loop emission and seemingly in a regime of their own. Models currently do not recreate the cooler blackbody feature during the flare decay. Unfortunately the simulations used to model flare behaviour are computationally expensive, currently limiting their use to the impulsive flare region. This is likely to be an area of focus in the future.

Another area of focus in the future will be the assumption of a single flare temperature. As shown above, while a 9000 K blackbody spectrum is a good first order approximation, recent photometric and spectroscopic observations have shown that the flare temperature changes with time, and can depart significantly from the 9000 K model on short timescales. This in particular can be seen in Fig. 1.10, where some flares reach temperatures of around 15,000 K at maximum emission during the impulsive phase, along with exhibiting a Balmer jump not included in the single temperature model. Consequently, studies using a 9000 K model (including those

presented in this thesis) may underestimate the energy emitted, especially during the impulsive phase. Single filter photometric observations are not able to capture the changing peak temperatures and timescales of the impulsive and decay phase, necessitating the use of a single-temperature model to calculate blackbody temperatures. Multi-filter photometry can avoid these issues in the future by simultaneously sampling different regions of the flare spectrum, capturing changes in flare temperature and allowing more accurate energy estimations.

1.4 Current Observations and the Impact of Stellar Flares

In this section I will discuss how more recent missions and surveys have built upon those outlined in Sect. 1.2. I will also discuss how stellar flares may affect exoplanet habitability, an area of fervent research in recent years.

Pushing mass and age limits with K2

After two of the *Kepler* reaction wheels failed, *Kepler* was reborn as *K2*(Howell et al., 2014). The *K2* mission surveyed a series of fields along the ecliptic for three months each. *K2* observations were driven by a guest investigator program, which led to greater numbers of observations of flares from mid to late M stars. Observations using *K2* even pushed down towards the brown dwarf boundary, detecting flares from L0-L2 stars (e.g. Gizis et al., 2017a,b; Paudel et al., 2018b) and characterising individual L star occurrence rates. These stars were found to still show strong flaring behaviour, with energies and occurrence rate power law indices comparable to early M stars. It also raised the question of when do high energy white-light flares stop being produced? Do they persist beyond the brown dwarf boundary to mid-late L stars, which exhibit aurora-like behaviour in radio observations (e.g. Kao et al., 2018)? Mid-late L dwarfs have also shown signs of activity termed "radio flares" associated with gyrosynchotron emission. If these are analogous to the gyrosynchotron emission from the flare accelerated electron beam, then perhaps some equivalent of white-light flares may be present as well. Unfortunately, due to the low luminosity of these sources only the nearest and earliest L type stars could be observed meaning studies with *K2* were limited. Observations of a single L5 star in *K2* showed no detectable flares, suggesting a cut-off or that such events occur less than once every $\approx$ 100 days (Gizis et al., 2017b). If these flares just happen to be rare, then studies of the mass limit for white-light flares would need to observe the nearest L dwarfs for very long periods of time. An alternative method is to observe many L dwarfs which are too faint to detect normally and wait for one to flare into

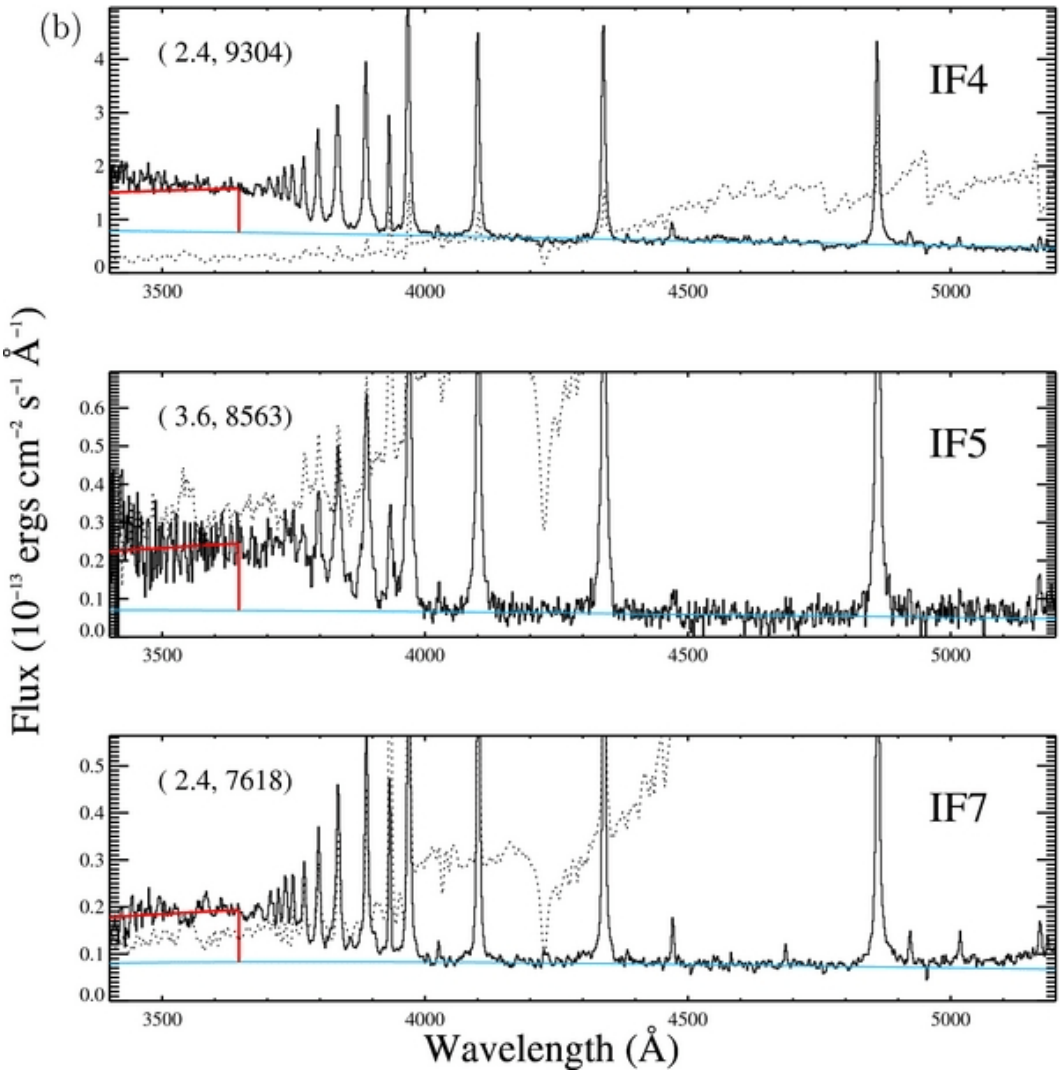

Figure 1.11: Example M dwarf decay phase flare spectra, taken from Kowalski et al. (2013). The solid line is the flare spectrum, the dashed is the quiescent M dwarf spectrum. The blue line on each indicates the best fitting Planck function, from fitting to the blue optical emission. The red line indicates the Balmer continuum emission. The χ^2 and blackbody temperature for each are shown in brackets.

view, which would allow studies to push to lower and lower mass stars. In Chapter 5 I present this method, pushing the cut-off to spectral type L2.5 for the first time.

The opportunity to target stars in upcoming *K2* fields meant that the proposed studies could better keep up to date with the field of research. One example of this was how flaring activity evolves as function of age. Almost all flaring stars within the *Kepler* field of view were main-sequence field stars, making determination of their age difficult. Some studies made use of kinematics in order to broadly classify groups of stars in thin and thick disc populations, while others made use of rotation periods and gyrochronology (Paudel et al., 2018b; Davenport et al., 2019). While these studies could broadly show that flaring activity decreases as stars age and spin down, the age determinations are not precise and could be plagued by external effects (e.g. tidal evolution of binaries). Studies of how flare behaviour changes as a function of age were therefore limited. In the *K2* campaigns various open clusters were targeted. As discussed in Sect. 1.1.6, open clusters are groups of stars associated with the same star-forming region and all have very similar ages. The ages of open clusters can also be determined precisely, from the main sequence turn off on the HR diagram. *K2* observations of the 125 Myr Pleiades and 630 Myr Praesepe open clusters were used to do this, showing a mass-dependent spin down rate between the two ages (Ilin et al., 2019). However, with only two clusters, limited conclusions could be drawn about the nature of this decrease and further observations are needed. This is something I work on improving by studying white-light flares from the Orion complex in Chapter 7.

TESS and *PLATO*

In late 2018 the *Kepler* spacecraft ran out of fuel, bringing the *K2* mission to a close. This however was by no means the end of space-based wide field photometric surveys, as seven months prior to this the Transiting Exoplanet Survey Satellite (*TESS*) was launched (Ricker et al., 2014). The primary mission of *TESS* is to search for transiting exoplanets by observing 85 per cent of the sky in month-long segments. The 2-minute cadence data from *TESS* has already been used for stellar flare work, for instance to continue probing the relation between flares and starspot phase (Doyle et al., 2019) and for large-scale flare studies of energies and occurrence rates (e.g. Günther et al., 2020). However, space based observations come with limitations.

In Sect. 1.2 I explained how the first ground based surveys could obtain impressive amounts of detail about individual flare events, but were limited by their sample sizes. The inverse problem is true for space surveys. Due to telemetry lim-

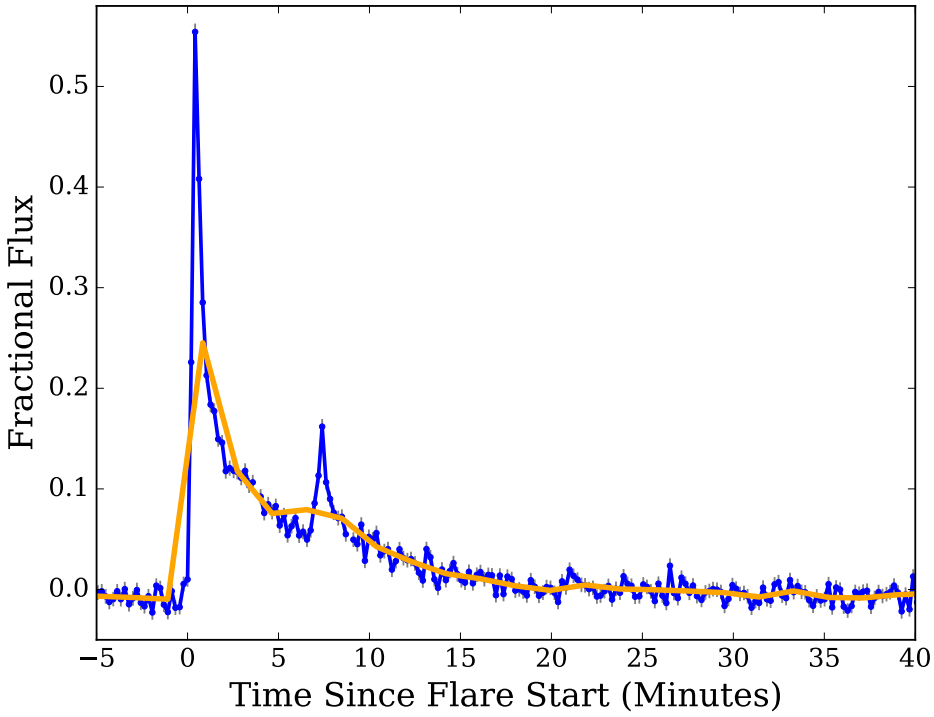

Figure 1.12: Example of how longer cadences can affect flare observations. The blue line is a flare observed with 13 second cadence, the orange line is the same flare simulated at a two minute cadence. Note the decreased amplitude, increased duration and removal of substructure at longer cadences.

itations, the amount of data that can be retrieved from space missions is limited. This manifests itself in two ways, target lists and cadence. Both *Kepler* and *TESS* observe(d) with two cadence modes, long and short. For both missions the long cadence mode is 30 minutes and the short cadence is one and two minutes for *Kepler* and *TESS* respectively. For both missions, the vast majority of stars observed are in the 30 minute long cadence mode. The minority of targets that were selected for the short cadence mode were pre-selected before launch. In fact for *Kepler* all targets were pre-selected before launch and apertures were placed only on those targets. Therefore, if a star flared within the *Kepler* field of view and didn't already have an aperture placed on it, it was not observed. The 2-minute *TESS* targets are also selected before a sector is observed, through a community-driven process. As with *Kepler*, this means that if a target is not selected in advance, it will not have short cadence photometry. However, this is less of a problem for *TESS*, as *TESS* obtains full frame images in which apertures can be placed anywhere. However, again the issue is that these full frame images have a 30 minute cadence, which limits the amount of data that can be obtained. The timescale of stellar flares is minutes to hours. Long cadences can smear out flares, reducing their measured amplitudes and energies. An example of this for 13 second and a 2-minute cadence is shown in Fig. 1.12. From a comparison of the same flares observed in the *Kepler* 1 and 30-minute cadence modes, Yang et al. (2018) found that the energies measured from the long cadence observations alone were reduced by 25 per cent compared to the short cadence data. Without a posteriori correction, this causes studies to systematically underestimate their measured flare energies. Along with this, short duration flares will be missed entirely.

A future space-based transiting exoplanet mission which will avoid these issues is *PLATO* (PLAnetary Transits and Oscillations of stars; Rauer et al., 2014). The primary mission of *PLATO* is to search for planets in the habitable zone of F–K dwarf and sub-giant stars. *PLATO* combines 26 cameras together to have a field of view of $\approx$ 2200 square degrees (*Kepler* had 96) with a observing cadence of 25 seconds. The combination of this cadence and field-of-view means *PLATO* will be a huge step forward for stellar flare studies. Due to the large amount of data to be transmitted back to Earth, lightcurves will be generated on board for selected targets, then beamed back. There is still therefore the inevitable possibility for flares from the faintest stars (especially those of mid-late L spectral type) to be missed. Along with this, the expected launch date of *PLATO* is 2026, meaning the smearing effect of long cadences in space will still be an issue for some time. To get around these issues, other facilities are required.

1.4.1 Back to Earth

In recent years exoplanet surveys have not just gone into space, they've exploded in numbers on the ground as well. Early ground based surveys included SuperWASP (Pollacco et al., 2006), HAT (Bakos et al., 2002, 2004) and KELT (Pepper et al., 2007, 2012). These surveys helped lead the way in the discovery of exoplanets via the transit method, employing wide fields of view to maximise the number of stars observed. Many of these surveys however employed observing strategies (e.g. nod on and off fields), which while good for finding exoplanets, were not particularly efficient for flare studies because of their low cadence.

The more recent ground based wide-field surveys have been able to combine the best of both worlds from previous space missions and targeted studies of flares. Thanks to their wide fields of view, thousands of stars can be observed simultaneously each night. As these surveys are ground based they don't suffer from the data processing limitations that can hold back space missions. Consequently not only can thousands of stars be observed in a single filter at any one time, but full frame images can be observed at high time cadences. This means targets don't need to be pre-selected before observations begin and apertures can be placed anywhere within images. Examples of these surveys include EvryScope (e.g. Howard et al., 2019a) and the Next Generation Transit Survey (NGTS; Wheatley et al., 2018). It is this latter survey that provides the bulk of observations used in this thesis and I describe the survey itself further in Sect. 2.1. Depending on the observing strategy, these surveys can complement those in space and each other. For instance, EvryScope and NGTS both obtain high cadence (2 minutes and 13 seconds respectively) observations of set fields over long time baselines. This allows for precise measurements of flare durations, amplitudes and energies. These in turn can be used to improve our measurements of occurrence rates and also search for flare substructure, which would be missed in long cadence studies. Transient surveys such as ASAS-SN (and LSST in future Kochanek et al., 2017; Ivezić et al., 2019), which search for supernovae (and other events) probe a different parameter space to other studies. ASAS-SN observes large areas of sky every night, making one or two observations per patch of sky before moving on. The huge swathes of sky covered means it can search for the rarest, highest energy, flares from very faint ultracool dwarfs. The flip side of these surveys is that, similar to SDSS, a sparse cadence is employed in order to cover such large patches of sky. The full frame images of higher cadence studies can now also be used to achieve similar scientific goals however, albeit for smaller patches of sky.

1.4.2 Flares and Exoplanet Habitability

In recent years different surveys have begun to detect Earth-sized exoplanets around M stars. Surveys such as MEarth (Irwin et al., 2009) and TRAPPIST (Jehin et al., 2011) have achieved this through the transit technique, where light from the host star is blocked out by the planet passing in front (see Sect. 1.5.1). Other surveys such as the Red Dot program (Escude, 2018) have achieved this through dedicated long term radial velocity programs of nearby M dwarfs, looking for the Doppler shift in stellar lines as the star and planet orbit a common barycentre (see Sect. 1.5.2). Some of the planets being discovered through these missions are in the so-called "habitable zone" (HZ) of their host stars. Examples of this include three of the planets in the TRAPPIST-1 system (TRAPPIST-1e, f, g) (Gillon et al., 2017) and Proxima Centauri b (Anglada-Escudé et al., 2016). The generally accepted definition of the HZ is the orbital region around a star within which an Earth-like planet receives enough heating to have an equilibrium temperature sufficient to retain liquid water on its surface. Due to the low effective temperatures of M dwarfs relative to the Sun, the HZ is much closer in for an M dwarf exoplanetary system than for the solar System. For instance, assuming a moist greenhouse model and using Eq. 2 and Eq. 3 from Kopparapu et al. (2013) the HZ for an M3 star is at approximately 0.14 AU. For an M8 star this shrinks to 0.02 AU. The energy emitted from flares does not scale at the same rates as the stellar luminosity (we can still have mid-M stars showing similar flare energies to G stars; Maehara et al., 2012; Davenport, 2016; Lin et al., 2019). Therefore, having planets so close in to their host star, without a drop in flare energy, will amplify the effects flares might have on their surface and atmosphere. This consequently brings the role of stellar flares in exoplanet habitability into question.

Flares are known to emit strongly at UV and X-ray wavelengths (e.g. Loyd et al., 2018), which are known to contribute to the removal of exoplanetary atmospheres. An example of this in quiescence is for Neptunes such as GJ 436b (Ehrenreich et al., 2015). If flares occur regularly enough then their XUV irradiation could contribute to the removal of upper atmospheres, particularly if those regions are H dominated, influencing the future atmospheric evolution (e.g. Venot et al., 2016). It has been suggested as well that flares may deplete planetary ozone (e.g. Segura et al., 2010; Tilley et al., 2017), although it has been shown that the dominating factor in these events are proton fluxes from flare-associated CMEs. Segura et al. (2010) and Tilley et al. (2017) estimated that for an unmagnetised planet the ozone would be depleted within 8 years if there was a Carrington energy flare and associated CME every week. A magnetised planet would be better protected against

CMEs, however Kay et al. (2016) showed that an Earth-like magnetic field would not suffice. Other studies have also shown that a magnetic field might accelerate atmospheric loss, by channelling charged particles towards the poles (via the same mechanism that results in aurora borealis). For solar flares, CMEs almost always accompany the large X-class flares. Assuming this relation translates to M stars, then almost all flares we observe will be accompanied by CMEs. If the ozone layer is strongly depleted, then the surface will be vulnerable to flare-related UV flux, which may cause biological damage to surface organisms. Organisms residing in the oceans are expected to be sufficiently shielded from this UV flux by the water column above them (Estrela and Valio, 2018).

There may be some positive effects from flares however. Due to their low temperature the peak of emission from M stars is shifted towards redder wavelengths. Consequently, the surface NUV flux levels for planets around M stars is diminished compared to their higher stellar mass counterparts (Rugheimer et al., 2015; Abrevaya et al., 2020). Prebiotic chemistry pathways such as those important for the synthesis of amino acids forebears (e.g. Sarker et al., 2013) and the formation of RNA (e.g. Mulkidjanian et al., 2003) likely require the presence of UV light to occur. In fact, components of RNA and DNA may even require a UV-rich environment to form (e.g. Pollum et al., 2016). If this UV flux isn't present, the required reactions for life-forming components do not occur at an efficient rate and other products can be formed instead. Flares, with their intense UV flux, have been postulated as a way of providing the required irradiation. If flares of a certain energy occur with high enough frequency, they could replace the quiescent NUV flux and reactions could occur on a stop-start basis (e.g. Ranjan et al., 2017). Rimmer et al. (2018) found from lab experiments that this would be a feasible mechanism for the most active M stars. However, it is also the most active M stars that could cause negative effects on their atmospheres through this UV flux and associated CMEs. Along with this, the occurrence rates used by Rimmer et al. (2018) were from *Kepler* main sequence sources. Younger stars are known to be more active and it is feasible that they may still provide the required fluxes at the earliest ages. It is therefore worth knowing what the average and individual flaring behaviour is at all ages to properly understand the exact balance of flare effects and their impact on exoplanet habitability, such as studied in Chapter 7.

1.5 Binarity & Stellar Activity

In Sect. 1.1.3 I explained how we can observe stellar activity signals from stars across the HR diagram. For individual, isolated, stars these signals are strongest at young ages and decrease with time. This is because as stars age they spin down through a process known as *magnetic braking* (Weber and Davis, 1967). Magnetic braking is the process in which the ionised material from the stellar wind is captured by the stellar magnetic field. As the star and its magnetic field rotates, this captured material will rotate with the same angular velocity as it moves outwards. It eventually will escape, carrying some amount of angular momentum with it and slowing the stellar rotation. This spinning down weakens the dynamo mechanism which generates observed magnetic activity such as starspots (e.g. Morris, 2020) and flares (e.g. Paudel et al., 2018b; Davenport et al., 2019). Flares of a given energy are expected to become rarer with age. However, this can change if the star is part of a binary system. When two stars are in a system, tidal interactions between them can interfere with the usual spin-down process. Tidal interactions can spin up one star in the system, which in turn can make it more active than expected for its age. This has been previously observed for individual systems in open clusters (e.g. Wheatley, 1998) and for red subdwarfs (Mace et al., 2018). In the case of red subdwarfs, these Gyr old stars can exhibit superflares after being spun up by a white dwarf companion. Tidal evolution can be an issue for gyrochronology, where the rotation period is required to estimate the age of a star. This is why open clusters are so useful for studies of activity with age, as I exploit in Chapter 7.

The increase in activity can sometimes act as a signpost to the system, as we can spot behaviour we wouldn't expect. One example of this is the red subdwarf—white dwarf system I mentioned above. Depending on the inclination of the system, this can sometimes lead to the detection of eclipses and even transits in wide-field exoplanet surveys. Depending on the mass of the primary star, substellar objects can exert enough torque to interact with and spin up their host star. I present an analysis of such a system in Chapter 6, where the brown dwarf NGTS-7Ab has spun up its host star to a period of 16.2 hours, resulting in strong magnetic activity.

Brown dwarfs are substellar objects with masses between 13 $M_{\rm J}$ and 75-80 $M_{\rm J}$. They reside in the mass region between planets and stars. The lower mass limit is defined as the mass at which deutrium can be fused in the core. The upper limit is when hydrogen can be fused consistently within the core and marks where the stellar regime begins. When brown dwarfs are formed they fuse any available deutrium in their cores. Once this is depleted they are unable to sustain their size

and undergo gravitational contraction, slowly cooling and shrinking. During this process brown dwarfs spin up.

The first detections of brown dwarfs came in the late 1980s, with GD 165B in 1988 (Becklin and Zuckerman, 1988). Although this was first presented as a "low-temperature companion to a white dwarf star", it was later retrospectively confirmed as a brown dwarf after a series of studies showed it to have a L spectral type (e.g. Zuckerman and Becklin, 1992; Kirkpatrick et al., 1993, 1999). In the meantime, other brown dwarf candidates and confirmation were presented. Examples of this include Teide 1 and Gliese 229B (Rebolo et al., 1995; Nakajima et al., 1995). All of these sources were detected in infrared photometric surveys, with GD 165B and Gliese 229B being found as substellar companions and Teide 1 being found as a lone brown dwarf in the Pleiades. Brown dwarfs are identified in photometric surveys as low luminosity sources which appear brightest towards infrared wavelengths. Depending on the system mass and age, brown dwarfs can confirmed by testing their spectra for lithium absorption. Lithium is burnt progressively quickly in brown dwarfs above $50M_{\rm J}$(Baraffe et al., 2015). For masses above $\approx 65M_{\rm J}$ it is burnt in approximately 100 Myr (Chabrier and Baraffe, 2000). As brown dwarfs are fully convective, this process is very efficient. Objects below $65M_{\rm J}$ and older than 100 Myr can be confirmed as brown dwarfs if they show lithium in their spectra. Above $65M_{\rm J}$ brown dwarfs fully burn lithium, meaning that, like low mass stars, lithium absorption is only present at young ages, limiting such a test.

Searching for faint red objects is still a method used to find brown dwarfs today, more recently with surveys such as SDSS and in particular *WISE* (Wright et al., 2010). These surveys are best for lone brown dwarfs and wide companions with common proper motions as the brown dwarf photometry can be identified outright or easily separated out from the host star. For closer in companions, especially those around main sequence stars, such surveys are not able to resolve the separate components. Along with this, the low luminosity of the brown dwarf compared to the host stars means they cannot easily be identified through colours in these surveys. To find brown dwarfs as close companions other techniques are required.

The first of these methods to achieve this was the radial velocity method, the details of which I discuss in Sect. 1.5.2. One of the first dedicated surveys for brown dwarfs acting as companions was performed by Mayor et al. (1998) using CORAVEL and then ELODIE. These were then followed by further precision radial velocity surveys (e.g. SDSS-III MARVELS; Ge et al., 2008; Eisenstein et al., 2011), increasing the sample of substellar companions. While the larger sample of radial velocity discovered systems have been excellent for probing formation and evolution

scenarios, characterisation of individual brown dwarfs from these systems is limited. The objects themselves are too close in to the host for their flux to be detectable and the radial velocity method only gives a minimum mass for the system (if the inclination isn't known). One of the best opportunities for characterising a companion brown dwarf comes from those which transit their host star. Transiting brown dwarfs offer us an opportunity to simultaneously measure both the radius and mass of these objects, constraining their density. If the brown dwarf is bright enough then we can also measure the dayside temperature and luminosity through measurements of the secondary eclipse. The first discovery of a transiting brown dwarf around a main sequence star came in the form of *CoRoT*-3b, a $21.7 \pm 1.0 M_{\rm J}$ brown dwarf around an F3V star (Deleuil et al., 2008). This was shortly followed by the discovery of NLTT 41135B, a $33.7 \pm 2.8 M_{\rm J}$ brown dwarf around an M5 dwarf which itself has a proper common motion partner (Irwin et al., 2010). Further discoveries followed these, with 23 transiting brown dwarfs around pre-main or main sequence stars in total discovered to date (see Šubjak et al., 2019, for an up to date table of all brown dwarfs as of 2019).

However, compared to the many more brown dwarfs identified either as alone or as wide companions there appears to be a dearth of brown dwarfs acting as close companions (usually noted to be $\leqslant$3 AU Marcy and Butler, 2000). This paucity was termed the "brown dwarf desert" (e.g. Grether and Lineweaver, 2006) and is typically attributed to different formation mechanisms for low and high mass brown dwarfs. Some studies have noted that some of the observed paucity may arise from selection effects in transit and RV surveys (most likely for brown dwarfs around M stars; Damiani and Díaz, 2016), although it is likely not the driving mechanism behind the desert. I will discuss the brown dwarf desert in more detail and in the context of NGTS-7Ab in Chapter 6.

1.5.1 Transits

The transit method is the most prolific way of detecting exoplanets to date and serves just as well for brown dwarfs. As a planet passes in front of its host star it will block a fraction of the detected starlight. For a perfect transit, the amount blocked is dependent on the ratio of planet size to the star size. If we know the radius of the star, we can use the fraction of light blocked to measure the radius of the planet using

$$\delta = \left(\frac{R_p}{R_*} \right)^2 \tag{1.6}$$

where δ is the fraction of light blocked, R_p is the planetary radius and R_* is the stellar radius (e.g. Perryman, 2018). Eq. 1.6 assumes no limb darkening, which changes the observed shape of the transit away from a box-shape to something closer to a U-shape.

Stellar limb-darkening is an effect due the non-uniform brightness across the visible disc of a star. An example of this can be seen for the Sun in Fig. 1.3. It occurs due to the changing line of sight of the observer between the centre and edge of the stellar disc. Across the disc the line of sight of the observer penetrates the photosphere at varying angles. At the centre the line of sight is normal to the surface, while towards the limb it penetrates at a shallower angle. This results in an optical depth of 1 being reached at a shallower depth towards the limb than at the centre of the disc. Consequently, we are observing a cooler layer of the photosphere and the disc towards the edge appears dimmer. The net result of this effect is a changing transit depth as the brown dwarf (or exoplanet) passes in front of its host star. An example of this for the transiting brown dwarf *CoRoT*-15b is shown in Fig. 1.13. The deepest part of the transit is in the centre of the disc, where the star is brightest and most light is blocked. In my analysis of NGTS-7Ab in Chapter 6 I used a quadratic limb darkening law,

$$\frac{I(\mu)}{I(1)} = 1 - u_1(1-\mu) - u_2(1-\mu)^2 \tag{1.7}$$

where $\mu = \cos\theta$, with θ being the angle from the centre of the disc. $\frac{I(\mu)}{I(1)}$ is the normalised intensity of the disc and u_n (n=1,2) are limb darkening coefficients. Along with the quadratic formulation for limb darkening there is a linear version and further non-linear formulations (e.g. Claret, 2000) which require increasing numbers of coefficients.

Typically once a brown dwarf (or exoplanet) candidate has been identified in a wide-field exoplanet survey it will be put forward for photometric and spectroscopic follow up observations. Follow up photometry is required for various reasons. From Eq. 1.6 we can see that even if a candidate has a Jupiter radius, if the stellar radius is also large than the transit depth will be shallow. Follow up photometry on a telescope with improved photometric precision (e.g. EulerCam, the SAAO 1.0m telescope, LCOGT) can be used to confirm the presence of a shallow transit. Follow up observations in different photometric filters to the original discovery can be used to rule out eclipsing binaries. Brown dwarfs and exoplanets do not emit significantly in visible wavelengths relative to their host star, therefore their transit depth is relatively constant when observed in different filters. A transiting star will

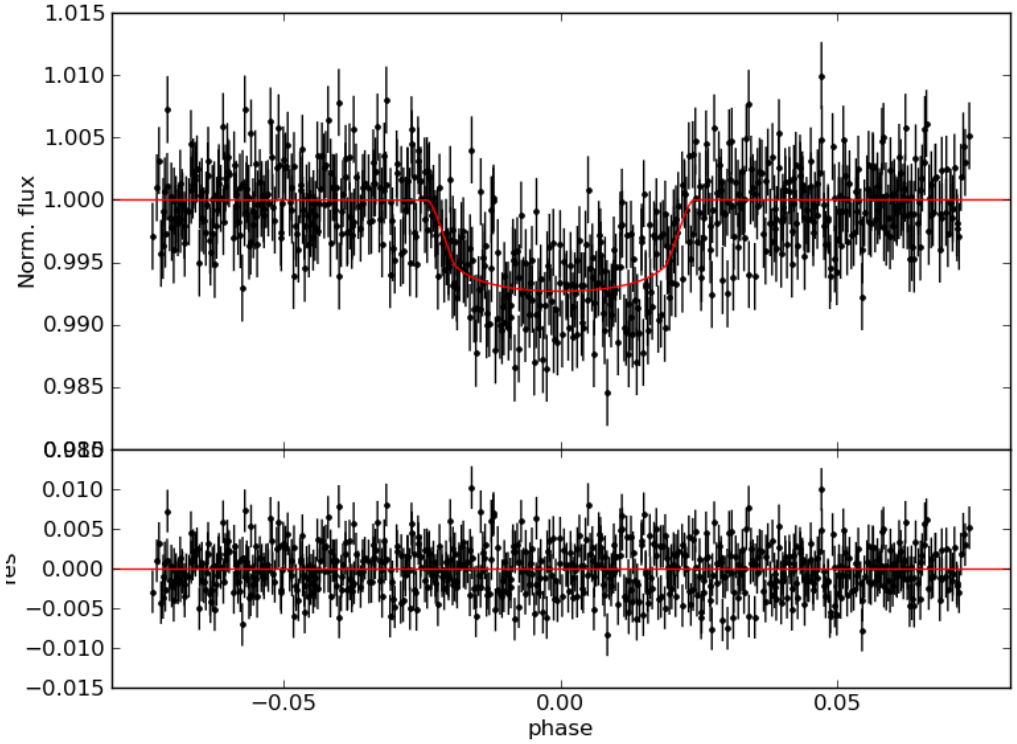

Figure 1.13: The folded, detrended *CoRoT* lightcurve showing the transit of the brown dwarf *CoRoT*-15b, taken from Bouchy et al. (2011).

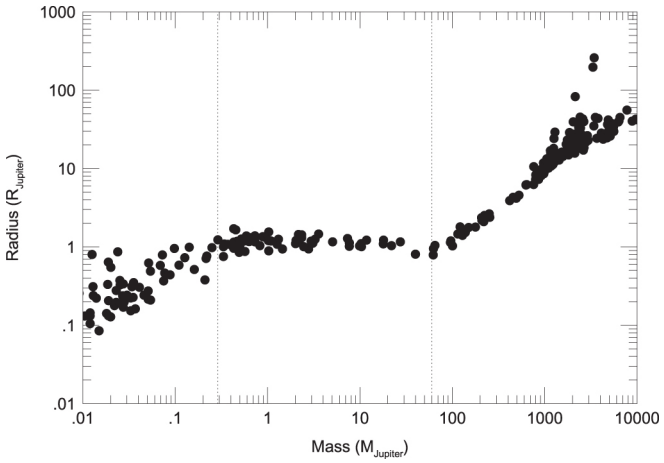

Figure 1.14: Mass-radius distribution for planets (below $13M_{\rm J}$), brown dwarfs (13-$75M_{\rm J}$) and stars (above $75M_{\rm J}$). The dashed lines show the dividing lines for each category. Note the nearly equal radius value for giant planets, brown dwarfs and low mass stars. Figure taken from Hatzes and Rauer (2015).

emit light of its own, with its own temperature-dependent spectrum, so the transit depth can appear significantly deeper in different filters (e.g. Colón et al., 2015). Follow up observations on telescopes with small pixel scales can be used to constrain blended systems as well, something that is particularly important for discoveries from *TESS*. As mentioned in Sect. 1.4, *TESS* has observed 85 per cent of the sky in its primary mission, to search for transiting exoplanets. *TESS* has a pixel scale of $21''$ meaning that targets of interest will be blended with nearby stars (Ricker et al., 2014). Finally, as many brown dwarf and exoplanet candidates are found long after the original observations, follow up photometry can be used to improve candidate ephemerides. The errors in the ephemeris from original observations will propagate with time, which can result in transits arriving early or late compared to predictions. Follow up photometry can refine these parameters. In Chapter 6 NGTS-7Ab was put forward for follow up photometry for all these reasons.

The transit method works equally well for brown dwarfs as it does for exoplanets. However, as seen in Fig. 1.14, high mass planets, brown dwarfs and even the lowest mass stars all have very similar radii (around $1R_{\rm J}$; e.g. Hatzes and Rauer, 2015). Consequently, while the transit method can tell you that you have a Jupiter radius object, due to the mass-radius distribution it is not possible to confirm whether it is a brown dwarf or not based on the transit alone. However, again as seen in Fig. 1.14, these objects do cover a wide range of masses. Therefore, measurements of the mass can be used to sufficiently separate out transiting brown dwarfs from transiting planets or low mass eclipsing binaries.

1.5.2 Radial Velocity

In order for one to determine that their transiting object is a brown dwarf, and not a Jupiter, a mass measurement is required. The way of measuring this is to use the *radial velocity* technique. This technique relies on the fact that in a star-companion system both bodies will be orbiting a common centre of mass, or a barycentre. As the star orbits this barycentre it will periodically move towards and then away from the observer. This causes a Doppler shift in the observed flux from the star, which can be seen in the periodic shifting in spectral lines throughout the orbit. The shift in these spectral lines can be converted into a velocity, whose semi-amplitude K_s is given by

$$K_s = \left(\frac{2\pi G}{P}\right)^{\frac{1}{3}} \frac{M_c \sin i}{(M_* + M_c)^{\frac{2}{3}}} \frac{1}{(1-e^2)^{\frac{1}{2}}} \tag{1.8}$$

where P is the orbital period, M_c is the companion mass, M_* is the stellar mass and e is the orbital eccentricity (e.g. Perryman, 2018). If the period and the stellar mass are known (usually through SED fitting and isochrone modelling), then measurements of the radial velocity semi-amplitude can be used to measure $M_c \sin i$. If the inclination is not known, then this value is a minimum mass. One benefit of transiting systems is that the inclination can be estimated and the mass can be well constrained.

It can be seen from Eq. 1.8 that the measured semi-amplitude is larger for shorter periods, lower stellar masses and importantly, for more massive companions. It is this final point that makes it possible to distinguish transiting brown dwarfs from exoplanets. As an example, the hot Jupiter 51 Pegasi b (Mayor and Queloz, 1995) which has a $M_c \sin i$ of $0.47 M_{\rm J}$, an orbital period of 4.23 days and orbits a star with mass $1.1 M_\odot$. This has a radial velocity amplitude of 59 ms^{-1}. However, a brown dwarf of $50 M_{\rm J}$ on the same period around the same star will have an amplitude of $5.7\,\mathrm{km\,s}^{-1}$. Consequently transiting brown dwarfs can be distinguished from Jupiter mass exoplanets relatively easily through radial velocity follow up. I use this radial velocity method in Chapter 6 to measure the mass of NGTS-7Ab from HARPS observations (Mayor et al., 2003).

1.5.3 Secondary Eclipse

Along with the mass and radius of a brown dwarf, transiting systems can sometimes offer a way of measuring their temperature. As transiting brown dwarfs travel along their orbit they will pass behind their host star. This eclipse blocks out any flux we may have been receiving from the transiting body. For a bright enough transiting

body on a circular orbit this will result in a transit-like feature at phase 0.5 in the phase-folded lightcurve. This however is not a transit but instead is called the *secondary eclipse*. For the vast majority of detected transiting exoplanets and brown dwarfs the amount of flux received from the transiting body relative to the host star is negligible, so this eclipse is not detected in their phase-folded lightcurves. However, for those systems that do emit enough light the secondary eclipse is a powerful tool which can be used to probe the temperature and even the atmospheric structure of the companion (e.g. Charbonneau et al., 2005). If we assume a non-reflective atmosphere, then the flux from the companion will be purely due to its own thermal emission. Measuring the depth will then give an estimate of the effective temperature of the *dayside* of the companion - the side facing the star during the eclipse. If the companion isn't tidally locked (and assuming heat circulation) then this temperature could be taken as representative of the companion equilibrium temperature. If the companion is tidally locked (e.g. HD189733b Knutson et al., 2012) then this measured flux will not be representative of the whole planet, only the dayside. However, it still can give important information about the heat distribution of the body.

In the above I assumed a non-reflective atmosphere, meaning all flux received comes directly from the companion emission. This however is an extreme case, as bodies will usually reflect some portion of the light received. An example of this for an astronomical body is the Moon, which reflects about 10-15 per cent of the light it receives from the Sun (in visual wavelengths) (Warell, 2004), which in turn both helps autumn harvests but frustrates observers. A measure of the amount of light reflected by a body is the geometric albedo, A_g. The geometric albedo is the fraction of flux reflected by a body relative to a *diffusively reflecting* Lambertian disc of the same size. A diffusively reflecting Lambertian disc is an idealised object that reflects any light isotropically (Lambert, 1760). The value of A_g determines the contribution of reflected light to the observed secondary eclipse. This plays off against the thermal contribution, as more reflected light means a cooler temperature is required for the same secondary eclipse depth. A_g=0 indicates that no light is reflected, such as in the case above. Due to the geometric albedo comparing a body to a disc which reflects isotropically, if a body reflects light back along the line of sight it could feasibly have $A_g > 1$. For astronomical objects A_g is usually fit for between chosen limits. These are sometimes physical and chosen based on the Bond albedo (the fraction of incident electromagnetic power re-radiated, which is fixed by definition to between 0 and 1) (e.g. Esteves et al., 2015) and other times chosen purely to explore the parameter space and determine temperature limits.

The balance between the two effects (in a given photometric filter) is encapsulated in the following equation for the eclipse depth $\delta_{eclipse}$,

$$\delta_{eclipse} = \left(\frac{R_{BD}}{R_A}\right)^2 \frac{\int F_{BD}(T_{BD})\, S(\lambda)\, d\lambda}{\int F_*\, S(\lambda)\, d\lambda} + A_g \left(\frac{R_{BD}}{a}\right)^2 \tag{1.9}$$

where $F_{\rm BD}(T_{\rm BD})$ and F_* are the SEDs of the brown dwarf (with temperature $T_{\rm BD}$) and the host star respectively and $S(\lambda)$ is the transmission curve chosen filter. I use Eq. 1.9 in Chapter 6 to analyse the secondary eclipse of NGTS-7Ab and constrain the dayside temperature.

1.6 Thesis Outline

In this thesis I present the results from a systematic search for stellar flares within the datasets of the Next Generation Transit Survey (NGTS). In Chapter 2 I describe NGTS, the methods used to detect flares in lightcurves and how I calculate flare energies. In Chapter 3 I present the detection of superflares from a young G star, showing how such events can now be detected in ground-based photometry. I also present a new empirical flare model, which I compare with those in the literature. In Chapter 4 I present the detection of a giant flare from a pre-main sequence M star. I discuss how the flare was identified and how the star was confirmed as pre-main sequence. In this chapter I identify oscillations in the peak of the flare as quasi-periodic pulsations and apply solar techniques to analyse their cause. I also use these oscillations to estimate the flare loop length, something rarely done for stellar white-light flares. In Chapter 5 I present the detection of a white-light flare from an L2.5 dwarf. This is the coolest star to show a white-light flare to date and one of the largest flares ever detected, with an amplitude of $\Delta V \sim$10. The detection of this flare highlights how the NGTS full frame images can be used to find the biggest flares from the smallest stars. In Chapter 6 I present the discovery of the ultra-short period transiting brown dwarf NGTS-7Ab. With a period of 16.2 hours, this is the shortest period transiting brown dwarf around a main or pre-main sequence star found to date. The brown dwarf has spun up its host star, resulting in NGTS-7A being a tidally locked and active M star. In Chapter 7 I present a study of white-light flares from stars associated with the Orion complex. I use these observations to measure the average occurrence rate of 4 Myr early M stars and compare these measurements to those of previous studies of older stars in order to understand how the flare occurrence rate changes with age. In Chapter 8 I summarise the results of these Chapters and discuss future missions and studies and how these might be

used to study stellar flares and transiting brown dwarfs.

Chapter 2

Methods

"Ah, there's nothing more exciting than science. You get all the fun of sitting still, being quiet, writing down numbers, paying attention. Science has it all."

Principal W. Seymour Skinner (born Armin Tamzarian), *Bart's Comet, The Simpsons*

In this section I introduce and describe the NGTS instrument and outline the methods used to detect flares in lightcurves, verify identified candidates and measure their energies. I also introduce and explain concepts and methods used repeatedly throughout the rest of this thesis. These are proper motion, parallax, SED fitting, Bayes theorem and Markov Chain Monte Carlo methods.

2.1 The Next Generation Transit Survey (NGTS)

The Next Generation Transit Survey (NGTS) is a current generation transiting exoplanet survey located at the Paranal Observatory in Chile. The primary mission of NGTS is to monitor K and M stars in the search for exoplanet transits (Wheatley et al., 2018). In particular, NGTS is searching for Neptune-sized exoplanets within the so-called *Neptune Desert*, a region of mass-period space marked by a lack of detected planetary systems. Neptune-sized exoplanets have very shallow transits (on the order of 0.1%), making them challenging to detect from the ground. In order to detect these transit events, NGTS is designed to achieve a photometric precision of 0.1 per cent in 1 hour for stars brighter than I=13.

NGTS consists of twelve, 20 cm f/2.8, optical telescopes each with a 520-890nm bandpass and exposure times of 10 seconds (Wheatley et al., 2018). The

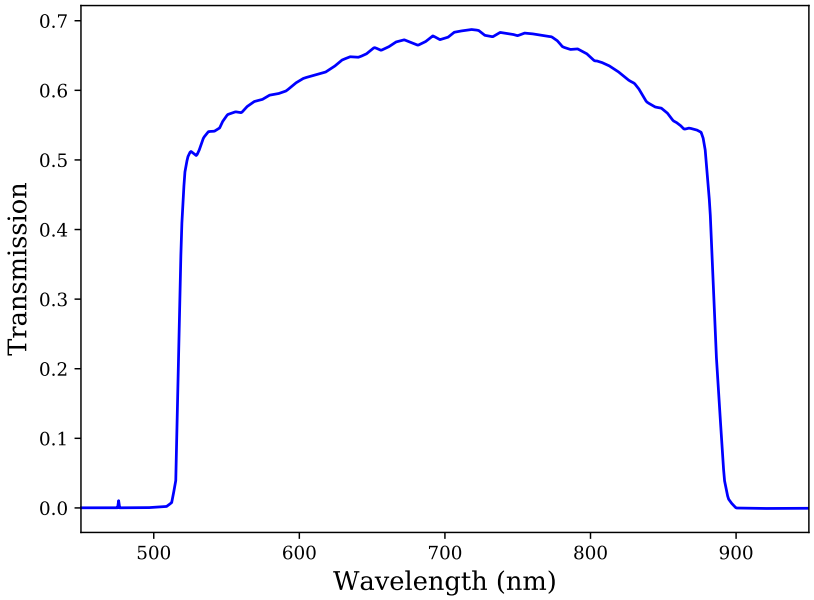

Figure 2.1: The NGTS transmission curve, including the CCD response and filter curve.

bandpass is shown in Fig. 2.1. Each single camera has a field of view of $\simeq 8\,\mathrm{deg}^2$ and combined has a total instantaneous field of view of $\simeq 96\,\mathrm{deg}^2$. The wide field of view of NGTS (comparable to the *Kepler* field of view) means that the high precision observations required for Neptune transits are extended to hundreds of thousands of stars. Each NGTS camera has a pixel scale of $5''$, meaning it is able to resolve targets that would be blended in *TESS* observations. In order to achieve the high photometric precision required, NGTS operates with precise autoguiding. Each telescope is on a separate equatorial mount and uses the DONUTS autoguiding system (McCormac et al., 2013), which is able to keep stars on the same pixels throughout the entirety of a night. This is done through real time analysis of the science images, by collapsing them in the x and y direction and cross correlating these with a reference image. By keeping stars on the same set of pixels, issues related to inter-pixel changes (e.g. flat field noise) in sensitivity can be minimised.

To date, NGTS has made a number of discoveries, in both exoplanet science and other areas of astronomy. In exoplanet science, this includes the discovery of NGTS-4b, a sub-Neptune around a 13th magnitude K dwarf. This was the shallowest ground-based transit detection, found only due to the high precision of the NGTS telescopes. Another discovery from NGTS was NGTS-10b (McCormac et al., 2020), the shortest period hot Jupiter discovered to date. Outside of exoplanet

discoveries, NGTS has discovered many interesting stellar systems. These include M dwarf-white dwarf binaries (of which NGTS is able to resolve the rapid ingress and egress) and M+M dwarf binaries (e.g. Casewell et al., 2018). Along with these discoveries, NGTS is now being used for follow up and vetting of candidates from the *TESS* mission (Ricker et al., 2015).

2.1.1 NGTS Lightcurves and Pipeline Products

The observing strategy of NGTS is for each camera to intensively monitor individual fields, obtaining full frame images with a 13 second cadence. Typically a single camera will observe 3-4 fields each year, for 8 months on average. At the end of a season, when a field is no longer visible, the data are returned to the University of Warwick for reduction and analysis. Datasets are reduced using the custom built NGTS pipeline. For each field, source detection is performed on a supersampled reference image, generated from a stack of NGTS images. In the standard NGTS source detection a limiting magnitude of I=16 is employed. The supersampled reference image is able to detect stars fainter than this, however I=16 is believed to be close to the detection limit for a single NGTS science image. An input catalogue is automatically generated from this list of objects with I<16, ready for use in the photometric pipeline.

The NGTS pipeline is also designed to accept custom generated input catalogues. As NGTS obtains full frame images, these custom input catalogues can specify source positions anywhere regardless of whether the star is detectable in quiescence. I do this in Chapter 5 to detect a flare from a i'=21.46 L2.5 dwarf, a star not normally detectable with NGTS. In all other chapters I use lightcurves generated using the standard source detection algorithm.

To generate lightcurves from the NGTS images the pipeline uses aperture photometry. Individual science images initially have their bias frames subtracted and are corrected for flat field effects. For more detail on how NGTS obtains flat field images, see Wheatley et al. (2018). Apertures are then placed on positions defined by the source list within the reduced science images. The standard NGTS aperture is a circular aperture with a radius of 3 pixels (15″). The sky background for each aperture is obtained from a median-clipped map of non-aperture positions, rather than from an annulus. For data from a given camera, the NGTS photometry pipeline is run for all stars across all available nights, to create a season's worth of lightcurves.

Along with lightcurves, various ancillary products are generated by the NGTS photometry pipeline. Two particularly important files are centroid x and y posi-

tions for each detected source. The centroid is defined as the centre of light of an aperture. For an isolated source we expect the centre of our aperture $x_{ap}(t)$ to be equal to the centre of flux $x_{flux}(t)$. We can define the centroid $\xi(t)$ as the difference in position between the two, or

$$\xi(t) = x_{flux}(t) - x_{ap}(t). \tag{2.1}$$

For a single source $\xi(t)$ should be consistent with zero. However, for a blended source there is an offset from the primary source due to the secondary flux contribution. This offset will change if one of the stars brightens or dims, for example during a flare or transit events respectively. Previous works have shown that the centroid positions are a useful way of vetting transit candidates (Günther et al., 2018). Multiple stars in an aperture will dilute the amplitude of an astrophysical signals. One example of this is if there are two stars in an aperture, one bright (the target) and a fainter source. If the fainter source is an eclipsing binary with a deep eclipse depth, the combined signal from the two stars may look like a exoplanet transit signal (as the brighter star will dilute the eclipse depth). During the eclipse the aperture centroid will move, not only telling us that the signal may be suspect but also which star the signal is coming from, which can then be analysed further. This method has been used previously to vet *Kepler* planet candidates (e.g. Bryson et al., 2013). The precise autoguiding combined with the $5''$ pixel scale means it has also been proven as a viable vetting method in NGTS transit searches, in particular being useful for ruling out blended eclipsing binaries. I use NGTS centroids to confirm flare and transit candidates in all science chapters in this thesis.

Detrending

Once lightcurves have been generated they are detrended using the SYSREM algorithm (Mazeh et al., 2007). Typically in astronomical observations a target star and a comparison star are observed. The comparison star is used to remove systematic effects from the target data, such as trends due to changing atmospheric extinction throughout the night. For wide field observations, SYSREM effectively treats every star as a comparison star and searches for trends common across the whole field of view. The common trend is then removed from all lightcurves, although with an object-dependent amplitude. SYSREM is run iteratively in the NGTS pipeline to remove all major first-order trends. The standard SYSREM pipeline also removes 7σ outliers from individual lightcurves. These outliers can often be due to clouds or satellites, introducing excess noise into lightcurves.

Figure 2.2: Telescopes within the NGTS enclosure at Paranal.

These standard SYSREM lightcurves are the ones used when searching for exoplanet transits. However, the flagging and removal of 7σ outliers from lightcurves means that the highest amplitude flares are removed before they can be searched for. Therefore in this thesis I use an adjusted version of the SYSREM pipeline, which does not mask 7σ outliers. The resultant lightcurves keep the observed high energy flare events, however also retain outliers due to clouds and satellites.

2.2 Detecting Flares

The distinctive shape of flares, as discussed in Chapter 1.2.3, means they can be targeted in a relatively simple manner, by looking for consecutive outliers which appear in single lightcurves. However, depending on the exact nature of the dataset different approaches can be taken. For long and continuous datasets such as those available from the main *Kepler* mission, detrending is often initially applied to remove trends in the quiescent flux (e.g. Davenport, 2016). These trends can be due to long term systematics or due to the star itself, notably from starspots travelling across the visible disc of the star as the star rotates. Basic versions of this detrending use a rolling median filter to remove variability. The smoothed lightcurve is then used to remove the long term features, ideally leaving a flat lightcurve with

flares remaining. These methods require the filter window to be longer in duration than any expected flares and often a period of one or two days is chosen (e.g. Pugh et al., 2015). More advanced versions of this detrending technique use multiple steps with varying filter timescales and initial sigma clipping, to fully remove any underlying variations and to keep as many flares as possible. These flattened lightcurves are then searched for outliers above some threshold (often based on the standard deviation of the data), which are chosen as flare candidates.

For ground-based observations such as with NGTS a different technique is required. This is because continuous observations are not possible from the ground, thanks to the day-night cycle. As a result, smoothing filters are not able to accurately model any variations with timescales on the order of a day. Instead, for a given star observed with NGTS, individual nights are directly searched for flares without any prior detrending. Flare timescales are typically minutes to hours, meaning a full flare can usually be observed in a given night. Flares with large enough amplitudes will dominate the variance of a given night, meaning that apart from the strongest rotators any stellar modulation can be ignored.

To flag flares in a given night, I calculate two statistics. First is the median flux value of the night. The second is the median absolute deviation (MAD). The MAD is calculated by taking the median of the absolute deviations from the median, or

$$MAD = median(|x_i - \overline{x}|) \tag{2.2}$$

where $\overline{x}$ is the median value in a dataset and x_i is the ith value in the dataset. The MAD is often used as a robust measure of the variance in a dataset. Unlike the standard deviation it is resistant against outliers, such as those introduced by a flare. Consequently, using these two values gives a measure of the background flux and its variance.

In the NGTS data the median and MAD were used in two ways to find flares. First, individual nights were tested for flares by searching for three consecutive outliers six MAD above the median of the night's lightcurve. An example of this for a real flare detection is shown in Fig. 2.3. Secondly, to search for long duration and high amplitude flares which may dominate the flux distribution of a given night (as in Chapter 5) I search for nights where the night median is 5 MAD above the season median, where the MAD is now of the entire lightcurve. This automated two step process was run on all stars in a given NGTS field of view.

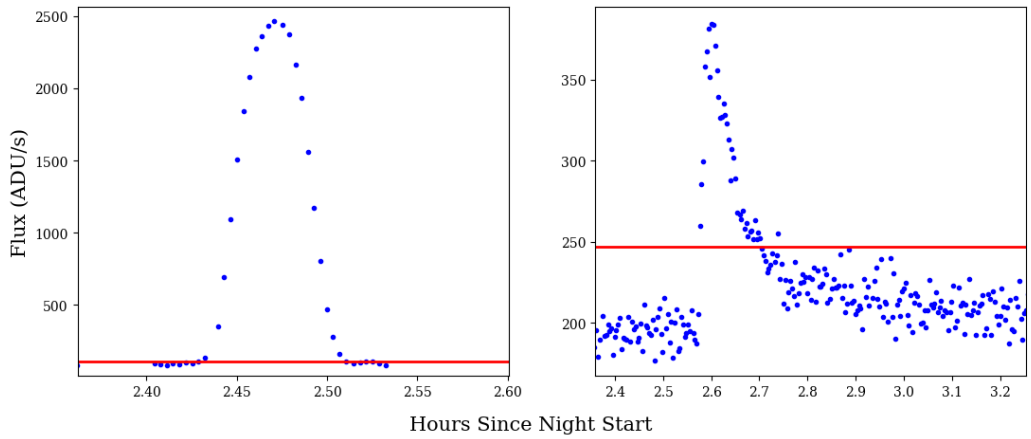

Figure 2.3: Left: An example of a false positive detection, caused by a satellite passing through the chosen aperture. Right: A real flare detection, showing the distinctive fast rise and exponential decay. On both the 6 MAD limit is shown with a red line.

2.2.1 Visual Inspection

Once this automated flagging procedure was complete, I inspected each flagged night visually and removed any false positives. Such false positives can be due to astrophysical events (e.g. short period variable stars), man-made (e.g. satellites passing through our aperture) or systematics (e.g. overlapping apertures). An example of a flare compared to a false positive from a satellite can be seen in Fig. 2.3. This example would likely be removed through visual inspection.

2.2.2 Image Inspection and Centroiding

It is important to be certain of the flare source. If multiple stars reside within an aperture (in aperture photometry), any one of them flaring could result in the observed signal. Without careful analysis this could result in ascribing the flare to the wrong source, e.g. a large flare ascribed to an inactive A star rather than the active M star also in the aperture. One way of verifying flare sources is to check the images themselves. If the flare is large enough and the sources are well separated, then it can be obvious which source is the flaring one. Another method, more quantitative in nature is to check how the centroid of the aperture moves during the flare. During a flaring event we would expect the centroid position to move towards the flaring source. By checking the x and y centroids of an aperture during a flare and combining this with source position information from an external catalogue (e.g. *Gaia* DR2) the true flaring source can be determined.

2.3 Stellar Flare Energies

To calculate flare energies, we used one of two methods depending on whether we could see the star in quiescence.

2.3.1 "Visible" star method

When the star is visible in quiescence, the method used to calculate the flare energy is based on that described by Shibayama et al. (2013), and makes the assumption that the flare and star behave like blackbody radiators in order to estimate the flare luminosity. The total flare energy ($E_{\rm flare}$) can be calculated by integrating the luminosity of the flare ($L_{\rm flare}$) with respect to time,

$$E_{\rm flare} = \int_{\rm flare} L_{\rm flare}(t)\,{\rm d}t. \tag{2.3}$$

The Stefan-Boltzmann relation can be used to estimate the bolometric luminosity of the flare,

$$L_{\rm flare}(t) = \sigma T_{\rm flare}^4 A_{\rm flare}(t), \tag{2.4}$$

where σ is the Stefan-Boltzmann constant, $T_{\rm flare}$ is the flare effective temperature, and $A_{\rm flare}$ is the area covered by the flare. Another estimate of the flare luminosity can be made from the blackbody flux through the instrument bandpass,

$$L_{\rm flare,obs} = A_{\rm flare}(t) \int r_\lambda B_{\lambda(T_{\rm flare})}\,{\rm d}\lambda, \tag{2.5}$$

and similarly the observed luminosity of the projected hemisphere of the star (assuming Lambertian blackbody emission) can be estimated from,

$$L_{\star,\rm obs} = \pi R_\star^2 \int r_\lambda B_{\lambda(T_{\rm eff})}\,{\rm d}\lambda, \tag{2.6}$$

where λ is the wavelength, r_λ is the instrument response function, $B_{\lambda(T)}$ is the Planck function, and $R_\star$ is the stellar radius. From the relationship $L = 4\pi d^2 F$ (where d is the distance to the star and F is the flux) it can be seen that the ratio of two luminosities will be equal to the ratio of two fluxes if the distances are the same. Hence the ratio of the flare and stellar fluxes can be written as,

$$\frac{\Delta F(t)}{F(t)} = \frac{A_{\rm flare}(t) \int r_\lambda B_{\lambda(T_{\rm flare})}\,{\rm d}\lambda}{\pi R_\star^2 \int r_\lambda B_{\lambda(T_{\rm eff})}\,{\rm d}\lambda}, \tag{2.7}$$

where $\frac{\Delta F}{F}$ is the change in flux due to the flare, normalised by the underlying

stellar flux. Rearranging this equation will give an expression for the area of the flare, $A_{\rm flare}(t)$, which can then be substituted into Eq. 2.4 in order to calculate the luminosity as a function of time, $L_{\rm flare}(t)$, and hence bolometric energy of the flare, $E_{\rm flare}$, from Eq. 2.3. We have chosen to calculate the total energy of the flare as opposed to just within the NGTS filter. This is to allow for comparisons of NGTS results to previous studies which followed the method above to calculate the total energy from *Kepler* observations (e.g. Maehara et al., 2012). In order to calculate the ratio $\frac{\Delta F}{F}$, the stellar flux during the flare is determined through linear interpolation, which is reasonable considering in nearly every case the timescale of any modulation of the stellar light curve (for example, due to the rotation of the star and the presence of starspots) is much less than the timescale of a flare. This method makes the assumption that the stellar blackbody emits with the Lambertian cosine law, resulting in an observed emission area of πR_*^2, while the flare emits as a small face-on area. We visually inspect each flare to determine where the start and end points are, which are only used when generating the baseline for each flare. The ratio was then calculated by subtracting this underlying stellar flux from the actual observed flux during the flare, and then dividing by the underlying stellar flux. In order to estimate the uncertainty of the flare energy, Monte Carlo simulations were performed using the uncertainties of the stellar radius, stellar effective temperature, and flare effective temperature. The stellar radius and effective temperature are derived from SED fitting, as I will discuss in Sect. 2.5. These simulations were carried out by randomly sampling each parameter 10,000 times, assuming a normal distribution for each. For each sample, the flare energy was calculated. The uncertainties on the flare energies were measured from the final distribution of the 10,000 calculated samples. The flare temperature was assumed to be 9000 ± 500 K, which is consistent with observations from Hawley and Fisher (1992). An uncertainty of 500 K on the flare temperature is chosen to account for some of the changing blackbody temperatures between flares (e.g. Kretzschmar, 2011; Kowalski et al., 2013). This assumption of a single 9000 K blackbody is commonly made in stellar flare studies (e.g. Maehara et al., 2012; Shibayama et al., 2013; Günther et al., 2020).

2.3.2 "Faint" star method

For stars too faint to be detected in quiescence with NGTS (as in Chapter 6) we calculate the flare energy in a different manner. However, these stars have quiescent magnitudes measured in similar filters by different surveys (e.g. i' band by SDSS). For a given NGTS flare lightcurve we first calculate the instrumental NGTS magnitude at every observation. We then convert this instrumental NGTS magnitude

to a magnitude in the filter in which the quiescent magnitude was measured. This is done through the use of measured zero point between the NGTS filter and the quiescent magnitude filter (e.g. SDSS i' band). For the brightest point in the flare lightcurve we simulate the $9000 \pm 500\,\mathrm{K}$ flare blackbody required to give that observed magnitude. We then multiply the normalised lightcurve by this value for the flare amplitude.

For each observation we integrate the flare blackbody over all wavelengths and multiply by $4\pi d^2$, where d is the distance to the star. This gives the bolometric flare luminosity, which is then integrated over the visible flare duration. These steps give the bolometric energy for the visible duration of the flare, which can be taken as a lower limit of the true value. This is because if there is substructure, or the flare decay persists for a long time below the NGTS detectability limit, it will not be taken into account in the energy calculation.

2.4 Proper Motions, Parallaxes and *Gaia*

Stars are not stationary objects stuck on a two-dimensional sphere above us. Stars have their own motions throughout the galaxy and are located at varying distances from us. Based on stellar colour/ temperature alone, it is impossible to confirm whether an object of some brightness is small, or far away. As shown in Fig. 1.1, a cool main sequence M star has the same colour as a red giant. For studies which want to focus only on main sequence stars (e.g. exoplanet surveys), we need some way of separating out these stars from far-off interlopers. The most successful way of doing this for many years was to use the *proper motion* of stars (e.g. Chromey, 2010). As stars move on their orbits each one will have some relative motion to the solar orbit. Over time, this motion causes these stars to change position in the sky. This is at a rate determined by the projection of their velocity onto the sky. Consequently, nearby stars tend to have higher proper motions than those that are further off. For the furthest stars, such as giants, which may reside kiloparsecs away, the proper motion is very small or negligible despite perhaps having similar absolute velocities to nearer stars. The proper motion of a star can be measured by comparing positions in different catalogues. This meant that any catalogues separated by a long enough timespan could be used to measure proper motions (e.g. UCAC5; Zacharias et al., 2017). A drawback of the proper motion method is that it works best when the motion is perpendicular to our line of sight. Stars moving radially to our line of sight will appear similar to those with low space velocities.

A better method for filtering out giant stars from main sequence samples

is to use their distances. Distances to astronomical objects can be calculated by measuring their *parallax* angle (e.g. Chromey, 2010). For ground-based observers, as the Earth moves along its orbit the apparent position of a nearby star will shift relative to distant background objects. An example of this is shown in Fig. 2.5. The shift in position increases with the baseline separation. Therefore, from Earth the parallax (rather, double the parallax) is best measured using observations separated by 6 months, or a baseline of 2 AU. Once the parallax angle has been measured and the baseline separation is known, the distance can be measured using trigonometry. Or, if the parallax, p, is measured in arcseconds, then the distance, D, in parsecs can be calculated using

$$D = 1/p \tag{2.8}$$

The parallax angles used in distance measurements are extremely small. For reference, the parallax of the closest star, Proxima Centauri, is 0.768 arcseconds (Gaia Collaboration et al., 2018b). For nearby stars, sensitive CCD cameras opened up faint close-by objects such as L and T dwarfs to parallax measurements, which previously could not be detected with photographic plates (Monet and Dahn, 1983; Monet et al., 1992; Dupuy and Liu, 2012). However, observations were still limited by the ability to measure small angles, limitations imposed by observing through the Earth's atmosphere such as atmospheric seeing. The way of getting around this was to go into space.

In 1989 the first space telescope dedicated to astrometry, *Hipparcos*, was launched (ESA, 1997). *Hipparcos* was designed to measure the astrometry of 118,218 pre-selected stars brighter than V=13 to a precision of 1 milliarcsecond (Perryman et al., 1997). *Hipparcos* had a 29cm aperture Schmidt telescope and a field of view of 0.9×0.9 square degrees. A "beam combining" mirror brought two fields of view 58 degrees apart into the same focal plane. During operations, the telescope rotated and tracked the positions of stars as they moved across the two fields of view. As the telescope rotated and stars were repeatedly scanned in different orientations, a catalogue of relative positions (both small and large-scale) was built up and used to measure their astrometry. At the same time, *Hipparcos* also used a star mapping instrument to determine the satellite attitude by observing the positions of known, bright, stars. The information from the star mapper was used to create the *Tycho* catalogue, which contained magnitudes and astrometry for 1,058,332 bright stars (Hoeg et al., 1997). The *Tycho-2* catalogue, an improved re-reduction of the star mapper data, increased this number to 2,539,913 stars (Høg et al., 2000). The Tycho-2 catalogue had a limiting magnitude of V≈12 and a median astrometric precision of 60 milliarcseconds. With these two catalogues, parallaxes and proper

motions for over 2 million stars were available.

The successor to the *Hipparcos* satellite is *Gaia*, the data from which I use repeatedly throughout this thesis. *Gaia* was launched in 2013 and was designed to measure the magnitude, positions and motions for over a billion stars, both in and outside the Milky Way. For a subset of these stars, spectra and colour photometry is measured as well. Like *Hipparcos*, *Gaia* rotates to scan the celestial sphere. However, instead of a single telescope, *Gaia* uses two telescopes separated by 106.5° (Gaia Collaboration et al., 2016b). Both telescopes have a common focal plane, where an array of 106 CCDs are located (Riello et al., 2018). As the stars move across this CCD array, their positions, magnitudes and spectra are measured.

Gaia observes with three filters, *Gaia* G, BP and RP. The *Gaia* G band is a wide bandpass covering wavelengths from 330 nm to 1050 nm. The *Gaia* G band photometry is measured from the same CCD array as the astrometry, using line profile fitting. This method uses source windows of $0.7'' \times 2.1''$, capable of resolving close sources (Arenou et al., 2018). The BP and RP photometry is measured by integrating two low-resolution spectra, covering wavelengths from 330 to 680 nm and 630 to 1050 nm respectively. The tranmission curves for G, BP and RP are shown in Fig. 2.4. The BP and RP photometry is measured from the total flux within a $3.5'' \times 2.1''$region (Evans et al., 2018). This means that sources that may be resolved in *Gaia* G can be blended in the BP and RP photometry. This is something I take into account in Chap. 6 when analysing the NGTS-7 system, which has two M stars separated by $1.14''$. In addition to the BP and RP spectra, *Gaia* also features a dedicated radial velocity spectrometer (RVS), designed to measure the radial velocities of stars brighter than G≈17. For stars brighter than G=10, *Gaia* is designed to have an end-of-mission median parallax error of 6 microarcseconds, which increases to 26 microarcseconds at G=15.

In the second data release of *Gaia* DR2, over 1.3 billion sources had positions, parallaxes and proper motions measured. *Gaia* DR2 is complete down to G=17, although magnitudes are measured down to G≈21. At the faint end, *Gaia* DR2 is able to detect ultracool and brown dwarfs within 20 pc. Beyond this distance, as shown in Chapter 5, these objects are too faint and their distances must be estimated using empirical spectral type-colour-distance relations (e.g. Dupuy and Liu, 2012). *Gaia* DR2 has a median parallax uncertainty of 40 microarcseconds for stars brighter than G=15 (Lindegren et al., 2018). The astrometry of *Gaia* DR2 has been shown to have a global parallax zero-point of 30 microarcseconds (Lindegren et al., 2018). However, Lindegren et al. (2018) also showed that there exist spatial correlations on various scales (1 and 25 degrees) on the order of 40 microseconds in parallax,

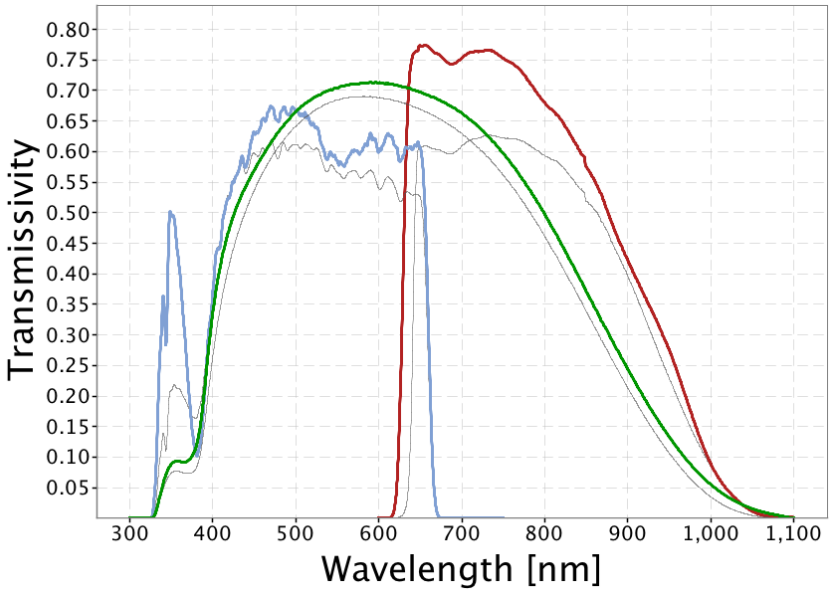

Figure 2.4: *Gaia* DR2 transmission curves. G is the green curve, BP is the blue curve, RP is the red curve. The grey lines show the pre-launch versions, from Jordi et al. (2010). Figure credit: *ESA/Gaia/DPAC, P. Montegriffo, F. De Angeli, C. Cacciari*

which act to increase the uncertainty. These uncertainties can be added to those listed in the *Gaia* DR2 catalogue when used in SED fitting to take account of any spatial correlations and the parallax zero-point. Along with this there exist some sources with spuriously high parallaxes and proper motions, which fortunately do not arise at in this thesis. I use the data from *Gaia* DR2 in Chapters 3, 4, 6 and 7. In particular, I use the parallaxes to identify pre-main sequence stars and during SED fitting to measure stellar radii.

2.5 SED Fitting and Broadband Photometry

In order to measure the properties of a stellar flare or a transiting brown dwarf, we first need to know the properties of the host star. Commonly used stellar properties in this thesis are the effective temperature, $T_{\rm eff}$, and the stellar radius, R_*. The most common method of measuring these properties is through fitting the *Spectral Energy Distribution* (SED) of the star. The SED is the distribution of emitted energy with wavelength or frequency. The SED of a perfect blackbody is described by the Planck function (see Golden, 2013, for a detailed explanation). However, elements and molecules within the stellar photosphere absorb light at different wavelengths.

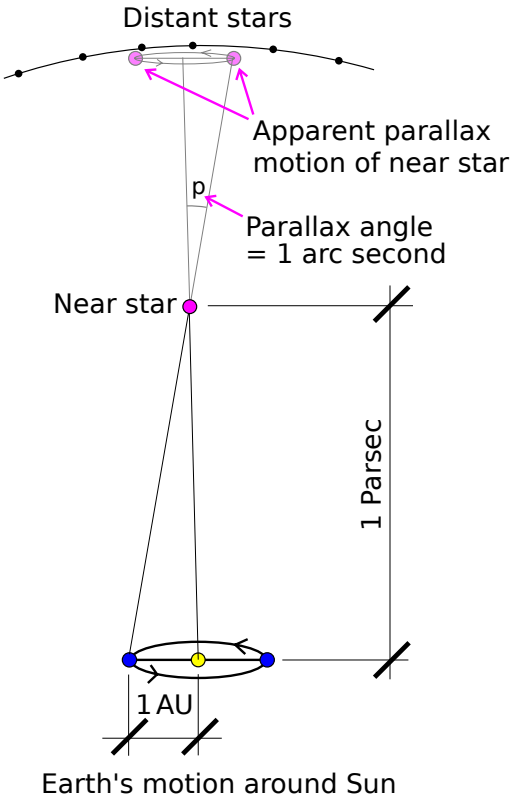

Figure 2.5: An example showing how the parallax angle can be measured. As the Earth moves around the Sun, the apparent position of the near star changes relative to more distance background stars.

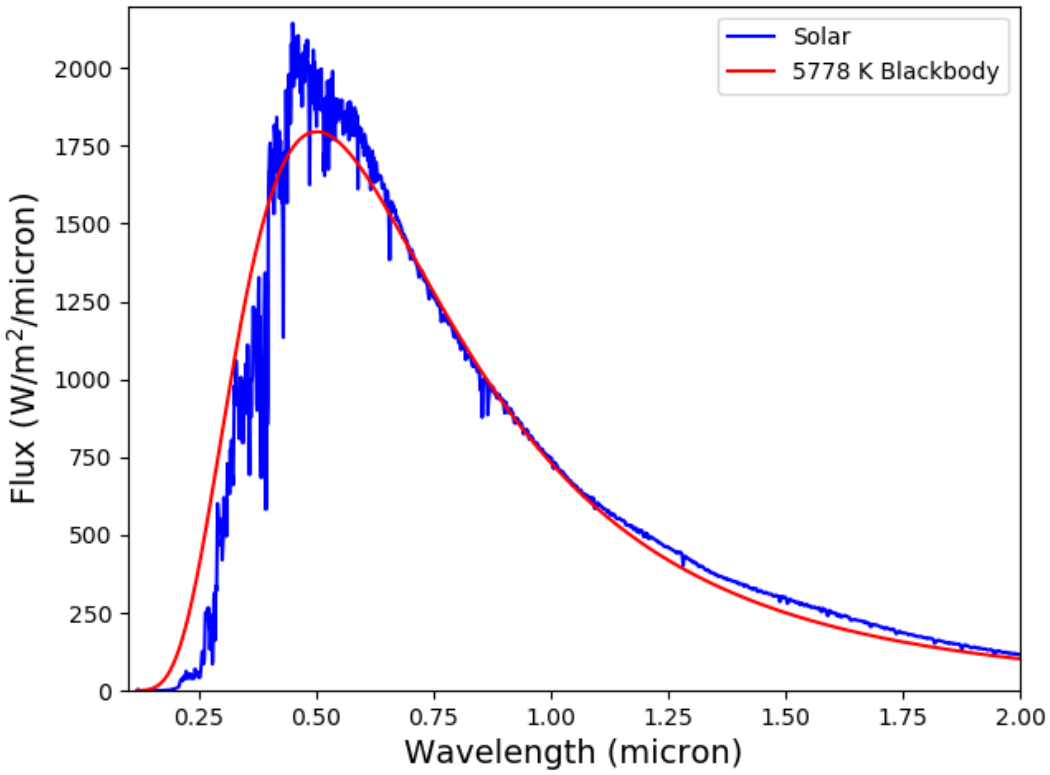

Figure 2.6: Comparison of the solar spectrum (blue) to a 5778 K blackbody (red). solar data is the 2000 ASTM Standard Extraterrestrial Spectrum Reference E-490-00, taken from https://www.nrel.gov/grid/solar-resource/spectra-astm-e490.html

This causes a departure from a perfect blackbody, as light is absorbed. An example of this for the Sun is shown in Fig. 2.6. As discussed in Chapter 1, cool M stars exhibit strong molecular features in their spectra. Consequently, a blackbody spectrum can be a poor fit for the SEDs of these stars. If the absorption lines and opacities of different elements and molecules are known then stellar spectra can be generated synthetically. Studies of line lists and opacities is a vital area of research in astronomy, as without these we wouldn't be able to accurately model stellar spectra.

Over the last 50 years many grids of synthetic stellar spectra have been generated (e.g. Kurucz, 1979). These grids encompass wide ranges of effective temperatures, surface gravities and metallicities. The two grids of atmospheric models used in this thesis are the PHOENIX v2 (Husser et al., 2013) and the BT-Settl grids (Allard et al., 2012). If one already knows the properties of their target star these pre-existing grids can be interpolated across to quickly generate an SED. If the stellar properties are not already known, but some measure of the SED has already

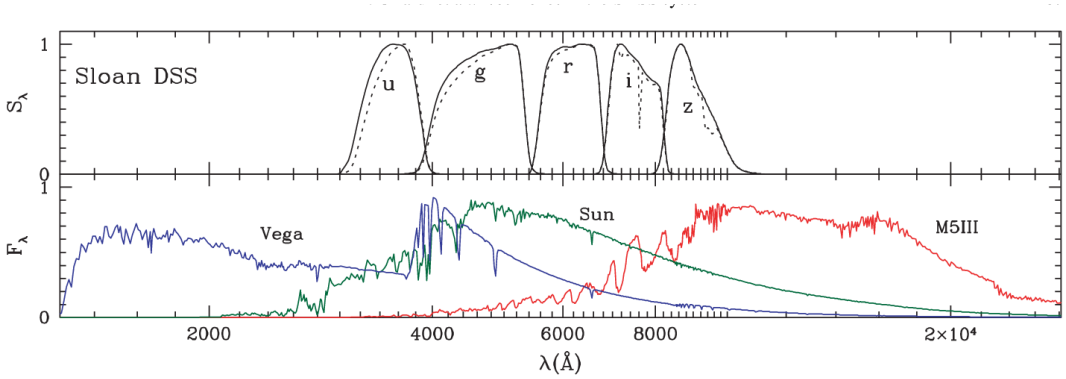

Figure 2.7: Comparison of the SDSS filters (top) with different stellar spectra (bottom). Each filter has been normalised, as in reality the z' filter is much less efficient than the others. Note how the majority of flux from Vega will be detected in u' and g', whereas for the M5 giant star it will be in i' and z'. Figure taken from Girardi et al. (2004).

been obtained, then different spectra can be compared to the SED to find the best fitting parameters.

One way of measuring an SED is to take multiple spectra in different wavelength regimes and stitch them together. This could be done with different instruments, or a single instrument which observes from the UV to near-IR wavelengths, such as X-SHOOTER on the VLT (Vernet et al., 2011). This observed SED can be then compared directly with synthetic stellar spectra. Along with providing a direct measurement of the stellar SED, this method has the benefit of measuring individual absorption lines. These absorption lines can be used to precisely measure surface gravities and also to check for signs of youth, e.g. through the Li 6708Å line. However, this method is also time intensive and therefore not suited to large samples, such as the one conducted in Chapter. 7. An alternate and quicker method is to fit to catalogue broadband photometry.

For centuries astronomers have made catalogues of the sky, charting the positions and brightness of stars. While originally performed using visible light, in the last few decades, surveys have expanded such surveys to cover the whole sky in a wide range of wavelengths. These range from the UV, through the visible and up to the mid-IR. Examples of such surveys include GALEX (Martin et al., 2005), SDSS (York et al., 2000), 2MASS (Skrutskie et al., 2006) and WISE (Cutri and et al., 2014). Importantly, many of these different surveys observed the same patches of sky in different filters. A single photometric filter only transmits photons within a set range of wavelengths. It is opaque to photons outside these limits. Therefore,

for a stellar spectrum a range of different photometric filters will receive light from different parts of the spectrum. An example of this is shown in Fig. 2.7. This means that an individual star, if observed by several surveys, will have catalogue photometry in many different filters. By combining these magnitudes, something akin to a low resolution spectrum can be formed. The grid of synthetic spectra can be convolved with the same set of photometric filters to generate synthetic fluxes (or magnitudes) for each model. This new grid of synthetic fluxes are then fitted directly to the catalogue photometry, in order to determine the best fitting stellar properties.

When fitting it is typical to fit at least for the effective temperature $T_{\rm eff}$, surface gravity $\log g$ and a scaling factor S. The effective temperature, as for a blackbody, determines the overall shape of the SED. The scale factor S determines the amplitude of the SED. The PHOENIX v2 and BT-Settl grids are generated to give the spectrum at the surface of the stellar photosphere. To rescale these spectra to the appropriate stellar radius and distance, the spectrum must be multiplied by S, which is equal to $(R_*/D)^2$ where D is the distance to the star. If the distance to a star is known before fitting, i.e. from *Gaia* parallaxes, then the radius and distance can be fit for directly using the known distance as a prior. Otherwise, only the scale factor can be fit for. Another fit parameter commonly used in this thesis (and in the literature) is an uncertainty inflation term σ. Other fit parameters commoσ is designed to account for underestimated catalogue photometry uncertainties and has the effect of forcing the reduced χ^2 of a fit to unity. It is added in quadrature to the catalogue reported uncertainties. Another fit parameter which is not intrinsic to the synthetic grids, but commonly used, is an extinction term A_V. Dust between an emitting source and an observer absorbs and scatters light. This effect is wavelength dependent, with blue light being scattered more than red light. For two identical stars at different distances, this effect will make the farther star appear redder, an effect called *interstellar reddening* (e.g. Cardelli et al., 1989). This dust can lie within the interstellar medium between the observer and the star, or can be associated with the star (e.g. circumstellar dust). By fitting A_V we can correct a synthetic spectrum for the effects of extinction and reddening. This is usually through the use of a known extinction law (e.g. Fitzpatrick, 1999) to correct the unreddened synthetic photometry before comparison with the catalogue values.

I perform SED fitting in Chapters 3, 4, 5, 6 and 7. Each time I fit a variation on the above stellar properties, depending on the scenario at hand.

2.6 Bayes Theorem and MCMC

Throughout much of this thesis I use Bayes Theorem and Markov Chain Monte Carlo (MCMC) methods to estimate the best model parameters that fit a set of data. Such methods are regularly used in astronomy, especially when the parameter space is complicated. MCMC methods explore this parameter space, finding regions of highest probability where best fitting model parameters may be located. I use them throughout this thesis for fitting flare models to lightcurves, SEDs to catalogue photometry to measure stellar properties, fitting a brown dwarf transit model to lightcurve, and to fit cross correlation functions.

For a model M and a set of data D, Bayes theorem is given as

$$P(M|D) = \frac{P(D|M)P(M)}{P(D)} \tag{2.9}$$

where P(M|D) is the probability of the model M being true, given your data D. This is commonly referred to as the posterior probability distribution. P(M) is the *prior* probability of your model, while P(D) is the *evidence*. The prior encapsulates the information you already have about your model, such as the physical constraints on different parameters (e.g. stellar radius must be positive). The evidence is the probability of your model being true. P(D|M) is the probability of your data given your underlying model and is called the *likelihood*. An example of this is in Chapter 6, where Bayes theorem is used (as part of an MCMC) to evaluate how well a given transit model explains a photometric lightcurve containing a brown dwarf transit.

The likelihood of the data D given your model M is given by,

$$P(D|M) = \prod_i P(D_i|M) = \prod_i \frac{1}{\sqrt{2\pi}\sigma_i} \exp\left(-\frac{\chi_i^2}{2}\right) \tag{2.10}$$

with

$$\chi_i^2 = \frac{(D_i - M)^2}{\sigma_i^2} \tag{2.11}$$

where D_i is the ith data point and σ_i is the associated uncertainty of the ith data point. The Bayesian methodology can be used to constrain the parameters of the model M to those which best fit the data. This is done by maximising the likelihood. However, for computational reasons we more often maximise the log-likelihood,

$$\ln P(D|M) = -\frac{1}{2}\left(n \ln 2\pi + \Sigma_i^n \ln \sigma_i^2 + \Sigma_i^n \frac{\chi_i^2}{2}\right) \tag{2.12}$$

which is sometimes changed in code such that we minimise the negative log-likelihood (-ln $P(D|M)$).

To implement Bayes' theorem in my work I use Markov Chain Monte Carlo (MCMC) processes. MCMC processes are now commonly used across all walks of astronomy, from models of gamma-ray burst progenitors (e.g. Chrimes et al., 2020) to studies of exoplanet atmospheres (e.g. Kirk et al., 2019). It is a powerful method which can be used to fully explore posterior parameter spaces and infer likelihoods of models. MCMCs use a Metropolis-Hastings sampling algorithm (Metropolis et al., 1953; Hastings, 1970) and MCMCs go as follows. At the start of an MCMC run an initial model M_{old} is generated and the posterior probability P(M_{old}|D) is calculated using Bayes theorem. In the next step a new model M_{new} is created, by taking a random step in parameter space away from M_{old}. The posterior probability of this new model is then calculated and compared to the old model. Here, the Metropolis-Hasting sampling algorithm is used to compare the posterior probabilities of the two models. The ratio between the new and old probability is calculated and compared to a random number between 0 and 1. If the ratio is greater than the randomly generated number, the new position in parameter space is taken as the starting point for the next step. This method keeps better fitting regions of parameter space and ideally works towards the best fitting region in the global parameter space.

MCMC processes in practice use multiple chains of what are called "walkers". Walkers are started in randomly chosen positions of parameter space and evolved. These n walkers sample the posterior probability distribution in n locations. After a given number of steps (the "burn-in" time) these multiple chains are expected to reach the highest probability region and can be used to fully sample the posterior probability parameter space. The burn-in steps are discarded when assessing the posterior distributions of parameter values.

I use MCMC processes multiple times in this thesis in various contexts, all using the Python module EMCEE (Foreman-Mackey et al., 2013). In chapters 3 and 5 I use it when fitting an empirical flare model to detected G and L star superflares. In chapters 5, 6 and 7 I use it for fitting spectral energy distributions to catalogue photometry, in order to determine stellar parameters. In chapter 6 I use it to fit the transit, secondary eclipse and out-of-transit modulation of NGTS-7Ab across NGTS and follow up datasets. It is also used in chapter 6 to fit the HARPS cross-correlation functions of NGTS-7A and NGTS-7B simultaneously. In all of these examples I use it to fully explore the posterior distribution of the parameter space I am investigating.

Chapter 3

Ground based detection of G star superflares

Are you going to Star-borough Flare?

Simon & Garfunkel, *Scarborough Fair*
(Adapted by James A. G. Jackman)

3.1 Introduction

In this chapter we present the first ground based CCD detections of superflares from a G type star. As described in Sect. 1.2, by taking measurements of G star superflares we can study the occurrence rates and energies of flares from stars similar to the Sun, make comparisons between Solar and stellar flare properties and see how these properties relate to Solar and stellar behaviour (e.g. the relation between flare occurrence and starspot phase). If the data quality is high enough, we can also apply Solar techniques to stellar flares. The flares presented in this chapter are some of the most well resolved superflares to date, with a higher cadence than all *Kepler* measurements and most ground based observations. We present our measurements of the stellar and flare parameters and make comparisons with previously detected G star flares. We also present our modelling of each flare using a solar inspired general flare model. This chapter uses material from Jackman et al. (2018), however we have updated this work to include parallax and proper motion measurements from *Gaia* DR2. Including these values has changed the distance and fitted stellar radius reported in Jackman et al. (2018).

Property	Value	Reference
RA_{NGTS}	03:08:34.9	
Dec_{NGTS}	-21:13:22	
RA_{NGTS} (Deg)	47.14557	
Dec_{NGTS} (Deg)	-21.22284	
$W3$	9.699 ± 0.034	4
$W2$	9.731 ± 0.020	4
$W1$	9.699 ± 0.022	4
K_s	9.768 ± 0.020	1
H	9.865 ± 0.023	1
J	10.216 ± 0.022	1
i'	11.174 ± 0.062	3
r'	11.356 ± 0.051	3
g'	11.899 ± 0.033	3
Gaia G	11.400 ± 0.002	2
Gaia RP	10.872 ± 0.004	2
Gaia BP	11.797 ± 0.006	2
V	11.562 ± 0.049	3
B	12.291 ± 0.058	3
NUV	16.943 ± 0.028	5
FUV	20.666 ± 0.245	5
ROSAT X-ray Count Rate (ct/s)	0.042	6
Extinction A_V	$0.07^{+0.05}_{-0.04}$	
μ_{RA}	-1.059 ± 0.065	7
μ_{DEC}	-6.371 ± 0.086	7
Parallax	2.9906 ± 0.0612	7
Distance	$331.3^{+4.9}_{-5.7}$	8

Table 3.1: Properties of NGTS J0308-2113. Coordinates are given in the J2000 system. References are as follows, 1. Skrutskie et al. (2006), 2. Gaia Collaboration et al. (2018b), 3. Henden and Munari (2014), 4.Cutri and et al. (2014), 5. Martin et al. (2005), 6. Boller et al. (2016) , 7. Zacharias et al. (2017), 8. Bailer-Jones et al. (2018). NUV, FUV, i', r', g' are AB magnitudes. Proper motions are in mas/yr. Parallax is in mas. Distance is in parsecs.

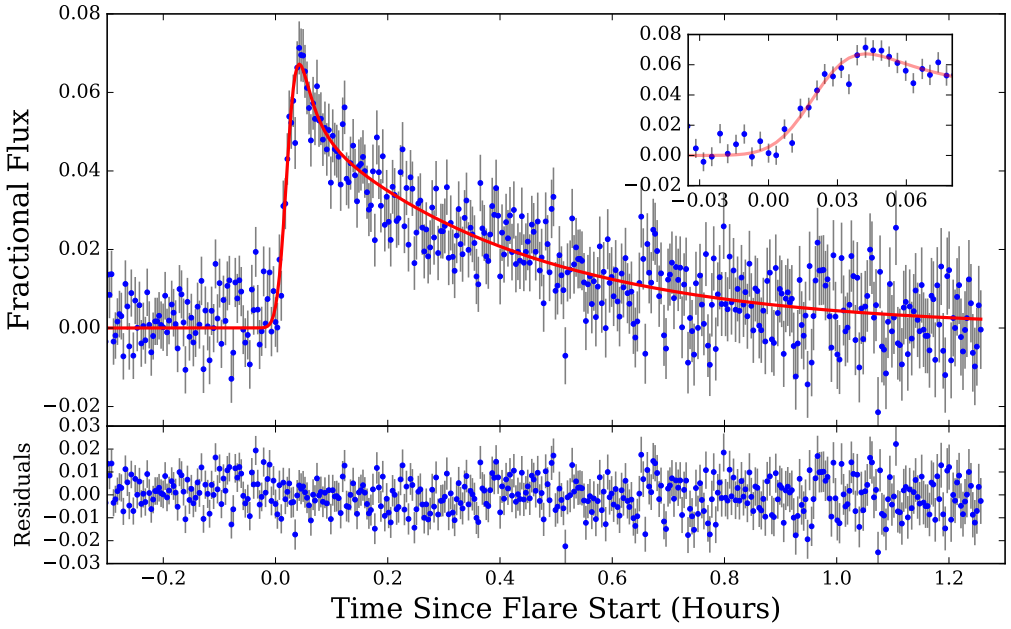

Figure 3.1: The superflare observed on NGTS J0308-2113 on 2016 January 3rd with best fitting model overlaid in red. The inset panel shows a zoomed in view of the data comprising the flare rise and peak, showing how the high cadence of NGTS has enabled us to resolve and fit to these regions. The bottom panel shows the residuals from our fitting. We note potential substructure in the flare decay around 0.7 hours and discuss this in Sect. 3.4.

3.2 Observations

The data presented in this chapter were collected with the Next Generation Transit Survey (NGTS; Wheatley et al., 2018) over 80 nights between 2015 November 4th and 2016 February 25th. The two flares in this Chapter were detected on the nights of the 2015 December 17th and 2016 January 3rd. NGTS is a ground-based transiting exoplanet survey, operating at Paranal. As described in Sect. 2.1, NGTS has twelve, 20 cm f/2.8, optical telescopes, each with a 520-890nm bandpass and exposure times of 10 seconds. Each single camera has a field of view of $\simeq 8\,\mathrm{deg}^2$. The NGTS field used in this work is NG0313-2230, which is centered on 03:13:38.2, -22:29:24.4.

3.3 Data Analysis and Results

3.3.1 Flare search algorithm

To search for flares we started from the raw NGTS lightcurves and detrended them using the SYSREM algorithm, as described in Sect. 2.1. For these detrended lightcurves, we applied an additional filter to remove frames which showed excess variance above an empirically defined limit, primarily to remove data adversely affected by clouds. The timescale of stellar flares is minutes to hours (e.g. Poletto, 1989), so most flares will have durations less than one night, and we searched for flares on a night-by-night basis.

In order to find flares in each night we followed the method outlined in Sect. 2.2, looking for 3 consecutive points greater than $6\,MAD$ from the median of the night, where MAD is the median absolute deviation. We applied no binning to the data, in order to fully utilise the time resolution of NGTS. Once the automated flagging procedure was complete, we inspected each flagged night visually and removed false positives. Examples of events which resulted in false positive flags include satellites passing through our aperture and high amplitude variable stars (e.g. RR Lyrae).

3.3.2 Flare detection

Using the method from Sect. 3.3.1 we detected a single flare, shown in Fig. 3.1, from the star NGTS J030834.9-211322 (NGTS J0308-2113). This star has also previously been identified as 2MASS J03083496-2113222. After identifying this flare we visually inspected each night to search for lower amplitude flares which were not flagged. From this, we identified a second flare, shown in Fig. 3.3.

Property	Value
Radius ($R_\odot$)	1.75 ± 0.04
$\log g$	$3.8^{+0.9}_{-0.6}$
$T_{\rm eff}$(K)	5462^{+71}_{-62}
Distance (pc)	331 ± 7
A_V	$0.07^{+0.05}_{-0.04}$
σ	0.03 ± 0.01

Table 3.2: SED fit results for NGTS J0308-2113.

To confirm the flares were not from a neighbouring source, we checked individual NGTS images from before and during the large flare, along with the positions of nearby stars from *Gaia* and 2MASS. The nearest source identified is from *Gaia*, a 20.658 magnitude star 10.5 arcseconds (2.1 pixels) away, placing it within our aperture. However, NGTS images reveal no shift in centroid position during the flare, and no light entering from outside the aperture, making us confident the flares are from NGTS J0308-2113.

3.3.3 Stellar Properties

To determine the stellar parameters for NGTS J0308-2113 we performed SED fitting using the broadband photometry listed in Tab. 3.1. These photometric values were obtained as part of the standard NGTS cross-matching pipeline (Wheatley et al., 2018). We used the SED modelling method described in Gillen et al. (2017) and Chapter 2, with the PHOENIX v2 model atmospheres (Husser et al., 2013). We fitted for $T_{\rm eff}$, $\log g$, radius R, distance D, extinction A_V and an uncertainty inflation term σ, to account for underestimated catalogue photometry uncertainties. We note that $\log g$ can only be loosely constrained by our SED fitting, which does not deeply probe individual absorption lines but rather bulk effects. We fitted to the catalogue photometry presented in Tab. 5.1. We applied a Gaussian prior on the extinction A_V using the Green et al. (2019) Bayestar 3D extinction map. We applied a Gaussian prior of 331 ± 7 pc on the distance using the *Gaia* DR2 value from Bailer-Jones et al. (2018). This distance value takes the global *Gaia* DR2 zero point into account, however does not take into account the larger scale parallax variations mentioned in Chap.2, which affects large groups of stars. As we are fitting for a single star, we have neglected to include this extra uncertainty but note that our radius uncertainty may be underestimated. The resultant SED fit is shown in Fig. 3.4 and the results are given in Tab. 3.2. From the SED fit we determined the effective temperature $T_{\rm eff} = 5405\,^{+45}_{-40}\,$K and a radius of $R = 1.75 \pm 0.04\,R_\odot$. In our fitting we assumed

solar metallicity. This is 2.16 times larger than the value reported in Jackman et al. (2018), which assumed NGTS J0308-2113 was on the main sequence. We then used the information presented in Table 5 of Pecaut and Mamajek (2013) to identify the temperature as consistent with spectral type of G8. The measured radius is larger than expected for a main sequence G star (Boyajian et al., 2012, 2017), something which would suggest that NGTS J0308-2113 is likely a pre-main sequence star. As a check, we compared the radius and temperature to the PARSEC stellar evolutionary models (Bressan et al., 2012) for masses above $0.7\,M_{\odot}$ and ages between 1 and 100 Myr. We also compared the HR diagram position of NGTS J0308-2113 to the MIST isochrones (Dotter, 2016; Choi et al., 2016). The HR diagram and MIST models are shown in Fig. 3.2. We found that the radius, temperature and the position on the HR diagram can be explained with an age between 5 and 10 Myr and an initial mass similar to that of a late F star. However, the position on the HR diagram also places NGTS J0308-2113 within the region typically occupied by subgiants. We discuss this further in Sect. 3.4.2.

We also note that this star was detected in X-rays with *ROSAT*. The detection of X-rays from this source can be a sign of an active stellar corona (Boller et al., 2016), especially if the emission is saturated. This is something we check for and find in Sect. 3.3.5. Strong X-ray emission has been detected from both pre-main sequence stars (e.g. Pizzolato et al., 2003) and from subgiants, both isolated (e.g. Howell et al., 2016) and in binaries (e.g. RS CVns; Perdelwitz et al., 2018).

Another possibility is that NGTS J0308-2113 is a binary star. The presence of two stars would result in an elevated position on the HR diagram and would explain the large fitted radius. The *Gaia* DR2 astrometric fitting assumes a single source. Depending on the projected separation, the single source solution can result in poor astrometric fits to binaries (Lindegren et al., 2018). We checked the quality of the *Gaia* DR2 photometry and astrometry using the quality checks recommended by Gaia Collaboration et al. (2018a) and Lindegren et al. (2018). This checks have been developed to remove spurious sources, such as partially resolved binaries where the photocentre changes between scans. NGTS J0308-2113 passes these tests, meaning we cannot immediately rule it out as a binary with a poor astrometric fit. We discuss the possiblity of NGTS J0308-2113 being a binary further in Sect. 3.4.

3.3.4 Stellar Rotation

The NGTS lightcurve of NGTS J0308-2113 shows periodic flux variations, which we attribute to starspots moving across the visible disc of the star. We use this behaviour to determine the rotation period of the star, using a Lomb-Scargle peri-

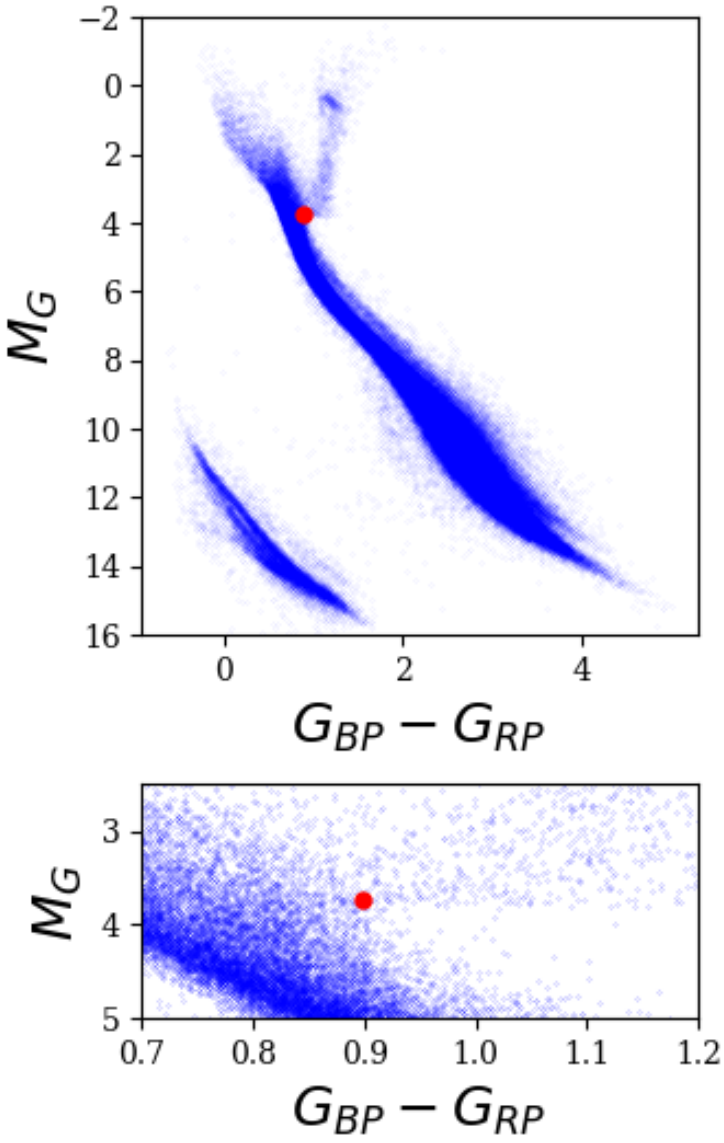

Figure 3.2: HR diagram for NGTS J0308-2113. Top: The full HR diagram. Blue points are stars within 100 pc which pass the astrometric and photometry quality checks recommended by Gaia Collaboration et al. (2018a) and Lindegren et al. (2018). The red circle is the unreddened photometry of NGTS J0308-2113. Bottom: A zoom in on the area around NGTS J0308-2113, showing its position near the subgiant region and red giant branch.

odgram. To do this, we use the ASTROPY package LombScargle (Astropy Collaboration et al., 2013) and test for 20000 periods spaced between 13 seconds and 80 days. We mask the flares from our lightcurve when performing this analysis. Our periodogram for the whole time series of NGTS J0308-2113 is shown in Fig. 3.5, from which the period of the main peak is 59.09±0.01 hours (0.41 d^{-1}). We calculate the uncertainty on this period by fitting a sine wave to the data. Using the analysis from Baluev (2008) we determine the false alarm probability (FAP) of this peak to be negligible, a result of the high amount of data. We also note a second peak at 40 hours, which we found to be an alias by performing an identical Lomb Scargle analysis on a sine wave of period 59 hours with the same time sampling as our lightcurve.

This short period fits with NGTS J0308-2113 either being a young star or a rapidly rotating subgiant. Through comparing to the observed spin-age relations of open clusters the rotation period alone suggests an age less than 600 Myr, consistent with our findings in Sect. 3.3.3 (e.g. Sadeghi Ardestani et al., 2017; Douglas et al., 2017; Stauffer et al., 2016). Using the measured period of 59 hours and our fitted stellar radius, we estimate an equatorial rotation velocity of 36km s^{-1}.

The amplitude of the observed spin modulation evolves with time. We split the lightcurve into three regions of activity, corresponding to an initial active portion, a secondary quiet portion and a final region where the amplitude increases once more. The 59 hour period phase folded data for these regions can be seen in Fig. 3.6. These regions are plotted in phase relative to the beginning of the lightcurve. The third region has a similar but slightly offset phase from the first, as well as less complete phase coverage due to a shorter duration. The durations of each region in the lightcurve are 40, 23 and 17 days respectively. The change in phase, along with the changing flux variation, can be explained by the decay of the original set of star spots and the formation of new ones. Starspot lifetimes have been studied by Bradshaw and Hartigan (2014) and for main sequence stars are on month timescales. One example is CoRoT-2, which has a starspot evolution timescale of 31±15 days (Silva-Valio and Lanza, 2011). Consequently we attribute our changing lightcurve modulation to starspot evolution.

We also searched for periodic signals separately in the three light curve regions. The three Lomb-Scargle periodograms are presented in Fig. 3.7. In the second, quiet, period of the light curve we see no evidence for periodic modulation. Calculating the modulation period of the third region gives a significantly longer rotation period of 60.87±0.04 hours (0.39 d^{-1}). This offset period suggests that the star exhibits differential rotation and that the new set of starspots are formed at a

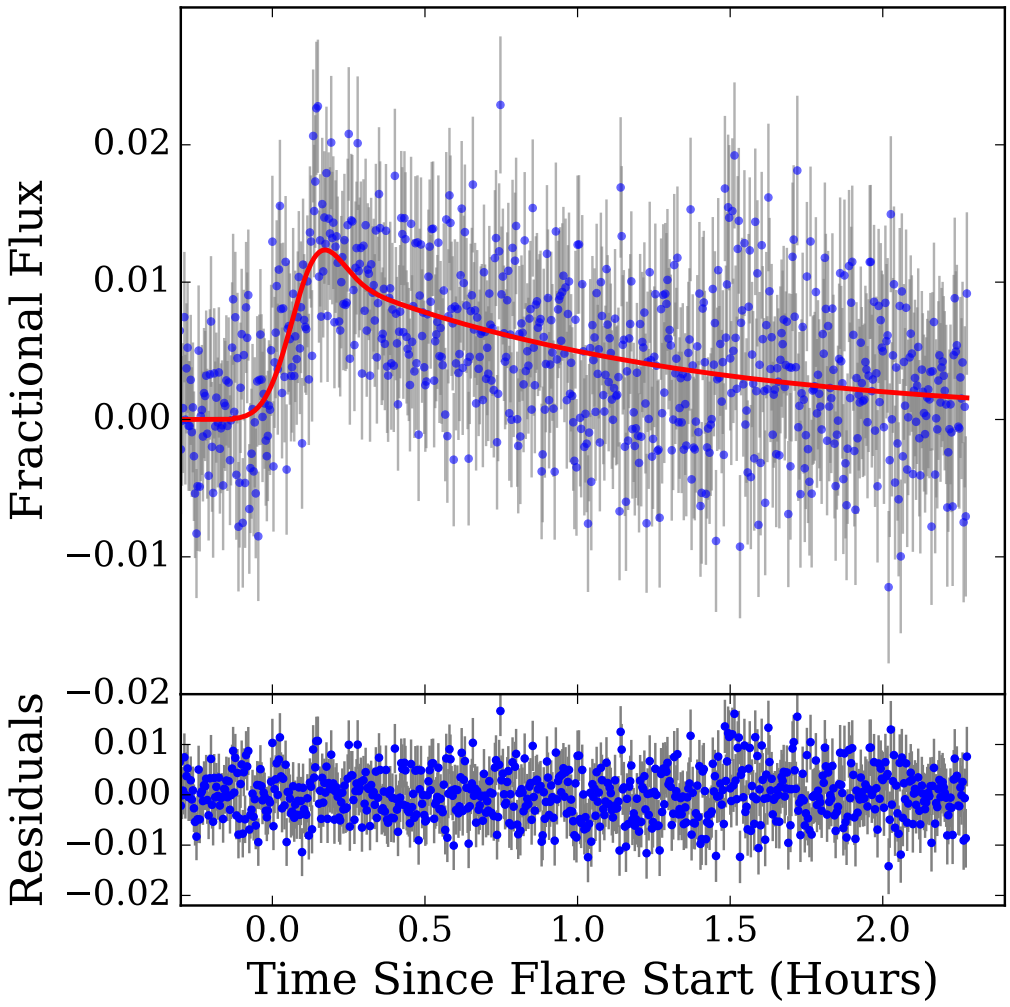

Figure 3.3: A lower amplitude flare, from 2015 December 17th. The best fitting model is overlaid in red. We note the appearance of substructure at the flare peak and at 1.5 hours and discuss this in Sect. 3.4. The flare start time is given here by where the fit goes above $1\,\sigma$ above the quiescent flux, as discussed in Sect. 3.3.6

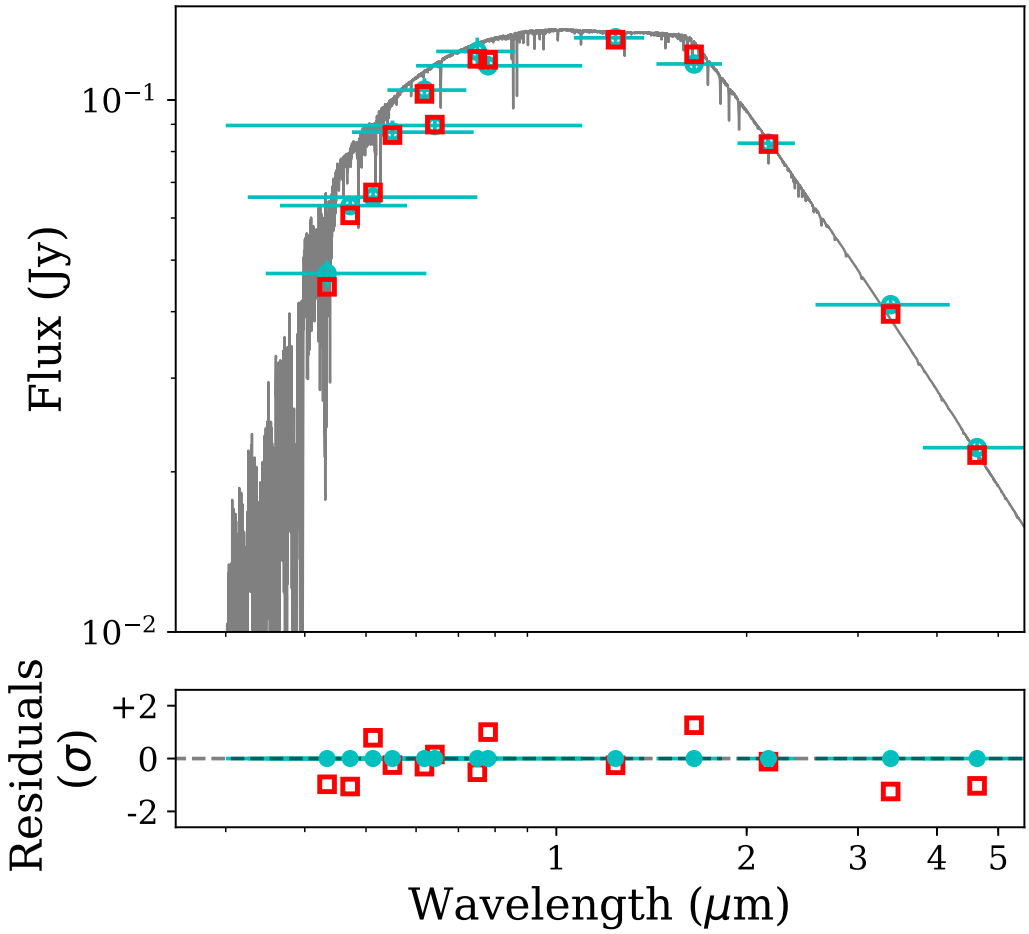

Figure 3.4: SED fit of NGTS J0308-2113 using the magnitudes listed in Tab. 3.1, matching best to a G8 spectral type. The cyan circles indicate the catalogue photometry, red squares are the fitted values. The residuals are in units of the adjusted catalogue photometry, adjusted using the uncertainty inflation term σ. The grey line is the best fitting PHOENIX v2 model, from which our best fit photometry was integrated.

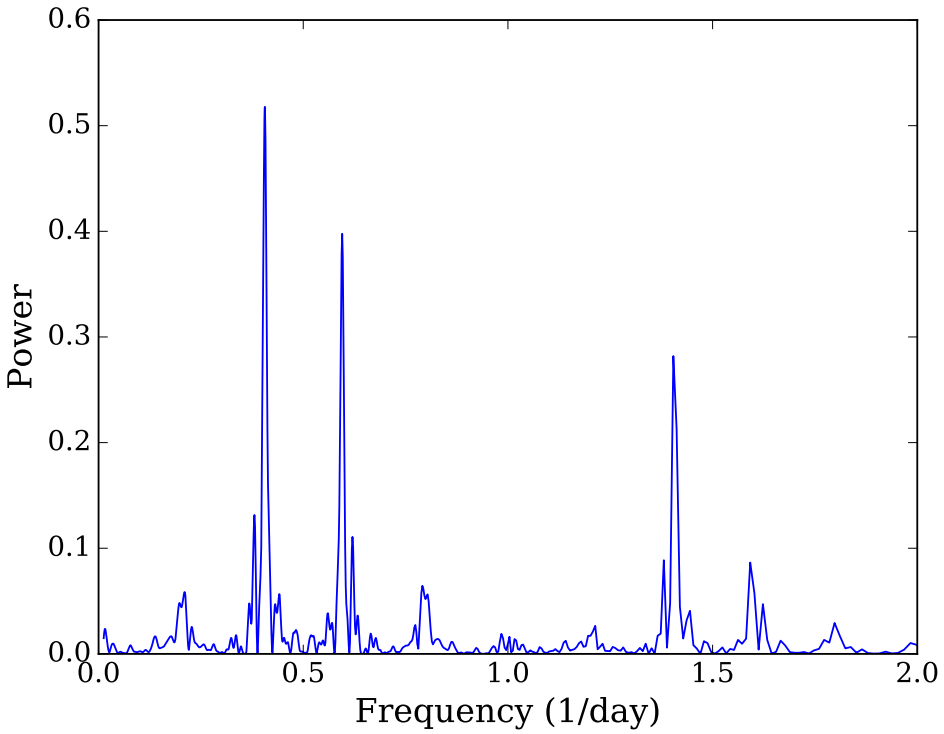

Figure 3.5: Lomb-Scargle periodogram for our full lightcurve. Here we show frequencies between 0 and 2 day^{-1}. Note the 1 day alias of the peak groups. The largest peak corresponds to our detected 59 hour period.

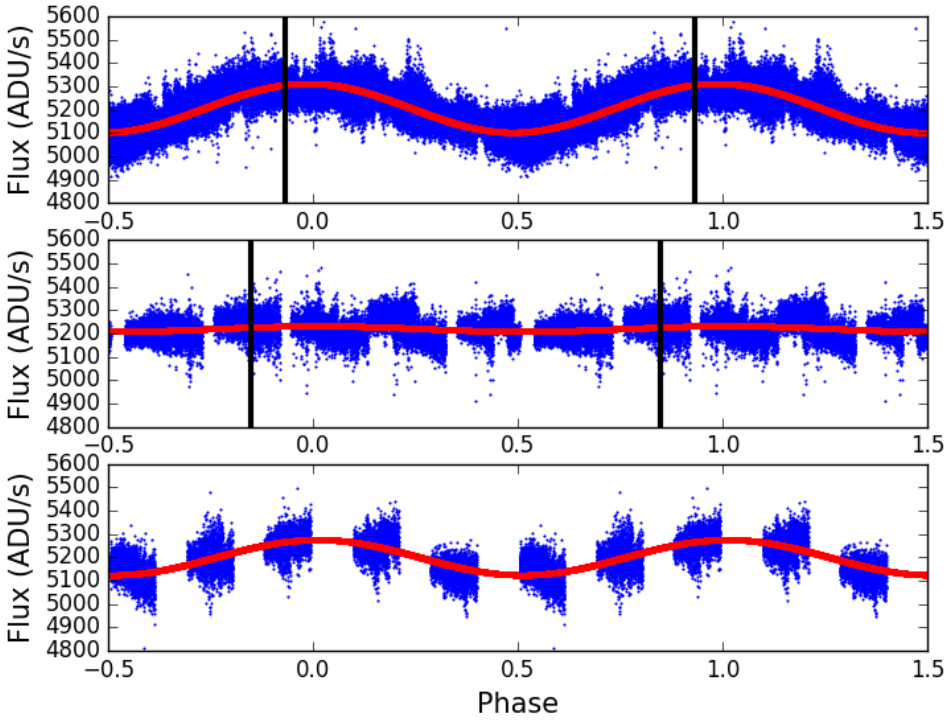

Figure 3.6: Phase folded data for the three regions of flux variation. Top is the initial active portion, middle is the quiet region and bottom is the following increase in activity. Overlaid in red is the sinusoidal fit for a 59 hour period. The black lines indicate the location of the small flare (top section) and the large flare (middle section).

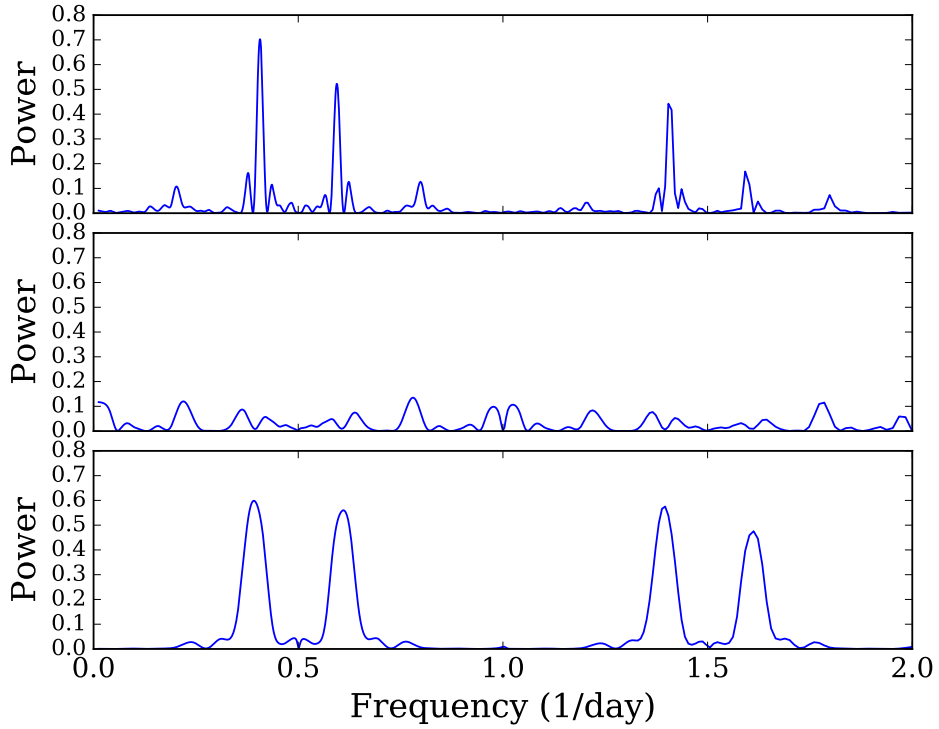

Figure 3.7: Lomb-Scargle periodograms for each section shown in Fig. 3.6. Note the lack of a period detection in the quiescent region.

different latitude to the original active region.

We also check where each flare occurs in phase, to search for any relation to the location of the active region. The smaller flare occurs towards the end of the first region, close to maximum optical brightness, while the larger flare occurs in the second, quiet region at similar rotation phase (see Fig. 3.6). To calculate the phase we used the emphemeris of the first region. For the smaller flare, this is opposite in phase to the dominant active region. Neither flare seems to be located at a rotation phase where a large star spot group is obviously visible, and we discuss this further in Sect. 3.4.

3.3.5 X-ray Activity

As noted in Sect. 3.3.3, NGTS J0308-2113 has been detected in X-rays with *ROSAT*. The detection was made during the *ROSAT* all sky survey, and we adopt count rates and hardness ratios from the 2RXS catalog (Boller et al., 2016). The *ROSAT* PSPC count rate was $0.042 \pm 0.018\,\mathrm{s}^{-1}$ and the hardness ratios in the standard *ROSAT* bands were HR1=1.000 ± 0.325 and HR2=-0.428 ± 0.243. The HR1 value indicates that the source was detected only in the *ROSAT* hard X-ray band (0.5–2.0 keV) and not in the soft band (0.1–0.4 keV).

The *ROSAT* PSPC count rate of NGTS J0308-2113 corresponds to a 0.1–2.4 keV energy flux of 5.7×10^{-13} erg s^{-1}cm^{-2}, using energy flux conversion factors determined for coronal sources by Fleming et al. (1995). This flux conversion uses the HR1 hardness ratio to account of the characteristic temperature of corona, and it has been applied to large samples of stars from the *ROSAT* all sky survey by Schmitt et al. (1995) and Huensch et al. (1998).

This X-ray flux corresponds to a 0.1–2.4 keV X-ray luminosity of $L_X = 7.5 \times 10^{30}$ erg s^{-1}, using the distance for NGTS J0308-2113 of 331 pc from Bailer-Jones et al. (2018). Using the values for $T_{\rm eff}$ and R_* from Sect. 3.3.3 we find the bolometric luminosity of the star to be $L_{Bol} = 9.2 \times 10^{33}$ erg s^{-1} and hence $\log L_X/L_{Bol} = -3.1$, which corresponds to saturated X-ray emission (Pizzolato et al., 2003; Wright et al., 2011).

We compared our calculated values for L_X and $\log L_X/L_{Bol}$ to the sample of open cluster measured X-ray luminosities from Núñez and Agüeros (2016). This sample combined *Chandra* observations of the $\approx$ 500 Myr open cluster M37 with literature X-ray studies of clusters with ages between $\approx$ 5 and 600 Myr. This sample includes G, K and M stars. From comparison with the Núñez and Agüeros (2016) samples, our values for L_X and $\log L_X/L_{Bol}$ are consistent with an of $\approx$ 5 Myr, which is the Orion complex in their sample. If we assume that NGTS J0308-2113 is

a pre-main sequence star and not a subgiant, then this estimated age would fit the $5-10$ Myr age of NGTS J0308-2113 inferred from the SED fitting and HR diagram analysis in Sect. 3.3.3. Alternatively, the value of $\log L_X/L_{Bol} \approx -3$ has previously been observed in rapidly rotating subgiant and giant stars (e.g. Howell et al., 2016).

Combining this X-ray luminosity with our measurement of the stellar rotation period (Sect. 3.3.4), we can place NGTS J0308-2113 on the rotation-activity relation of Wright et al. (2011). This is shown in Fig. 3.8 where NGTS J0308-2113 can be seen to reside close to the break point between saturated X-ray emission and the power law decrease in activity to slower rotation. We have also calculated the Rossby number, Ro $=P_{\rm rot}/\tau$ where τ is the convective turnover time. The convective turnover time is believed to be strongly time-dependent during the pre-main sequence phase of a star's life (e.g. Kim and Demarque, 1996). To estimate the convective turnover time for NGTS J0308-2113 we use the theoretical local values from Landin et al. (2010). Assuming NGTS J0308-2113 is a pre-main sequence star, we calculate a Rossby number of 0.03, placing NGTS J0308-2113 well within the X-ray saturated region.

Using the relation between the X-ray surface flux and average coronal temperature from Johnstone and Güdel (2015) we estimate an average coronal temperature of 10 MK. This is similar to the coronal temperature of 7.5 MK predicted from the rotation period using the relation by Telleschi et al. (2005).

The lack of detection of NGTS J0308-2113 in the *ROSAT* soft band, as well as its relatively large distance, suggests that it may be subject to stronger interstellar absorption than the sample of stars used to determine the flux conversion factors of Fleming et al. (1995). We therefore double checked our flux estimation using WEBPIMMS.[1] We assumed a characteristic coronal temperature of 7.5 MK and an interstellar column density equal to the total Galactic columnn the direction of NGTS J0308-2113, which is $N_{\rm H} = 2 \times 10^{20}\,{\rm cm}^{-2}$ (Dickey and Lockman, 1990; Kalberla et al., 2005). The measured *ROSAT* PSPC count rate then corresponds to an unabsorbed 0.1–2.4 keV energy flux of $4.6 \times 10^{-13}\,{\rm erg\,cm^{-2}\,s^{-1}}$, which is within 20 percent of our calculation using the flux conversion factors of Fleming et al. (1995).

3.3.6 Flare Modelling

We model our flares following a similar method to Gryciuk et al. (2017), who fitted solar flares in soft X-rays. For both flares, we use the convolution of a Gaussian with a double exponential. A Gaussian is used to account for the heating in the flare rise, which has been found to be appropriate for solar flares (e.g. Aschwanden et al.,

[1] https://heasarc.gsfc.nasa.gov/cgi-bin/Tools/w3pimms/w3pimms.pl

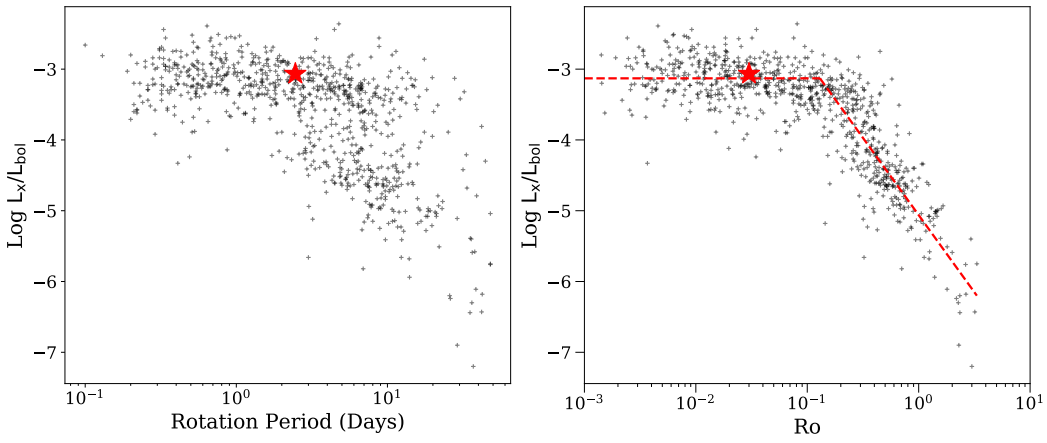

Figure 3.8: Left: Stellar X-ray to bolometric luminosity ratio vs rotation period for NGTS J0308-2113 with the data from Wright et al. (2011). Right: Same, but for Rossby number. We have also overlaid the power law fit from Wright et al. (2011), with β=-2.18. NGTS J0308-2113 is shown here with a red star. Note the position of NGTS J0308-2113 is within the X-ray saturated regime.

1998). A double exponential is used for the decay, accounting for thermal and non-thermal cooling processes, which has been used previously for the decay of stellar flares (e.g. Davenport et al., 2014). A convolution of these Gaussian and exponential functions is then analogous to the heating and cooling processes occurring during the flare (Gryciuk et al., 2017). With this physically motivated model we can utilise the high cadence of NGTS, in particular the flare rise which in the past has been fit using a polynomial or disregarded due to a lack of data points (e.g. Davenport et al., 2014; Pugh et al., 2016).

The mathematical form of this model, where $g(t)$ represents the flare, is as adapted from Gryciuk et al. (2017),

$$g(t) = \left(\frac{\sqrt{\pi}AC}{2}\right)\left(F_1 \exp\left[D_1(B-t) + \frac{C^2D_1^2}{4}\right]\left[\mathrm{erf}(Z_1) - \mathrm{erf}\left(Z_1 - \frac{t}{C}\right)\right] + F_2 \exp\left[D_2(B-t) + \frac{C^2D_2^2}{4}\right]\left[\mathrm{erf}(Z_2) - \mathrm{erf}\left(Z_2 - \frac{t}{C}\right)\right]\right) \tag{3.1}$$

where A is a normalisation factor, B is the central position of the Gaussian pulse, C is the width of the Gaussian, D_1 and D_2 are the constants of the exponential decays and F_1 and F_2 are their relative amplitudes. Z_1 and Z_2 are

$$Z_{1,2} = \frac{2B + C^2D_{1,2}}{2C} \tag{3.2}$$

and erf is the Gauss error function. F_1 and F_2 are related by

$$F_2 = 1 - F_1 \tag{3.3}$$

Before performing fitting, we inspected the full lightcurve and noted that nights exhibited behaviour consistent with atmospheric extinction. We identified this trend by using the full lightcurve to fit for a first order atmospheric extinction term. This trend was then removed from the lightcurve, including the nights showing our flares. The nights before and after each flare were used to check the quality of this fit and were found to have the atmospheric extinction successfully removed. We also account for the flux modulation effects from starspots. To do this we use the preceding two and subsequent two nights and fit a sinusoid at the calculated 59 hour stellar rotation period. With this sinusoid we are able to remove any gradient due to rotation from the night. This is required most for the smaller flare, which sits in the first, more active region of the lightcurve (Sect. 3.3.4).

For both flares we perform fitting using an MCMC analysis with the python package EMCEE (Foreman-Mackey et al., 2013), using 100 walkers for 20000 steps and discarding the first 5000 as a burn-in. During modelling we have increased our error bars to account for scintillation using the modified Young's approximation with the empirical coefficient for Paranal (Young, 1967; Osborn et al., 2015). Prior to fitting we reformatted the lightcurve in units of "hours since night start", rather than the standard HJD (in seconds) used in NGTS lightcurves. This was to avoid the effect of large HJD values being used in the calculation of $Z_{1,2}$ and consequently the error function in Eq. 3.1. The HJD start of night times for the large and small flare were 2457391.5344097223 and 2457374.535011574 respectively. These correspond to 63334173 and 61865425 seconds in the NGTS lightcurve respectively (seconds after 1st Jan 2014). During fitting we required A to be greater than zero and B to vary freely within the night. We required C to be less than 4 hours and that $D_1 < D_2$. We required D_1 and D_2 to be less than 275 hours^{-1}, the reciprocal of one NGTS exposure. The best fitting models for the two flares are overlaid on Figs. 3.1 & 3.3. We have reformatted the time units in Figs. 3.1 & 3.3 to be relative to the flare. The best fitting parameters are presented in Tab. 3.3 and the derived properties are presented in Tab. 3.4.

Flare Amplitude and Duration

To determine the amplitude of each flare we use the maximum value of our fit. For the larger flare this gives a fractional amplitude of 6.9 per cent. For the smaller flare,

Property	Large	Small
A	$2.90^{+0.49}_{-0.39}$	$0.53^{+0.95}_{-0.31}$
B (hours)	3.43 ± 0.01	$2.01^{+0.05}_{-0.03}$
C (hours)	0.02 ± 0.01	$0.11^{+0.02}_{-0.10}$
D_1 (hours^{-1})	2.59 ± 0.14	$0.89^{+0.12}_{-0.15}$
D_2 (hours^{-1})	$45.48^{+20.97}_{-17.50}$	$69.83^{+46.28}_{-53.18}$
F_1	0.52 ± 0.10	$0.14^{+0.39}_{-0.08}$

Table 3.3: Fitted model properties of each superflare detected from NGTS J0308-2113.

using the value from the fit gives a fractional amplitude of 1.2 per cent. Inspecting Fig. 3.3, there appears to be impulsive substructure at the flare peak, which is not accounted for in our model. Taking the average of the five data points around the peak gives an peak amplitude of 2.0±0.3 per cent.

To obtain a measure of the full duration of the flare, we again make use of our fit. We define the start and end of the flare as the points where the model rises and then falls more than 1σ above the background flux level, as in Gryciuk et al. (2017). Here σ is determined from the quiescent flux before the flare. From this, we determine the flare duration of the larger flare to be 55 minutes. Due to the decreased amplitude to error ratio of the smaller flare, we do not calculate the full flare duration using this method. However, we also calculate the flare duration with two additional methods - using its e-folding timescale (as performed in Shibayama et al., 2013) and its scale time (the duration where the flare is above half the maximum flux value). Again, we use our fit for these. For the large and small flare, we calculate the e-folding timescale as 16 and 55.5 minutes respectively, and the scale time as 11 and 42 minutes respectively. With our fit we can also calculate the timescale of the flare rise, using the time from the flare start to the peak of the model. Using this, we calculate the flare rise time as 2.5 minutes for the larger flare. If we use the $1\,\sigma$ start limit for the smaller flare, we estimate the flare rise as at least 7.4 minutes.

3.3.7 Flare Energy

The method used to calculate the flare energy is based on that described by Shibayama et al. (2013), and makes the assumption that the flare and star act as blackbody radiators, with the flare having a blackbody spectrum of temperature 9000 ± 500 K in order to estimate the flare luminosity. Using the stellar effective temperature and radius from Sect. 3.3.3, we calculate the bolometric energy of the larger and smaller

Property	Large	Small
Energy (erg)	$2.5^{+0.3}_{-0.2} \times 10^{35}$	$5.4^{+0.5}_{-0.4} \times 10^{34}$
Fit Amplitude (per cent)	6.9	1.2
Full Duration (min)	55	N/A
e-folding duration (min)	16	55.5
Scale time (min)	11	42
Flare rise (min)	2.5	>7.4

Table 3.4: Overall properties of each superflare detected from NGTS J0308-2113.

flare to be $2.5^{+0.3}_{-0.2} \times 10^{35}$ erg and $5.4^{+0.5}_{-0.4} \times 10^{34}$ erg respectively. We integrated over the duration of each flare by integrating from 5 minutes before the flare star to the end of the night. It is striking that the smaller flare is only a factor two less energetic despite having an amplitude around six times lower. Comparing to the Carrington event energy of $\approx 10^{32}$ ergs (Tsurutani et al., 2003), we can see that each flare had a bolometric energy several hundred to thousands of times greater than this.

From a total of 422 hours of observation for this star, we have detected two flares. We can use this measurement to estimate the flaring rate for flares above $5.4^{+0.5}_{-0.4} \times 10^{34}$ erg as approximately 40 per year.

3.4 Discussion

3.4.1 Flare Properties

We have detected two superflares from the young star NGTS J0308-2113 with high-cadence NGTS optical photometry. These are the first ground-based CCD detections of superflares from a G temperature star. Our NGTS observations have much higher cadence than the *Kepler* flare detections, allowing us to resolve the flare rise and substructure.

The larger flare is shown in Fig. 3.1 and was calculated to have a bolometric energy of $2.5^{+0.3}_{-0.2} \times 10^{35}$erg and a fractional amplitude of 6.9 per cent. Due to the increased time resolution of our measurements compared to almost all previous superflare detections, we have been able to fit this flare with a physically-motivated model that includes a Gaussian pulse to describe the impulsive flare rise (as employed previously for solar flares). For the decay, our data require two exponential components. Separate impulsive and gradual decay components been seen previously in some stellar flares, and attributed to decay of blackbody-like emission and chromospheric emission respectively (Hawley et al., 2014; Kowalski et al., 2013). We can also see that this flare displays a flattening around the peak, or a "roll-over".

Similar flare peak behaviour has been seen by Kowalski et al. (2011) from ULTRACAM observations of the dM3.5e star EQ Peg A. This behaviour is captured in the fitted model as a result of the observed combination of Gaussian heating and exponential cooling. Further, we can identify smaller peaks in the decay of the flare, located at approximately 0.7 and 1.0 hour after the flare start in Fig. 3.1. Structure, or "bumps", such as this have been previously identified in flare decays with *Kepler* (e.g Balona et al., 2015).

Our model has also been used to fit the smaller flare of NGTS J0308-2113, shown in Fig. 3.3. This flare has a much lower relative amplitude of just 1.2 per cent, making it the lowest-amplitude G star flare to have been detected from the ground. Despite its low amplitude, this smaller flare has a much slower rise and longer duration than the larger flare (by factors of 3–4) so that it has a high total energy of $5.4^{+0.5}_{-0.4} \times 10^{34}$erg, which is only a factor of approximately 2 lower than the larger flare. When fitting this smaller flare it became apparent that there was additional structure at the flare peak. This can be seen in the residuals of Fig. 3.3, as a small spike lasting approximately one minute. This is a sign of an additional heating pulse at the end of the initial flare rise. In this flare we also detect subtructure around 1.5 hours after the flare start (visible in the residuals). The amplitude of the peak at this time is approximately 1 per cent, which is comparable with the amplitude of the main flare. Considering the timing of this substructure relative to the main flare peak, it is likely an example of sympathetic flaring (e.g. Moon et al., 2002).

One advantage of our flare model, combining a Gaussian heating pulse with exponential cooling, is that it avoids an arbitary discontinuity between the end of the rise and the beginning of the decay. This has generally not been the case with previous stellar flare models, which have tended to include an instantaneous transition between functions describing the rise and decay (e.g. Davenport et al., 2014). Our model also provides a well-defined measure of the rise timescale, allowing for studies of how the flare rise time changes between flares. In this case we see the lower amplitude flare rising much more slowly than the high amplitude example. This highlights how wide-field high-cadence surveys such as NGTS can contribute to the quantitative characterisation of stellar flares.

3.4.2 Stellar Age

In Sect. 3.3.3 we determined that NGTS J0308-2113 had an age of $5 - 10$ Myr. We estimated this age through comparison of the stellar properties from our SED fitting to the PARSEC stellar evolutionary models and through comparison of its position on the HR diagram to the MIST isochrones. This analysis assumes the star is

an isolated single star. We investigated the possibility that NGTS J0308-2113 is a member of a young moving group or star-forming region, something that would help explain its extremely young age. We compared the position of NGTS J0308-2113 with the Zari et al. (2018) and Cantat-Gaudin and Anders (2020) pre-main sequence and open cluster stellar catalogues. We matched with no associations or clusters in the Zari et al. (2018) or Cantat-Gaudin and Anders (2020) catalogues within 10 degrees of NGTS J0308-2113. This would suggest that while the stellar properties of NGTS J0308-2113 are consistent with a young G star, it may not be a young star.

As noted in Sect. 3.3.3, the position of NGTS J0308-2113 on the HR diagram overlaps with the region occupied by subgiant stars. Subgiant stars have begun to evolve off of the main sequence and many types show forms of activity. Notsu et al. (2019) found in a reanalysis of the Maehara et al. (2012); Shibayama et al. (2013); Maehara et al. (2017) *Kepler* G star superflare samples, using *Gaia* DR2 parallaxes, that approximately 40% of their stars overlapped could be classified as subgiants. This classification was based on their radii. Therefore, it is possible that NGTS J0308-2113 is instead a subgiant star. A subgiant type which are known to show flares and spot modulation are RS CVns. RS CVns are binary stars with active chromospheres, of which one of the components can be an F or G type main sequence or subgiant star. The strong activity results in spot modulation and flares (e.g. Roettenbacher et al., 2016). The position of NGTS J0308-2113 overlaps with those of confirmed RS CVn sources on the *Gaia* HR diagram (Gaia Collaboration et al., 2019).

In order to confirm either scenario, spectroscopic observations are required. If NGTS J0308-2113 is very young, then lithium should be present in the photosphere and the Li 6708$\mathring{A}$ absorption line can be detected. If the spectrum of NGTS J0308-2113 shifts in wavelength between observations due to being in an orbit with a companion, then this would confirm it as a possible RS CVn.

Binarity

Another possibility raised in Sect. 3.3.3 is that NGTS J0308-2113 is a binary source. As noted in Sect. 3.3.3, the presence of a second star would result in the apparent elevated position on the HR diagram in Fig. 3.2 and large fitted radius. If the object is a close equal mass system, which has undergone tidal synchronisation to the observed 59 hour period, then this may result in the observed X-ray saturation also. Alternatively, a longer period system (tens of days) which has just arrived on the zero-age main sequence could also show similar behaviour. To confirm whether NGTS J0308-2113 is a binary system, multiple spectroscopic observations should be

obtained, to look for the Doppler shift of each component with time.

3.4.3 Starspots and Flare Phases

Our analysis of the NGTS light curve of NGTS J0308-2113 revealed a 59.09 ± 0.01 h periodic modulation that we interpreted as the changing visibility of starspots on the stellar rotation period (Sect. 3.3.4). The initial set of starspots appear to decay during the observations, and no spin modulation is detected for an interval of around 23 d. Periodic modulation begins again towards the end of the NGTS observations, and at a slightly longer period, suggesting that the star exhibits differential rotation and that new starspots have emerged at a different latitude.

Checking where the flares occur in rotation phase reveals that the smallest flare occurs in antiphase to the dominant starspot group, while the larger flare occurs during the quiescent interval of the lightcurve (at a similar spin phase to the first flare). These flare timings are perhaps surprising, as we might expect to see superflares when large active regions are present and visible. Instead, our results suggest that the observed superflares do not emerge from the dominant active regions on the stellar surface. Such behaviour is not unprecedented, as observations of the M dwarfs AD Leo and GJ 1243 showed no correlation between stellar flare occurrence and rotational phase (Hunt-Walker et al., 2012; Hawley et al., 2014). A similar result was found for the K dwarf KIC 5110407, with all but the two strongest flares showing no correlation with the most active regions (Roettenbacher et al., 2013). In these cases it was suggested that the dominant active region might be located at the pole, such that it is always in view and flares can be seen at any spin phase. An alternative is that the majority of flares originate from smaller spot groups that do not cause the dominant flux modulation.

3.4.4 Comparison with *Kepler*

In Fig. 3.9 we compare the superflares of NGTS J0308-2113 with G star superflares detected with *Kepler*. We use the samples from Shibayama et al. (2013) and Maehara et al. (2015) for the long and short cadence *Kepler* data respectively. NGTS J0308-2113 has a *Kepler* magnitude of 11.4, calculated using the stellar *g'* and *r'* magnitudes and Eqn. 2a from Brown et al. (2011). This magnitude makes it one of the brightest G stars seen to exhibit a superflare (see Fig. 3.9). The larger flare from NGTS J0308-2113 also has a greater amplitude than all but one of those detected in short cadence *Kepler* data. This flare also has a shorter duration than most detected with *Kepler*. This comparison demonstrates that NGTS has a sufficiently

wide-field of view and high photometric precision to detect rare and interesting stellar flares from bright stars. Each flare is also observed with higher cadence than has previously been possible.

3.4.5 X-ray Activity

Thanks to the strong activity of NGTS J0308-2113 we were able to measure its X-ray luminosity using archival *ROSAT* data (Sect. 3.3.5). We found that the star is in the saturated X-ray regime, with $\log L_X/L_{Bol} = -3.1$, and that its X-ray emission is consistent with the rotation activity relation of Wright et al. (2011). It was not detected in the *ROSAT* soft X-ray band, likely due to interstellar absorption. Using our measured spin period and the theoretical value for the convective turnover time from Landin et al. (2010), assuming a pre-main sequence star, we estimated the Rossby number of NGTS J0308-2113 to be 0.03. Interestingly, this places the star close to the peak of superflare occurrence rates found by Candelaresi et al. (2014).

We can also compare the X-ray luminosity of NGTS J0308-2113 with that of other G stars exhibiting superflares. Yabuki et al. (2017) found nine stars with X-ray detections from the *Kepler* superflare sample of Shibayama et al. (2013). Using these nine X-ray detections they identified a correlation between the largest white-light flare energies (estimated from *Kepler* data) and quiescent L_X with

$$E_{Bol} \propto L_X^{1.2\pm0.3}. \tag{3.4}$$

Based on this relation, we would expect NGTS J0308-2113 to exhibit flares of energies up to approximately 5×10^{36} erg. This is around 25 times greater than the energy of our larger flare, suggesting NGTS J0308-2113 sometimes exhibits even more energetic flares than the examples we have detected with NGTS.

Maximum Flare Energy

An alternative method to estimate the potential maximum flare energy is to use the starspot activity. This is done using equation (1) from Shibata et al. (2013),

$$E_{flare} \approx 7 \times 10^{32}(\mathrm{erg}) \left(\frac{f}{0.1}\right) \left(\frac{B}{10^3 \mathrm{G}}\right)^2 \left(\frac{A_{\mathrm{spot}}}{3 \times 10^{19} \mathrm{cm}^2}\right)^{3/2} \tag{3.5}$$

where f, B and A_{spot} are the fraction of magnetic energy that can be released as flare energy and the magnetic field strength and area of the starspot respectively. We estimate the starspot area from the lightcurve modulation normalised by the average brightness, following the method of Notsu et al. (2013). We use the region

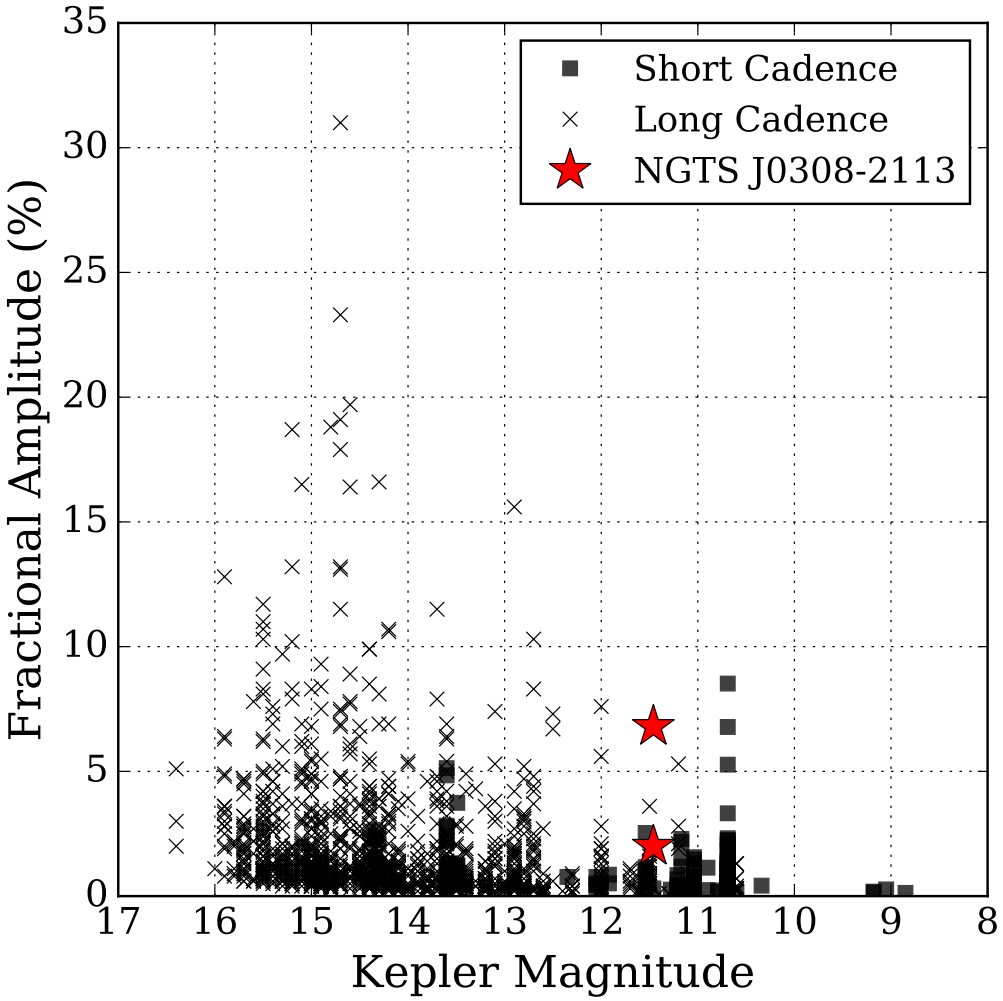

Figure 3.9: Comparison of the fractional amplitudes and *Kepler* magnitude of our flares from NGTS J0308-2113 (red stars) with G star superflares detected in short cadence (black squares) and long cadence (black crosses) *Kepler* data. When comparing fractional amplitudes between NGTS and *Kepler* it should be noted that the *Kepler* bandpass extends blueward of NGTS.

of greatest brightness variation to estimate the area, obtaining a value equivalent to 0.04 of the visible stellar surface. We assume f=0.1 (Aschwanden et al., 2014) and B=1000 - 3000G (typical comparison values for solar-type stars e.g. Solanki, 2003; Maehara et al., 2015) and calculate $E_{flare} = 1 - 9 \times 10^{36}$ erg. This estimated value is the same order of magnitude as that calculated from the X-ray data, predicting a flare of greater energy than our largest event.

3.4.6 Implications For Exoplanet Habitability

Understanding the properties of superflares from G stars is important when considering the habitability of Earth-like exoplanets, including those expected to be detected with *PLATO* (Rauer et al., 2014). Stellar flares are known to be associated with intense ultraviolet radiation (e.g. Stelzer et al., 2006; Tsang et al., 2012), which can reduce levels of atmospheric ozone (e.g. Lingam and Loeb, 2017) and damage the DNA of biological organisms (e.g. Castenholz and Garcia-Pichel, 2012). Associated X-ray and extreme-ultraviolet radiation can also erode the planetary atmosphere and drive water loss. Stellar flares are also associated with Coronal Mass Ejections (CMEs), and while planetary magnetospheres may protect against the quiescent stellar wind, CMEs can act to compress the magnetosphere and expose the planetary atmosphere to further erosion and dessication (e.g. Kay et al., 2016; Lammer et al., 2007).

The detections of superflares presented in this Chapter demonstrate that wide-field ground-based surveys such as NGTS are capable of characterising the rates and energies of superflares from G-type stars, despite their relatively low fractional amplitude. Since flare detections with ground-based telescopes can be made and announced in real time it may also be possible to trigger immediate follow up of superflares with larger narrow-field telescopes while the flares are still in progress. This has not been possible to date due to the unpredictable nature of superflares and inevitable delays in downlinking and processing data from space telescopes such as *Kepler*. Real-time follow up of NGTS flares might then provide the multi-wavelength observations needed to assess the impact of superflares on potentially habitable exoplanet atmospheres.

3.5 Conclusions

In this work we have presented the detection of two superflares from the G type star NGTS J030834.9-211322 using NGTS. These are the first G star superflares detected from the ground using a CCD, and they are among the highest cadence measure-

ments of any superflares to date. We fit both flares with a model that incorporates a Gaussian heating pulse, as seen previously in solar flares, and exponential decay on two timescales. The model fit provides the amplitude, energy and duration of each flare, and we find the two flares have similar total energies despite their different amplitudes and durations. The larger flare has an unusually high amplitude and short duration for a G star superflare. Our model also allows us to measure the timescale of the flare rise, an interval that has been undersampled in previous studies, and we find the longer duration flare has a slower rise. We have also detected substructure in both flares.

The stellar rotation period of NGTS J0308-2113 was measured to be 59 hours, and we found evidence for differential rotation. The X-ray luminosity of the star was calculated to be 7.4×10^{30} erg s^{-1}, with $\log L_X/L_{Bol} = -3.1$ implying saturated X-ray emission, as expected for a G8 star with such a short spin period. The Rossby number of 0.03 places NGTS J0308-2113 close to the peak of the occurence rate distribution implied by previous flare detections.

Our results highlight the potential for wide-field ground-based surveys such as NGTS to determine the rates, energies and morphologies of superflares from G stars, despite the modest white-light amplitudes of such flares. Further detections and real-time multi-wavelength follow up will be important in assessing the habitability of Earth-like exoplanets around G stars, including those to be found with *PLATO*.

Chapter 4

Detection of a giant flare displaying quasi-periodic pulsations from a pre-main sequence M star with NGTS

All I want is a star somewhere
Far away from the moonlight glare
With one enormous flare
Oh, wouldn't it be loverly?

Wouldn't it be Loverly from *My Fair Lady*
(My Flare Lady, adapted by James A. G. Jackman)

4.1 Introduction

Stellar flares from M stars provide some of the most dramatic stellar events, yet they cannot be predicted beforehand. Catching the relatively-rare high-energy events therefore requires long-duration measurements of many stars, such as that from wide-field surveys for transiting exoplanets. The energies output in such events often dwarf the Carrington event and can be seen over a wide range of wavelengths, notably in the optical, ultraviolet and in X-rays.

When observed in the optical, the highest energy white-light flares from mid-M and later spectral types can change the brightness of the star by magnitudes for

hours before returning to quiescence (e.g. Gizis et al., 2017a; Paudel et al., 2018b). As described in Sect. 1.4, the largest amplitude events can also make stars that normally reside below the sensitivity of a survey visible for short periods of time (e.g. the $\Delta V < -11$ flare from ASASSN-16ae identified by Schmidt et al., 2016). Some large amplitude stellar flares exhibit complex substructure, one type of which is the oscillations of flare intensity with time, commonly referred to as quasi-periodic pulsations (QPPs, introduced previously in Sect. 1.2.3). A common phenomenon on the Sun (Kupriyanova et al., 2010; Simões et al., 2015; Inglis et al., 2016), QPPs remain relatively rare in stellar flare observations. Those which have been observed have been seen in the optical (e.g. Balona et al., 2015), microwave (Zaitsev et al., 2004), UV (Welsh et al., 2006; Doyle et al., 2018) and X-ray (Mitra-Kraev et al., 2005; Pandey and Srivastava, 2009; Cho et al., 2016).

As mentioned in Sect. 1.2.3, the exact cause of these pulsations is not yet known, however numerous mechanisms have been proposed and it is indeed possible that different mechanisms act in different cases. These mechanisms can be split into two groups: those where the flare emission is modulated by magnetohydrodynamic (MHD) oscillations, and those based on some regime of repetitive magnetic reconnection (Nakariakov et al., 2016). In the first case, MHD oscillations may directly affect the flare emission by modulating the plasma parameters (e.g. Nakariakov and Melnikov, 2009); for example variations of the magnetic field strength would cause gyrosynchrotron emission to vary. In addition the oscillations could indirectly affect the emission by modulating the kinematics of charged particles in the flaring coronal loops, which in turn would cause bremsstrahlung emission at the footpoints to appear periodically (e.g. Zaitsev and Stepanov, 2008). For the second case, the repetitive reconnection could be the result of external triggering, for example by leakage of MHD oscillations of a nearby structure (Nakariakov et al., 2006). Alternatively it could result from a 'magnetic dripping' mechanism which does not require an external trigger (e.g. McLaughlin et al., 2018). For this scenario, only when some threshold energy is reached does magnetic reconnection occur. This reconnection then releases energy and the process repeats periodically. Examples of this regime are reported by Murray et al. (2009); McLaughlin et al. (2012); Thurgood et al. (2017). If the mechanism behind a particular observation of QPPs in a flare can be determined, then it may be possible to estimate coronal plasma parameters in the vicinity of the flare via coronal seismology (e.g. Van Doorsselaere et al., 2016).

The timescale of QPPs can range from milliseconds to minutes (e.g. McLaughlin et al., 2018) and as a result, without observations of a similar or higher cadence these short-lived behaviours will be missed. For solar flares this cadence is regularly

achieved (e.g. Dolla et al., 2012; Kumar et al., 2017), as it can be for targeted observations of stellar flares for individual stars (e.g. Mathioudakis et al., 2003). However, in order to identify more of these events on stellar flares, long duration observations with a high cadence are required for a large number of stars. As outlined in Sect. 1.2, this became possible with the *Kepler* satellite. Indeed, short cadence observations from *Kepler* have been used to increase the number of white-light QPP detections (e.g. Balona et al., 2015; Pugh et al., 2016). However, only a small fraction of targets were observed in the one-minute short cadence mode (e.g. Gilliland et al., 2010) and not for the full duration of the mission, reducing the potential for detecting short timescale QPPs. Consequently it is apparent that to increase not only the number of both QPPs and high energy flares observed, long duration, wide field observations are required with a high cadence for all stars.

This has become possible with the Next Generation Transit Survey (NGTS). As described in Chapter 2, NGTS is a ground-based transiting exoplanet survey and consists of 12 telescopes, each with a 520-890nm bandpass (Wheatley et al., 2018). Each camera operates with an exposure time of 10 seconds and has a field of view of ≈ 8 square degrees, resulting in a total instantaneous field of view of 96 square degrees. NGTS also benefits from high-precision autoguiding (McCormac et al., 2013) which, when combined with a pixel scale of 4.97 arcseconds per camera, enables the use of centroid analysis to rule out false positive planet candidates due to blended sources (Günther et al., 2017). With stable tracking and wide fields, NGTS is able to detect and resolve flares on both single and blended objects.

In this chapter we present the detection of a high energy stellar flare with QPPs from the pre-main sequence M star NGTS J121939.5-355557. This chapter uses material from Jackman et al. (2019a). This is one of the best resolved observations of stellar flare substructure from a wide-field survey, allowing us to apply methods developed for Solar flares. We present our detection with NGTS and discuss how we identified the source of the flare and derived its properties. We also present the oscillations of the flare and assess their significance, along with comparing them to previous observations of stellar and solar QPPs.

4.2 Observations

The data presented in this chapter were collected with NGTS over 115 nights between 2015 November 28th and 2016 August 4th. The detected flare occurred on the night of 2016 January 31st. The NGTS field used in this chapter is NG1213-3633, which is centered on 12:13:50.7, -36:33:43.9.

4.2.1 Flare Detection

To identify flares in our data, we initially detrended the raw NGTS lightcurves using a custom version of the SYSREM algorithm, as detailed in Sect. 2.1. To search for flares within these lightcurves we followed the method discussed in Sect. 2.2. This method searches individual nights for 3 consecutive points greater than 6 MAD above the night median. Along with this it searches for nights which reside 5 MAD above the season median, indicative of a longer timescale flare where a single night of observations may only capture a portion of the event.

Following this method we detected a flare from the blended source NGTS J121939.5-355557 (hereafter, NGTS J1219-3555). *Gaia* astrometry reveals that two sources reside within the NGTS aperture, separated by 6.7 arcseconds. The flare was flagged as a night 5 MAD above the median of the lightcurve and is shown in Fig. 4.1. Fig. 4.1 shows the flare after we have removed the flux contribution from the background star, using the method described in Sect. 4.2.4. The two sources and the NGTS aperture are shown in Fig. 4.2.

Following the detection of the flare in Fig. 4.1, we checked each individual night to find low amplitude flares which may not have been flagged. Through doing this we found three additional lower-amplitude flares towards the end of the season, shown in Fig. 4.3.

4.2.2 Centroid Analysis

As two sources are present inside the NGTS aperture, we needed to determine on which star the flare occurred. To determine this, we followed the centroiding analysis outlined in Sect. 2.1. For this analysis we utilised centroid positions calculated as part of the NGTS data analysis pipeline. Comparison of the centroid position with time for the flare is shown in Fig. 4.1. We also compared this centroid movement with the images of the source before and during the flare to confirm the position of the flaring source, identifying the source as NGTS J121939.5-355557 (NGTS J1219-3555). This is the south east source in Fig. 4.2 and has previously been identified as 2MASS J12193970-3556017.

4.2.3 Stellar Properties

Spectral energy distribution

With this positional information we obtained catalogue magnitudes, making sure to only use catalogues that are able to identify the two sources separately. The results of this matching is shown in Tab. 4.2. Using the available 2MASS (Skrutskie

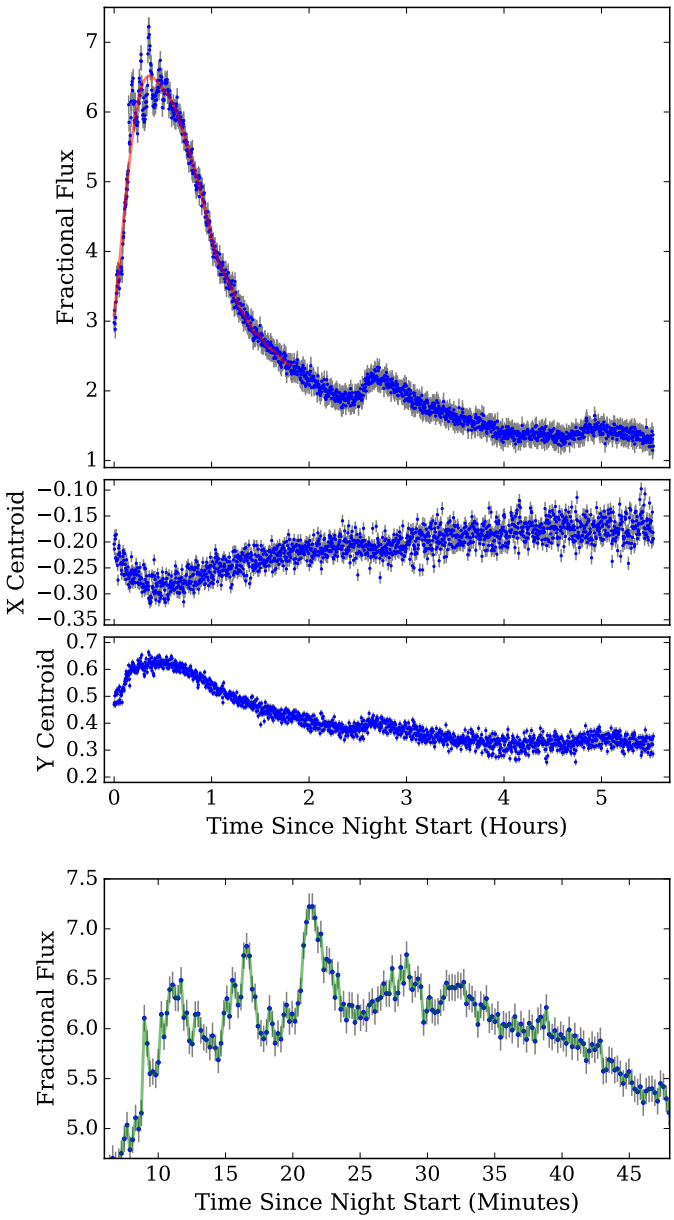

Figure 4.1: NGTS data from the night of the flare. Top: The flare after the removal of the background source flux, as discussed in Sect. 4.2.4. Not shown are the quiescent nights before and after the flare, which are at an average value of 0 with this normalisation. In red is the trend of the flare from an EMD analysis, discussed in Sect. 4.3.4. Middle: Centroid movement (in pixels) during the night, showing correlation with the flux. X and Y correspond to the movement along the axes specified in Fig. 4.2. Bottom: Zoom in of the flare peak, in which oscillations are clearly seen. A flux spike, lasting only about 20-30 seconds, is seen at the beginning of the oscillations approximately 8 minutes after the night start. A green interpolating line is shown to aid the eye.

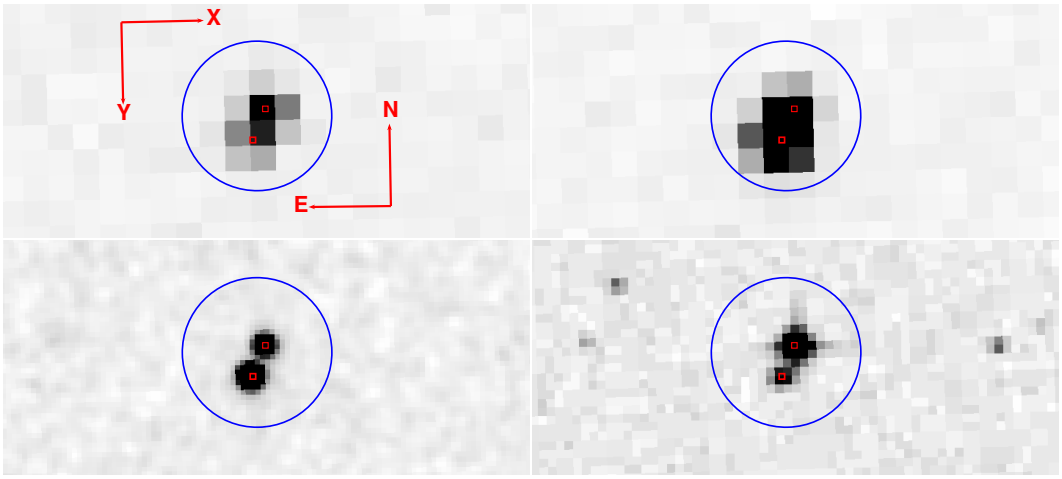

Figure 4.2: Comparison of NGTS images with 2MASS and DSS. Top left is our reference image of the source, top right is the image of the source at the peak of the flare. The flaring source is located at the south east. Bottom left is the available 2MASS image and bottom right is from DSS. The blue circle shows our aperture used, red squares are the positions of each individual source from *Gaia*. We have also plotted the NGTS image coordinate axes for reference to Fig. 4.1.

et al., 2006), *Gaia* (Gaia Collaboration et al., 2016b, 2018b), SkyMapper (Wolf et al., 2018) and WISE (Cutri and et al., 2014) information, we performed spectral energy distribution (SED) fitting using PHOENIX models (Allard, 2016). From this SED fitting and the *Gaia* DR2 parallax we obtain stellar temperature and radius estimates. We find an effective temperature of 3090±30 K and a radius of 1.04±0.02 $R_{\odot}$ for the flare star.

The large radius is not consistent with the expected value for a main sequence M dwarf of this temperature (∼0.2 $R_{\odot}$; Mann et al., 2015), suggesting NGTS J1219-3555 is not a single main sequence object. NGTS J1219-3555 is shown on a HR diagram in Fig. 4.4, where it resides around 1.5 magnitudes above stars of the same G_{BP}-G_{RP} colour. If it were a binary star we would expect it to reside no more than 0.753 magnitudes above the main sequence (Gaia Collaboration et al., 2018a), which is not consistent with our observation.

An alternative possibility is that NGTS J1219-3555 is a pre-main sequence object. Interpolating the MESA Isochrones and Stellar Tracks (MIST) v1.1 models (Dotter, 2016; Choi et al., 2016, with updated *Gaia* DR2 passbands and zeropoints) at the position of NGTS J1219-3555 in Fig. 4.4 and assuming zero interstellar reddening, we estimate an age of 2.2 Myr and a mass of 0.18 $M_{\odot}$. These correspond to a $T_{\rm eff}$ of 3180 K and a radius of 0.96 $R_{\odot}$, very similar to the values obtained from

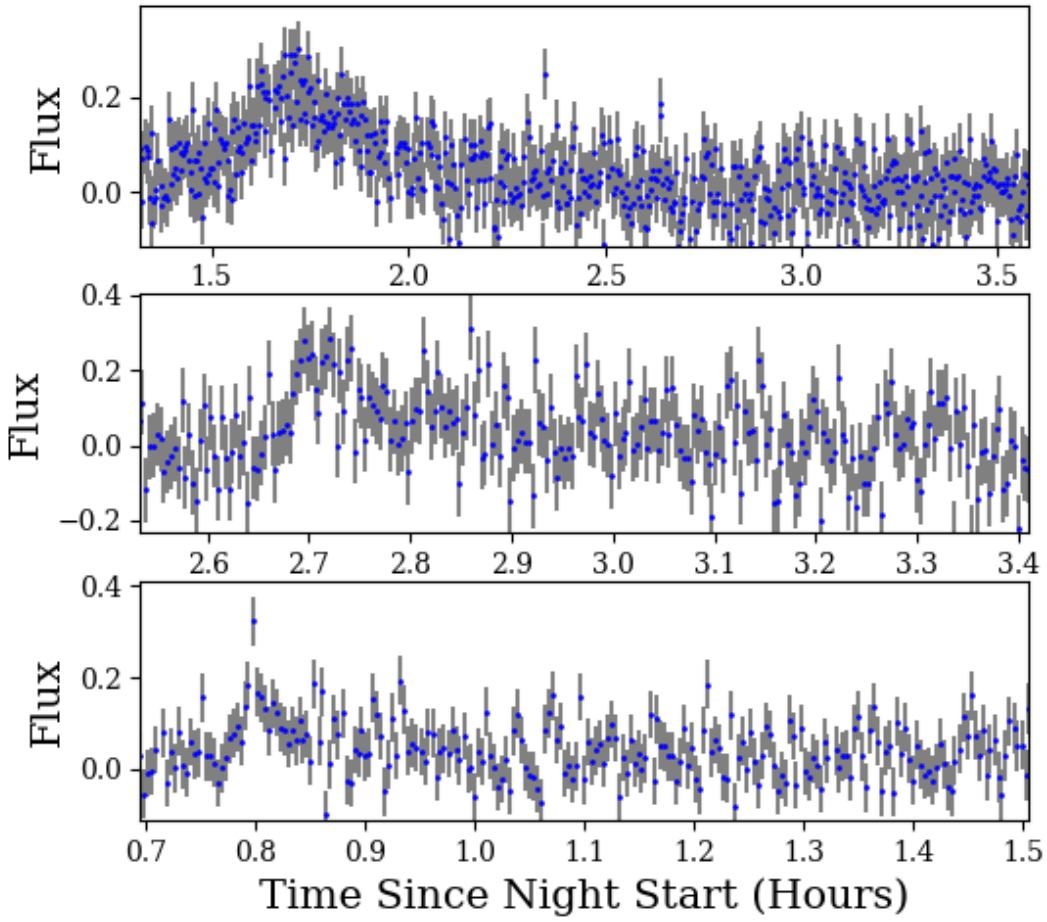

Figure 4.3: The three smaller flares visually identified in the NGTS lightcurve.

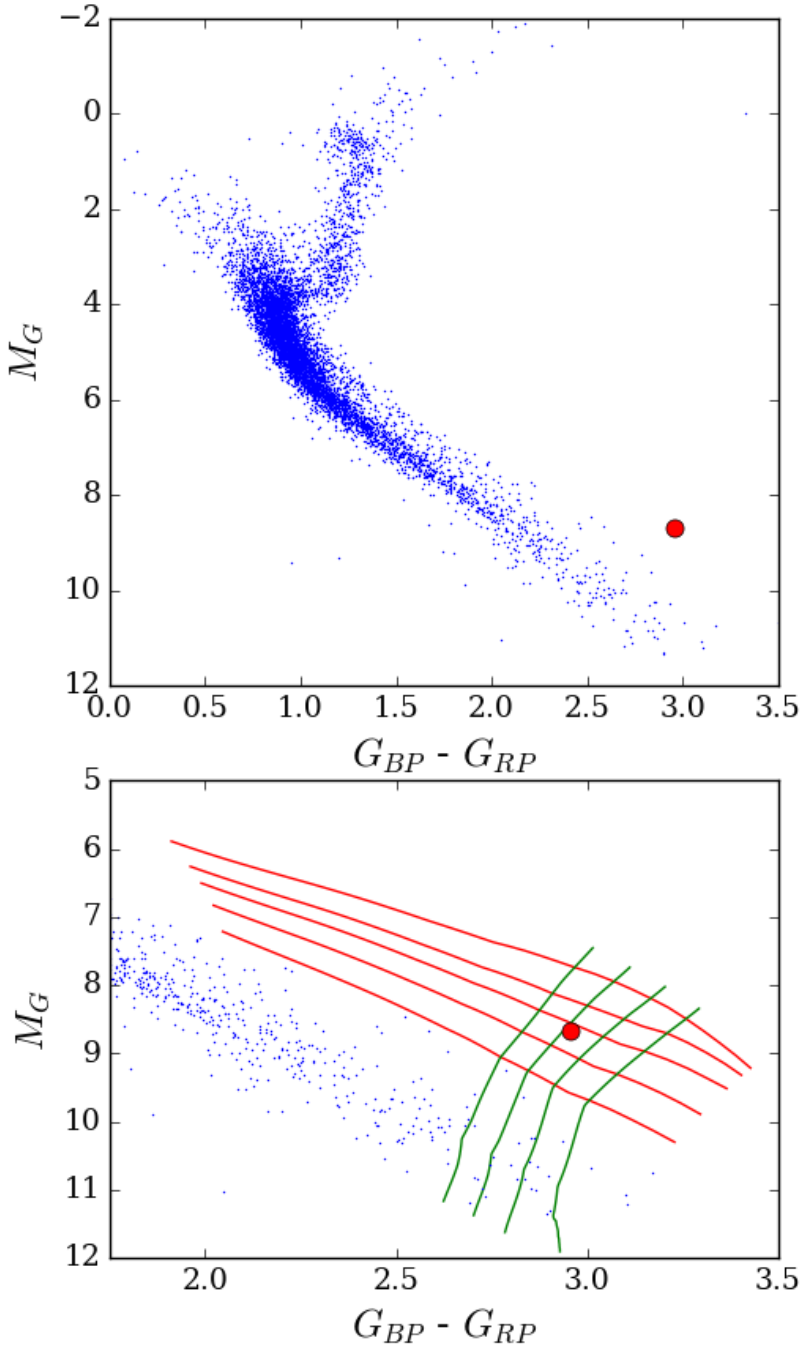

Figure 4.4: Top: Hertzsprung-Russell diagram of *Gaia* crossmatched stars in our NGTS field. The red marker indicates the position of NGTS J1219-3555 approximately 1.5 magnitudes above the main sequence. Bottom: The same HR diagram, but now zoomed in and with selected MIST models overlaid. Green lines indicate stellar mass tracks between 0.14 and 0.2 $M_{\odot}$and red line indicate isochrones of 1, 1.5, 2, 3 and 5 Myr.

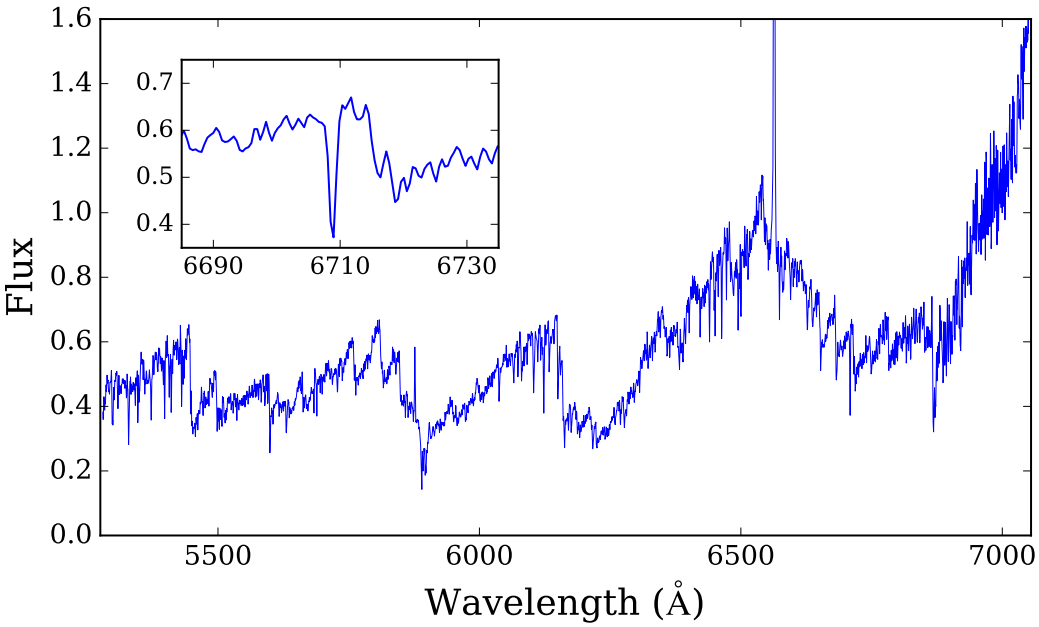

Figure 4.5: Mean quiescent WiFeS/R7000 spectrum of NGTS J1219-3555, normalised at 7000 Å. Hα continues to a peak flux of 6.5 on this scale. Inset is the Li I λ6708 absorption line.

the SED fit above. We do not identify any IR-excess from our SED fitting on either star, which implies that if NGTS J1219-3555 is a pre-main sequence star it has already lost the majority of any disc that was present during formation. Near- and mid-infrared disc fractions in young clusters and star-forming regions are consistent with median primordial disc lifetimes of 4–5 Myr for solar and later type stars (Bell et al., 2013; Pecaut and Mamajek, 2016), suggesting that if NGTS J1219-3555 is as young as 2 Myr, its disc dissipated earlier than expected, perhaps due to enhanced mass accretion as a result of strong flares (e.g. Orlando et al., 2011). We would expect a low mass star such as NGTS J1219-3555 to be moving almost isothermally along its Hayashi track and thus remain at a similar G_{BP}-G_{RP} colour as currently observed. As a further test we compare the 2MASS J,H,K photometry of NGTS J1219-3555 to those from giants and dwarfs in Bessell and Brett (1988). Doing this we find that NGTS J1219-3555 resides in the region occupied by dwarfs, supporting our interpretation that NGTS J1219-3555 is a pre-main sequence star as opposed to a subgiant or an unresolved binary system.

From our SED fitting we determine the neighbouring star to be a background G type star. From the *Gaia* parallax and proper motions it is clear that these two sources are unrelated, with the G type star being much more distant than

NGTS J1219-3555. The *Gaia* astrometry for NGTS J1219-3555 are not consistent with membership in any known young moving group, association or open cluster. Although spatially coincident with TW Hya Association members in the Northern reaches of the Scorpius-Centaurus OB association, the 210 ± 3 pc distance to NGTS J1219-3555 means it is likely a young background object or escapee from the region.

Optical spectroscopy

To confirm that NGTS J1219-3555 is a pre-main sequence star we acquired six 1800 s spectra on 2018 July 17 using the Wide Field Spectrograph (WiFeS; Dopita et al., 2007) on the ANU 2.3-m telescope at Siding Spring Observatory. The R7000 grating and RT480 dichroic used gave a resolution of $R \approx 7000$ over a wavelength range of 5250–7000 Å. Details of the instrument setup and reduction process are provided in Murphy and Lawson (2015). While the absence of strong emission lines other than Hα in the first spectrum indicates that the star was likely seen in quiescence, we appear to have serendipitously observed a flare event in subsequent spectra, with enhanced continuum emission, a rapid increase in the strength and width of the Hα and He I 5876/6678 Å emission lines and delayed Na D emission evident.

We observed NGTS J1219-3555 twice more in quiescence on July 18 and the average of the three quiescent spectra is plotted in Fig. 4.5. NGTS J1219-3555 is clearly of M spectral type, with strong Hα emission (EW $= -12 \pm 1$ Å) and Li I λ6708 absorption (EW $= 610 \pm 60$ mÅ). The uncertainty in each case is the standard deviation across the three observations. Comparing the spectra to M dwarf templates and radial velocity standards observed each night we estimate a spectral type of M3–3.5 and measure a mean radial velocity of 18.5 ± 1.4 km s^{-1}. Within the limits of WiFeS' modest velocity resolution the star's cross correlation function is consistent with a slowly-rotating ($v \sin i \lesssim 45$ km s^{-1}) single star (see discussion in Murphy and Lawson, 2015). We note that the SED and MIST $T_{\rm eff}$ values are 200–300 K cooler than the corresponding pre-main sequence temperature (3360 K) for an M3 star from the scale of Pecaut and Mamajek (2013). However, their sample of mid-M pre-main sequence stars was dominated by older, higher surface gravity stars from the 10–25 Myr-old η Cha, TW Hya, and β Pic moving groups, whereas NGTS J1219-3555 may be as young as 2 Myr old.

The detection of essentially undepleted lithium in an M3 star is immediate evidence of youth. The MIST models above predict that a 0.18 $M_{\odot}$ star will retain its primordial lithium for 30–35 Myr then rapidly deplete the element to zero photospheric abundance by an age of 40 Myr. Any detection of lithium in such a star therefore sets this as an upper age limit. Combining the lithium detection with the

position of the star in Fig. 4.4, we are confident that NGTS J1219-3555 is a very young pre-main sequence star.

By using the measured mean radial velocity of 18.5 ± 1.4 km s^{-1} we can test whether NGTS J1219-3555 is consistent with being an escapee from the TW Hya association. We find that for ages between 7 and 10 Myr that NGTS J1219-3555 could have travelled between 130 and 190 pc, which would place its origin within the TW Hya Assocation ($\sim$ 60 pc Zuckerman and Song, 2004; Gaia Collaboration et al., 2018a). This finding reinforces the pre-main sequence nature and suggests the age of NGTS J1219-3555 is around 5-10 Myr.

X-ray emission

As a young and active pre-main sequence star, we can expect NGTS J1219-3555 to be a relatively luminous X-ray source. Fortunately, it was observed serendipitously in X-rays with *XMM-Newton* for 27 ks on 2016 December 20 (ObsID: 0784370101; PI: Loiseau) and inspection of the pipeline-processed images shows that an X-ray source is indeed detected at the position of NGTS J1219-3555. The spatial resolution of *XMM-Newton* telescopes is around 5 arcsec (Jansen et al., 2001) and the detected X-ray source is clearly centered on the position of the pre-main sequence star, and not the background G star. There is no evidence for significant X-ray emission from this neighbouring object.

We extracted an X-ray light curve and spectrum for NGTS J1219-3555 from the EPIC-pn camera using the *Gaia* position and a 20 arcsec radius aperture. The background counts were estimated using a source-free circular region of radius 54 arcsec located nearby on the same CCD detector. We followed the standard data reduction methods as described in data analysis threads provided with the Science Analysis System[1] (SAS version 17.0). We found that a background flare had occurred during the final 4.2 ks of the *XMM-Newton* observation, and we excluded this interval when extracting the X-ray spectrum.

We inspected the X-ray light curve of NGTS J1219-3555 and found no evidence for significant variability during the *XMM-Newton* observation. This indicates that the observation was free of any large stellar flares and that the X-ray flux can be taken as representative of the quiescent level.

The X-ray spectrum of NGTS J1219-3555 is plotted in Fig. 4.6. We binned the spectrum to a minimum of 20 counts per bin, while ensuring that the spectral resolution would not be oversampled by more than a factor of 3, and we fitted the

[1] http://www.cosmos.esa.int/web/xmm-newton/sas

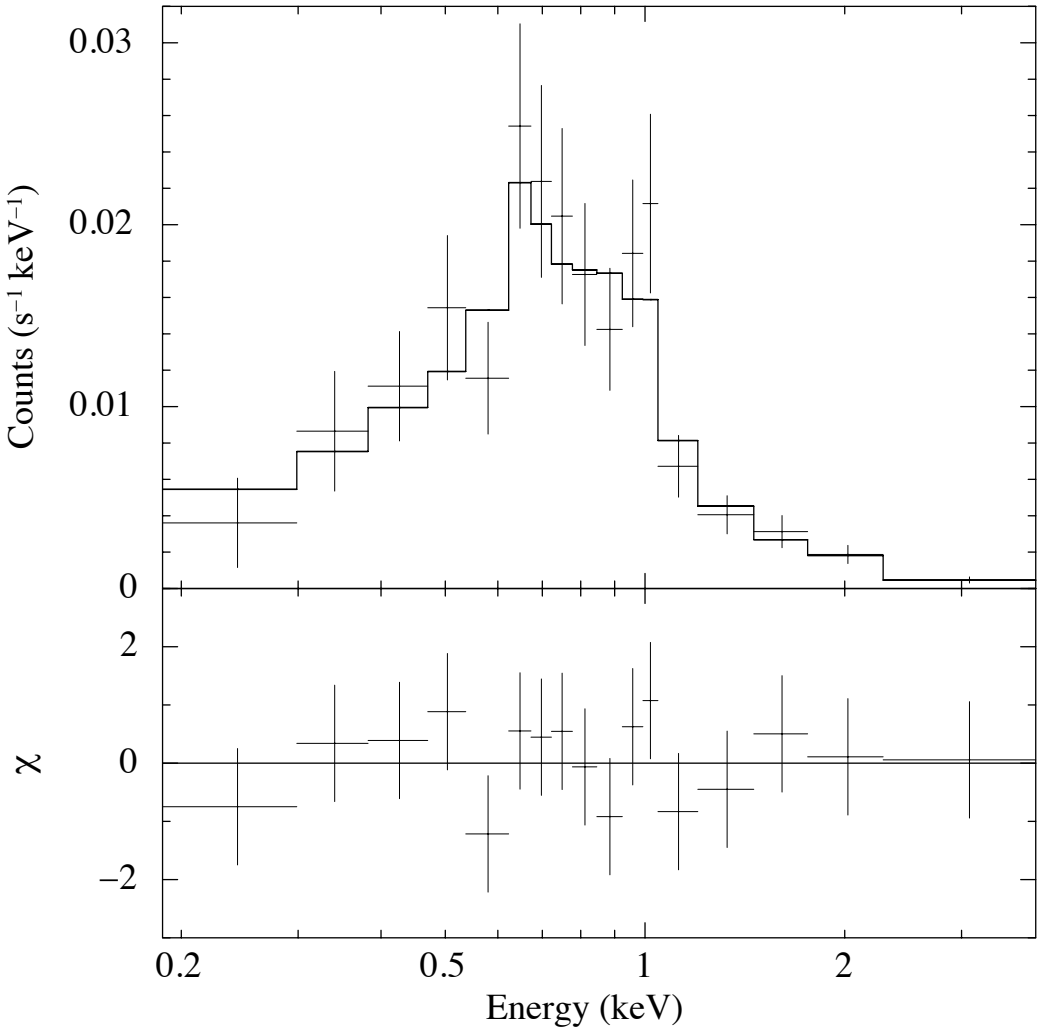

Figure 4.6: *XMM-Newton* EPIC-pn X-ray spectrum of NGTS J1219-3555 fitted using a two-temperature thermal plasma model, with abundances consistent with the inverse FIP effect, and circumstellar photoelectric absorption. The model and best fitting parameters are described in Sect. 4.2.3.

spectrum using XSPEC[2] (version 12.10).

The X-ray spectra of active late-type stars are characterized by optically-thin thermal emission from the corona with temperatures typically in the range 10^6–10^7 K, and we fitted the EPIC-pn spectrum of NGTS J1219-3555 using the APEC optically-thin thermal plasma model (Smith et al., 2001). We found it necessary to include two APEC components (as an approximation to the expected multi-temperature plasma) as well as photoelectric absorption by neutral material (using the TBABS model; Wilms et al., 2000).

We initially set elemental abundances to Solar values (Asplund et al., 2009), but we found that the spectral fit was improved significantly around 1 keV by allowing the Fe and Mg abundances to drop below Solar values (values of 0.03–0.19 Solar). This is consistent with the "inverse FIP effect" seen in very active stars and M dwarfs (where FIP refers to the first ionisation potential of the element; Wood and Linsky, 2010; Wood et al., 2012; Laming, 2015).

Our best fitting model and residuals are also plotted in Fig. 4.6. The fitted absorption column density was found to be $N_{\rm H} = 1.2 \pm^{0.6}_{0.4} \times 10^{21}\,{\rm cm}^{-2}$, which is larger than the total Galactic column density in the direction of NGTS J1219-3555 ($N_{\rm H} = 0.65 \times 10^{21}\,{\rm cm}^{-2}$; Kalberla et al., 2005). This suggests that the line of sight absorption is dominated by circumstellar material, as might be expected for such a young star. The best fitting temperatures in our model were $0.52 \pm^{0.08}_{0.12}$ and > 2.5 keV (6 and >29 MK).

The absorbed X-ray flux in the energy range 0.1–2.5 keV is $3.3 \pm^{2.1}_{1.3} \times 10^{-14}\,{\rm erg\,s^{-1}\,cm^{-2}}$, corresponding to an X-ray luminosity of $1.6 \pm^{1.0}_{0.6} \times 10^{29}\,{\rm erg\,s^{-1}}$ at a distance of 210 pc (Table 4.2). Setting the absorption column density in the model to zero, we can infer the inherent unabsorbed flux to be approximately $6 \times 10^{-14}\,{\rm erg\,s^{-1}\,cm^{-2}}$, corresponding to an X-ray luminosity of $3 \times 10^{29}\,{\rm erg\,s^{-1}}$. Comparing to the bolometric luminosity of the star (calculated from effective temperature and radius reported in Tab. 4.2) gives a ratio $logL_X/L_{Bol} = -3.1$. This X-ray activity level is characteristic of saturated X-ray emission, as expected for a young and active star (e.g. de la Reza and Pinzón, 2004; Stassun et al., 2004; López-Santiago et al., 2010).

4.2.4 Flux Removal

To calculate the true flare amplitude and energy we needed to remove the flux contribution from the background G star. To do this we used the PHOENIX spectra from our SED fitting in Sect. 4.2.3 and the NGTS sensitivity curve from Wheatley

[2]https://heasarc.gsfc.nasa.gov/xanadu/xspec/

et al. (2018) to estimate the NGTS count rates of the two sources. To account for sky extinction we assumed an atmospheric transmission curve for an airmass of 1.5.

Doing this gave a predicted total flux within 7 per cent of the observed value and the expected ratio of flux from each source. We corrected the predicted total flux to match the observed value, resulting in a quiescent NGTS count rate of 175 ± 20 ADU/s for the flaring star. We corrected the median level of our lightcurve to this value.

Stellar Rotation

Once we had removed the background flux from the NGTS lightcurve, we investigated the possibility of lightcurve modulation due to stellar rotation from NGTS J1219-3555. This was to identify potential starspots and active regions. To do this we used a generalised Lomb-Scargle periodogram from the ASTROPY LombScargle package (Astropy Collaboration et al., 2013). The flares were removed from the lightcurve when calculating the periodogram. We sampled periods between 1 hour and 25 days, requiring 10 samples per peak. This resulted in roughly 60000 periods to sample on (VanderPlas, 2018). 25 days was chosen as our maximum period to avoid the lunar period. During our analysis we masked suspicious periods due to 1 day aliases. We were unable to identify any convincing period of flux modulation from our analysis.

4.3 Results

4.3.1 Flare Amplitude and Energy

To measure the maximum amplitude of the flare we use the fractional flare amplitude, $\frac{\Delta F}{F}$, which gives the observed flare in units of the quiescent stellar flux. Using the value from Sect. 4.2.4 of 175 ± 20 ADU/s for the median flux level we measured the maximum fractional flare amplitude as 7.2 ± 0.8. The quoted error here is larger than that shown in Fig. 4.1 due to incorporating the error on the quiescent flux of both stars. In Fig. 4.1 and elsewhere we use the NGTS errors for our analysis.

We calculate the flare energy following the method of Shibayama et al. (2013), as outlined in Sect. 7.2.3, assuming the flare emission to be from a blackbody of temperature of 9000 ± 500 K. Blackbody-like emission from flares has been observed previously on main sequence M dwarfs (e.g. Hawley and Fisher, 1992) and this method has been used for M dwarf flare calculations elsewhere, such as Yang et al. (2017) and chapters 6 and 7. From this, we calculate the bolometric energy of the

flare as $3.2 \pm^{0.4}_{0.3} \times 10^{36}$erg. As we do not observe the entirety of the flare, this value acts as a lower limit. It is worth noting that this is roughly 10,000 times greater than the Carrington event energy of $\approx 10^{32}$erg (Carrington, 1859; Tsurutani et al., 2003).

We repeated our calculation for the three smaller flares we have identified. Doing this gives energies of $2.3 \pm 0.2 \times 10^{34}$erg, $7.2^{+0.7}_{-0.6} \times 10^{33}$erg and $2.9 \pm 0.3 \times 10^{33}$erg respectively. Consequently, from a total of 484 hours of observations on NGTS J1219-3555 we found four flares above 10^{33}erg in energy. This gives an estimated occurrence rate of flares above 10^{33}erg for NGTS J1219-3555 as 72 ± 36 flares per year.

4.3.2 Flare Duration

To measure the flare duration we make use of two timescales to account for not observing the full extent of the flare. We first use the e-folding timescale, defined as the time from the flare maximum to 1/e of this value. We measure the e-folding timescale as initially 1.8 hours. However, at around 2.7 hours in Fig. 4.1 there is a bump which increases the flux back above the 1/e threshold. It is uncertain whether this bump is due to this flaring event or from elsewhere on the flaring star, so we have decided to use our original e-folding timescale of 1.8 hours. From the centroid movement of this bump in Fig. 4.1 we are confident this bump is not due to the background star.

Secondly we use the "scale time", the duration for which the flare is above half the maximum flux value. This gives a measure of the duration including the flare rise without the uncertainties associated with determining where the flare begins. We calculate a scale time of 1.3 hours. We can also put a limit on the minimum and maximum full duration of the flare, using nights before and after. We calculate the absolute minimum and maximum durations as 5.5 and 42.4 hours respectively.

4.3.3 Significance of the Oscillations

In order to determine whether a statistically significant periodic component is present in the flare light curve, and if so to estimate its period, the Fourier power spectrum during the flare was examined, using the method from Pugh et al. (2017), which does not initially detrend the data.

The finite nature of time series data combined with the trends and astrophysical noise seen in flares means that the exact shape of the power spectrum will vary depending on where the start and end times of the flare light curve are defined.

Therefore the start and end times that gave the most visible periodic signal in the power spectrum were chosen manually. Flare power spectra tend to have a power that is related to the frequency by a power law, which may be due to trends and/or the presence of red noise, and this power law dependence needs to be carefully accounted for when assessing the significance of a periodic signal. For this part of the analysis, the first step was to fit the power law dependence with a simple model, which was done in log space where the power law appears as a straight line. A broken power law model was used to account for white noise that starts to dominate at higher frequencies (Gruber et al., 2011), resulting in a levelling off of the power law, and this model can be written:

$$\log\left[\hat{\mathcal{P}}(f)\right] = \begin{cases} -\alpha \log\left[f\right] + c & \text{if } f < f_{break} \\ -\left(\alpha - \beta\right)\log\left[f_{break}\right] - \beta \log\left[f\right] + c & \text{if } f > f_{break}\,, \end{cases} \tag{4.1}$$

where f_{break} is the frequency at which the power law break occurs, α and β are power law indices, and c is a constant. Estimates of the uncertainties of the fitted model were made by performing 10,000 Monte Carlo simulations using the uncertainties of the original light curve data. The following initial parameters were used: $\alpha = 2.0$, $\beta = 0.1$, $c = -0.1$, $\log f_{break} = -1.8$, and these were allowed to vary with a standard deviation equal to 10% of the parameter values in order to reduce of the possibility of the least-squares fit finding a local minimum rather than the global minimum.

Two approaches were used in order to assess the significance of a peak in the power spectrum corresponding to a periodic signal, which are based on the method described by Vaughan (2005) and account for data uncertainties as well as the power-law dependence of the spectrum. These approaches, which make use of regular and binned power spectra, are given in detail in Pugh et al. (2017).

From this analysis we find a peak in the regular power spectrum corresponding to a period of 320^{+40}_{-35} s (or $5.2^{+0.7}_{-0.6}$ min) which reaches the 98.8% confidence level, as shown by Fig. 4.7. The uncertainty was taken to be the standard deviation of a Gaussian model fitted to the peak. Because the peak in Fig. 4.7 appears to span more than one frequency bin, if we sum together the powers in every two frequency bins and assess the significance of the same peak in this binned power spectrum, shown by Fig. 4.8, then the peak reaches the 99.8% confidence level. Hence the periodic component of the flare light curve is highly significant and very unlikely to be the result of noise.

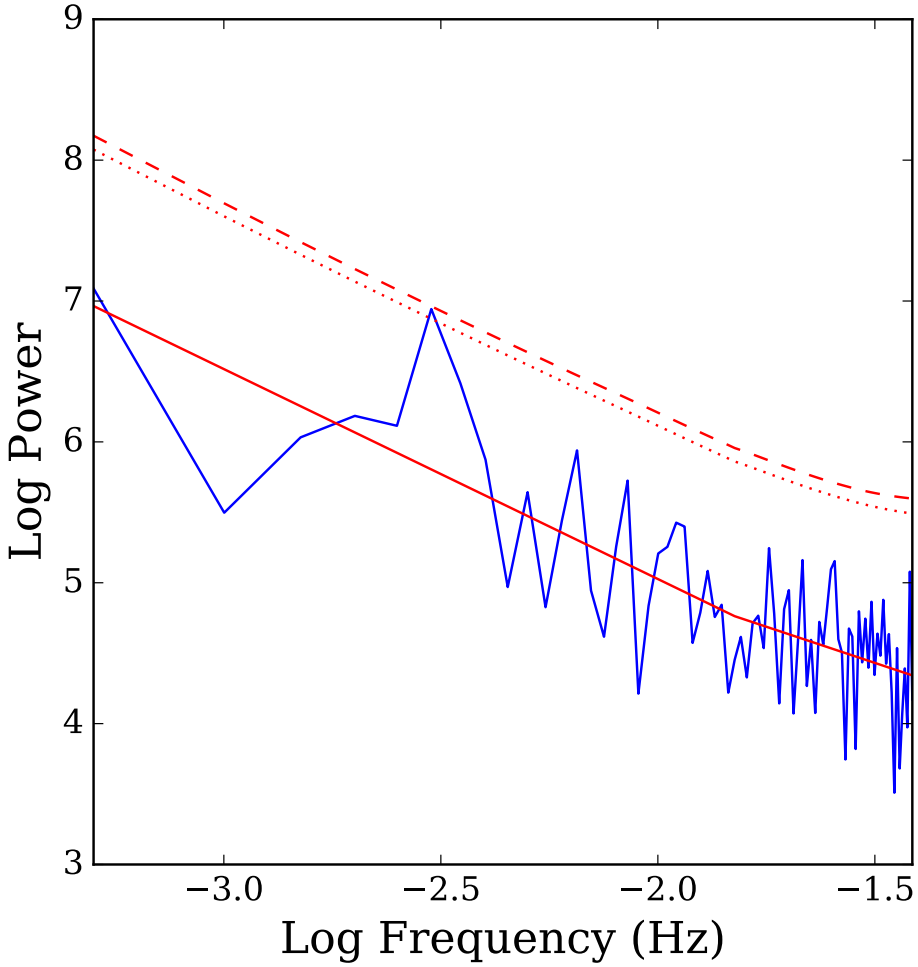

Figure 4.7: The regular power spectrum for the flare, shown in blue. The solid red line indicates the power law fit, while the two dashed lines are the 95 and 99% confidence levels respectively. This uses data between HJDs of 2457419.6607291666 and 2457419.6839814815.

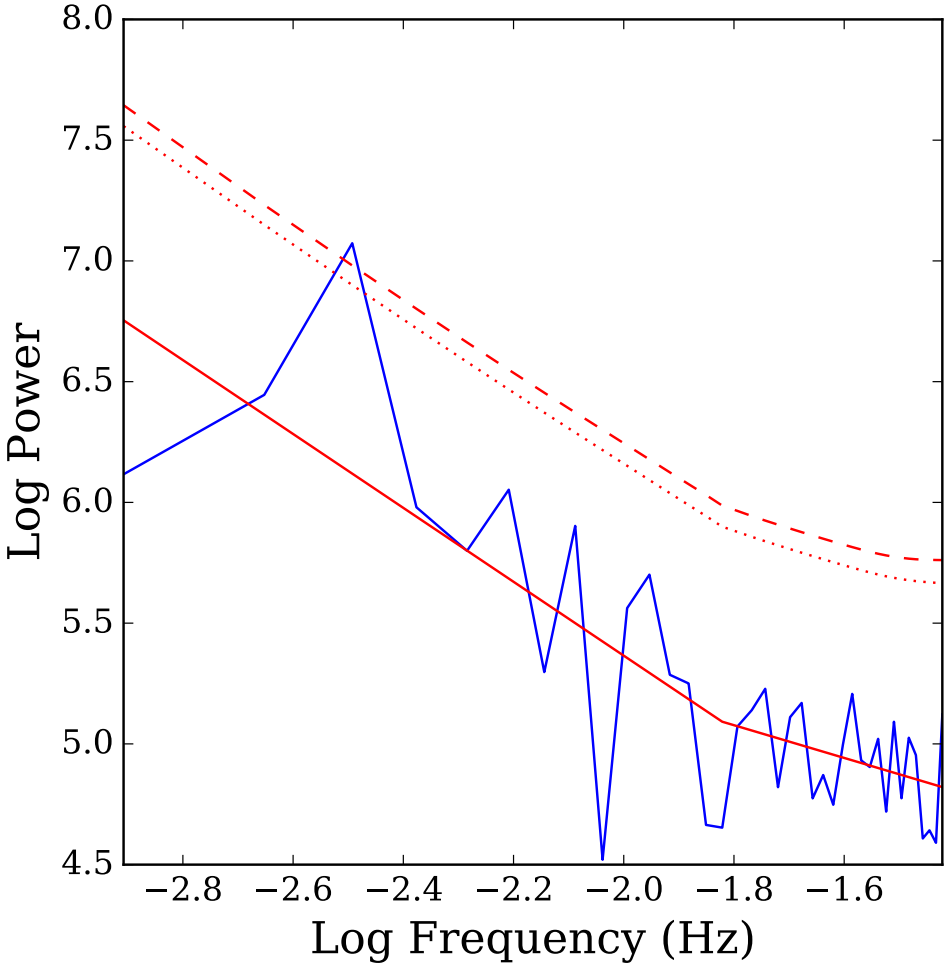

Figure 4.8: The binned power spectrum for the flare. This uses data between HJDs of 2457419.6607291666 and 2457419.684270833.

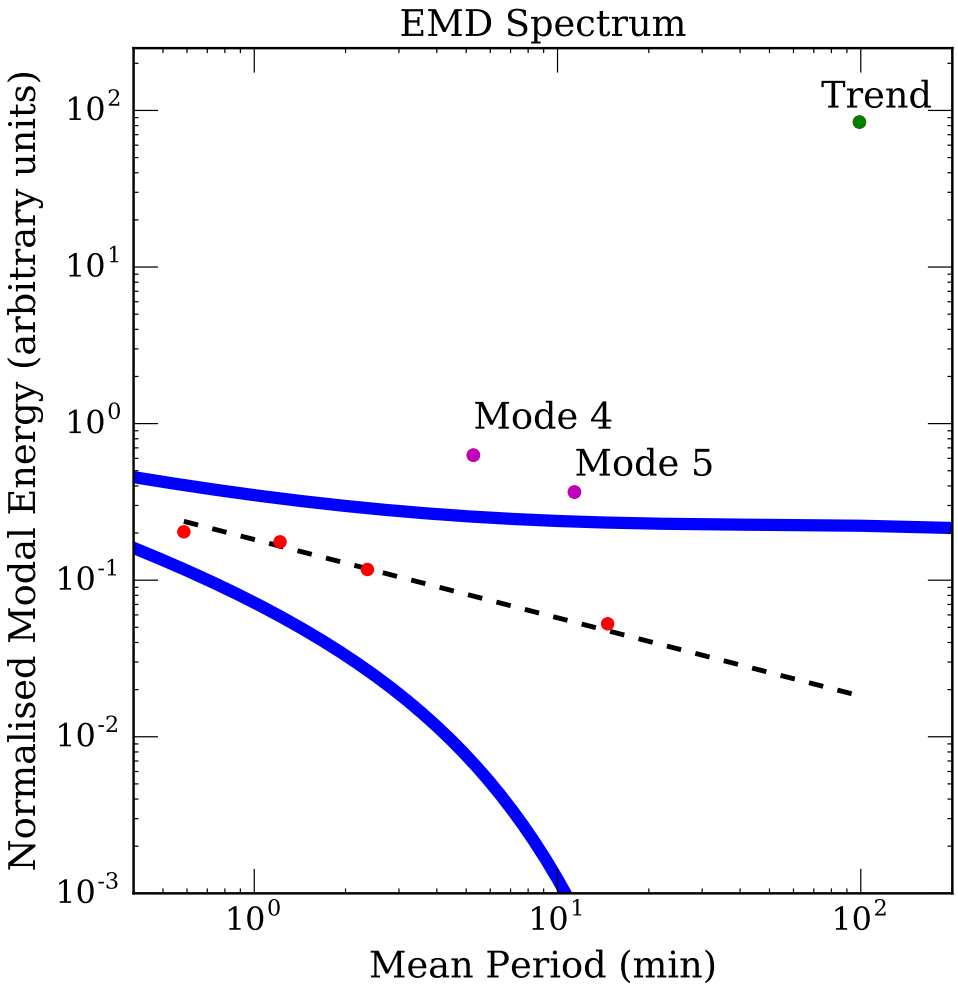

Figure 4.9: EMD spectrum for the identified modes, the normalised energy E_m versus the mean period P_m for each mode is shown. Modes 4 and 5 are shown with magenta points, the trend is shown in green, all other modes are in red. Plotted in black is the expected behaviour ($E_m P_m^{1-\alpha} = \text{const}$) for noise with $\alpha \approx 0.5$. Plotted in blue are the 99 per cent uncertainty levels, showing modes 4, 5 and the trend to be statistically significant.

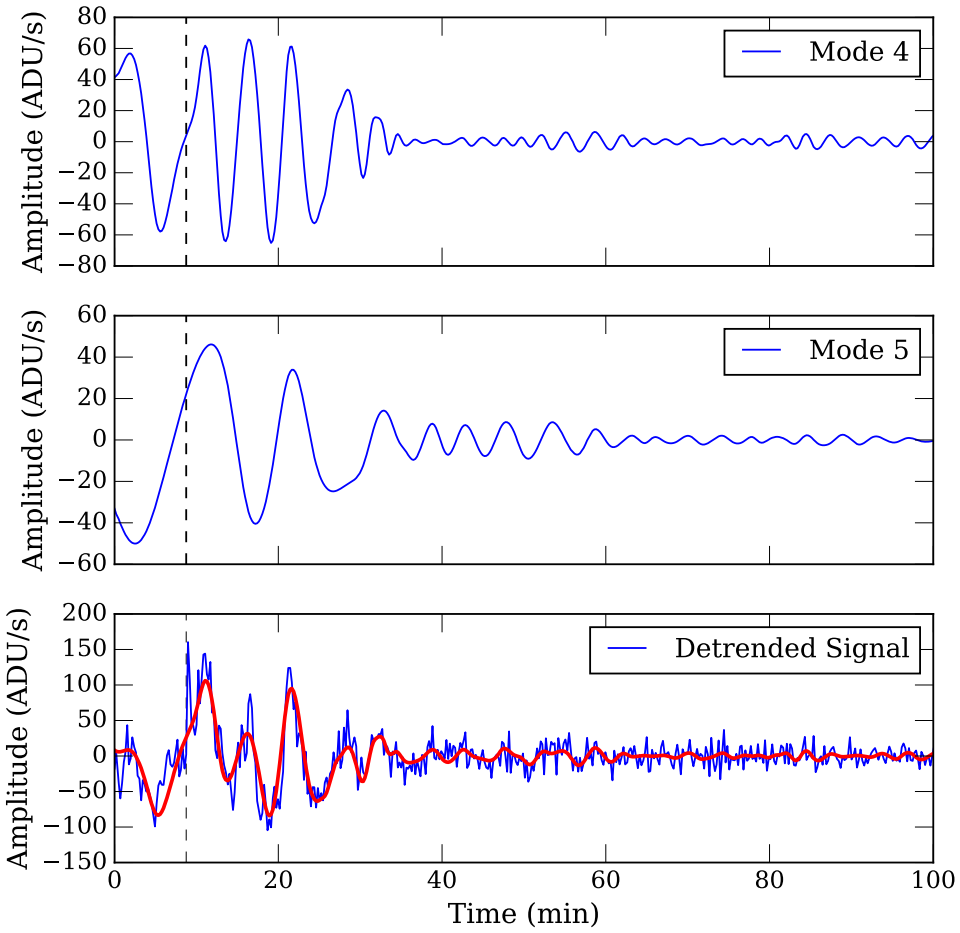

Figure 4.10: Modes 4 and 5 from the EMD analysis. The bottom row shows them combined (red) over the trend subtracted flare peak. The dashed vertical line indicates the start of a flux pulse, discussed in Sect. 4.4.

4.3.4 Empirical Mode Decomposition

An alternative method of investigating the periodicity of QPP signals is to use empirical mode decomposition (EMD) (e.g. Kolotkov et al., 2015; Cho et al., 2016). This method has been utilised previously for solar and stellar QPPs and is used to reduce signals into intrinsic mode functions (IMFs), which can be used to describe natural timescales appearing in the original dataset. In particular, the combination of modes can be used to model the longer timescale flare shape. We perform EMD on our flare and obtain seven modes, including the background trend. This trend contains the longest timescale behaviour and is used to fit for the overall flare shape (see Fig. 4.1 for this trend on the flare peak), as it does not include substructure.

In order to determine whether these modes are statistically significant we follow the method of Kolotkov et al. (2016), of which we give a brief overview. When performing EMD of coloured noise, the obtained IMFs have the relation $E_m P_m^{1-\alpha}$ =const, where E_m and P_m are the energy density and the modal period of each IMF and α is the power law index. α is used to describe the colour of the noise present, from the classical definition of the Fourier power spectral density, S, of the noise, $S = C/f^{\alpha}$. For example, $\alpha = 0$ for white noise, 1 for pink noise and 2 for red noise. Using this IMF energy-period relation and assuming all modes follow the same noise power, plotting the energy and period of each mode in logarithmic space and using a linear fit should give α. However, any modes with different behaviour, due to some underlying process, will lie off this line. We perform this for our modes, giving $\alpha \approx 0.5$, shown in Fig. 4.9, suggesting low levels of correlated noise. What can be seen in Fig. 4.9 is that modes 4, 5 and the background trend lie off this fitted model, suggesting additional signals are present in these modes which cannot be explained by noise. Using the full method from Kolotkov et al. (2016) we calculate 99 per cent significance levels for α=0.5 noise, shown by the blue lines in Fig. 4.9 for the upper and lower confidence levels. As a result, we see that modes 4 and 5 are statistically significant and proceed to analyse their morphology, regarding the other modes as noise. The trend is also outside this confidence interval, as expected.

For part of the above method we calculated the average modal periods of modes 4 and 5. These are 316 and 682 seconds respectively. As another test we also follow the method of Kolotkov et al. (2015) and use a Hilbert transform to calculate their instantaneous frequencies and periods. Constraining our region to the same area used in Sect. 4.3.3 we obtain median instantaneous periods of 338 and 625 seconds for modes 4 and 5 respectively. To obtain an estimate of the period error we use the mean and the standard deviation of these periods, giving periods of 327±11 and 654±30 seconds for modes 4 and 5 respectively.

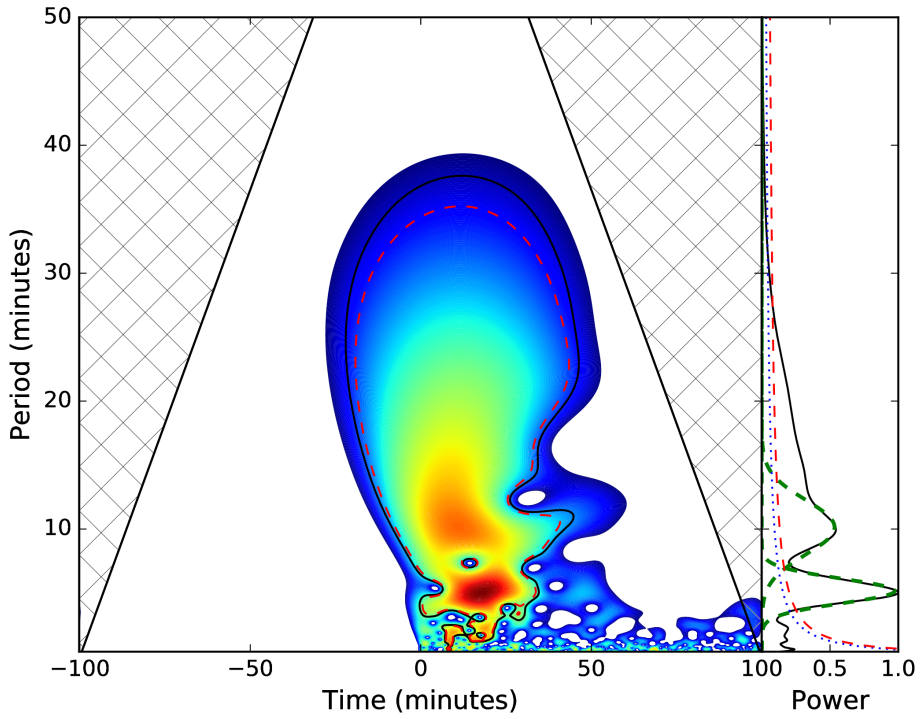

Figure 4.11: Wavelet analysis of the flare, showing two peaks at 309.2 and 608.5 seconds respectively. Red depicts the periods with greatest power. The black wavelet boundary is the 99 per cent confidence level and the red line is the modified confidence level, based on Auchère et al. (2016). The right hand panel shows the peaks of the two components, with Gaussian fits in green.

QPP Signal and Amplitude

Fig. 4.10 shows modes 4 and 5, along with their combination and the trend-subtracted flare. We can see that the combination of both modes is able to reproduce the observed QPPs. We note here that the periodicity of mode 4 appears to begin after a 20-30 second duration spike in flux, approximately 8 minutes into the night, whereas mode 5 is present from the start of the night. This spike in flux is also clearly visible in Fig. 4.1. We can use the trend in conjunction with the QPP signal to also determine the fractional flux amplitude, $\frac{\Delta F_{osc}}{F_{tr}}$, of the oscillations. Here we have denoted F_{tr} as the trend flux. Doing this and ignoring the flux spike we obtain the fractional flux of the combined oscillations $\frac{\Delta F_{osc}}{F_{tr}}$=0.1.

Property	Value
Energy (erg)	$>3.2 \pm^{0.4}_{0.3} \times 10^{36}$
Trend Amplitude (per cent)	650
Peak Flare Amplitude (per cent)	720
Min Duration (Hours)	5.5
Max Duration (Hours)	42.4
e-folding duration (Hours)	1.8-2.6
Scale time (Hours)	1.3
QPP Period, Fourier (s)	320^{+40}_{-35}
QPP Period, EMD - modal (s)	316 (Mode 4), 682 (Mode 5)
QPP Period, Wavelet (s)	309 (Mode 4), 609 (Mode 5)
QPP Amplitude (per cent)	10

Table 4.1: Properties of the superflare detected from NGTS J1219-3555.

Wavelet Analysis

In order to help confirm the periods from our previous two methods, we have performed a wavelet analysis. This was done incorporating the method of Auchère et al. (2016), which takes into account the total number of degrees of freedom of the wavelet spectrum when assessing the significance of identified peaks in power. To perform this analysis we used a detrended lightcurve, obtained by dividing our lightcurve by the overall flare trend identified through our EMD analysis. The results of our wavelet analysis are shown in Fig. 4.11. From Fig. 4.11 we can see two peaks in power, at 309 and 609 seconds. These agree with the period identified from our power spectrum analysis and the two periods identified with the EMD analysis, adding weight to there being two periods present. The ratio between these periods suggests that they may be harmonics of the same MHD mode, something which we discuss in Sect. 4.4.5. The 309 second period appears to show a slight offset from the 609 second peak, something that is also seen in our EMD analysis and is also discussed in more depth in Sect. 4.4.5.

4.4 Discussion

We have detected a large white-light stellar flare from the pre-main sequence M star NGTS J121939.5-355557. This star is extremely young with an estimated age of 2.2 Myr and undepleted lithium in the stellar spectrum. From SED fitting and optical spectroscopy we estimate a spectral type of M3-3.5. The flare displays multi-mode quasi-periodic pulsations in the peak. We have calculated the energy of this flare as $3.2 \pm^{0.4}_{0.3} \times 10^{36}$erg and the maximum amplitude as 7.2 ± 0.8. Through multiple

methods we have identified the periods of oscillations as approximately 320 and 660 seconds, with an oscillation amplitude ($\frac{\Delta F_{osc}}{F_{tr}}$) of 0.1. The 320 second oscillation mode appears to begin after a 20-30 second spike in flux during the flare rise. The observation of this spike and the resolution at which the 320 second mode is seen is a testament to the high cadence of NGTS compared to the *Kepler* and *TESS* short cadence modes, which would not obtain such detail.

4.4.1 Flare Energy

In Sect. 4.3.1 we calculated the lower limit of the flare energy as $3.2 \pm^{0.4}_{0.3} \times 10^{36}$erg. This energy is greater than all M dwarf flares observed with *Kepler* by Yang et al. (2017) and is comparable to that emitted by the highest energy G star superflares (e.g. Shibayama et al., 2013; Wu et al., 2015). This value sits within the range of bolometric flare energies calculated for 3 Myr stars in NGC2264 by Flaccomio et al. (2018), using targeted *CoRoT* observations. It is also similar to the energies of flares observed from long cadence K2 observations of the 1 Myr brown dwarf CFHT-BD-Tau 4 by Paudel et al. (2018b).

As mentioned in Sect. 4.3.1, due to us not observing the entirety of the flare this energy is a lower limit. Previous works that have observed only a portion of long duration flare events have been able to estimate the full energy through using empirical flare models to obtain the full flare shape (Schmidt et al., 2016). These models typically assume the flare is a "simple" event, i.e. with no significant substructure (e.g. Davenport et al., 2014; Jackman et al., 2018, also Chapter 3). However, "complex" flares such as the one observed do not strictly follow such models and have a range of morphologies (e.g. multiple peaks). Consequently, we have decided against applying an empirical flare model to estimate the full energy.

When calculating the bolometric energy, it was assumed that the flare could be modelled as a 9000K blackbody. This method assumes that the spectrum of the flare is constant for the total duration. Previous observations have shown this may not be the case (e.g. Kowalski et al., 2013) and has resulted in other works resorting to alternative methods. One commonly used method is to calculate the equivalent duration of the flare and multiply this by the quiescent luminosity of the star in the instrument bandpass (e.g. Hawley et al., 2014; Davenport, 2016; Vida et al., 2017). For our observed flare we have decided not to use such a method. Our reasoning for this is that using the quiescent luminosity in such a way assumes the flare emits with the same spectrum as the star, which for M stars is not the case - particularly over a wide bandpass such as NGTS. By using a 9000K blackbody we expect to remain close to an expected flare spectrum.

4.4.2 Occurrence Rate of Flares

In Sect. 4.3.1 we estimated the occurrence rate for flares above 10^{33}erg as 72 ± 36 per year for NGTS J1219-3555. For the flare in Fig. 4.1, a simple scaling of a single detection in 484 hours gives an estimated occurrence rate for flares above 10^{36}erg for NGTS J1219-3555 alone as 18 per year. A more reliable estimate can be made by assuming stellar flares on NGTS J1219-3555 occur with a power law distribution of flare energies (e.g Lacy et al., 1976). By normalising to our lower energy occurrence rate we can estimate the distribution at higher energies.

From X-ray observations of the Orion Nebula Cluster by Caramazza et al. (2007), the power law index of X-ray flares from low mass stars has been measured as 2.2 ± 0.2. However, Flaccomio et al. (2018) have shown from simultaneous optical and X-ray observations that X-ray flares do not always have an optical counterpart. From their analysis, between 19 and 31 per cent of X-ray flares lack an optical counterpart. Consequently, as our observation is of a white-light flare we have decided to make use of power law indices obtained from white-light measurements. The power law index for white-light flares on active M stars has been measured for both individual stars (e.g. Moffett, 1974; Lacy et al., 1976; Ramsay and Doyle, 2015) and groups (e.g. Hilton, 2011). These measurements have shown that active M stars can have a range of power law indices. Due to this scatter we have chosen a range of power law indices for predicting the flare rate. We have chosen limits of 1.53 and 2.01, taken from Hawley et al. (2014) and Hilton (2011) for observations of active M stars. We note that the upper limit here is still similar to that from Caramazza et al. (2007). We have used these limits for the power law index to estimate the occurrence rate of our highest energy flare, assuming that flares above 10^{36} erg follow the same distribution as those at lower energies. For each power law limit we initially solve Eq. 1.3 for the normalisation constant, using the power law value and measured occurrence rate for flares above 10^{33} erg. We then used Eq. 1.3, with the new normalisation value, to estimate the occurrence rate of flares above 10^{36} erg. With these values for the power law index and our lower energy occurrence rate, we reestimate our occurrence rates for flares above 10^{36} erg from NGTS J1219-3555 as between 3 ± 1.5 per year and 2 ± 1 per decade.

While this is a wide range of values, it provides a more robust estimate of the occurrence rate of high energy flares from NGTS J1219-3555. By using the three lower energy flares, as opposed to the single high energy event which drew our attention to this star in the first place, we can avoid making estimates for an occurrence rate based on a single event. However, these estimates do still make the assumption that the high energy event we observed follows the same power law as

lower energy events. It has previously been noted that the occurrence rate may drop off at the highest energies, giving a broken power law (e.g. Davenport, 2016). As this break energy may vary from star to star, we have not incorporated this into our estimations. However, we do note that if our flare is in the "drop off" regime then this would make it even rarer than our estimations above. This highlights not only the rarity of this event, but the need for long-duration wide-field surveys such as NGTS to find them. Repeated seasons of observation with NGTS and incorporating the *TESS* data into similar analysis in the future will help further constrain the flare occurrence rate at all energies for this star.

4.4.3 Flare Amplitude

We can compare this flare to previous white light observations of QPP bearing stellar flares and see that it is the largest observed for its period timescale (between 5 and 15 minutes) and one of the largest detected overall. The maximum change in NGTS magnitude is $\Delta m_{NGTS} = 2.28$ for $\frac{\Delta F}{F}$=7.2$\pm$0.8. Of similar oscillation period were the flares from II Peg and EV Lac observed by Mathioudakis et al. (2003) and Zhilyaev et al. (2000) respectively. These both had observations in the U band, with flare amplitudes of 0.85 and $\approx$ 2.5. As stellar flares are blue in colour (particularly during the impulsive phase), we would expect increased amplitudes in the U band compared to the NGTS bandpass (e.g. as for *Kepler* Hawley et al., 2014). Using our SED fit from Sect. 4.2.3 with the assumed 9000K flare blackbody (using a Sloan SDSS U band filter[3]) we estimate $\Delta m_U = 6$ for the observed flare, equivalent in amplitude to the 32 minute period oscillating megaflare on YZ CMi (Kowalski et al., 2010; Anfinogentov et al., 2013). Consequently, we believe this flare to be one of the largest observed in white-light showing QPPs for both its period timescale and possibly overall.

4.4.4 Formation and Habitability of M Star Exoplanet Systems

Flares and associated Coronal Mass Ejections (CMEs) from pre-main sequence stars could have an important role in planetary formation and habitability. For example, these transient events have been proposed as a possible mechanism for the formation of chondrules found in meteorites (Feigelson, 2010). The flash-melting of these rocks requires a transient heat source, which could be provided either by direct absorption of flare XUV irradiation (Shu et al., 2001), or through a flare associated shock wave (Nakamoto et al., 2005).

[3]http://svo2.cab.inta-csic.es/svo/theory/fps3/index.php?id=SLOAN/SDSS.u&&mode=browse&gname=SLOAN&

Flares and CMEs have also been linked to high stellar mass-loss rates by Osten and Wolk (2015) for young stars and for those with debris discs, CMEs have been highlighted as a possible cause for observed IR variability. This is due to the removal of IR-emitting dust by CMEs on the timescales of days (Osten et al., 2013). For protoplanetary discs, large X-ray flares could, along with altering the structure and ionisation fraction of the disc (e.g. Ilgner and Nelson, 2006), cause increased mass transfer from the disc onto the star. This is through perturbations from flare loops linking the star and inner disc (Orlando et al., 2011) which result in bursts of accretion.

Once planets are formed, they will also be subject to irradiation from flares and CMEs. The transient increase of the stellar wind through CMEs may negatively influence the formation of a planetary dynamo (Heyner et al., 2012), resulting in a weakened planetary magnetic field. The planetary magnetic field is one of the main defences against the detrimental effects of CMEs, which can compress the planetary magnetosphere and expose the atmosphere to erosion (e.g. Kay et al., 2016). Along with this, X-ray and UV irradiation from the flare itself may cause intense planetary ozone depletion (Segura et al., 2010), altered atmospheric chemical abundances (Venot et al., 2016) and potential damage to the DNA of surface organisms (e.g. Lingam and Loeb, 2017).

M stars have been noted for emitting less steady-state NUV radiation compared to earlier spectral types. This could limit possible UV-sensitive prebiotic chemistry (e.g. Ranjan et al., 2017), calling into question whether or not life could appear in these systems. The highest energy flares such as the one observed have been suggested as a possible way of delivering required levels of UV irradiation to kick-start such prebiotic reactions (Buccino et al., 2007; Ranjan et al., 2017; Rimmer et al., 2018). Due to the rarity of these high energy events, studies of their occurrence rates (as in Sect. 4.4.2) with surveys such as NGTS are vital in helping to determine whether prebiotic chemistry could take place or whether more negative effects limit habitability.

4.4.5 MHD Modes

Using the fourth and fifth modes generated from the EMD method outlined in Sect. 4.3.4 we found that the QPPs could be reproduced. We calculated the average modal periods as 316 and 682 seconds, and their median instantaneous periods as 338 and 625 seconds.

These instantaneous periods were obtained by using the region of data used in Figure 4.7, from the flare peak. We note that this still includes a small section

in the flare tail where the oscillations are indistinguishable from the noise in the data. Excluding this and constraining the Hilbert spectrum region further results in instantaneous periods of 330 and 660 seconds for modes 4 and 5. The period for mode 4 is in agreement with the period obtained from Sect. 4.3.3 and this brings the period of mode 5 into better agreement with its average modal period. Therefore the period ratio for modes 4 and 5 is approximately two, as would be expected if these modes were fundamental and secondary harmonics, but we note that even for harmonics this period ratio can deviate from two due to the dispersive nature of some MHD waves and the local geometry (e.g. Inglis and Nakariakov, 2009).

We note also that the appearance of modes 4 and 5 are similar to those of modes 4 and 5 from Kolotkov et al. (2015), which were oscillation periods of 45 and 100 seconds and were associated with potentially being harmonics of the MHD kink mode. The period ratio of modes 4 and 5 suggests that they are both from the same MHD process, possibly a standing slow magnetoacoustic wave. In this mode, excitations of both the fundamental and second harmonic can be produced, with their relative amplitudes being dependent on the location of the flare trigger. Specifically, pulses closer to the flare loop footpoint will excite the fundamental mode, whereas those closer to the apex will excite the second harmonic (Selwa et al., 2005). Selwa et al. (2005) also found that pulse triggers in locations other than the apex and footpoint can result in the excitation of a packet of standing waves with different modes, with the lowest-frequency two modes having the greatest contribution.

If this were the case, we may expect mode 4 to have an appearance similar to mode 5, namely that of an exponentially decaying sinusoid. However, the appearance of mode 4 is more similar to that of previously observed wave trains (e.g. Nakariakov et al., 2004), which occur due to fast magneto-acoustic waves propagating in the plasma non-uniformity. These wave trains are highly dispersive in nature and can be created via an impulsive driving pulse or perturbation (Roberts et al., 1984). We observe a spike in flux during the flare rise, immediately after which the observed periodicity of mode 4 begins. This flux spike lasts for approximately 20-30 seconds in total, meaning it would not be identified in *Kepler* or *TESS* short cadence observations. The amplitude of this spike is greater than the detrended signal, making it possible that this is a driving pulse which triggers the appearance of mode 4. A similar example has been observed in the Sun by Nisticò et al. (2014), where a pulse from a single source set off a quasi-periodic wave train. We do not see a similar change in period from mode 5 in Fig. 4.10.

This behaviour is also seen in Fig. 4.11 from our wavelet analysis, where the

shorter period peak is offset from the longer period. Consequently we propose that this is a broadband driving pulse which results in the excitation of a quasi-periodic wave train (Nakariakov and Melnikov, 2009; Nakariakov et al., 2016), resulting in mode 4. This wave train could then be a combination of fast magnetoacoustic harmonics.

Mode 5

As mentioned previously, mode 5 does not share a similar appearance to mode 4 and seems generally unaffected by the observed flux spike. Instead it has the appearance of a decaying mode with a damping time of ∼20 minutes. Comparing this damping time to the oscillation period of ∼660 seconds, we find it is in agreement with the upper limit of the relation found by Ofman and Wang (2002). This relation is for the oscillation period and damping timescale of hot flare loops observed by the SUMER instrument aboard *SOHO* (Wang, 2011).

To test the hypothesis that mode 5 is indeed due to a standing slow mode, we can compare the period ratio between our two modes. If we assume the coronal loop to be represented by a magnetic cylinder of radius a and length L, in the low β limit (where magnetic pressure dominates) we can write the period of mode 4 as

$$P_1 = \frac{2\pi a}{j_{0,1} v_A}\left(1 - \frac{\rho_e}{\rho_o}\right) \tag{4.2}$$

where v_A is the Alfvén speed within the loop, ρ_e and ρ_o are the external and internal plasma densities and $j_{0,1}$ is the first zero of the Bessel function $J_0(z)$ (Roberts et al., 1984). For $\rho_e << \rho_o$, the fast mode is highly dispersive. Consequently, the bracketed term reduces to unity and we can rewrite equation 4.2 as

$$P_1 \approx \frac{2.62a}{v_A} \tag{4.3}$$

For a standing slow mode the period, P_2, is given by Roberts et al. (1984) as

$$P_2 \approx \frac{2L}{c_s} \tag{4.4}$$

where c_s is the internal sound speed of the cylinder. From our observations, $\frac{P_2}{P_1} \approx 2$, so

$$\frac{P_2}{P_1} = \frac{2L}{c_s} \cdot \frac{v_A}{2.62a} \tag{4.5}$$

which approximates to $\frac{v_A L}{c_s a}$. Hence, $\frac{L}{a} \approx 2\frac{c_s}{v_A}$. The Alfvén speed is typically greater

than the sound speed, resulting in $L < a$, namely the length of the cylinder is less than its radius. This is an unrealistic expectation for coronal loops and is not supported by observations from solar flares, making it unlikely mode 5 is a standing slow mode. An alternative option is that mode 5 is instead a standing kink mode with a decaying amplitude. The period of a standing kink mode is given by Edwin and Roberts (1983) as

$$P_2 \approx \frac{2L}{c_k} \tag{4.6}$$

where c_k is the internal kink speed and in this low β regime is approximately $\sqrt{2}v_A$ (e.g. Nakariakov and Ofman, 2001). From this, we can write the period ratio $\frac{P_2}{P_1}$ as

$$\frac{P_2}{P_1} = \frac{2L}{c_k} \cdot \frac{v_A}{2.62a} \tag{4.7}$$

which approximates to $\frac{L}{2a} = 2$, or $\frac{L}{a} = 4$, which is closer to what we would expect from a coronal cylinder (e.g. Van Doorsselaere et al., 2011). Standing kink oscillations associated with flaring events have been observed previously on the Sun (e.g. Ofman and Wang, 2008; Zimovets and Nakariakov, 2015; Goddard et al., 2016) and have previously been suggested as the cause for QPPs in some observed stellar flares (e.g. Anfinogentov et al., 2013). Consequently, we propose that a plausible explanation for mode 5 is a standing kink mode which was triggered at the start of the flare.

4.4.6 Seismology of mode 4

The generation of impulsive fast waves can be used to investigate the behaviour of the oscillating region. To do this, we first rearrange equation 4.3, to obtain the ratio between a and v_A. We can then substitute in our observed fast mode period of 320s to determine the ratio as $a/v_A = 123$ s.

If we assume the cylinder radius of 1×10^{10}cm, similar to X-ray flares previously observed on pre-main sequence stars (e.g. López-Santiago et al., 2010; Favata et al., 2005), we estimate the Alfvén speed as $8 \times 10^7 \mathrm{cm\,s^{-1}}$. This estimated value is similar to those calculated for QPPs from main sequence M4 stars (e.g. Zaitsev et al., 2004; Mitra-Kraev et al., 2005; Anfinogentov et al., 2013), suggesting that our assumed cylinder radius value is a sensible one. Following this, if we use an aspect ratio of $\simeq 0.25$ (e.g. Mathioudakis et al., 2003) then the loop length is $\simeq 0.55\mathrm{R}_*$. Assuming the loop is semicircular we also estimate the height as $\simeq 0.18\mathrm{R}_*$, similar to the average loop height for X-ray detected flares from pre-main sequence stars studied by Flaccomio et al. (2018).

This ratio of loop length to stellar radius, while too large for the Sun and similar spectral types, is consistent with previous inferred measurements of loop lengths on main-sequence M dwarfs (which can go up to $2R_*$ in length, Mullan et al., 2006) and is well within loop lengths for pre-main sequence stars (e.g. Favata et al., 2005; Johnstone et al., 2012). Loop lengths of flares on pre-main and main-sequence M dwarfs were calculated by Favata et al. (2005) Mullan et al. (2006) using X-ray observations and relations derived from analytical modelling. These relations used to calculate the loop geometries make use of the cooling timescales of the T$\sim 10^6$ K plasma within the newly formed coronal loop (e.g. Haisch, 1983; Serio et al., 1991), the emission of which is observed in X-ray studies. For a given peak temperarture, a fast cooling timescale indicates a short loop which does not hold much plasma. Conversely, a large loop, with a lot of heated plasma, should take longer to cool (Serio et al., 1991). Depending on the exact method, the peak plasma temperature (used by Favata et al., 2005) or the emission measure (used by Mullan et al., 2006) is also used with the cooling timescale to infer the loop length. For stars with a measured NIR excess Favata et al. (2005) inferred loop lengths up to tens of times the stellar radii, with the flaring loops connecting the star and disc. For stars in their sample with no measurable NIR excess (such as we find for NGTS J1219-3555) Favata et al. (2005) found more compact loop lengths, similar to what we find for NGTS J1219-3555. These smaller loops were suggested to be anchored into the photosphere only.

4.4.7 Flare Decay

We also note the flare exhibits a "bump" at about 2.6 hours after the start of the night and another at 4.9 hours. Relative to the flare peak, they are 2.3 and 4.6 hours afterwards. Bumps have been observed in *Kepler* stellar flares by Balona et al. (2015) who argued that they cannot be due to simultaneous independent flaring events, nor due to forced global oscillations. One possibility is that while these bumps are not from independent flares, they are instead due to sympathetic flaring. Sympathetic flaring occurs when the primary flare triggers a successive flare, due to a physical connection (Moon et al., 2002). Such behaviour would result in the observed flux increases in the flare tail, making it a possible cause.

4.5 Conclusions

In this chapter we have detected a high energy stellar flare from the 2 Myr old pre-main sequence M star NGTS J121939.5-355557 with NGTS. This flare has a

Parameter	Value (Flaring)	Value (Companion)	Reference
	Position		
RA ICRS	184.9153111262°	184.9144202	1
Dec ICRS	-35.9338316576°	-35.9321149	1
	Photometric		
SkyMapper u	N/A	15.930 ± 0.009	2
SkyMapper v	N/A	15.523 ± 0.008	2
SkyMapper g	17.060 ± 0.009	14.521 ± 0.003	2
SkyMapper r	16.125 ± 0.011	14.227 ± 0.005	2
SkyMapper i	14.379 ± 0.014	14.063 ± 0.008	2
SkyMapper z	13.651 ± 0.004	14.019 ± 0.009	2
Gaia G	15.286 ± 0.001	14.237 ± 0.001	1
Gaia BP	16.972 ± 0.009	14.576 ± 0.001	1
Gaia RP	14.017 ± 0.003	13.738 ± 0.001	1
J	12.086 ± 0.024	13.162 ± 0.030	3
H	11.520 ± 0.025	12.846 ± 0.041	3
K_s	11.160 ± 0.021	12.842 ± 0.034	3
$W1$	11.000 ± 0.024	12.575 ± 0.049	4
$W2$	10.792 ± 0.021	12.594 ± 0.052	4
$W3$	10.778 ± 0.071	12.867 ± 0.463	4
$W4$	8.704	8.680	3
	Kinematic		
μ_{RA} [mas yr^{-1}]	-19.177 ± 0.108	-2.653 ± 0.108	1
μ_{DEC} [mas yr^{-1}]	-8.490 ± 0.083	-4.644 ± 0.037	1
Parallax [mas]	4.733 ± 0.072	1.098 ± 0.032	1
Distance [pc]	210 ± 3	887 ± 26	
	SED Fit		
T_{eff} [K]	3090 ± 30	5610 ± 30	
R [$R_\odot$]	1.05 ± 0.02	1.22 ± 0.03	
	X-ray emission		
L_X [erg s^{-1}]	3×10^{29}		
$\log L_{\rm X}/L_{\rm Bol}$	-3.1		

Table 4.2: Parameters for our sources. References are 1. *Gaia* Gaia Collaboration et al. (2018b) 2. SkyMapper DR1.1 Wolf et al. (2018) 3. 2MASS Skrutskie et al. (2006). 4. WISE Cutri and et al. (2014). For distances we have used the values from Bailer-Jones et al. (2018). SkyMapper magnitudes are AB magnitudes.

minimum energy of $3.2 \pm^{0.4}_{0.3} \times 10^{36}$erg, making it one of the largest energy M star flares observed. In the peak of this high energy flare we have detected statistically significant quasi-periodic pulsations with an oscillation amplitude $\frac{\Delta F_{osc}}{F_{tr}}$ of 0.1. We have applied techniques typically used for analysis of solar flare QPPs to determine that the pulsations were formed of two distinct modes. The periods of these modes are approximately 320 and 660 seconds. With a measured amplitude of $\Delta m_{NGTS} = 2.28$ and an estimated amplitude of $\Delta m_U = 6$ we believe this is one of the largest white-light stellar flares to show QPPs of this timescale, if not QPPs in general.

Investigating these modes further, we have identified that the shorter period mode appeared after a high amplitude spike in flux during the flare rise. This spike lasted for 20-30 seconds and was only resolvable due to the high cadence of NGTS. We postulate that the short period mode is a highly dispersive fast mode excited by the observed flux spike, similar to events seen in the Sun. We hypothesize the longer period mode is a kink mode excited at the flare start, however we cannot categorically rule out other proposed methods for the QPP excitation (McLaughlin et al., 2018).

We have also detected three more lower energy flares in our data. Using these to estimate the flare occurrence rate, we find the high energy flare to be a rare event, with a possible occurrence rate of between 3 ± 1.5 per year and 2 ± 1 per decade, depending on the power law index of the assumed flare distribution. We use this to stress the importance of wide field, long timescale surveys such as NGTS in finding these high energy events, which must also have high cadence in order to characterise oscillation modes. This is not only for constraining their occurrence rates, but in helping to determine their role in the formation and habitability of Earth-like exoplanets around M-type stars.

Chapter 5

A white-light flare from an L2.5 dwarf

"I need the reddest flare star you have. No... that's too red."

Hans Moleman, *"Itchy & Scratchy Land"*, *The Simpsons* (adapted by J. A. G. Jackman)

5.1 Introduction

Previous studies of L dwarfs (T_{eff}= 1300-2300 K; Stephens et al., 2009) have shown them to be variable in a number of ways. Examples of this include periodic modulation due to clouds (e.g Gizis et al., 2015), radio emission due to aurora in late L dwarfs (e.g. Kao et al., 2018) and the presence of white-light flares (e.g. Gizis et al., 2013). As described in Chapter 1, white-light flares occur through reconnection events in the stellar magnetic field, which result in heating of the lower chromosphere/ upper photosphere (e.g. Benz and Güdel, 2010), resulting in white-light emission. While seen regularly on GKM stars, observations of white-light flares on L dwarfs remain rare, with only a handful of stars showing them to date (e.g. Paudel et al., 2018b). However, those observed have included some of the largest amplitude flares ever recorded, reaching up to $\Delta V \approx -11$ (Schmidt et al., 2016). This shows that white-light flaring activity persists into the L spectral type, despite previous studies of L dwarfs showing their chromospheres and magnetic activity to be diminished compared to those of late M dwarfs (e.g Schmidt et al., 2015).

Due to the rarity of these large amplitude flares, long duration observations

are required when targeting L dwarfs specifically. As described in Sect. 1.2 and 1.4, this became possible with the *Kepler* (Borucki et al., 2010) and *K2* (Howell et al., 2014) missions, which allowed continuous high precision monitoring of chosen objects (Gizis et al., 2013, 2017a; Paudel et al., 2018b). Through this, large amplitude flares ($\Delta V \approx -8$, $\Delta K_p = -5.4$) were detected on an L0 and L1 dwarf (Gizis et al., 2017a; Paudel et al., 2018b), along with smaller flares on two early L dwarfs (Gizis et al., 2013; Paudel et al., 2018b). Spectroscopy of an L5 dwarf by Liebert et al. (2003) showed an Hα flare, although this event lacked the continuum enhancement associated with white light flares. Observations of an L5 dwarf (Gizis et al., 2017b) with *K2* showed no detectable white light flares, suggesting such events are suppressed at late spectral types.

For targeted observations it is typically required that the star be visible in quiescence. For optical surveys which are not sensitive to late spectral types, this requirement limits observations to a small number of nearby early L dwarfs. Wide-field surveys (e.g. ASAS-SN), which obtain full frame images of large areas of sky per night allow studies to push to fainter stars. In these surveys, full frame images can be used to search for very faint stars that only become detectable when flaring. This led to the detection of a $\Delta V \approx -11$ flare from the L0 dwarf ASASSN-16ae (Schmidt et al., 2016), previously the only L dwarf flare detected from the ground with optical photometry. While these surveys can detect large flares, the low cadence lightcurves limit the study of shape and substructure, and hence also the accuracy of flare energy calculations (e.g. Schmidt et al., 2019). Consequently, in order to detect and characterise the largest flare events on the latest spectral types, high cadence wide-field observations with full-frame images are required.

In this chapter we present the detection of a white-light superflare from the L2.5 dwarf ULAS J224940.13-011236.9, which was observed at high cadence with the Next Generation Transit Survey (NGTS). This chapter is based on material from Jackman et al. (2019b). The source discussed in this chapter has also previously been identified as 2MASS J22494010-0112372. We describe the detection of the flare and how we derived the properties of the flare and the host star.

5.2 Observations

As described in Chapter 2, NGTS is a ground-based wide-field exoplanet survey, which obtains full-frame images from twelve independent telescopes at 12 s cadence (Wheatley et al., 2018). The telescopes have apertures of 20 cm and operate with a bandpass of 520-890nm. They have a total instantaneous field of view of 96 square

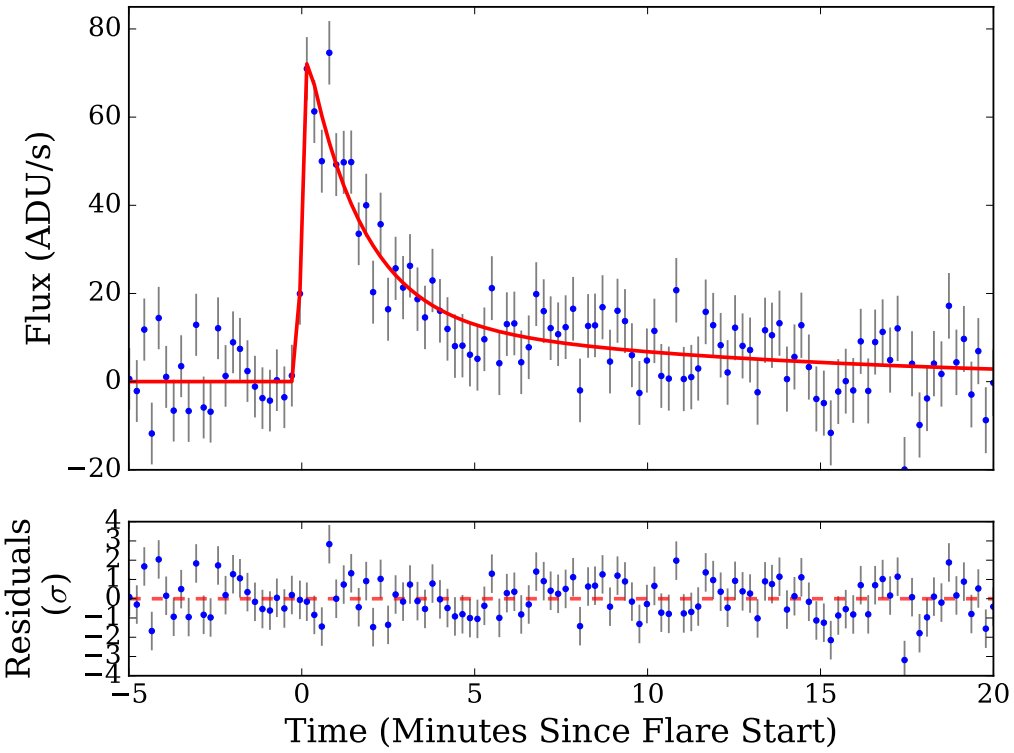

Figure 5.1: Top: NGTS lightcurve of the flare from ULAS J2249-0112. Blue points are NGTS photometry and the best fitting model is overlaid in red. Note the outlier near the flare peak, something we discuss further in Sect. 5.4.2. Bottom: Residuals from the model fit.

degrees.

The data presented in this chapter were collected with NGTS between 2017 May 07 and 2017 Dec 14, comprising 146 nights of data. The detected flare occurred on the night of 2017 Aug 13. The NGTS field used in this chapter is NG2251+0000, which is centered on 22:51:59.1, +00:00:02.7.

5.2.1 Input Catalogue and Flare Detection

In the normal mode of operations NGTS obtains lightcurves for all stars brighter than I = 16 (Wheatley et al., 2018). However, in each NGTS field there exist on average 2500 red stars fainter than this limit which can be identified using 2MASS (Skrutskie et al., 2006) and *Gaia* (Gaia Collaboration et al., 2018b). While too faint to observe as primary targets, by placing photometric apertures on their positions we can capture any variability, such as flares, that may result in them becoming bright enough to detect. To this end, for each NGTS field we compiled input catalogues

of known red stars using positions from 2MASS and the colour cuts for ultracool dwarfs specified by Muirhead et al. (2018). Where possible, 2MASS positions were replaced with the more precise values from *Gaia* DR2. However, many of the stars targeted were too faint to be detected with *Gaia*. These colour cuts are adapted from Lépine and Gaidos (2011) and are as follows. For sources with $H - K_s < 0.25$ we require

- J-H <1.0
- $0.746 < J - K_s < 0.914$

and for $H - K_s \geqslant 0.25$ we require $J - H < 0.914$. We have generated these input catalogues for 22 NGTS fields to date. The initial J, H and K_s infrared colour limits were used by Lépine and Gaidos (2011) to both identify possible M dwarfs and to separate low proper motion M dwarfs from giant stars in an all sky survey of bright M stars. Giant stars, which can appear similar in optical colours, have different near-infrared opacities, resulting in different colours (Bessell et al., 1998). Muirhead et al. (2018) found that for $H - K_s \geqslant 0.25$ the initial limits of Lépine and Gaidos (2011) removed many mid to late M dwarfs, along with early L dwarfs. The more liberal limit for $H - K_s \geqslant 0.25$ was adopted to keep these stars to allow the targeting of large numbers of ultracool dwarfs, while still excluding bluer giant contaminants.

The normal NGTS pipeline (Wheatley et al., 2018) was then run on these positions. To search for flares we follow the procedure outlined in Sect. 2.2 and look for consecutive outliers 6 median absolute deviations (MAD) above the median of a single night.

Using this method we detected a flare from the star ULAS J224940.13-011236.9 (Skrzypek et al., 2016) (hereafter ULAS J2249-0112), shown in Fig. 5.1. To confirm this star is the source of the flare we checked the centroiding of this source, along with the NGTS images before, during and after the flare. We can see no measurable centroid shift during the flare and do not identify any brightening from a nearby source or from a satellite passing through our aperture. Consequently, we are confident the detected flare comes from ULAS J2249-0112.

5.2.2 Stellar Properties

ULAS J2249-0112 has previously been identified as an L2.5($\pm$1) dwarf by Skrzypek et al. (2016), as part of a sample of photometrically classified L and T dwarfs from SDSS (York et al., 2000), UKIDSS (Lawrence et al., 2007) and WISE (Wright et al.,

2010). To confirm this and measure the effective temperature of ULAS J2249-0112 we fit the spectral energy distribution (SED) using the BT-Settl models (Allard et al., 2012). We fit to the catalogue photometry in Tab. 5.1, following a similar method to Gillen et al. (2017). We note here that this source is too faint to be detected by *Gaia*. From our fitting we measure an effective temperature of T_{eff}=1930±100 K, consistent with that expected for the L2.5 spectral type (Stephens et al., 2009).

ULAS J2249-0112 was also observed by the Baryon Oscillation Spectroscopic Survey (BOSS; Dawson et al., 2013). BOSS obtains optical spectra with a resolution of R ≈ 2000 over a wavelength range 3600-10000 Å. ULAS J2249-0112 also sits in SDSS stripe 82, however due to its faint i magnitude was not included in the analysis of BOSS ultracool dwarfs by Schmidt et al. (2015). We excluded wavelengths below 5400 Å in our analysis due to the lack of emission in the blue from ULAS J2249-0112.

Fitting this spectrum using the empirical L dwarf templates of Schmidt et al. (2015) gives a best fitting spectral type of L2.6±0.1, again confirming our spectral type determination and the low temperature. The BOSS spectrum with the best fitting template is shown in Fig. 5.2. Due to the low S/N ratio (1.2 around Hα) of the spectrum we are not able to clearly identify the presence of Hα emission in quiescence.

Kinematics

In order to estimate the distance to ULAS J2249-0112 we initially calculate the absolute 2MASS and WISE magnitudes using the relations of Dupuy and Liu (2012), derived from ground-based infrared astrometry, using the L2.5 spectral type. When calculating the distances using these individual absolute magnitudes, we found all calculated distances to be consistent. We thus took a weighted mean of the individual photometric distances, which we calculate as 76^{+8}_{-7} pc. For the proper motion we have used the measurements of Bramich et al. (2008), which are given in Tab. 5.1. These values were obtained using the repeat measurements of ULAS J2249-0112 as part of SDSS stripe 82. For the radial velocity we have used the value provided with the BOSS spectrum, $v_{rad} = -14 \pm 10\,\mathrm{km\,s^{-1}}$. By combining these values together we calculate the three-dimensional velocities (U, V, W)=$(-33.5 \pm 4.2,\ -10.3 \pm 6.1,\ 0.5 \pm 7.9)\,\mathrm{km\,s^{-1}}$. These values appear to place ULAS J2249-0112 within the thin disc (Schmidt et al., 2010; Burgasser et al., 2015).

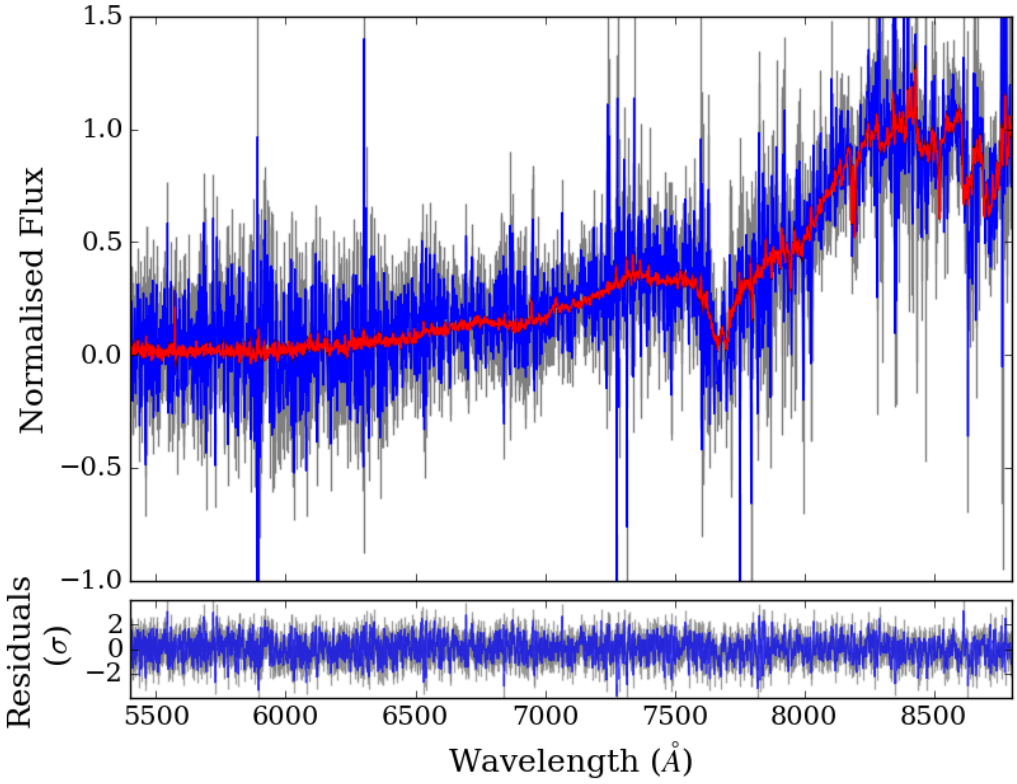

Figure 5.2: Top: BOSS spectrum of ULAS J2249-0112 in blue, with errors in grey. The spectrum has been normalised at 8350–8450 Å with the best-fitting L-dwarf template overlaid in red. Bottom: Residuals from the fit.

Property	Value	Reference
R.A (J2000, Deg)	342.417115	1
Dec (J2000, Deg)	−1.210352	1
i'	21.461 ± 0.101	2
z'	19.627 ± 0.102	2
J	16.832 ± 0.138	1
H	16.065 ± 0.177	1
K_s	15.610 ± 0.215	1
$W1$	15.091 ± 0.037	3
$W2$	14.775 ± 0.082	3
$\mu_{R.A.}$ (mas yr^{-1})	87.4 ± 4.2	2
μ_{Dec} (mas yr^{-1})	22.6 ± 4.2	2
$T_{\rm eff}$ (K)	1930 ± 100	This work
Distance (pc)	76^{+8}_{-7}	This work
Radius ($R_\odot$)	0.10 ± 0.02	This work

Table 5.1: Properties of ULAS J224940.13-011236.9. References: 1. Skrutskie et al. (2006), 2. Bramich et al. (2008), 3. Cutri and et al. (2014).

5.3 Results

5.3.1 Amplitude and Duration

To determine the amplitude and duration of the flare, and to search for signs of substructure, we fit the NGTS data with the solar-flare inspired model from Jackman et al. (2018), also Chapter 3. This model incorporates both a Gaussian heating term and a double exponential for the flare cooling. We fit the model using an MCMC process with 100 walkers for 20000 steps. We disregard the first 1000 steps as a burn-in. The result of this fit is shown in Fig. 5.1. From looking at the residuals to the fit we can identify a single outlier around the flare peak which may be signs of partially resolved flare substructure, something we discuss further in Sect. 5.4.2. We use the best fitting model to measure the duration for which the flare is at least 1σ above the background, where σ is the standard deviation of the lightcurve when the star is in quiescence. We measure the visible duration as 9.5 minutes. We can use also use our fit to measure the e-folding timescale and the $t_{1/2}$ duration of the flare. These parameters are often used in flare analysis (e.g. Shibayama et al., 2013; Davenport et al., 2014) and provide separate measures of the duration. We measure these as 2.1 and 1.5 minutes respectively. The FWHM of the Gaussian heating term also gives a measure of the flare rise-time, something not typically measured in other surveys due to its short duration. We find this to be 12 seconds, indicating rapid heating.

We can also use our fitted model to measure the amplitude of the flare, using the peak count rate. In order to determine what magnitude this corresponds to (in order to calculate the fractional amplitude of the flare) we have crossmatched all NGTS sources in this field with SDSS to obtain a linear relation between the NGTS instrumental magnitude and SDSS i' band. Using this relation we convert the NGTS instrumental flux to a proxy i' band magnitude of 15.3, resulting in $\Delta i' \simeq -6$. For comparison with previous works on large L dwarf flares, we also estimate the magnitude in the V band. To do this we use the best fitting BT-Settl model and assume the flare is given by a 9000 ± 500K blackbody-like emitter (e.g. Hawley and Fisher, 1992). We note that studies of flare spectra have currently not gone further than mid-M (e.g. Kowalski et al., 2013). Consequently, there is currently no direct evidence that flares on L dwarfs have the same spectrum as those on earlier spectral types. However, assuming the same physical flare processes are at work as for G to mid-M type stars, it is not unreasonable to assume the general flare spectrum would be similar, however we note this should be constrained further in the future through mulit-colour photometry and spectroscopy. From this

assumption we estimate $\Delta V \sim -10$ and $\Delta U \sim -15$. This is consequently the second largest observed white-light flare from an L dwarf, following ASASSN-16ae (ΔV=-11 Schmidt et al., 2016), and larger than those observed with *Kepler* (Gizis et al., 2013, 2017a; Paudel et al., 2018b).

5.3.2 Flare Energy

To calculate the flare energy we have again assumed the flare is given by a 9000 ± 500 K blackbody. We initially renormalise the blackbody to match the SDSS i' band magnitude for each point in the calibrated flare amplitude lightcurve from Sect. 5.3.1. For each time step we integrate the corresponding renormalised flare blackbody over all wavelengths and multiply by $4\pi d^2$, where $d = 76^{+8}_{-7}$ pc, to calculate the bolometric flare luminosity. Finally we integrate over the visible duration to calculate the total bolometric energy of the flare. This results in a bolometric flare energy of $3.4^{+0.9}_{-0.7} \times 10^{33}$erg, which is over an order of magnitude greater than the energy of the Carrington event on the Sun (10^{32} erg Carrington, 1859; Tsurutani et al., 2003). Another way of analysing this is to compare it to the total bolometric luminosity of the star in quiescence. Integrating over our best fitting SED results in a luminosity of 5.3×10^{29}erg s^{-1}, meaning the flare is equivalent in energy to 1.8 hours of quiescent emission from ULAS J2249-0112. We note that this energy is only for the visible duration of the flare and is thus a lower limit.

5.4 Discussion

We have detected a large amplitude white-light superflare on the L2.5 star ULAS J2249-0112. This is only the second L-dwarf flare to be detected from the ground and the sixth L-dwarf to have exhibited flaring activity. It is the coolest star ever found to exhibit a white-light flare. The flare had an amplitude of $\Delta V \sim$ -10 and an energy of $3.4^{+0.9}_{-0.7} \times 10^{33}$erg, making it the second largest amplitude L dwarf flare, following that of ASASSN-16ae (Schmidt et al., 2016). With a cadence of 12 seconds this is the best resolved detection of a giant white-light flare, allowing direct measurements of the amplitude and duration without relying on extrapolation.

5.4.1 Magnetic Activity of L dwarfs

The detection of a white-light flare from an L2.5 dwarf makes this the coolest star to show such an event and shows strong chromospheric activity can persist to this spectral type. Studies of the Hα emission from ultracool dwarfs using BOSS spectra

(Schmidt et al., 2015) has found the activity strength $\log(L_{H\alpha}/L_{bol})$ to decrease from approximately -3.8 at the M4 spectral type towards -5.7 at L3. This decrease in Hα activity may imply the chromospheres of early L dwarfs are significantly cooler than their late-M dwarf counterparts, or cover a smaller fraction of the surface (lower filling factor) (Schmidt et al., 2015). Recent discoveries of mid-L dwarfs with Hα emission have shown this decrease in chromospheric strength seems to continue with spectral type (e.g. Pérez-Garrido et al., 2017) and can be linked to the decreasing ionisation in the L dwarf photosphere (e.g. Miles-Páez et al., 2017).

Ultracool dwarfs are also known to exhibit auroral activity (e.g. Kao et al., 2018), which may account for observed Hα emission in these systems. It is expected that the transition from predominantly chromospheric to auroral Hα emission occurs during the L spectral type (Pineda et al., 2017). Many ultracool dwarfs which show activity such as radio emission and flaring also tend to be fast rotators, with rotation periods on the order of hours. However, neither the L1 dwarf SDSSp J005406.55-003101.8 (Gizis et al., 2017a) nor the L0 dwarf J12321827-0951502 (Paudel et al., 2018b) showed any sign of rapid rotation when observed by *K2*, despite showing large amplitude white-light flares. Consequently, we do not attempt to predict whether ULAS J2249-0112 is a fast rotator. Regardless of this, studies of white-light flares such as from ULAS J2249-0112 can aid in understanding exactly how far into the L spectral type chromospheric activity persists.

5.4.2 Flare Structure

In Sect. 5.3.1 we fitted the flare using a single continuous model, shown in Fig. 5.1. This model incorporates a Gaussian heating pulse with two exponential decays, for thermal and non-thermal cooling respectively (Jackman et al., 2018). From our fit we can also identify the presence of a possible second peak. This is from an outlier lying $2.8\,\sigma$ from the fitted model and occurring approximately 40 seconds after the fitted peak. Multiple peaks in flares have previously been attributed to flares occurring on different parts of the star and previous studies have found that higher energy flares are more likely to be complex (e.g. Hawley et al., 2014). One possibility for multiple peaks is sympathetic flaring, where one flare triggers flaring in nearby active regions (e.g. Moon et al., 2002). By assuming the flare is accurately described by a 9000 K blackbody we can estimate the maximum area of emission. We estimate our flare has a maximum emitting area of $5.6 \times 10^{19}\mathrm{cm}^2$, or 37 per cent of the visible disc (e.g. Hawley et al., 2003). This value for the emitting area is similar to those for flares on M dwarfs (e.g. Osten et al., 2010), however covers a much greater fraction of the surface. For example, a flare of similar energy observed

by Hawley et al. (2003) from the M3.5 dwarf AD Leo (which had multiple peaks) had a covering fraction of ≈ 1 per cent. If we assume this emission area is related to the area of the flare footpoints (as in Osten et al., 2010) and that only flares of similar energy would cause visible substructure, then multiple flares with large footpoints on the stellar surface in quick succession would be required. This requirement may inhibit the presence of multiple peaks in L dwarf flares, suggesting the observed outlier is perhaps not due to a separate event. If this is the case, then the lack of complexity would make it similar to the ΔK_p=-5.4 flare detected by Paudel et al. (2018b) on the L0 dwarf 2MASS J12321827-0951502. This flare showed no obvious substructure other than an extended decay when observed in the *K2* 1 minute short cadence mode. Another possibility is that the outlier is instead due to variability within the same flare region, such as rapidly damped QPPs.

In Sect. 5.3.1 we measured the visible duration of ULAS J2249-0112 as 9.5 minutes. Along with this, we were able to measure the e-folding duration as 2.1 minutes, the $t_{1/2}$ duration as 1.5 minutes and the FWHM of the Gaussian heating pulse as 12 seconds. Comparing the $t_{1/2}$ duration to other L dwarf flares, we find it is smaller than the three other large amplitude L dwarf flares (Schmidt et al., 2016; Gizis et al., 2017a; Paudel et al., 2018b) and is more comparable to the smaller flares observed from the L1 dwarf WISEP J190648.47+401106.8 (e.g. Gizis et al., 2013). While this implies that this is the most rapid large amplitude flare observed from an L dwarf, we note that all large amplitude L dwarf flares have had $t_{1/2}$ values below 10 minutes. As such, other observations may have been hindered by the resolution of observations, as noted by Paudel et al. (2018b), which would smear out flares in time (e.g Yang et al., 2018). To estimate this effect we bin our data to cadences of 1 and 2 minutes, to simulate the *Kepler* and *TESS* short cadence modes. We measure $t_{1/2}$ timescales of 2 and 3.25 minutes respectively, showing that $t_{1/2}$ measurements can be significantly affected by the longer cadence of these space telescopes. The short duration of our flare thus highlights the requirement of high cadence observations in order to detect and characterise these events. This behaviour would not be visible in the *TESS* 30 minute cadence full frame images (Ricker et al., 2015), nor in all-sky surveys which monitor large areas of sky each night. This shows how NGTS is in an ideal position to probe flare behaviour on the latest spectral types.

In Sect. 5.3.2 we measured the flare equivalent duration to be 1.8 hours. The same energy flare would have an equivalent duration of approximately 1 minute on an M3 star (using the value of 5.9×10^{31} erg s^{-1} for AD Leo from Hawley et al., 2003) and 0.9 seconds for the Sun. The measured equivalent duration highlights the sheer amount of energy that can be stored within the magnetic field of ULAS

J2249-0112. It has recently been suggested (De Luca et al., 2020) that L dwarfs may release their magnetic energy mainly through superflares, rather than through the power law distribution seen for earlier spectral types. This detection may support this theory, although without the detection of the star in quiescence it is not possible to say. Either way, it is still a remarkable finding.

Occurrence rate of flares from L dwarfs

To further estimate how common this finding is, we have crossmatched the NGTS input catalogues described in Sect. 5.2.1 with 2MASS. We estimated how many L dwarfs were in each field by selecting stars with $J - H > 0.8$ and $H - K_s > 0.5$, loose limits based on the colour templates for ultracool dwarfs of Skrzypek et al. (2015). These colour templates were derived by combining SDSS, UKIDSS, and WISE data for known ultracool and brown dwarfs. We estimate that in the fields observed are 4500 objects with NIR colours consistent with being an early L dwarf. Of these, 3350 have a J magnitude equal to or brighter than ULAS J2249-0112, meaning we would expect to see a similar flare event from these stars. Combining this value with the total amount of time these stars have been observed with NGTS gives a loose estimate for similar flares on early L dwarfs as 1 every 200 years. This would suggest such a high energy flare is a rare event. This is two orders of magnitude below the value for 10^{33} erg flares predicted by Paudel et al. (2020) from *K2* observations. This discrepancy may be related to our use of stars which are not always visible. Flares with lower amplitudes and longer durations (giving the same energy) may not be detected with NGTS, making the star appear erroneously quiet. In contrast, the stars observed with *K2* were permanently visible in quiescence. However, those observed with *K2* comprise a much smaller sample size (45), which may not fully probe the full parameter space of flaring and non-flaring L dwarfs. Either way, further observations with NGTS and further testing to fully understand the sensitivity of NGTS to flares from faint stars (e.g. using flare injection tests as performed in Chap.7) will aid in this work.

5.5 Conclusions

In this chapter we have presented the detection of a giant white-light flare from the L2.5 star ULAS J224940.13-011236.9. The flare was detected from a dedicated search for stellar flares on low mass stars in the NGTS full frame images and has an amplitude of $\Delta i' \approx$ -6, or $\Delta V \sim$ -10. This makes it the second largest flare to be detected from an L dwarf and is the second to be detected from the ground. With

a spectral type of L2.5 we believe ULAS J2249-0112 is the coolest star to show a white-light flare to date. This flare detection also highlights the value of the NGTS high-cadence full-frame images in studying the largest stellar flares from the coolest stars.

Chapter 6

A 16.2 hour period transiting brown dwarf

What do you get when you mix a Labour leader with stellar activity? Tony Flare.
What do you get when you mix a Labour leader with substellar objects? Gordon Brown Dwarf.

Puns from "Studying Only Red Stars - A Labour of Love"[1]

6.1 Introduction

The discovery of brown dwarfs in transiting exoplanet surveys provides a unique opportunity to probe the parameters of these substellar objects. In Sect. 1.5 I discussed how transiting systems allow us to precisely constrain both the brown dwarf mass and radius and the temperature via the detection of a secondary eclipse. I also detailed how brown dwarfs are detected and briefly mentioned the apparent paucity of brown dwarfs on short periods around main sequence stars, known as the *brown dwarf desert*. Here I will introduce brown dwarf formation and the desert in more detail. This chapter uses material from Jackman et al. (2019c).

As mentioned above, the brown dwarf desert refers to the apparent lack of brown dwarfs acting as close companions (typically within 3 AU; e.g. Marcy and Butler, 2000) to main sequence stars. Various studies have been performed to test whether the desert is an observational bias. From a radial velocity study of nearby Sun-like stars, Grether and Lineweaver (2006) found that 16% had a nearby companion. 11% were stellar, 5% were giant planets, while less than 1% could be

[1] A figment of James A. G. Jackman's imagination

a brown dwarf. This was later reinforced by Ma and Ge (2014) who found that for periods less than 100 days around main-sequence stars there was decrease in the number of known brown dwarfs, especially for masses in the range of 35-55$M_{\rm J}$. Some however have suggested that the brown dwarf desert may not extend as far as 3 AU. Troup et al. (2016) using APOGEE data of main sequence and evolved stars found that, while confirming the apparent presence of the brown dwarf desert, it's extent was limited to 0.2 AU, or periods of 30 days. However, a later study by Grieves et al. (2017), excluding evolved stars, found similar results to Ma and Ge (2014), suggesting the desert is a physical phenomenon, rather than due to observational bias.

The driving factor behind the brown dwarf desert is typically attributed to the different formation mechanisms of low and high mass brown dwarfs in binary systems (e.g. Ma and Ge, 2014). High mass brown dwarfs ($\gtrapprox$ 43 $M_{\rm J}$) are believed to form through molecular cloud fragmentation, whereas their lower mass counterparts form within the protoplanetary disc (e.g. Stamatellos and Whitworth, 2009; Hennebelle and Chabrier, 2013). However, along with their formation pathways, a contributing element for the brown dwarf desert may be inward orbital migration of the brown dwarf (e.g. Armitage and Bonnell, 2002). One way of driving this is thought to be through tidal interactions between brown dwarfs and their host stars (e.g. Pätzold and Rauer, 2002; Damiani and Díaz, 2016), along with the effect of the magnetic braking of the host star (e.g. Barker and Ogilvie, 2009; Brown et al., 2011). If the companion is close enough, tidal interactions can decay its orbit, moving the companion inwards. The angular momentum lost from this orbit is expected to be transferred to the spin of the host star (e.g. Bolmont et al., 2012), eventually resulting in a state of spin-orbit synchronisation. In this state, the orbital and spin periods are equal. Such synchronisation has been detected in transiting brown dwarf systems before, for example in *CoRoT*-15b (Bouchy et al., 2011), a 63$M_{\rm J}$ brown dwarf orbiting an F7V star with a period of 3.06 days. Along with this, brown dwarf systems have shown behaviour close to synchronisation (e.g. WASP-128b Hodžić et al., 2018). However, during this process, magnetic braking will remove angular momentum from the system (Barker and Ogilvie, 2009). This acts to spin down the star, which should result in a decrease of the magnetic activity and braking. However, any lost angular momentum is replaced by the decaying orbit of the companion. Consequently, the host star does not spin down and the magnetic braking does not slow, continuing the orbital decay of the companion. As such, even though (pseudo) spin-orbit synchronisation may be achieved, for active stars the magnetic braking can still drive the decay of the companion orbit. The

combination of these effects eventually results in the engulfment of the brown dwarf by the host star. The timescale of this orbital decay is dependent on a number of factors, notably the stellar radius (Damiani and Díaz, 2016). Consequently, the decay timescale is expected to be shortest for brown dwarfs around G and K type stars (e.g. Guillot et al., 2014), making brown dwarf companions rarer around these stars (as noted by Hodžić et al., 2018) and contributing to the desert.

For M stars the orbital decay timescale is expected to be longer than G and K stars, due to the strong dependence of tides on stellar radius (e.g. Damiani and Díaz, 2016). This is in spite of the strong magnetic activity of M stars, which can manifest itself as both saturated quiescent X-ray emission and transient activity such as stellar flares (e.g. Hilton, 2011; Jackman et al., 2019a). Of the 23 transiting brown dwarfs known to date, 5 brown dwarfs have been identified transiting M stars. Two of these systems are hierarchical triples consisting of two M dwarfs and a brown dwarf (NLTT41135 B, LHS 6343C; Irwin et al., 2010; Johnson et al., 2011), with the two M dwarfs in close proximity on the sky (2.4″, 55 AU and 0.55″, 20 AU respectively). Both these systems are believed to have ages greater than 1 Gyr and be in stable configurations. The third system, AD 3116 (Gillen et al., 2017), is a M+BD system discovered in the Praesepe open cluster and has an age of $\sim$ 700 Myr. This age makes it one of the younger transiting brown dwarf systems and useful for testing brown dwarf models with age. The fourth M+BD system is LP 261-75 (Irwin et al., 2018), a M+BD transiting pair with a distant visual brown dwarf companion (Reid and Walkowicz, 2006). LP 261-75 is expected by Irwin et al. (2018) to have an age of several Gyrs despite the high activity of the M dwarf primary, which instead suggests an age in the 130-200 Myr range (e.g. Reid and Walkowicz, 2006). This strong activity instead is associated with tides from interactions between the brown dwarf and the host star. The fifth system is RIK 72b, a 10 Myr transiting brown dwarf in the Upper Scorpius open cluster (David et al., 2019). The young age and high temperature and luminosity (for a brown dwarf) of RIK 72b means its secondary eclipse could be detected with *K2*, instead of requiring infrared *Spitzer* observations. Like AD 3116, this made it an excellent test for young brown dwarf evolutionary models.

These five systems show the range of ages and configurations these systems can have, highlighting how further observations of transiting brown dwarfs are required to understand their formation and evolution. In particular, the discovery of unstable systems are needed in order to test evolutionary scenarios. This is an inherently difficult task, due to their short-lived nature.

In this chapter we report the discovery of NGTS-7Ab, a brown dwarf tran-

Property	NGTS-7A	NGTS-7B	Source
R.A [°]	352.5216665551376	352.52202473338	1
Dec [°]	-38.96992064512876	-38.97006605140	1
Gaia Source ID	6538398353024629888	6538398353024172032	1
$\mu_{R.A.}$ (mas yr^{-1})	-27.003 ± 0.112	-28.601 ± 0.112	1
μ_{Dec} (mas yr^{-1})	-16.225 ± 0.178	-14.776 ± 0.364	1
Parallax (mas)	7.2497 ± 0.1203	6.5232 ± 0.0787	1
B	17.091 ± 0.072		2
V	15.502 ± 0.028		2
g'	16.187 ± 0.044		2
r'	14.940 ± 0.010		2
i'	13.822 ± 0.127		2
Gaia G	14.9154 ± 0.0020	15.5134 ± 0.0012	1
J	11.832 ± 0.030		3
H	11.145 ± 0.026		3
K_s	10.870 ± 0.019		3
$W1$	10.740 ± 0.022		4
$W2$	10.660 ± 0.020		4

Table 6.1: Stellar properties for each star. We have listed the photometry used in our SED fitting. We show the parallax and proper motions for reference, however do not use them all in our analysis for the reasons outlined in Sect. 6.3.2. The references are: 1. Gaia Collaboration et al. (2018b), 2. Henden and Munari (2014), 3. Skrutskie et al. (2006), 4. Cutri and et al. (2014).

siting an active M star on a 16.2 hour orbital period. The host star's rotation period is locked to the orbit of the brown dwarf. We present our detection with NGTS, along with follow up photometric and spectroscopic measurements to constrain the radius and mass of the brown dwarf and M star host. We also present a detection of the secondary eclipse with NGTS, which we use to measure the temperature of NGTS-7Ab. This system is heavily diluted by a nearby M star that is likely to be physically bound. We describe the steps taken to account for this, along with presenting different scenarios based on the assumptions taken. We also discuss the possible formation scenarios of this system and outline how it may evolve in the future.

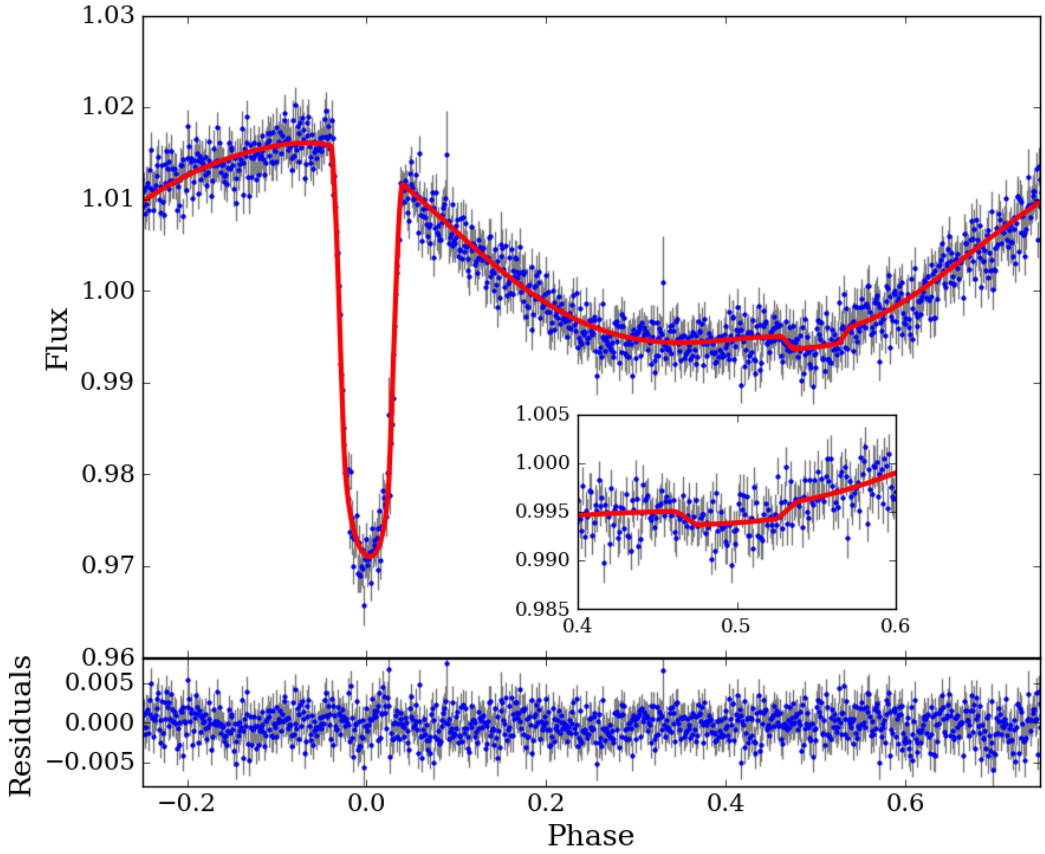

Figure 6.1: The binned, phase-folded NGTS lightcurve showing both the transit and starspot modulation. The NGTS data (in blue) has been placed into 1000 bins, equal to approximately 1 minute each. We have overlaid the best fitting model in red. The inset plot shows a zoom in of the secondary eclipse. Lower panel shows the residuals of our fitting.

6.2 Observations

6.2.1 Photometry

NGTS

NGTS-7 was observed with NGTS for 130 nights between 2016 May 04 and 2017 Jan 11, using a single camera. The phase folded lightcurve is shown in Fig. 6.1. Observations were obtained in the custom NGTS filter (520-890nm) with a cadence of 13 seconds. For a full description of the NGTS instrument and pipeline processing see Chapter 2 and Wheatley et al. (2018). The NGTS lightcurves were detrended using a version of the SYSREM algorithm, as done for previous NGTS discoveries (e.g. Bayliss et al., 2018; Raynard et al., 2018; West et al., 2019). The NGTS field used in this chapter is NG2331-3922, which is centered on 23:31:10.1, -39:16:53.9.

This star was originally identified as an object of interest due to the detection of flares as part of the NGTS flare survey (Chapters 3, 4, 7; Jackman et al., 2018, 2019a, Jackman et al., submitted). We subsequently identified a 16.2 hour periodicity. We then noted transit events of 4.3 per cent depth occurring on the same period.

Gaia DR2 resolves two stars with a separation of $1.13''$, while all other catalogues list it as a single source. The catalogue photometry and astrometry is given in Tab. 6.1. To confirm the source of the transits we perform centroiding using the vetting procedure described by Günther et al. (2017). We describe this analysis in Sect. 6.3.1 and refer to the two sources as NGTS-7A and NGTS-7B where NGTS-7A is the transit source. The two stars have *Gaia* G magnitudes of 14.9 (NGTS-7A) and 15.5 (NGTS-7B), meaning that there is non-negligible dilution present in our photometry, something we discuss and account for in Sect. 6.3.3.

SAAO

Follow up photometry of NGTS-7 was obtained at the South African Astronomical Observatory (SAAO) on 2018 Aug 08 (I band, secondary eclipse), 2018 Aug 11 (I band, primary transit), and again on 2018 Oct 04 (I band, secondary eclipse) using the 1.0m Elizabeth telescope and "*shocnawe*", one of the SHOC high speed CCD cameras (Coppejans et al., 2013). On each occasion, sky conditions were clear throughout the observations, with the seeing around 2 arcseconds. The data were reduced with the local SAAO SHOC pipeline developed by Marissa Kotze, which is driven by PYTHON scripts running IRAF tasks (PYFITS and PYRAF), and incorporating the usual bias and flat-field calibrations. Aperture photometry was

performed using the STARLINK package AUTOPHOTOM. We used a 5 pixel radius aperture that maximised the signal to noise ratio, and the background was measured in an annulus surrounding this aperture. One bright comparison star in the 2.85 × 2.85 arcminute field of view was then used to perform differential photometry on the target. The two stars identified by *Gaia* DR2 coincident with the position of NGTS-7 were not resolved in these data. Figure 6.2 shows the primary transit observed on 2018 Aug 11. A stellar flare can be clearly seen shortly before transit ingress.

EulerCam

One transit of NGTS-7 was observed with EulerCam on the 1.2m Euler Telescope at La Silla Observatory (Lendl et al., 2012). These observations were obtained on the night of 2018 Sept 01, in the V band filter and are shown in Fig. 6.2. The data were bias and flat field corrected then reduced using the PyRAF implementation of the "PHOT" routine. An aperture radius and ensemble of comparison stars were used such that the scatter in the out of transit portion of the lightcurve was minimised.

TESS

NGTS-7 was observed at a 30 minute cadence with the NASA Transiting Exoplanet Survey Satellite (*TESS*) (Ricker et al., 2015) between 2018 Aug 27 and 2018 Sep 19, in Sector 2. A 15 × 15 pixel (5.25' × 5.25') cutout was obtained from the *TESS* full-frame image stacks using the TESSCUT routine [2]. This cutout is shown in Fig. 6.3. Aperture masks were chosen by-eye to exclude nearby bright sources up to 2.5' away. The 21" pixel-scale of *TESS* creates a PSF of NGTS-7 which is blended with at least 3 significantly bright stars ($\Delta G < 3.5$ mag.) As it is not possible to completely exclude the flux from these blended stars in *TESS* we chose our aperture to enclose them, with the knowledge the *TESS* lightcurve will be diluted. We estimated the per-pixel background contribution by selecting 8 pixels West of the aperture that do not include any stars brighter than $G = 18.4$ (3.5 magnitudes fainter than NGTS-7A). This region is shown as the magenta box in Fig. 6.3. This was subtracted from the aperture-summed flux to create a background-corrected light curve.

The transit seen in the *TESS* light curve is both shallower and more V-shaped than that from NGTS, despite the similar bandpasses of NGTS and *TESS*. This is due to a combination of additional dilution in the *TESS* data (from the neighbouring sources) and the 30 min cadence which smears out the transit (which

[2] https://github.com/spacetelescope/tesscut

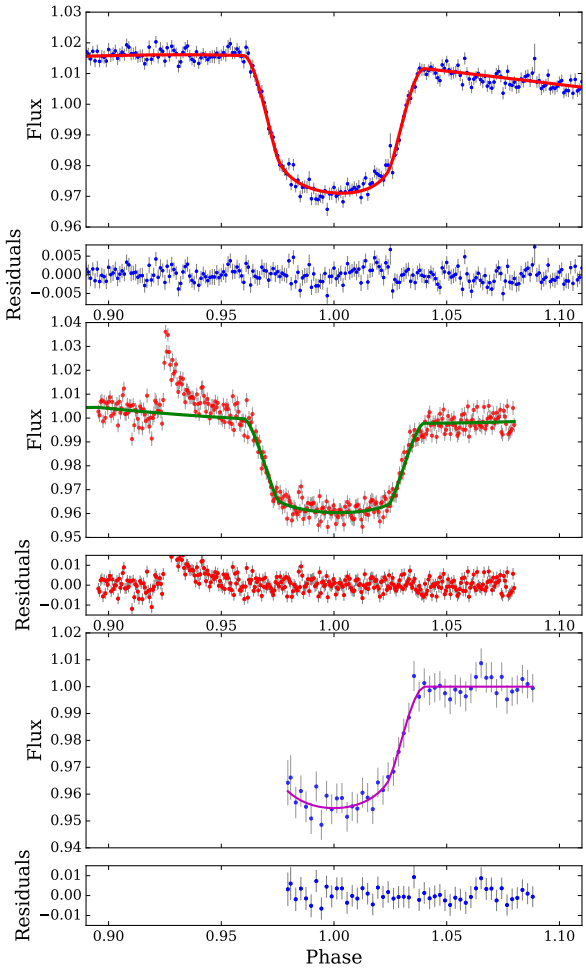

Figure 6.2: Transit lightcurves of NGTS-7Ab. Top: phase folded NGTS lightcurve (as in Fig. 6.1) with the best fitting model overlaid in red. Middle: Primary transit lightcurve from SAAO in I band, with the best fitting model in green. Bottom: Primary transit lightcurve from EulerCam in V band, with the best fitting model in magenta. Residuals for each fit are shown underneath each respective plot.

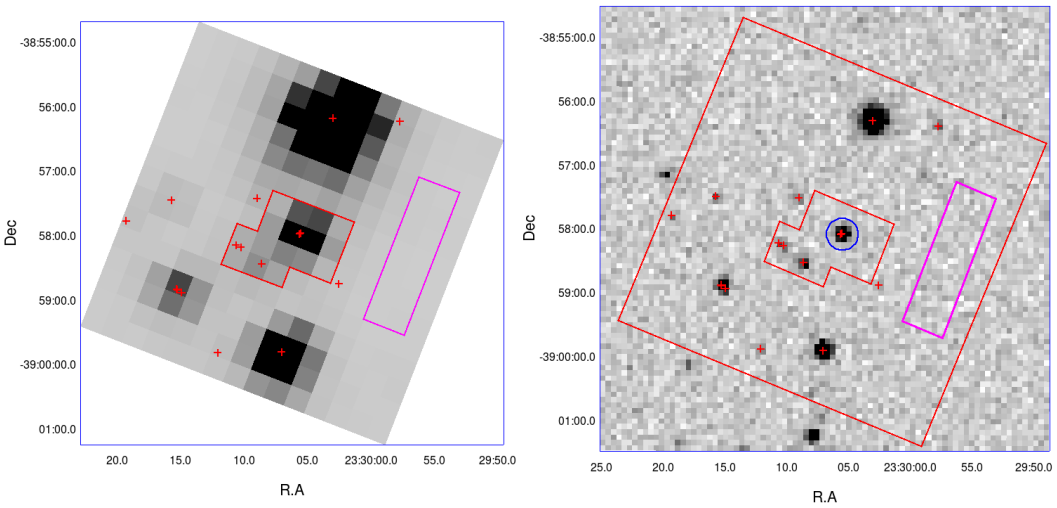

Figure 6.3: Left: the first image of the *TESS* full-frame image stack (15 × 15 pixel) showing the field surrounding NGTS-7A. Nearby companions with *Gaia* magnitudes brighter than $G = 18.4$ (3.5 magnitudes fainter than NGTS-7A) are plotted with red crosses. The aperture used to extract the *TESS* lightcurve is outlined in red. We subtracted the per-pixel background contribution estimated from selecting a region (outlined in magenta) free of *Gaia* stars brighter than $G = 18.4$. Right: an example NGTS image of the same region of sky with the TESS FFI region shown. The aperture used for the NGTS photometry is shown in blue. We have overlaid the *TESS* apertures in this image for reference.

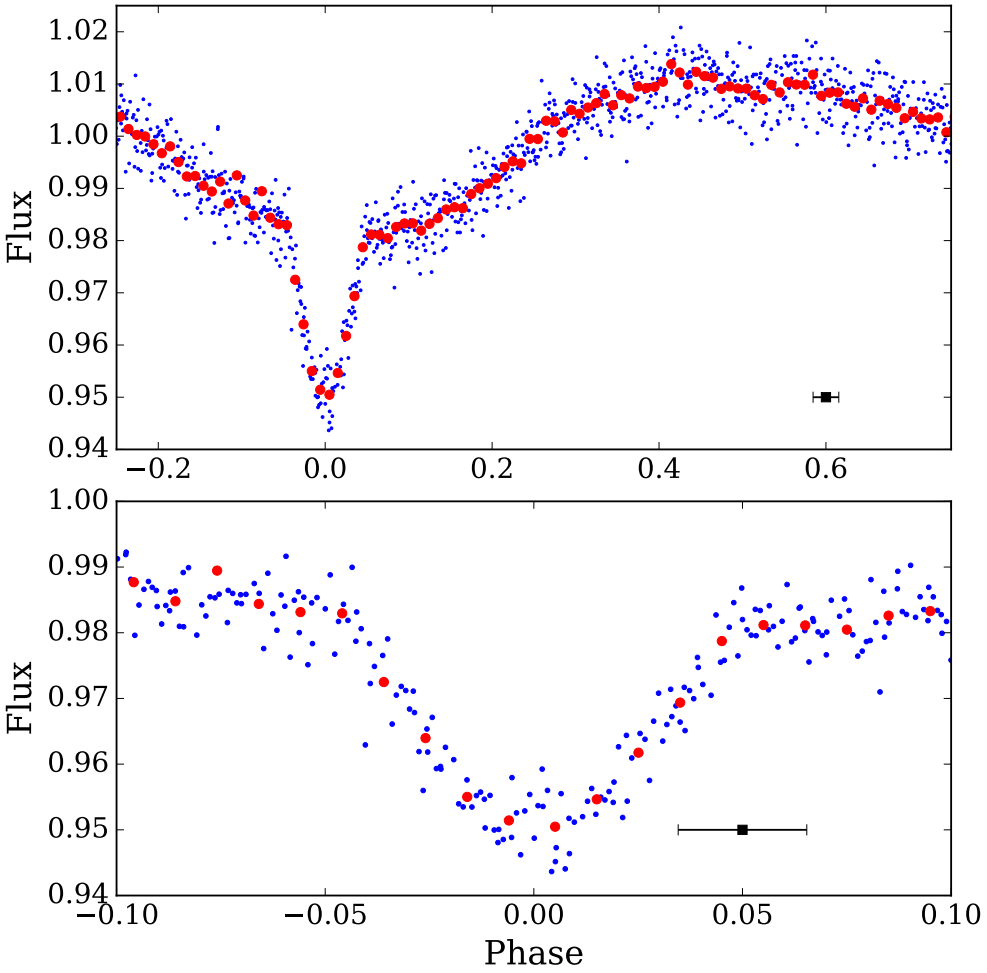

Figure 6.4: Top: Phase folded *TESS* lightcurve from the sector 2 full frame images. Blue points indicate individual *TESS* observations and the red points are the phase fold binned to 100 bins in phase. The black point represents the length of an individual 30 minute cadence *TESS* observation in phase. Note how the out of transit modulation has changed in phase from the original NGTS observations. Bottom: Zoom in of the primary transit. Note the more V-shaped appearance of the primary transit compared to those in Fig. 6.2, due to the smearing effect of the 30 minute cadence observations.

has a duration of only 1.3 hours, e.g. Smith et al., 2018). Due to these effects we do not use the *TESS* lightcurve in our transit fitting (Sect. 6.3.3). However, we do use it in Sect. 6.3.7 where we discuss the phase of the out-of-transit variations of NGTS-7.

6.2.2 Spectroscopy

HARPS

We obtained high-resolution spectroscopy for NGTS-7A with the HARPS spectrograph on the ESO 3.6m telescope (Mayor et al., 2003). Five measurements with an exposure time of 1800s were taken on the nights beginning 2018 Sept 02 and 2018 Sept 11 as part of programme ID 0101.C-0889(A). Due to the relative faintness of the source we used the high efficiency fibre link (EGGS), with a fibre size of 1.4″ instead of the usual 1.0″ mode. Consequently, these spectra contain light from both NGTS-7A and NGTS-7B and we see a narrow and a broad peak in the Cross Correlation Functions (CCFs) shown in Fig. 6.5. The RVs of NGTS-7A and NGTS-7B along with the respective contrasts from our analysis in Sect. 6.3.4 are given in Tab. 6.3.

SAAO

Follow up spectroscopy of NGTS-7 was also obtained from SAAO on the 1.9m telescope using the SpUpNIC instrument (Crause et al., 2016) between the dates 2018 Sept 09 and 2018 Sept 11. 14 spectra with a resolution of R=2500 were obtained in total, with a wavelength range of 3860-5060Å. We have combined these spectra to give the average spectrum shown in Fig. 6.6. Observations were performed with a slit width of 1.8″ and average seeing of 2″, once again meaning both NGTS-7A and NGTS-7B are present in our data. Figure 6.6 shows clear TiO and CaI absorption features expected for M dwarf spectra. Along with this, we see several emission lines from the Balmer series, as well as He I and Ca II, showing at least one of the stars is chromospherically active.

6.3 Analysis

The observations of Sect. 6.2 were combined with available catalogue photometric and astrometric information. We use this information to confirm the source of the transits and characterise both NGTS-7A and NGTS-7B.

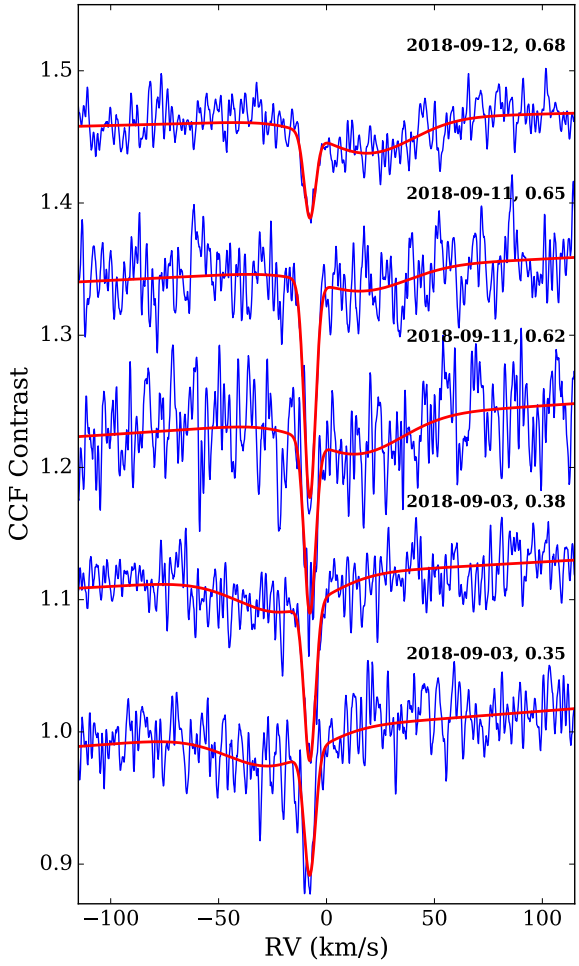

Figure 6.5: CCFs from HARPS, using a K5 mask and offset in contrast. The HARPS data is shown blue, with observation date and orbital phase for each CCF provided. For each HARPS CCF we have simultaneously fitted two Gaussians along with a varying baseline, which are overlaid in red. We can see that along with the narrow peak with a constant RV due to NGTS-7B, there is a clear shift of a wide Gaussian, which we attribute to NGTS-7A.

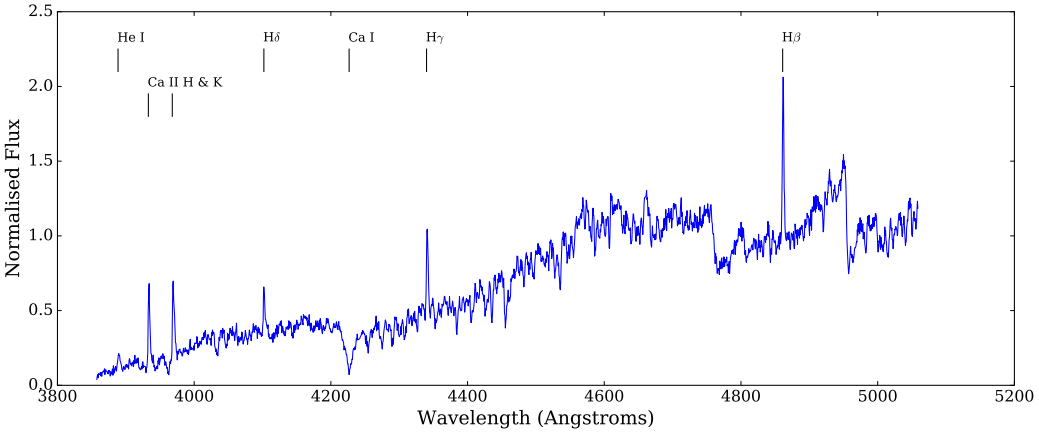

Figure 6.6: SAAO spectrum of NGTS-7 with H, He and Ca emission and absorption lines marked. The spectrum has been normalised to the flux at 5000 Å. The emission lines show that the NGTS-7 stars are chromospherically active.

6.3.1 Identifying the Source of the Transit

In Sect. 6.2 we noted that *Gaia* DR2 resolves two sources with a separation of 1.13″ at the position of NGTS-7. To confirm which source our transit signal is coming from, we performed centroiding using the vetting procedure described by Günther et al. (2017). We identify that the transit and the out-of-transit modulation comes from *Gaia* DR2 6538398353024629888, the brighter of the two sources. Figure 6.7 shows the phase folded transit and X centroid position, showing how the shape of the phase-folded centroid data follows the shape of the phase-folded lightcurve. While individual NGTS pixels are 5" across, the NGTS centroiding procedure is able to identify centroid shifts below 1" in size, meaning we are confident that we have identified the correct host star and now refer to this star as the primary star, or NGTS-7A. We refer to the neighbouring source as NGTS-7B and discuss it further in Sect. 6.3.2.

Out of transit modulation on the orbital period can be due to either ellipsoidal variation (e.g. Drake, 2003; Welsh et al., 2010) or reflection effects (e.g. Armstrong et al., 2016; Eigmüller et al., 2018). However, neither of these could adequately explain the number or position in phase of the maxima seen in Fig. 6.1 (just before the primary transit). The most natural explanation is that this out-of-transit modulation is due to starspots on the host star and that the spin period of NGTS-7A is locked to the orbital period of the transiting body. This places NGTS-7A in a state of spin-orbit synchronisation (e.g. Ogilvie, 2014). The change in the out of transit modulation in the *TESS* data can be explained by the evolution of starspots

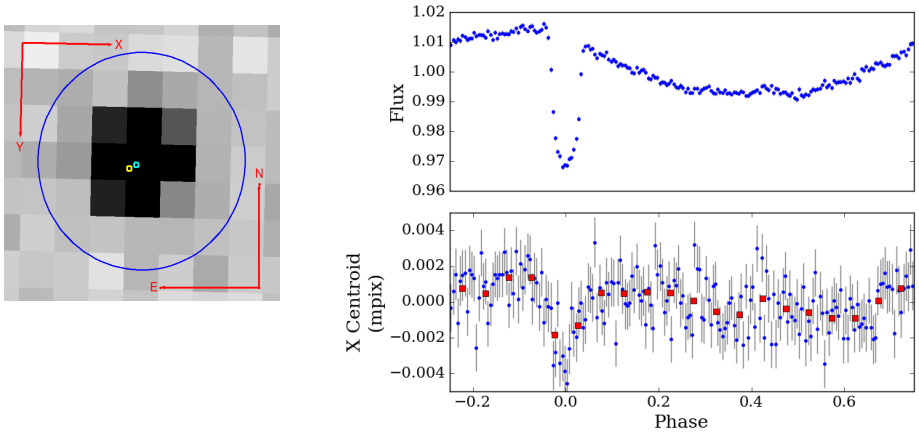

Figure 6.7: Left: NGTS image of NGTS-7 with the aperture shown as the blue circle. The *Gaia* DR2 positions of NGTS-7A and NGTS-7B are shown with the cyan and yellow points respectively. Right: Our centroid analysis of NGTS-7. The top panel shows the phase folded NGTS lightcurve, placed into 200 bins. The bottom panel shows the phase folded X centroid position. The blue points indicate the same 200 bins as the top panel, while the red points are the same data binned up by a factor of 10. We can see both the clear centroid movement during the transit and with the out of transit modulation.

in the interval between the NGTS and *TESS* observations, something we discuss further in Sect. 6.3.7.

The 16.2 hour period rotation of NGTS-7A will result in its observed CCF in our HARPS spectra being rotationally broadened. This broadened peak will also move around with a 16.2 hour period. In Sect. 6.2.2 we noted that our HARPS spectra contain light from NGTS-7A and NGTS-7B and the presence of a narrow and broad peak in our HARPS CCFs, seen in Fig. 6.5. As we will discuss in Sect. 6.3.4 we find the broad peak moves on a 16.2 hour period, as we might expect if NGTS-7A has a transiting body and itself is in a state of spin-orbit synchronisation. The rapid rotation of NGTS-7A and it being chromospherically active (as evidenced by the observed starspots) presumably means NGTS-7A is the source of the multiple stellar flares in the NGTS and SAAO lightcurves (e.g. Hawley et al., 2014). Along with this, NGTS-7A is likely the dominant source of the observed emission lines in our SAAO spectra.

Based on our observations and the evidence presented here we are confident that NGTS-7A is the source of the observed transits. Along with this we believe NGTS-7A is in a state of spin-orbit synchronisation with its companion, which will have spun up NGTS-7A to keep it at the observed period.

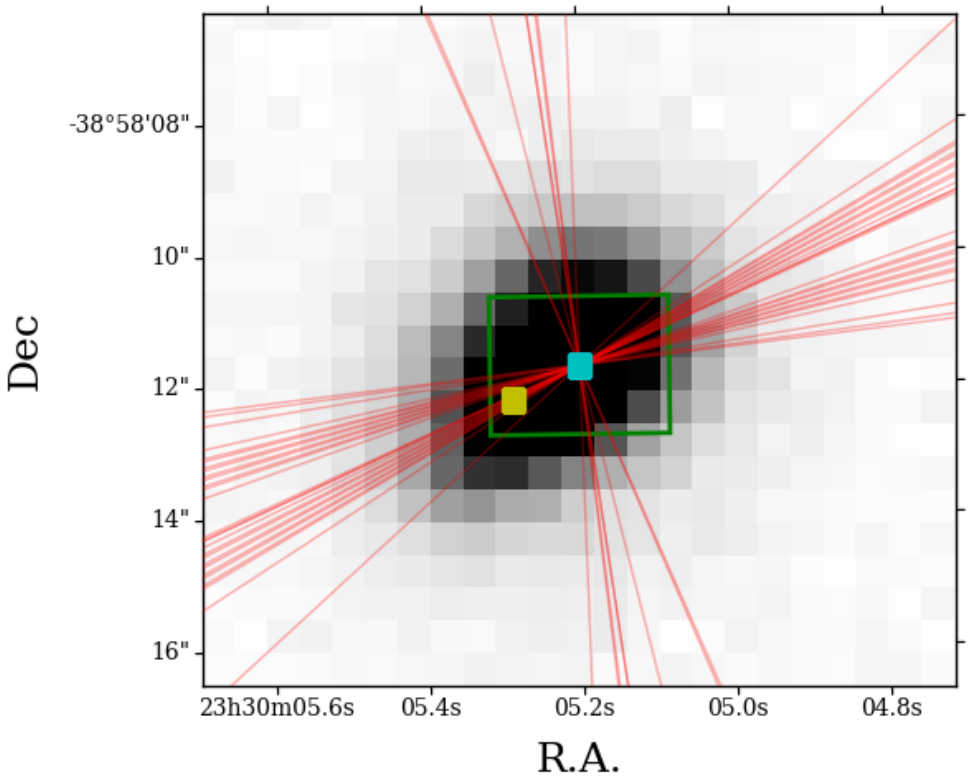

Figure 6.8: SkyMapper i band image of NGTS-7A and NGTS-7B, with their *Gaia* DR2 positions shown as the cyan and yellow squares respectively. The green rectangle is an example 3.5x2.1 arcsec^2 region used for calculating the *BP* and *RP* flux, centered on NGTS-7A. The red lines are the *Gaia* scan directions obtained from GOST, which we have fixed to pass through the centre of NGTS-7A. Note the significant fraction that pass through, or close to, both NGTS-7A and NGTS-7B.

6.3.2 Stellar Parameters

Throughout this chapter, all of our photometry is measured in apertures which contain the light from both NGTS-7A and NGTS-7B. Consequently, in order to obtain accurate parameters for NGTS-7Ab we need to estimate the dilution from NGTS-7B. We have done this through fitting the Spectral Energy Distribution (SED) of both NGTS-7A and NGTS-7B, using a combination of the information available from blended catalogue photometry and *Gaia* photometric and astrometric data. This information is listed in Tab. 6.1.

Gaia Photometry

While both sources have a *Gaia G* magnitude, only the primary star has *BP* and *RP* photometry. The *Gaia G* magnitudes for both stars are published in *Gaia* DR2 and,

as explained in Chapter 2, are derived from fitting the line spread function (LSF) of each star from windows which are approximately 0.7×2.1 arcsec^2 in the along scan and across scan directions respectively (Gaia Collaboration et al., 2016b). We used the *Gaia* Observation Scheduling Tool (GOST[3]) to check the scans of NGTS-7A and NGTS-7B used for *Gaia* DR2. We obtained 35 scans, which are plotted over a SkyMapper i band image (Wolf et al., 2018) in Fig. 6.8. From Fig. 6.8 we can see that over 75 per cent of the scans which went into *Gaia* DR2 fall along (or close to) the position angle separating the two stars. Given the $1.13''$ separation of the stars and the ability of the LSF to resolve sources of this separation (e.g. Fig. 7 in Fabricius et al., 2016), we expect only minimal contamination between the stars in the *Gaia* G band photometry. Consequently, we use the *Gaia* G band photometry in our analysis.

On the other hand, the BP and RP photometry is measured from the total flux in a 3.5x2.1 arcsec^2 region (Evans et al., 2018). An example of this region is shown in Fig. 6.8, showing that the BP and RP photometry will be of both NGTS-7A and NGTS-7B combined. This is reflected in the BP-RP EXCESS FACTOR of 2.054 for NGTS-7A. The BP-RP EXCESS FACTOR is the sum of light from the BP and RP bands compared to the G band, and should ideally be around 1 for a single, non-contaminated, star. A value around 2 suggests the BP and RP photometry is comprised of flux from two similar stars. Indeed, we find that the BP and RP photometry of NGTS-7A fails the filter from Arenou et al. (2018), which is used to remove contaminated stars from their analysis. Consequently we do not use the *Gaia* BP and RP photometry of NGTS-7A in our analysis.

Gaia Astrometry

For both sources we initially test the quality of the *Gaia* astrometry by calculating both the Unit Weight Error (UWE) and the Renormalised UWE (RUWE). We compare the UWE against the filter specified by Lindegren et al. (2018) and check whether the RUWE is below the recommended value of 1.4 for a clean astrometric sample. We found that NGTS-7A suffers from significant astrometric excess noise (ASTROMETIC EXCESS NOISE SIG=71.6, RUWE=3.4), resulting in it failing both filters. NGTS-7B, while having non-zero astrometric excess noise (ASTROMETIC EXCESS NOISE SIG=4.4, RUWE=1.3), passes both filters. When calculating the astrometric solution of each star, *Gaia* DR2 assumes a single object. The astrometric excess noise is the extra noise that is required by the single source solution to fit the observed behaviour. High levels of astrometric excess noise are a sign that

[3]https://gaia.esac.esa.int/gost/

the single source solution has failed, possibly due to unresolved binarity (e.g. Gaia Collaboration et al., 2018a). We also check each star further by comparing them against sources of similar magnitude, colour and parallax in the full *Gaia* DR2 sample. Both stars are outliers from the main sample in terms of their astrometric quality. We note in particular that each has a correlation between their parallax and proper motion components. One possibility for the low quality of the astrometric parameters for NGTS-7A and NGTS-7B may be levels of blending due to their proximity. Lindegren et al. (2018) has noted that during scanning of close sources the components can become confused, through a changing photocentre.

Due to it failing the recommended astrometry filters we have decided not to use the astrometric solution of NGTS-7A in our analysis. As we explain in Sect. 6.3.2 we consider two scenarios. The first of these uses only the astrometric solution of NGTS-7B and fixes both NGTS-7A and NGTS-7B at the distance of NGTS-7B, while the second doesn't use *Gaia* parallaxes and assumes both sources are on the main sequence.

A possible wide binary

A scenario mentioned in Sect. 6.3.2 which may be responsible for the low quality astrometry of NGTS-7A and NGTS-7B is that the two sources are a wide binary. If they are a wide binary, then we would expect them to be at the same distance. NGTS-7A and NGTS-7B have very similar proper motions, which supports this assumption, which are shown for reference in Tab. 6.1. However, as the proper motions are measured as part of the *Gaia* astrometry and may have levels of contamination, we have decided to seek out additional evidence. Wide binaries have previously been identified in both TGAS (e.g. Andrews et al., 2017) and *Gaia* DR2, with Andrews et al. (2018) finding that, as expected, real binaries will have similar systemic velocities, whereas chance alignments will not. From our radial velocity analysis in Sect. 6.3.4 we found that NGTS-7A and NGTS-7B have systemic velocities of -4.2 ± 0.8 km s^{-1} and -7.7 ± 0.1 km s^{-1} respectively. Using the distance of NGTS-7B results in a projected separation of 173 AU. This projected separation and the difference in systemic velocities places NGTS-7A and NGTS-7B well within the Andrews et al. (2018) sample of genuine wide binaries, instead of being a chance alignment on the sky. Consequently, it is very likely that NGTS-7A and NGTS-7B are in fact a wide binary and are at the same distance. Assuming a maximum distance of 10^5 AU (placing them with the widest separation likely gravitationally bound pairs identified with SUPERBLINK and *Gaia* DR2 by Hartman and Lépine, 2020), then we also note the chance these sources could be within 0.05 pc of each

other and still be gravitationally bound. However, for simplicity, we shall assume they are at the same distance. If so, this would provide a way of constraining the distance to NGTS-7Ab, along with placing it in a hierarchical triple system. Checking for possible memberships of known associations using the BANYAN Σ online tool [4] with the astrometry of NGTS-7B reveals no likely associations (Gagné et al., 2018).

Following this, we have devised two separate scenarios on the assumption that NGTS-7A and NGTS-7B are in a wide binary. These are as follows:

1. We fix both sources at the distance of NGTS-7B, assuming they are a wide binary.

2. We believe neither *Gaia* DR2 parallax, instead fixing them at the same distance and assuming they are on the main sequence.

These scenarios both avoid using the poor astrometric solution of NGTS-7A.

SED Fitting

To determine the SED of both stars we have fitted two separate components simultaneously using a custom SED fitting process which utilises the PHOENIX v2 grid of models (Husser et al., 2013), following a similar method to Gillen et al. (2017) and as described in Chapter 2. Initially we generated a grid of bandpass fluxes and spectra in $T_{\rm eff}$-$\log g$ space, which allowed us to interpolate across these parameters. We fit for $T_{\rm eff}$, $\log g$, along with the radius, R, and distance, D, of each star. We have chosen to fix the metallicity at the Solar value. Prior to fitting we inflated the errors of catalogue photometry by 2.5 per cent to account for the observed variability in the NGTS lightcurve. During fitting we compare the combination of fluxes from each star to the observed values, for all filters in Tab. 6.1 except *Gaia* G (which is used as a prior to normalise the respective SEDs). To explore the full posterior parameter space we use EMCEE (Foreman-Mackey et al., 2013) to generate an MCMC process, using 200 walkers for 50,000 steps, disregarding the first 25,000 as a burn in.

We have used a range of physically motivated priors in our modelling which we outline here. Firstly, the radii and distances are used in our model to scale the flux from each star by $(R/D)^2$. For scenario (i) (Sect. 6.3.2) we have placed a Gaussian prior on the distance of each star, using the value from Bailer-Jones et al. (2018) for NGTS-7B, 152.7 ± 1.9 pc. In this scenario the fitted radius of each star is

[4] http://www.exoplanetes.umontreal.ca/banyan/banyansigma.php

allowed to vary freely. For scenario (ii) we fit for the distance, which we also force to be the same for the two stars. We have placed a Gaussian prior on the fitted radius for each star, using the Mann et al. (2015) T_{eff}-radius relation. For this prior, we have used the 13.4 per cent error given by Mann et al. (2015) as the standard deviation of the Gaussian prior to allow some variation. In both scenarios we have placed a prior on the synthetic *Gaia* G band flux for each star, using the observed flux values. This was done to anchor each star to observations.

Table 6.2 gives the results of each fit. For both scenarios we retrieve two stars with temperatures corresponding to M3-M4 spectral type (e.g. Pecaut and Mamajek, 2013). This similarity in spectral type matches what we would expect from the *Gaia* BP-RP excess factor, as discussed in Sect. 6.3.2. However, for scenarios (i) and (ii) we measure very different stellar radii for NGTS-7A and NGTS-7B. Investigating the posterior distribution of our SED fit reveals a strong correlation between the T_{eff} and radius values of NGTS-7A and NGTS-7B. An example of this for T_{eff} is shown in Fig. 6.9, with the full corner plot shown in Fig. 6.10. The full corner plot for scenario (ii) is shown in Fig. 6.11. The correlation between T_{eff} and radius arises from the similarity of the two sources in spectral type, along with the availability of only the *Gaia* G magnitude to separate them. This correlation needs to be taken into account when determining the uncertainties in the age and mass of NGTS-7A. To incorporate these correlations we fit the 2D posterior distributions from our SED fitting with ellipses covering 68 per cent of our distribution. We have used these ellipses to probe the extremes of parameter space and incorporate the observed correlations into our analysis (Sect. 6.3.2). For each parameter we also report the 16th, 50th and 84th percentile of the marginalised 1D distributions in Tab. 6.2.

Primary Mass

When we fix both stars to the *Gaia* distance for NGTS-7B (scenario (i)), the median radius of the primary star is approximately 75 per cent oversized in radius compared to that of a main sequence star of the median T_{eff}. One possible reason for this is that NGTS-7A and NGTS-7B are pre-main sequence stars and as such both have a larger than expected radius (e.g Jackman et al., 2019a). In order to estimate the mass of the primary star we compared each source to the PARSEC isochrones (Bressan et al., 2012), assuming that NGTS-7A and NGTS-7B are the same age (reasonable if we assume they are bound). From comparing the median radius and T_{eff} of NGTS-7B to the PARSEC isochrones we obtained an age estimate of 55 Myr and a mass of $0.35\,M_{\odot}$ for NGTS-7B. However, using this age estimate with the fitted parameters of NGTS-7A results in different mass estimates based on whether

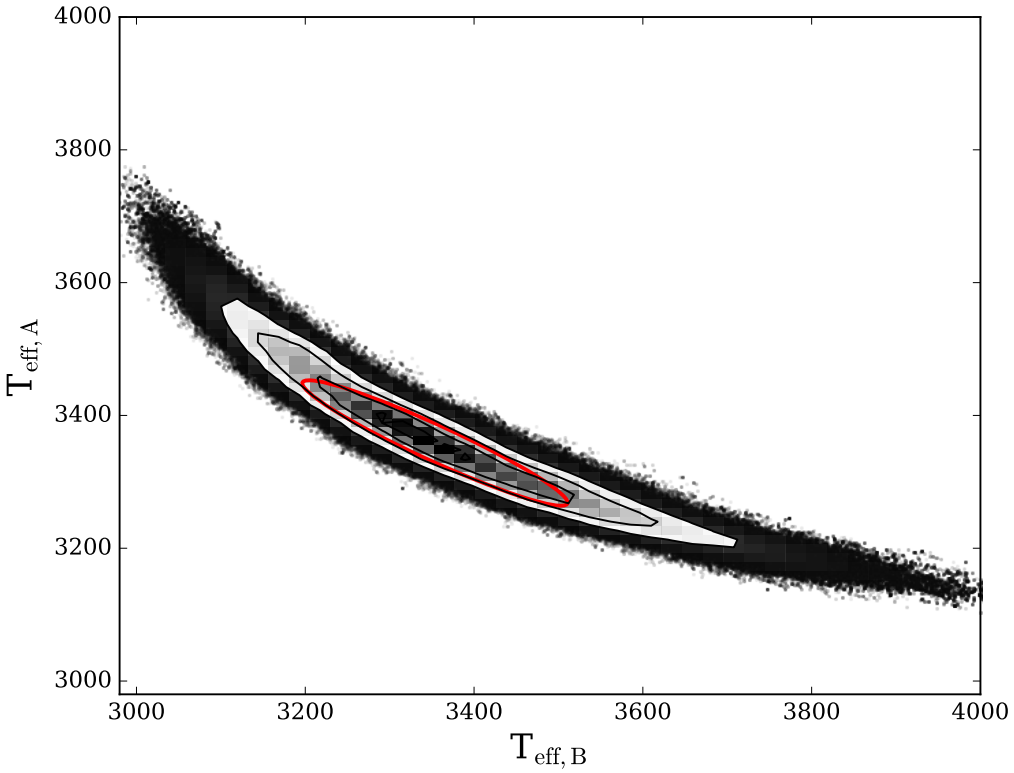

Figure 6.9: The posterior $T_{eff,A}$-$T_{eff,B}$ distribution of the scenario (i) (Sect. 6.3.2) SED fit, showing the correlation between the effective temperatures of NGTS-7A and NGTS-7B. The red ellipse indicates the estimate of the 1σ region.

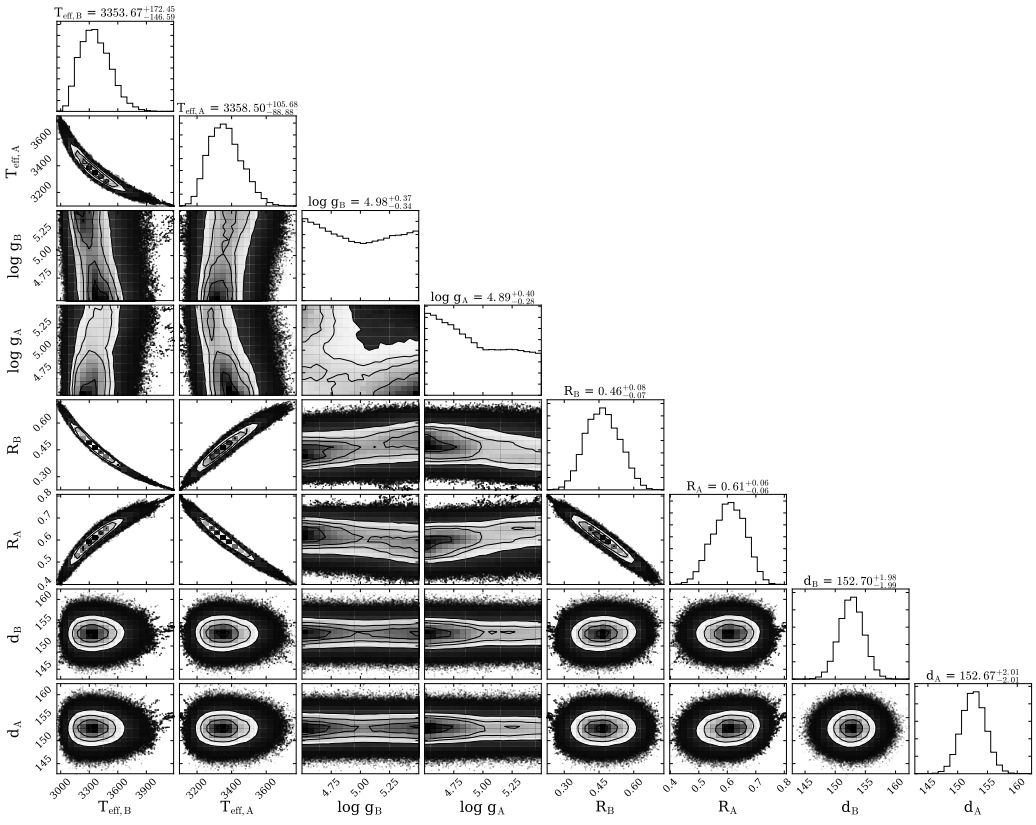

Figure 6.10: The full corner plot for the scenario (i) SED fitting. Note the strong correlation between T_{eff} and radius, which we have accounted for in our analysis.

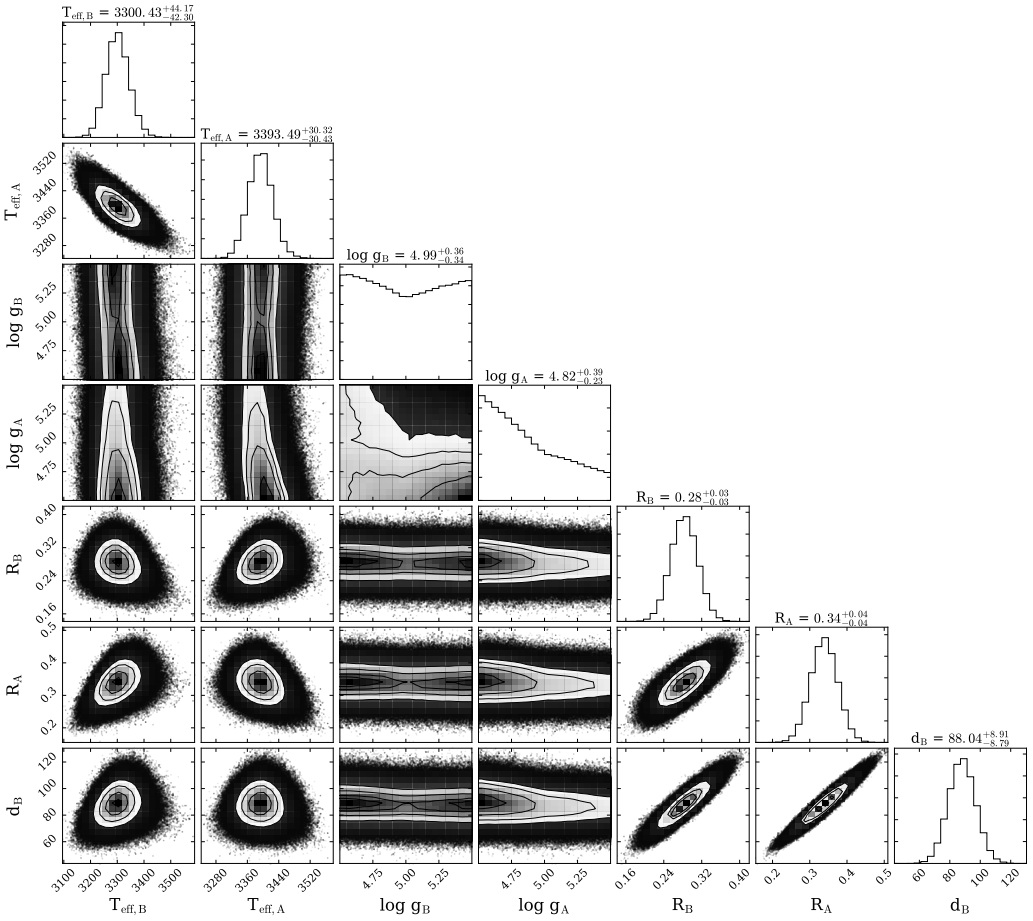

Figure 6.11: The full corner plot for the scenario (ii) SED fitting.

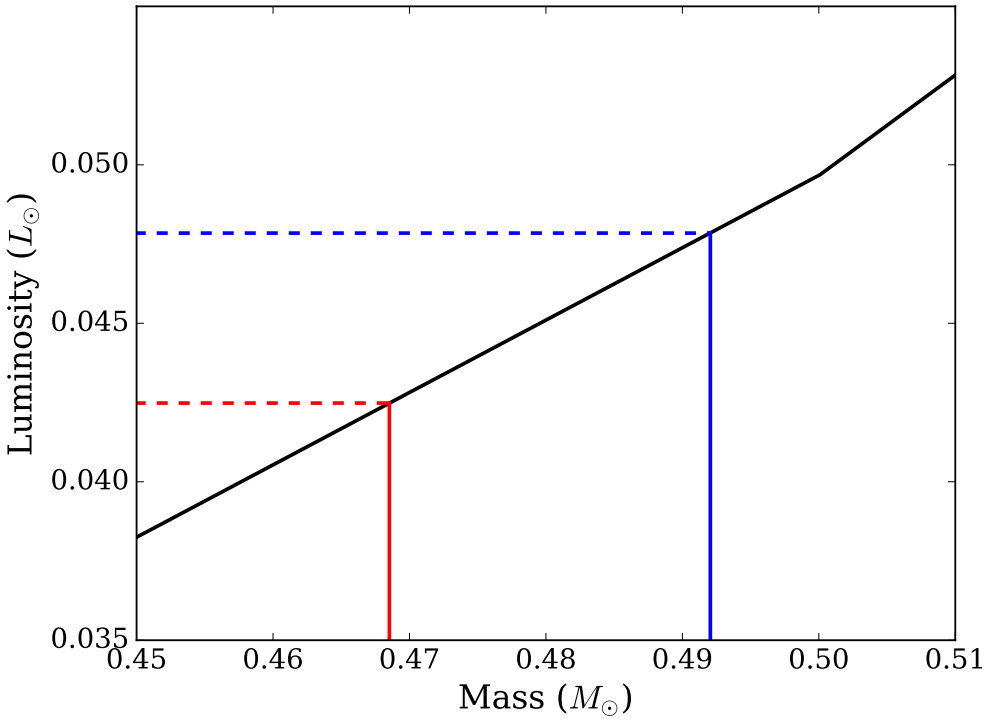

Figure 6.12: An example of the starspot correction described in Sect. 6.3.2. In black is the PARSEC mass-luminosity isochrone for 55 Myr. The red and blue lines correspond the unspotted models with luminosity equal to our SED fit and before the appearance of spots respectively.

we use the median $T_{\rm eff}$ (0.35 $M_\odot$) or the radius (0.55 $M_\odot$).

A potential reason for this discrepancy is the effect of starspots on NGTS-7A. For both main and pre-main sequence stars, modelling of starspots has shown they can act to both increase the stellar radius and decrease $T_{\rm eff}$ (Jackson and Jeffries, 2014; Somers and Pinsonneault, 2016). The combined effect of these changes can be a diminished stellar luminosity (Jackson and Jeffries, 2014), which results in discrepancies when comparing to unspotted stellar models.

To correct for the effects of spots on our mass estimate for a given age, we used the PARSEC models to identify which unspotted models give a luminosity equal to or up to 10 per cent greater than the current value (this is approximately the change in luminosity caused by the sudden appearance of spots simulated by Jackson and Jeffries, 2014). This was done for the median $T_{\rm eff}$ and radius values of each parameter, as given in Tab. 6.1. In this analysis we used the 1σ extremes determined from the posterior distribution error ellipses from Sect. 6.3.2, in order to

take correlations into account. This resulted in an age of 55^{+80}_{-30} Myr for NGTS-7B. We calculate the luminosity of NGTS-7A based on the median and the error ellipse also, to give a range of possible masses depending on the obtained primary parameters and age of NGTS-7B. Using the possible ages of the neighbour to determine the unspotted model we estimate the mass of the primary as $0.48^{+0.03}_{-0.12} M_{\odot}$. For the errors we have combined the extremes from the age of the neighbour and whether the luminosity is altered by the appearance of spots.

Based on the age estimate of 55^{+80}_{-30} Myr for this system we have also searched for signs of Li 6708Å absorption in our HARPS spectra. Primordial lithium is quickly depleted within the interiors of M stars (e.g. Chabrier et al., 1996) and is typically removed from their photosphere within 45-50 Myr (see Fig. 4 of Murphy et al., 2018). We do not find any sign of Li 6708Å absorption in our HARPS spectra, consistent with our estimate of 55^{+80}_{-30} Myr and it suggests that the system cannot be much younger than this if scenario (i) is true.

We note we have assumed in this section that the companion star does not also suffer from spots, which may be unlikely for a young system. The presence of spots would alter the inferred age and hence mass of the primary star. However, we do not identify any significant modulation in either the NGTS or *TESS* lightcurves which could be attributed to spots on the companion.

We also note that there exist empirical relations to attempt to correct for the effects of magnetic activity on measured $T_{\rm eff}$ and radii (Stassun et al., 2012), using the ratio of the Hα and bolometric luminosity, $\log L_{\rm H\alpha}/L_{\rm Bol}$. These relations are used to bring the $T_{\rm eff}$ and radius values closer to expected model values, which can then be used to calculate the age and mass of NGTS-7A. Unfortunately it is likely that our measurements of Hα luminosity for NGTS-7A are contaminated by NGTS-7B to an uncertain degree (from Hα emission of its own). Consequently, we have chosen not to use these relations to adjust our fitted values here, but do discuss this further in Sect. 6.4.4.

For the second scenario where we have assumed both stars are drawn from the Mann et al. (2015) $T_{\rm eff}$-radius relation, we calculate a distance of $88.0^{+8.9}_{-8.8}$pc, given in Tab.6.2. To calculate the mass in this scenario we use the empirical mass relation of Benedict et al. (2016) for main sequence M stars. We have calculated the value of $M_{\rm K_s}$ for NGTS-7A using the best fitting SED model and the fitted distance. Using this relation with calculated distance of $88.0^{+8.9}_{-8.8}$ pc for the NGTS-7A we calculate the primary mass $M_{\rm A}$ to be $0.24 \pm 0.03 M_{\odot}$.

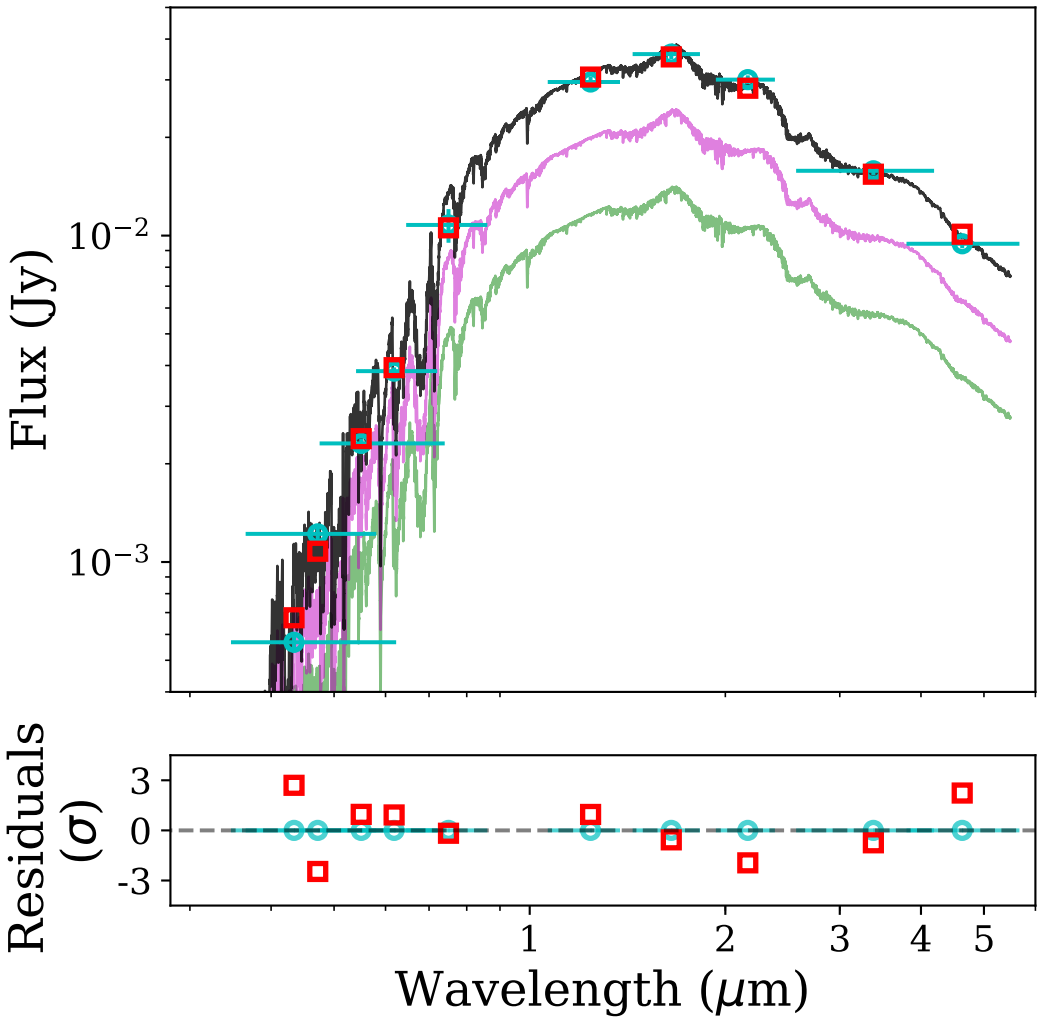

Figure 6.13: Top: The best fitting two-component PHOENIX v2 SED model for scenario (i). The magenta and green curves are the best fitting models for NGTS-7A and NGTS-7B, while the cyan and red points indicate the catalogue and synthetic photometry respectively. The horizontal error bars represent the spectral range of each filter. Bottom: Residuals of the synthetic photometry, normalised to the adjusted catalogue errors.

Table 6.2: Parameters from our fitting of NGTS-7AB system for the scenarios defined in Sect. 6.3.2. In scenario (i) we have placed both stars at the distance of NGTS-7B and fit for the radius, whereas in scenario (ii) we assumed both stars were on the main sequence and fit for both radius and distance. The bold values for scenario (i) are to indicate it is our favoured scenario, as discussed in Sect. 6.4.1. Here we report the median of the 1D distribution for each parameter, along with the errors determined from the 16th and 84th percentiles. Limb darkening parameters with asterisks had priors applied when fitting (Sect. 6.3.3).

Scenario	**(i)**	(ii)
SED Fitting		
$T_{\mathrm{eff}\,A}$ (K)	$\mathbf{3359^{+106}_{-89}}$	3393^{+30}_{-31}
$T_{\mathrm{eff}\,B}$ (K)	$\mathbf{3354^{+172}_{-147}}$	3300^{+44}_{-42}
$\log g_A$	$\mathbf{4.89^{+0.40}_{-0.28}}$	$4.82^{+0.39}_{-0.23}$
$\log g_B$	$\mathbf{4.98^{+0.37}_{-0.34}}$	$4.99^{+0.36}_{-0.34}$
R_A ($R_\odot$)	$\mathbf{0.61^{+0.06}_{-0.06}}$	$0.34^{+0.04}_{-0.04}$
R_B ($R_\odot$)	$\mathbf{0.46^{+0.08}_{-0.07}}$	$0.28^{+0.03}_{-0.03}$
D_A (pc)	$\mathbf{152.67^{+2.01}_{-2.01}}$	$88.04^{+8.91}_{-8.79}$
D_B (pc)	$\mathbf{152.70^{+1.98}_{-1.99}}$	$88.04^{+8.91}_{-8.79}$
Transit Parameters		
Period (hours)	$\mathbf{16.2237952^{+0.0000026}_{-0.0000018}}$	$16.2237957^{+0.0000024}_{-0.0000021}$
Time of transit centre (days) T_{centre} (HJD - 2456658.5)	$\mathbf{1050.053304^{+0.0000017}_{-0.0000055}}$	$1050.053311^{+0.0000099}_{-0.0000125}$
R_A/a	$\mathbf{0.20213^{+0.00310}_{-0.00257}}$	$0.20215^{+0.00366}_{-0.00258}$
R_{BD}/a	$\mathbf{0.04710^{+0.00093}_{-0.00061}}$	$0.04725^{+0.00121}_{-0.00062}$

a (AU)	$\mathbf{0.0139^{+0.0013}_{-0.0014}}$	$0.0078^{+0.0009}_{-0.0008}$
i (°)	$\mathbf{88.43520^{+0.98314}_{-1.10843}}$	$88.43124^{+1.01065}_{-1.29644}$
Surface brightness ratio	$\mathbf{0.03620^{+0.01148}_{-0.01198}}$	$0.03763^{+0.01296}_{-0.01225}$
SAAO LD1*	$\mathbf{0.24872^{+0.02043}_{-0.02002}}$	$0.25023^{+0.02006}_{-0.02080}$
SAAO LD2	$\mathbf{0.06045^{+0.12719}_{-0.12362}}$	$0.06297^{+0.12759}_{-0.14502}$
EulerCam LD1*	$\mathbf{0.53550^{+0.01645}_{-0.01732}}$	$0.53480^{+0.01760}_{-0.01690}$
EulerCam LD2	$\mathbf{0.15415^{+0.19985}_{-0.24625}}$	$0.17269^{+0.17810}_{-0.22253}$
NGTS LD1*	$\mathbf{0.36273^{+0.02752}_{-0.05013}}$	$0.36208^{+0.02798}_{-0.05178}$
NGTS LD2	$\mathbf{0.38254^{+0.12664}_{-0.11373}}$	$0.36759^{+0.14530}_{-0.12993}$
Spot Parameters		
Spot 1 l (°)	$\mathbf{74.68895^{+3.82344}_{-3.21393}}$	$75.22438^{+4.62037}_{-3.48933}$
Spot 1 b (°)	$\mathbf{50.01602^{+8.70891}_{-11.89659}}$	$49.48639^{+9.24656}_{-12.49710}$
Spot 1 size (°)	$\mathbf{13.87737^{+3.60749}_{-2.67395}}$	$13.76827^{+3.05474}_{-2.56000}$
Spot 1 brightness factor	$\mathbf{0.48236^{+0.18490}_{-0.25854}}$	$0.46430^{+0.17512}_{-0.24309}$
Spot 2 l (°)	$\mathbf{176.06974^{+4.63372}_{-3.76279}}$	$176.58879^{+5.62414}_{-4.08154}$
Spot 2 b (°)	$\mathbf{77.97929^{+1.81747}_{-2.10508}}$	$77.47726^{+1.98424}_{-2.56784}$
Spot 2 size (°)	$\mathbf{30.25273^{+3.62982}_{-3.82615}}$	$30.22503^{+3.72268}_{-4.27825}$
Spot 2 brightness factor	$\mathbf{0.27168^{+0.16630}_{-0.17487}}$	$0.30954^{+0.15558}_{-0.19153}$

6.3.3 Transit and Spot Fitting

In order to model the transits of NGTS-7Ab we used the ELLC package (Maxted, 2016). ELLC is a binary star model that allows for multiple spots to be included on each star and as such can be used to model both transits and spot modulation at the same time.

We simultaneously fit the NGTS, SAAO and EulerCam lightcurves to ensure consistent transit parameters across our entire dataset. For the NGTS data we fit a transit model combined with a two spot model, to account for the out of transit modulation. We tested our fitting using both a single and double spot model, however we found a single spot was unable to match the average out of transit behaviour seen in Fig. 6.1. The transit in the *TESS* data is blurred by the 30 min cadence of the observations, and also suffers additional dilution from a number of blended sources (see Fig.6.3), and so we decided not to include the *TESS* light curve in our fit. We can use the *TESS* data to see spot modulation has changed between the NGTS observations and the SAAO and EulerCam follow up lightcurves (which were obtained at similar times to the *TESS* data). Consequently we did not use the NGTS spot model to fit the SAAO or EulerCam follow up lightcurves. However, the SAAO lightcurve of primary transit on 2018 Aug 11 does show evidence of the spot minimum during the single night, consistent with the *TESS* data. We incorporated this into our fitting as a quadratic term which we fit simultaneously with the transits.

The SAAO lightcurve also includes a flare just before ingress, which we masked out for our fitting but analyse in Sect. 6.3.8. For each bandpass we directly fitted independent limb darkening profiles. We used a quadratic limb darkening profile and generated our initial limb darkening parameters using the Limb Darkening Toolkit, (LDtk; Parviainen and Aigrain, 2015), using the best fitting SED from Sect. 6.3.2. During fitting we allowed each second limb darkening coefficient (LD2) to vary, while keeping the first (LD1) constant to reduce degeneracy in the fit. For each photometric band we also incorporate a dilution term, to account for the flux from the neighbouring star. For each band we use a Gaussian prior based on the expected dilution (and standard deviation) from our SED fitting. To estimate the expected dilution in a given bandpass we convolve the SED for each star with the specified filter curve and take the ratio of measured values. In order to take the observed correlations into account we sample the expected values for the Gaussian prior directly from the posterior distribution of the SED fits. For each filter we use

the dilution term to correct the transit model as

$$\delta_{filter} = \left(\frac{R_{BD}}{R_A}\right)^2 \left(1 + \left(\frac{F_B}{F_A}\right)\right)^{-1} \tag{6.1}$$

where δ_{filter}, R_{BD}, R_A are the transit depth in the chosen filter, radii of the companion and NGTS-7A respectively, while F_B and F_A are the fluxes of NGTS-7B and NGTS-7A in the specified bandpass. In the ideal scenario where F_B=0 we can see this becomes the usual transit depth equation. During our preliminary fitting we found the eccentricity to be consistent with zero when applying the Lucy and Sweeney (1971) criterion. Consequently for our final fitting we fixed the eccentricity at zero, i.e that the orbit has circularised. Due to the high time cadence of NGTS it is not feasible to fit the entire NGTS lightcurve for each step of the MCMC process. Instead we bin the lightcurve to 1000 bins in phase, using the period and epoch specified for that step. We chose 1000 bins in order to preserve the information in the ingress and egress. In order to sample the posterior parameter space we used EMCEE with 200 walkers for 50,000 steps and disregarding the first 25,000 as a burn in. We did this for both scenarios (i) and (ii), using the dilution values from the relevant SED model. The values of the best fitting parameters are shown in Tab. 6.2.

Using the results of our transit fitting for scenarios (i) and (ii), we measure the radius of NGTS-7Ab to be $1.38^{+0.13}_{-0.14}\,\mathrm{R_J}$ and $0.77 \pm 0.08\,\mathrm{R_J}$ respectively. As brown dwarfs are expected to shrink with age (e.g. Baraffe et al., 2003), scenario (i) would imply a younger brown dwarf than scenario (ii). A younger implied age is more consistent with our age estimation from Sect. 6.3.2. The single period in our fitting is able to model both the orbital and spin periods, supporting our conclusion in Sect. 6.3.1 that the system is in a state of spin-orbit synchronisation.

Our best fitting spot model suggests the presence of two spot regions with a large size and a low brightness factor. Each region can be interpreted either as a single large spot of constant brightness, or as a series of smaller, darker, spots spread over a similar area. As we only fit for the dominant spots, our model is unable to rule out the presence of spots elsewhere on the star. It is most likely that these are smaller than our fitted regions however, as large spots elsewhere could act to decrease the observed variability (e.g. Rackham et al., 2018).

BJD_{TDB} (-2,450,000)	RV_A (km s^{-1})	RV_A error (km s^{-1})	$Contrast_A$ (per cent)	RV_B (km s^{-1})	RV_B error (km s^{-1})	$Contrast_B$ (per cent)	S/N
8364.50765417	-25.369	1.513	2.584	-7.751	0.054	9.261	6.1
8364.52902662	-20.596	1.640	2.673	-7.751	0.054	11.787	6.7
8373.47768215	14.435	2.326	2.703	-7.751	0.054	12.936	4.5
8373.49931132	17.142	3.578	1.744	-7.751	0.054	16.270	5.8
8373.52064613	19.385	1.159	2.608	-7.751	0.054	6.286	7.7

Table 6.3: HARPS radial velocities for NGTS-7A and NGTS-7B from our analysis in Sect. 6.3.4. The radial velocity of NGTS-7B is fixed to be constant during our analysis. The signal-to-noise ratios correspond to the spectral order 66 centered at 653 nm.

6.3.4 Radial Velocity

When analysing the HARPS data to measure the radial velocity shifts due to NGTS-7Ab we used the standard HARPS data reduction software (DRS) to obtain our measured CCFs. Initial analysis with the M2 mask showed no variation between phases in the CCFs, with a seemingly unchanging peak at -7.7 ± 0.1 km s^{-1}. It was realised that due to the fast rotation of NGTS-7A, the spectral lines were too broadened for the M2 mask (which uses a fine grid of molecular lines), resulting in a low signal-to-noise ratio CCF. It was found that analysing with the K5 mask (which uses fewer lines and is less susceptible to the fast rotation) showed both a CCF peak due to the background source and a shallow wide peak due to the motion of NGTS-7A, shown in Fig. 6.5. The increased width of this peak is due to the fast rotation of NGTS-7A. We confirmed both peaks were also present when using earlier spectral type masks, albeit at a lower signal to noise. With the CCFs from the K5 mask we simultaneously fit all our HARPS CCFs with two Gaussians plus an additional linear background term. Each Gaussian is allowed to vary in amplitude and midpoint, but is required to have a constant width. To perform our simultaneous fitting we once again use an MCMC process with EMCEE, with 200 walkers for 20,000 steps. We use the final 5000 steps to calculate our parameters and the results of our fitting are shown in Fig. 6.5. We folded the measured CCF peak midpoints in phase using the orbital period from Sect. 6.3.3 and fit a sinusoidal signal, shown in Fig. 6.14. We also list the measured midpoints and amplitudes in Tab. 6.3. As the orbit of NGTS-7Ab to likely to have circularised (Sect. 6.3.3), we fitted the RV data using a single sinusoid. We fixed the period and epoch of this sinusoid to the values measured from our transit fitting. With this fit we measure a systemic velocity of -4.2 ± 0.8 km s^{-1} and a semi-amplitude of 25.9 ± 0.9 km s^{-1} for NGTS-7A. We measure a systemic velocity of -7.7 ± 0.1 km s^{-1} for NGTS-7B. Combining our measurement of the semi-amplitude for the radial velocity curve with the mass of NGTS-7A we calculate a mass of $75.5^{+3.0}_{-13.7}\,\mathrm{M_J}$ for the transiting source for scenario (i). For scenario (ii) we obtain a value of $48.5 \pm 4.3\,\mathrm{M_J}$.

The measured $48.5 \pm 4.3\,\mathrm{M_J}$ mass for scenario (ii) places NGTS-7Ab within the brown dwarf regime, making the system an brown dwarf transiting a main sequence M star. Our result for scenario (i) places NGTS-7Ab at the upper end of the brown dwarf regime, near the hydrogen-burning mass limit of $\sim 78 M_\mathrm{J}$ (Chabrier et al., 2000).

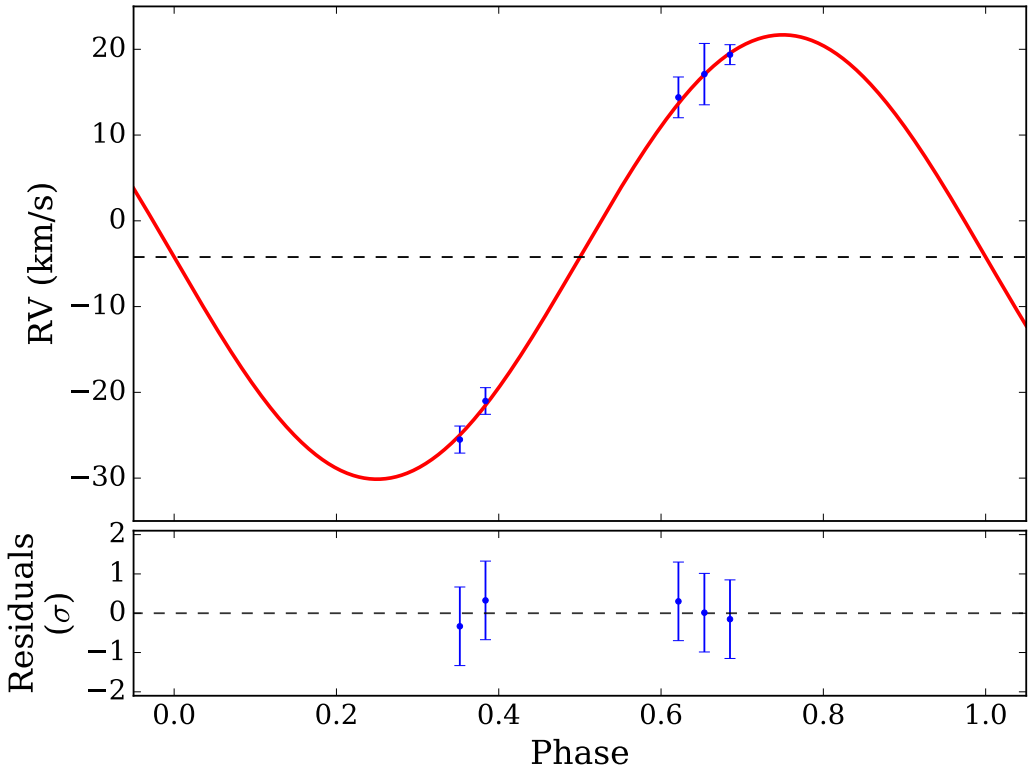

Figure 6.14: HARPS radial velocity data for NGTS-7Ab in blue with the best fitting radial velocity model overlaid in red. We have fixed the eccentricity of the model to 0 (as implied by the phasing of the transit and secondary eclipse in Sect. 6.3.3). We also fixed the period and epoch to those measured from our transit fitting. Bottom: Residuals of the model fit.

6.3.5 Rotational Broadening

We can also use our HARPS data to investigate the level of rotational broadening for NGTS-7A and in turn constrain our radius measurement. We can construct a lower limit by assuming the profile of NGTS-7B is non-rotating and assuming a Gray (2005) profile to artificially broaden it to match the profile of NGTS-7A. We have assumed a limb darkening coefficient for the rotational profile of 0.55. Artificially broadening the CCF of NGTS-7B gives a lower limit of $31\,\mathrm{km\,s^{-1}}$ for $v \sin i$, equivalent to a radius of $0.41\,R_{\odot}$. This value is greater than the measured radius for NGTS-7A for scenario (ii) (a main sequence system with R_A=$0.34\,R_{\odot}$) and is only consistent with scenario (i) (a pre-main sequence system with R_A=$0.61\,R_{\odot}$).

6.3.6 Secondary Eclipse and Brown Dwarf temperature

As part of our fitting of the NGTS lightcurve we have identified evidence of a secondary eclipse for NGTS-7Ab, shown in Fig. 6.1. The presence of a secondary eclipse by its very nature implies non-negligible levels of flux from the brown dwarf itself. To estimate the temperature of NGTS-7Ab we equate the depth of the secondary eclipse to the ratio of fluxes in the NGTS bandpass,

$$\delta_{eclipse} = \left(\frac{R_{BD}}{R_A}\right)^2 \frac{\int F_{BD}(T_{BD})\, S(\lambda)\, d\lambda}{\int F_A\, S(\lambda)\, d\lambda} + A_g \left(\frac{R_{BD}}{a}\right)^2 \tag{6.2}$$

where $F_{\mathrm{BD}}(T_{\mathrm{BD}})$ and F_{A} are the SEDs of the brown dwarf (with temperature T_{BD}) and NGTS-7A respectively, $S(\lambda)$ is the transmission curve of the NGTS filter (Wheatley et al., 2018) and A_{g} is the geometric albedo. For the SED of the primary star we use the results from our SED fitting. To generate the spectrum of the brown dwarf we have used the BT-Settl models (Allard et al., 2012), since the PHOENIX v2 models do not cover the full range of temperatures we wish to probe. For each model spectrum we have renormalised it to the distance of the primary star and to the expected brown dwarf radius. We opted to use these models instead of a blackbody due to the strong absorption features expected in the brown dwarf spectrum (e.g. Martín et al., 1999). We measured $\delta_{\mathrm{eclipse}}$ from the best fitting transit and spot model, making sure to correct for the effect of dilution in the NGTS bandpass. By including A_{g} we can also account for reflection. We have solved Eq. 6.2 in two limiting cases. These are A_{g}=0 (no light is reflected) and A_{g}=0.5. Iterating T_{BD} between 1200 and 3500 K returns estimates of 2880 K (A_{g}=0.5) and 3200 K (A_{g}=0) for scenarios (i) and (ii).

Comparing these temperatures to the Baraffe et al. (2015) models for an

isolated 75.5 M_J brown dwarf results in ages up to 80 Myr, depending on the chosen value of A_g. This is in agreement with our estimate of 55 Myr for the age of this system assuming our scenario (i) in which the system is located at the distance implied by the Gaia DR2 parallax of the companion NGTS-7B (Sect. 6.3.2). In contrast, the Baraffe et al. (2015) models for a 48.5 M_J brown dwarf is not able to match the measured temperature range at any age. This high temperature of the brown dwarf heavily disfavours and effectively rules out scenario (ii), in which both M stars were assumed be on the main sequence and hence at a smaller distance. Note that in scenario (ii) the brown dwarf would have to have a mass that was well below the hydrogen burning limit (Sect. 6.3.4).

6.3.7 Starspots

As part of our analysis in Sect. 6.3.1 and Sect. 6.3.3 we identified starspots were present in the NGTS and *TESS* data. When fitting the NGTS data, we allowed for two starspots in our model and assumed they were representative of the average starspot behaviour of NGTS-7A. Another check for whether this modulation is due to starspots is to look for evolution throughout the NGTS lightcurve. As starspots form and dissipate they will alter both the level of lightcurve modulation and the phase at which it occurs (e.g. Davenport et al., 2015; Jackman et al., 2018). To search for such changes within the NGTS data we split our data into 20 day sections. Visual inspection of the phase folded lightcurve in these sections showed that the modulation was slowly changing with time, indicative of starspot evolution. To show this we have phase folded each section in bins of 0.04 in phase and plotted the flux of each phase folded lightcurve against time in Fig. 6.15, following the method of Davenport et al. (2015).

From Fig. 6.15 we can see the movement of a dominant starspot group from around phase 0.5 to 0.25 over approximately 70 days. The level of modulation from this group is not constant, as the amplitude decreases at around 60 days in Fig. 6.15 before increasing again. One reason for this may be the dissipation and then formation of starspots from a large active region, which would act to change the overall level of modulation. From Fig. 6.15 we cannot identify any regions in the lightcurve where the starspot modulation disappears completely, meaning we are unable to measure the full starspot lifetime. Observations of M stars with *Kepler* have shown that they can have starspots with lifetimes on the order of years (Davenport et al., 2015; Giles et al., 2017). Consequently, it is not unexpected that we do not observe drastically changing spot regions within the NGTS data alone.

A possibility for the apparent shift in starspot phase is that the stellar spin

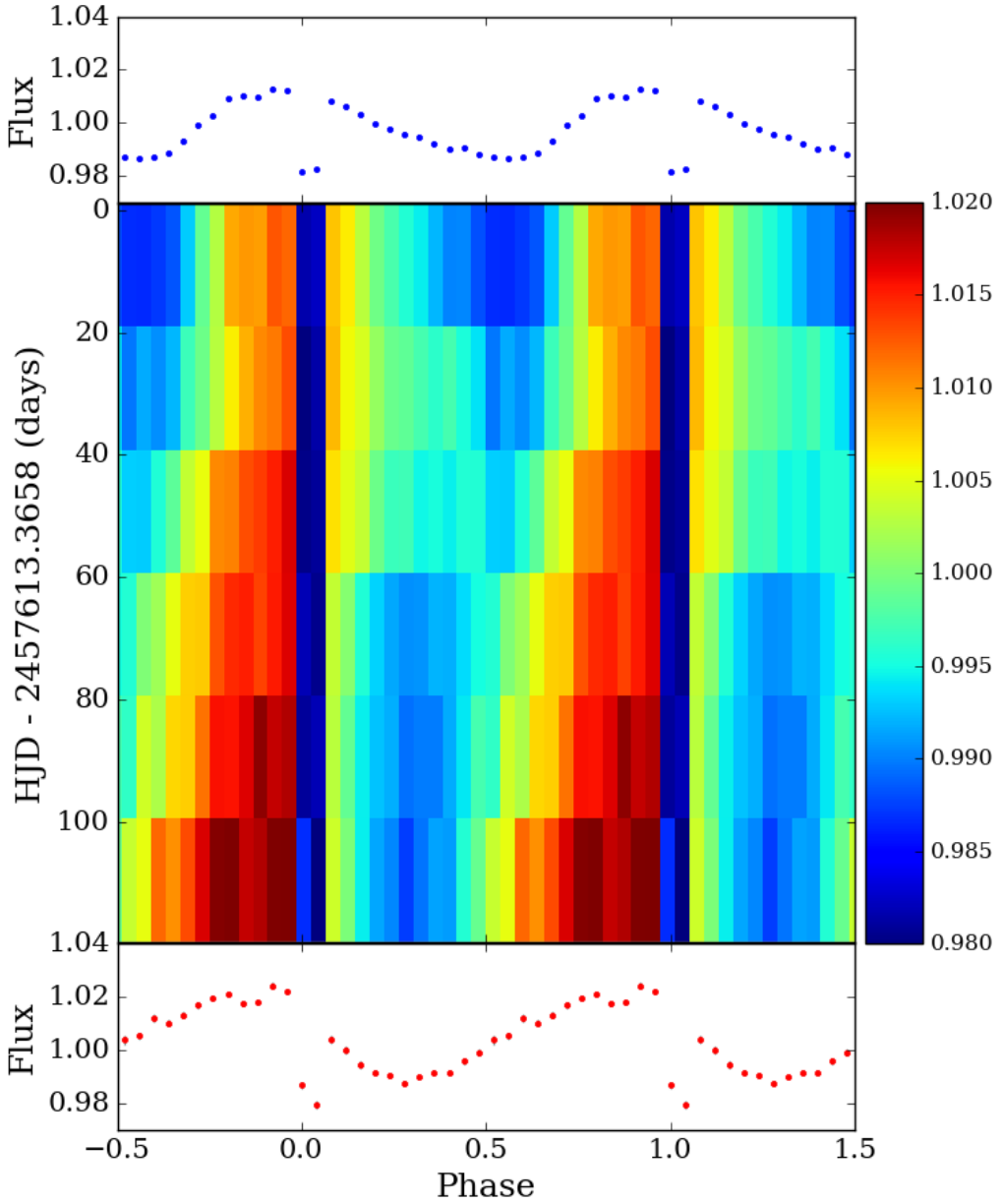

Figure 6.15: The evolution of starspot phase with time for NGTS-7A. Each pixel represents 0.04 in orbital phase and approximately 20 days in time. The flux is normalised to the median value of the entire NGTS dataset. The time is offset relative to 100 days into the season. Shown above and below are the phase folds corresponding to the first and last time bins respectively. The dark regions at phases 0 and 1 indicate where the transit occurs.

period is not exactly the same as the orbital period. A small enough offset may appear as a drift in phase without appearing as an anomaly in the phase folded data. We use Fig. 6.15 to estimate what this drift may be, by assuming that the starspot distribution remains constant and using the change in phase as an estimate of the period difference. From this we find a shift of -0.28 in phase over 100 days, approximately equal to a difference of 162 seconds per day. The starspots moving backwards in orbital phase would imply the star is spinning slightly faster than the orbital period ($P_{\rm orb}/P_{\rm spin} = 1.002$). One check for this is to mask the transits out of the original NGTS lightcurve and search for periodicity in the remaining data using a generalised Lomb-Scargle periodogram, using the ASTROPY LombScargle package (Astropy Collaboration et al., 2013). Doing this and using 20,000 steps between 0 and 2 days returns a best fitting period of 16.204 hours, implying that NGTS-7A is slightly supersynchronous, spinning roughly 1 minute faster than the orbital period. From a sample of *Kepler* eclipsing binaries Lurie et al. (2017) noted a subset of short period, slightly supersynchronous systems. It was suggested that the slight supersynchronous nature of these systems may be due to them having a non-zero eccenticity (yet too small to be measured), which may be the case for NGTS-7A.

If we assume the starspot drift is constant with time, we can calculate the expected shift during the approximately 620 day gap between the end of NGTS and the start of *TESS* observations. We expect the starspot minimum to have shifted to phase 0.5 during the *TESS* observations. However, as seen in Fig. 6.4 this is where the starspot maximum occurs. This discrepancy however does not rule out the slight period difference, as the original starspot group may have decayed and been replaced by a new one at a different phase (e.g. Jackman et al., 2018).

6.3.8 Magnetic Activity

Along with the presence of starspots, NGTS-7A shows other clear signatures of magnetic activity. For instance, this source was originally highlighted as part of the NGTS flare survey described in Chapters 3-5 and 7-8. To find flares in the NGTS data, lightcurves are searched night by night for consecutive outliers about a set threshold. Full information about our detection method can be found in Chapter 2 and Jackman et al. (2018, 2019a,b). From this process we identified four flares in the NGTS lightcurve and we have also identified one from our SAAO follow up lightcurve, which can be seen in Fig. 6.2. To calculate the flare energies we follow the method of Shibayama et al. (2013) and have assumed the flare can be modelled as a 9000 K blackbody. When calculating the flare energy, we have corrected each lightcurve for the expected dilution in the respective bandpass using

our best SED fits from Sect. 6.3.2. From this we calculated energies ranging between $7.7^{+2.4}_{-1.8} \times 10^{32}$erg and $3.3^{+1.0}_{-0.8} \times 10^{33}$erg or $2.5^{+0.7}_{-0.6} \times 10^{32}$erg and $1.1^{+0.3}_{-0.2} \times 10^{33}$erg for scenarios (i) and (ii) respectively. Based on the total observing time in the NGTS and I band filters, we measure the rate of flares above the minimum measured energy for NGTS-7A as 72 ± 32 per year. The high rate of flares is similar to that of other known active M stars, such as GJ 1243 (Ramsay et al., 2013; Hawley et al., 2014) and YZ CMi (Lacy et al., 1976).

In Sect. 6.2.2 we noted the presence of emission lines from the Balmer series, helium and calcium, as shown in Fig. 6.6. By co-adding our HARPS spectra we were also able to identify the presence of $H\alpha$ emission. All of these emission lines are persistent, i.e. they appear in each individual spectrum, making us confident they are not just the product of a flare. In Sect. 6.3.1 we attributed these strong emission lines to NGTS-7A and their presence during quiescence is a clear sign that NGTS-7A is chromospherically active (e.g. Reid et al., 1995; Walkowicz and Hawley, 2009). Active M stars are known to show high energy flares more frequently than their inactive counterparts (Hawley et al., 2014), fitting in with our observation of multiple flares across datasets.

For our NGTS and SAAO data we have also checked where the flares occur in starspot phase. We find that the flares occur in the NGTS data at phases 0.42, 0.43, 0.30 and 0.56. All of these phases are when the two dominant active regions are in view. From comparing to spot modulation in the *TESS* lightcurve we also know that the flare observed in the SAAO follow up lightcurve occurred when the spots were in view, close to the spot modulation minimum. Previous studies of the flare-starspot phase relation for M stars have found flares appear to occur with a uniform distribution in starspot phase (e.g. Hawley et al., 2014; Doyle et al., 2018). This uniform distribution has been explained as either flares occuring in small active region, which do not not cause detectable spot modulation, or flares occuring in permanently visible active regions.

Systems with known inclinations can constrain which latitudes are permanently visible, something not known for the majority of stars. As we believe NGTS-7A has been spun up by NGTS-7Ab and the system is not inclined relative to us, the only permanently visible active regions would be at the pole. The fact that none appear when the dominant starspots are not in view suggests the flares are associated with the starspots dominating the modulation, as opposed to a permanently visible polar region or smaller spots elsewhere.

X-ray Activity

To determine the X-ray luminosity of NGTS-7A we have searched through available archival X-ray catalogues. NGTS-7 was detected during the Einstein 2 sigma survey conducted with the IPC instrument (Moran et al., 1996). It has an upper limit entry in the XMM upper limit server[5] (from an 8 second exposure slew observation) and was not detected in the ROSAT All-Sky Survey. For our analysis we have chosen to use the Einstein 2 sigma entry, due to it being a detection as opposed to an upper limit. Given a count excess of 8.1 counts over an exposure time of 1223 seconds, we obtain an Einstein IPC count rate of 6.6×10^{-3} counts s^{-1}, with a signal-to-noise ratio of 2.35. We use the WebPIMMS interface[6] to calculate the flux in the 0.2-12.0 keV energy range. When doing this we use a Galactic nH column density of $1.7 \times 10^{20} cm^{-2}$ and an APEC optically-thin plasma model with $\log T(K) = 6.5$. From this we estimate an unabsorbed flux of 1.66×10^{-13} erg $cm^{-2}s^{-1}$ between 0.2 and 12.0 keV. For our two scenarios of Sect. 6.3.2 we estimate L_X and L_{Bol} using the parameters from our best fitting SED. From this we obtain $\log L_X = 29.2$ and $\log L_X/L_{Bol}$= -2.54 for both scenarios. Taking into account the low signal to noise of the detection (corresponding to an error of $\approx 40\%$) and that the nH column density used in an upper limit, this luminosity value is consistent with saturated X-ray emission ($\log L_X/L_{Bol} \approx$ -3; Pizzolato et al., 2003; Wright et al., 2018). However, one has to take into account that NGTS-7B is within the Einstein IPC aperture, which has a spatial resolution of only ca. $1'$. The detected flux may therefore stem from both stars together. If both are equally X-ray bright, this would reduce the $\log L_X/L_{Bol}$ level for NGTS-7A to -2.84. Another possibility is that the Einstein exposure covered a flare of one of the stars, therefore registering a higher X-ray flux level compared to the quiescent level. To check for very large flares and confirm our choice of parameters in WebPIMMS we calculated the expected count rates in XMM-Newton and the ROSAT All-Sky Survey for comparison. In both cases we find find that the expected counts for the existing exposure times of XMM and ROSAT are below or at the respective upper limits. While this does not completely rule out a flare during the Einstein observation, it makes less likely; we are therefore confident that NGTS-7A is indeed an X-ray saturated star, fitting with our observations of rapid spin and magnetic activity.

[5] http://xmm2.esac.esa.int/UpperLimitsServer/

[6] https://heasarc.gsfc.nasa.gov/cgi-bin/Tools/w3pimms/w3pimms.pl

6.4 Discussion

6.4.1 The nature of NGTS-7Ab

With an orbital period of 16.2 hours, NGTS-7Ab is the shortest period transiting brown dwarf around a main or pre-main sequence star to date. It is also only the fifth known brown dwarf transiting an M star (Irwin et al., 2010; Johnson et al., 2011; Gillen et al., 2017; Irwin et al., 2018). The host star is magnetically active, showing starspot modulation and flaring activity in both the NGTS and follow up lightcurves.

In Sect. 6.3.2 we formulated two possible scenarios for the nature of the NGTS-7 system. Scenario (i) places both stars at the distance implied by the Gaia DR2 parallax of NGTS-7B and results in a pre-main sequence system of roughly 55 Myr (Sect. 6.3.2), while scenario (ii) assumes both stars are on the main sequence. These two scenarios resulted in brown dwarf masses of $75.5^{+3.0}_{-13.7}\,\mathrm{M_J}$ and $48.5 \pm 4.3\,\mathrm{M_J}$ respectively. In Sect. 6.3.5 we measured the rotational broadening of NGTS-7A and obtained a value of $31\mathrm{km\,s^{-1}}$, a value too high for a main sequence M star rotating with a period of 16.2 hours. In Sect. 6.3.6 we used the detection of the secondary eclipse of NGTS-7Ab to measure its temperature. We measured temperatures between 2880 K and 3200 K, depending on the geometric albedo of NGTS-7Ab. We found these measured temperatures could not be explained by a $48.5 M_\mathrm{J}$ brown dwarf at any age, heavily disfavouring scenario (ii) once again. Based on these pieces of evidence we conclude that scenario (i) is the most likely scenario and that NGTS-7Ab is a 55^{+80}_{-30} Myr brown dwarf, transiting a tidally-locked chromospherically active pre-main sequence M dwarf in a state of spin-orbit synchronisation.

6.4.2 Formation of NGTS-7Ab

It has previously been suggested that brown dwarfs around stars fall into two separate mass regimes (Ma and Ge, 2014; Grieves et al., 2017), with a boundary at around $42.5 M_\mathrm{J}$. It was suggested by Ma and Ge (2014) that the two populations of companion brown dwarfs are related to their formation mechanism. Lower mass brown dwarfs ($< 42.5 M_\mathrm{J}$) are thought to form in the protoplanetary disc, in a mechanism similar to giant planets. Whereas, higher mass brown dwarfs may follow a formation path similar to stellar binaries and form through molecular cloud fragmentation. One reason for this separate mechanism is the limited mass available in protoplanetary discs to form companions, especially for discs around M dwarfs (e.g. Andrews et al., 2013; Ansdell et al., 2017). Based on this analysis and the mass of NGTS-7Ab, we might expect molecular cloud fragmentation to be a more likely

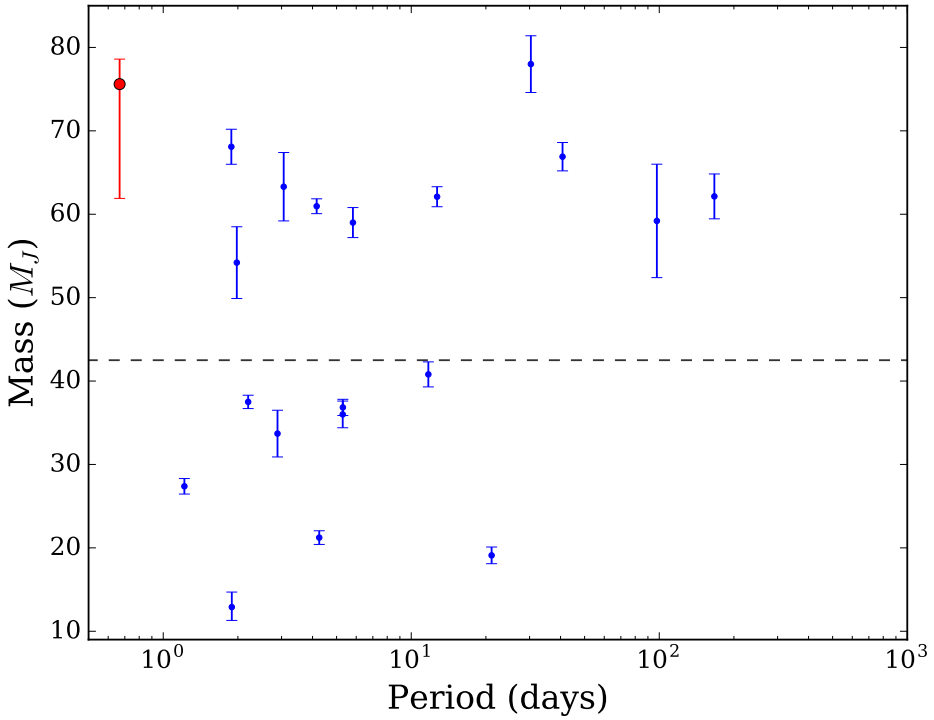

Figure 6.16: The mass period distribution of known transiting brown dwarfs, with the position of NGTS-7Ab from scenario (i) shown in red. This is an updated version of the same plot from Bayliss et al. (2017), using the table of transiting brown dwarfs compiled by Carmichael et al. (2019), along with values for AD 3116 and RIK 72 from Gillen et al. (2017); David et al. (2019).The dashed line indicates $42.5 M_{\rm J}$, where Ma and Ge (2014) identify a gap in the mass distribution of brown dwarfs.

pathway for the formation of NGTS-7Ab.

If we believe that the two *Gaia* sources are physically bound and that this is a hierarchical triple system, then NGTS-7Ab is similar to both NLTT41135 B (Irwin et al., 2010) and LHS 6343C (Johnson et al., 2011). These systems are both M+M visual binaries where one star hosts a transiting brown dwarf. Both systems are stable with ages greater than 1 Gyr, however the presence of an outer body could help explain how NGTS-7Ab found its way onto a close orbit. One explanation for the tight orbit of NGTS-7Ab is that is has been moved inwards via the Kozai-Lidov mechanism (Kozai, 1962; Lidov, 1962), where an outer body drives periodic oscillations between the inclination and eccentricity of the inner orbit. If the brown dwarf is driven into a highly eccentric orbit it may then circularise via tidal forces, resulting in both the observed tight orbit and the spin up of NGTS-7A (e.g. Bolmont et al., 2012). From a sample of 38 high mass ($> 7\ M_{\rm J}$) exoplanets and brown dwarfs, Fontanive et al. (2019) found that companions with orbital periods less than 10 days have circularisation timescales consistent with the Kozai-Lidov mechanism. We have estimated the timescale of the Kozai-Lidov mechanism (τ_{KL}) for the NGTS-7 system using the formalism from Kiseleva et al. (1998) and find τ_{KL} <55 Myr for initial orbits beyond 0.1 AU. For the outer orbit (of NGTS-7A and NGTS-7B) we have assumed a period of 2500 years (see Sect. 6.4.5) and an eccentricity of 0.5 (e.g. Raghavan et al., 2010). This timescale increases for wider orbits. For the closer separations where the Kozai-Lidov mechanism may not have had enough time to operate, an alternative explanation may be that dynamical interactions during formation may have scattered NGTS-7Ab inwards and onto an eccentric orbit which was was then circularised through tidal forces.

On the other hand, if the two *Gaia* sources are not physically bound then NGTS-7Ab would be more similar to AD 3116 and RIK 72b, young (sub-Gyr and 10 Myr) brown dwarfs orbiting M stars in the Praesepe and Upper Scorpius open clusters (Gillen et al., 2017; David et al., 2019). Neither of these show any sign of a nearby binary component. AD 3116 and RIK 72b have orbital periods of 1.98 and 110 days respectively. In this situation, the brown dwarf companion likely formed close enough to its host star to migrate inwards to its current position through interactions with the primary itself (e.g. Armitage and Bonnell, 2002), rather than being driven to a close orbit by a third body. However, both brown dwarfs have eccentric orbits (e=0.15 and 0.11 respectively), suggesting circularisation and migration timescales in this scenario take longer than the estimated 55 Myr age of the NGTS-7 system.

As mentioned previously, one mechanism for migrating orbiting bodies in-

wards is through the combination of tidal forces and the magnetic wind of the host star (e.g. Damiani and Díaz, 2016). These forces act in conjunction to migrate brown dwarfs inwards by transferring angular momentum from the orbit to the spin of the host star, which is then lost via magnetic breaking. The process acts with varying efficiency for different spectral types. These interactions have been argued to be particularly efficient for G and K stars (Guillot et al., 2014), due to their radiative interiors and moderate magnetic winds. F stars however have a much weaker wind, and the low masses and radii of M stars result in reduced tidal forces (Damiani and Díaz, 2016). Both of these factors result in increased migration timescales for F and M stars. While this depends on the initial position and age of system, these interactions could provide a feasible mechanism for moving NGTS-7Ab into its current position.

6.4.3 Future Evolution of NGTS-7Ab

The remaining lifetime of NGTS-7Ab will be set by the combination of tidal dissipation and magnetic braking from the spin-down of the star which together act to remove angular momentum from the orbit of the brown dwarf. In the synchronised state, the torque on the star due to the stellar wind is equal to the tidal torque (e.g. Damiani and Lanza, 2015; Damiani and Díaz, 2016) and the orbit of NGTS-7Ab is expected to decay on a timescale set primarily by the magnetic braking of the host star (e.g. Barker and Ogilvie, 2009).

To estimate the in-spiral time $\tau_{\rm a}$ of the orbit we follow Damiani and Díaz (2016) and use

$$\tau_a \approx \frac{1}{13} \frac{h}{\alpha_{mb} C_* \Omega^3} \tag{6.3}$$

where h is the orbital angular momentum of the system, $\alpha_{\rm mb} = 1.5 \times 10^{-14}$ is the magnetic braking parameter (Dobbs-Dixon et al., 2004; Damiani and Díaz, 2016), C_* is the primary star moment of inertia and Ω is the angular velocity of the star in the synchronised state. For our two scenarios we estimate $\tau_{\rm a}$ as 5 and 10 Myr respectively, implying that NGTS-7Ab will not remain in the current state for long and is very close to the end of its lifetime.

This short remaining lifetime strengthens our conclusion in Sect. 6.4.1 that NGTS-7 is a young system consisting of pre-main sequence stars and a hot brown dwarf with an age of only 55 Myr.

6.4.4 The mass of NGTS-7A

To account for the effects of starspots on our stellar mass estimate for NGTS-7A in Sect. 6.3.2, we corrected for the expected decrease in luminosity, using the age from NGTS-7B. This was then compared directly to the unspotted PARSEC models to estimate the mass. This method assumes a limiting drop in luminosity up to 10 per cent, however it may be possible that the change is greater than this. An alternative way of accounting for starspots is to use the empirical relations of Stassun et al. (2012). These relations, from observations of low mass stars and eclipsing binaries, can be used to estimate the difference between observations and models due to magnetic activity. These corrections can be utilised with either $\log L_{\mathrm{H}\alpha}/L_{\mathrm{Bol}}$ or $\log L_X/L_{\mathrm{Bol}}$. In Sect. 6.3.8 we estimated $\log L_X/L_{\mathrm{Bol}}$ for the primary star, assuming both that it was the sole X-ray emitter ($\log L_X/L_{\mathrm{Bol}}$=-2.54) and that both stars were equally X-ray bright ($\log L_X/L_{\mathrm{Bol}}$=-2.84). $\log L_X/L_{\mathrm{Bol}}$ was calculated using the best fitting SED of the primary star alone and should thus provide a more constrained estimate of the magnetic activity. Using an average of the two values with the relations for $\mathrm{T_{eff}}$ and radius of Stassun et al. (2012), we obtain correction factors of -6.5 per cent and 17 per cent respectively. Applying these correction factors and comparing the new model $\mathrm{T_{eff}}$ and radius estimates to the PARSEC models, we obtain an age of 65 Myr and a mass of $0.47\,M_{\odot}$. These values are consistent with the age and mass obtained in Sect. 6.3.2, supporting our conclusion that magnetic activity (starspots) may have altered the SED of the primary star.

We have compared the fitted and derived masses, radii and temperatures of NGTS-7A, NGTS-7B and NGTS-7Ab to the Baraffe et al. (2015) isochrones in Fig. 6.17 and Fig. 6.18. This was done using the values from scenario (i). In Fig. 6.17 we can see that the positions of NGTS-7A and 7B appear to have larger radii than expected from the models for their mass and fitted age. We believe this is due to the effects of spots in our SED fitting, which are not accounted for in the models and can result in radius inflation, as discussed in Sect. 6.3.2. A greater discrepancy can be observed when comparing effective temperature to the models in Fig. 6.18, where neither NGTS-7A or 7B appears to agree with the Baraffe et al. (2015) models. Again, we believe this is due the effects of spots, which as discussed in Sect. 6.3.2, will decrease the observed luminosity and measured effective temperature relative to models (Jackson and Jeffries, 2014). We find that the derived mass and radius of NGTS-7Ab is seemingly more consistent with an age of around 135 Myr. However, this is in contrast to the measured dayside temperature of NGTS-7Ab, which suggests an age more similar to 25 Myr. These contrasting discrepancies are likely due to both the effect of spots on our fitted and derived properties, but also

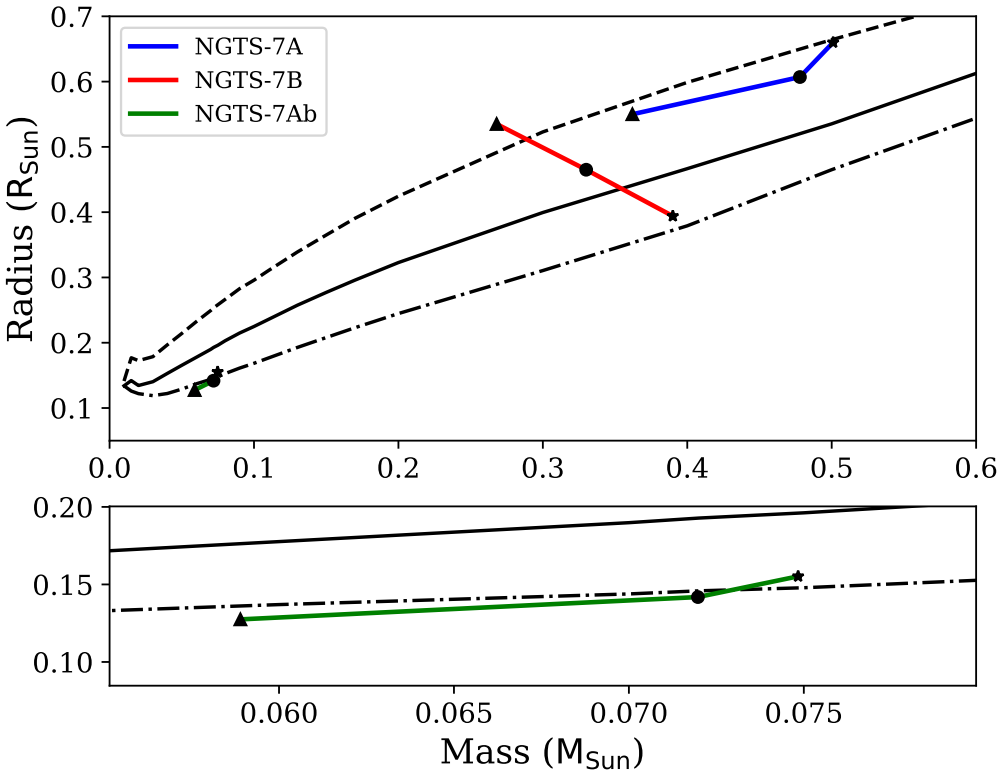

Figure 6.17: Comparison of the fitted masses and radii of NGTS-7A (blue line) and NGTS-7B (red line) and the derived mass and radii of NGTS-7Ab (green line, zoomed in in the bottom panel) with the Baraffe et al. (2015) models. The solid, dashed and dot-dashed black lines are the isochrones for 55, 25 and 135 Myr respectively, the one-sigma values for our best fitting system ages. For each object we have plotted the 25, 55 and 135 Myr values, corresponding to the triangle, circle and star respectively, to show how the correlations between the fitted properties and age.

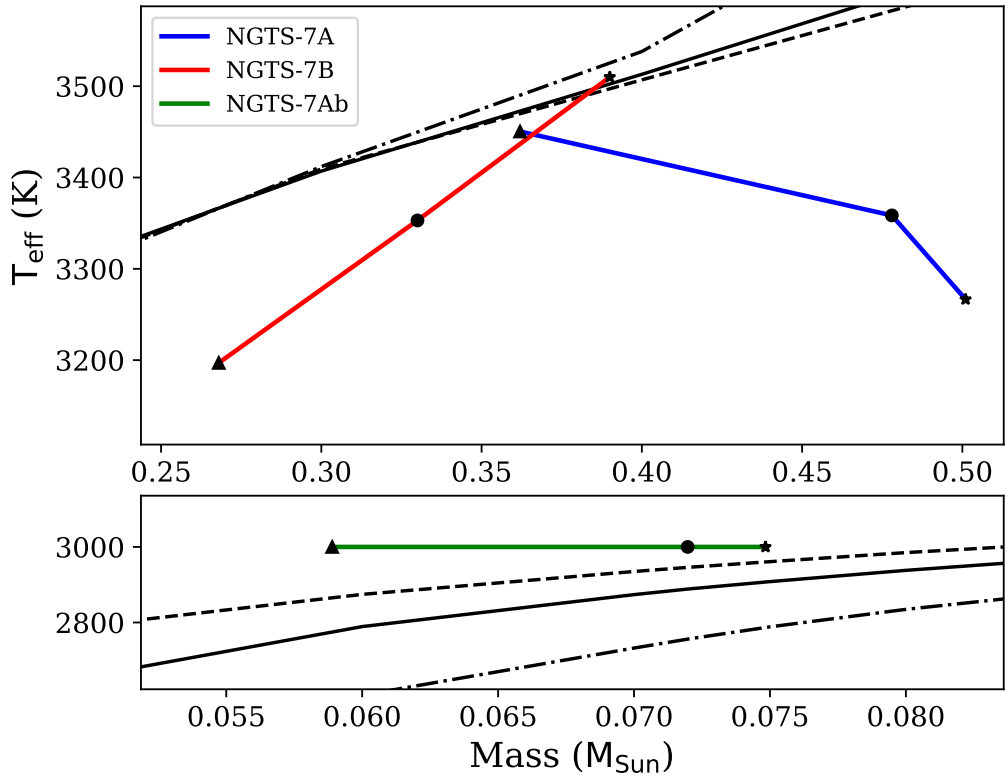

Figure 6.18: Comparison of the fitted masses and effective temperatures of NGTS-7A (blue line) and NGTS-7B (red line) and the derived mass and dayside temperature of NGTS-7Ab (green line, zoomed in in the bottom panel) with the Baraffe et al. (2015) models. Here we have used a fixed representative dayside temperature of 3000. The solid, dashed and dot-dashed black lines are the isochrones for 55, 25 and 135 Myr respectively, the one-sigma values for our best fitting system ages. For each object we have plotted the 25, 55 and 135 Myr values, corresponding to the triangle, circle and star respectively, to show how the correlations between the fitted properties and age.

the degeneracies between our fitted SED properties. Future observations which can separate out the photometric and astrometric components of NGTS-7, along with obtaining independent, non-blended, measurements of activity indicators for the two stars will help resolve these issues.

6.4.5 The orbit of the wide binary NGTS-7AB

In Sect. 6.3.2 and Sect. 6.3.2 we discussed the issues present in both the *Gaia* astrometry and photometry. Investigation of the scan angles used in *Gaia* DR2 showed over 75 per cent of scans passed through both NGTS-7A and NGTS-7B. We determined that the $1.13''$ separation of the two sources was not enough to result in significant contamination of the *Gaia* G band photometry, however would result in blended BP and RP photometry. We determined that the close proximity may be responsible for the perturbed astrometric solution of each source, due to a shifting photocentre between scans.

Something else which has been noted as perturbing the astrometry of sources in *Gaia* DR2 is orbital motion. *Gaia* DR2 uses measurements obtained over an approximately two year timespan and orbital motion of a similar period could significantly affect the measured proper motions and parallaxes (Gaia Collaboration et al., 2018b). To see whether orbital motion could affect the astrometric solutions for NGTS-7A and NGTS-7B in a similar manner we have estimated the orbital period of the system, assuming a circular orbit. Using the masses of $0.48\,M_{\odot}$ and $0.35\,M_{\odot}$ for NGTS-7A and NGTS-7B and a separation of 173 AU we estimate the period as 2500 years. Consequently, if these sources are on a circular orbit it is unlikely orbital motion dominates the astrometric issues. We have also estimated the astrometric motion of NGTS-7A due to NGTS-7Ab to see whether this could be contributing to the astrometric noise. We estimate astrometric shifts of 0.012 and 0.013 mas for scenarios (i) and (ii) respectively, meaning it is unlikely NGTS-7Ab is causing significant astrometric noise (see also the analysis of the GJ2069 system from Mann et al., 2019).

The third data release of *Gaia* is planned to include information about binarity (e.g. Lindegren et al., 2018; Gaia Collaboration et al., 2018b,a), meaning we will be able to constrain these scenarios further. Along with this, it is expected that blending between close sources will be improved upon. AO-assisted photometric observations could also help improve the SED fitting, better defining the parameters of the system.

6.5 Conclusions

We have reported the discovery of NGTS-7Ab, a high mass transiting brown dwarf orbiting an M star with an orbital period of 16.2 hours. This is the shortest period transiting brown dwarf around a pre-main or main sequence star known to date and only the fifth brown dwarf transiting an M star host. Through the detection of starspot modulation in the NGTS data we have identified that the M star is in a state of spin-orbit synchronisation. We estimated an in-spiral time of 5 to 10 Myr. The short in-spiral time fits with the system being young and NGTS-7A being a pre-main sequence M dwarf with an age of 55^{+80}_{-30} Myr. If so, then NGTS-7Ab has a mass of $75.5^{+3.0}_{-13.7}\,\mathrm{M_J}$, placing it at the upper end of the brown dwarf regime. Through our analysis we identified that NGTS-7A is chromospherically active, showing emission lines in spectra, strong X-ray emission and exhibiting multiple flares in our photometry. These flares appear to occur more often when the starspots are in view, suggesting the two are related.

The host star NGTS-7A has a neighbouring source, NGTS-7B, of similar brightness and proper motion and systemic velocity 1.13 arcsec away. By accounting for both stars in our SED fitting, we determined the two stars to have similar temperatures. Their very similar kinematics and close proximity on the sky strongly suggest they constitute a bound binary system. If so, we believe NGTS-7Ab is part of a hierarchical triple system and the presence of NGTS-7B may have had a role in moving the brown dwarf into its close orbit. *Gaia* DR3 and AO-assisted observations will be valuable in determining the system parameters more precisely in the future.

Chapter 7

White-Light Flares Detected From Orion

The way we look to a distant constellation
That's flaring in a corner of the sky.

Paul Simon, *Boy In The Bubble* (Boy In The Hubble, adapted by James A. G. Jackman)

7.1 Introduction

The pre-main sequence represents the most active period in a star's lifetime, something reflected in their lightcurves. Material from surrounding discs passing in front the star can cause deep drops in their apparent flux (e.g. Cody et al., 2014; Ansdell et al., 2016), while accretion events can cause rapid rises in flux (e.g. Guo et al., 2018). Another source of variability is stellar flares, which as described in Chapter 1 are explosive phenomena caused by reconnection events in the stellar magnetic field, resulting in intense white-light emission.(e.g. Benz and Güdel, 2010).

The amplitudes and measured energies from stellar flares from pre-main sequence stars regularly dwarf those from their main sequence counterparts, such as the result presented in Chapter 4. The associated loop lengths from these flares can even dwarf the star itself, with X-ray studies measuring loop lengths of several stellar radii (e.g. Favata et al., 2005). If these loops link to a surrounding disc, these flares could drive accretion of disc material onto the star (Orlando et al., 2011; Colombo et al., 2019).

In recent years, studies of white-light flares have begun to move towards how flare properties evolve as a function of age (e.g Chang et al., 2015; Davenport

et al., 2019; Ilin et al., 2019). As stars age after they have reached the zero age main sequence, they are expected to spin down and lose angular momentum through magnetic braking (Weber and Davis, 1967). Studies of open clusters and associations of known ages have shown this occurs in a mass-dependent fashion, with higher mass stars spinning down first (e.g. Epstein and Pinsonneault, 2014; Matt et al., 2015; Douglas et al., 2019). This spin down is expected to affect the internal dynamo also, weakening it and the magnetic field it generates. This decrease in the magnetic activity with time has already been observed in XUV observations which probe the coronal activity (e.g. Jackson et al., 2012), suggesting a drop in field stength. A weakening of the magnetic activity is also expected to be reflected in a decrease in the measured energies and average occurrence rates of stellar flares. Indeed, recent studies have begun to see this in white-light flare observations. Davenport et al. (2019) has studied how flare occurrence rates vary with age by combining gyrochronology with the Davenport (2016) *Kepler* flare sample. They were able to derive a mass and age dependent model for the flare occurrence rate, however note that their results may be affected by tidal evolution of binaries which can bias age estimates to younger ages. By using *K2* observations of flares from stars within the 125 and 630 Myr Pleiades and Praesepe clusters Ilin et al. (2019) measured the decrease in average flare rates between these two ages for K and M stars. They found the decrease occurs quicker than predicted from the Skumanich (1972) $t^{-1/2}$ law, suggesting they are still in a regime of time-variable spin down which cannot be parameterised by a single law (e.g. Barnes, 2010).

Measurements of average white-light flare occurrence rates so far have used clusters older than 100 Myr. Observations of systems younger than this have typically been of individual stars (e.g. Chapter 4; Jackman et al., 2019a) or been X-ray observations which probe different parts of the flare reconnection model (e.g. Stelzer et al., 2007; Flaccomio et al., 2018). During the first 100 Myr, stars with masses above $0.4 M_{\odot}$ form their radiative zone (Baraffe et al., 2015). Gregory et al. (2016) found evidence that the formation of the radiative zone is accompanied by a drop in the coronal X-ray luminosity, a parameter used as a probe of stellar magnetic activity. Studies of clusters up to 100 Myr would allow us to see whether the formation of the radiative zone has an impact on the average flaring activity. Along with this we can constrain the starting point of flare occurrence rates, informing studies of flares on the habitability of the youngest exoplanetary systems and their planetary formation, as discussed in Chapter 4.

In this chapter we report the detection of white-light flares from pre-main sequence stars in the Orion Complex with the Next Generation Transit Survey

Group	$N_{stars,total}$	$N_{stars,flare}$	Age_{CMD} (Myr)	Age_{HR} (Myr)
L1641N-1	31	7	3.47 ± 1.89	2.18 ± 1.60
onc-1	4	2	3.98 ± 1.79	4.06 ± 1.48
onc-3	1	1	3.31 ± 1.72	2.36 ± 1.79
onc-8	1	1	3.37 ± 1.98	2.99 ± 2.11
onc-11	1	0	3.58 ± 1.34	4.85 ± 1.97
onc-15	1	0	2.51 ± 1.86	2.34 ± 1.79
oriDS-1	19	5	3.02 ± 1.78	N/A
oriDS-2	1	0	6.61 ± 1.76	N/A
oriDS-3	7	1	5.13 ± 2.14	N/A
oriDS-4	7	0	8.71 ± 2.48	N/A
oriDS-5	2	1	5.01 ± 1.51	N/A
oriDS-6	1	0	4.79 ± 1.41	N/A
oriDS-7	5	1	6.01 ± 1.65	N/A
oriDS-8	2	0	2.19 ± 2.51	N/A

Table 7.1: Identified groups for NGTS flare stars in Orion with ages from Kounkel et al. (2018). $N_{stars,total}$ indicates the number of stars in our field associated with the respective group, while $N_{stars,flare}$ is the number of those stars which flared. We use the Age_{CMD} in our analysis and list Age_{HR} for reference.

(NGTS). These stars have an average age of 4.0 ± 0.2 Myr. The work presented in this chapter is based on Jackman et al., (submitted). We describe how the maximum energies of these flares compare with those from main sequence stars and present measurements of the average flare occurrence rate for early M stars. We also compare our occurrence rates to those for the Pleiades and Praesepe from Ilin et al. (2019) and predict upper limits on flare occurrence rates for nearby young associations.

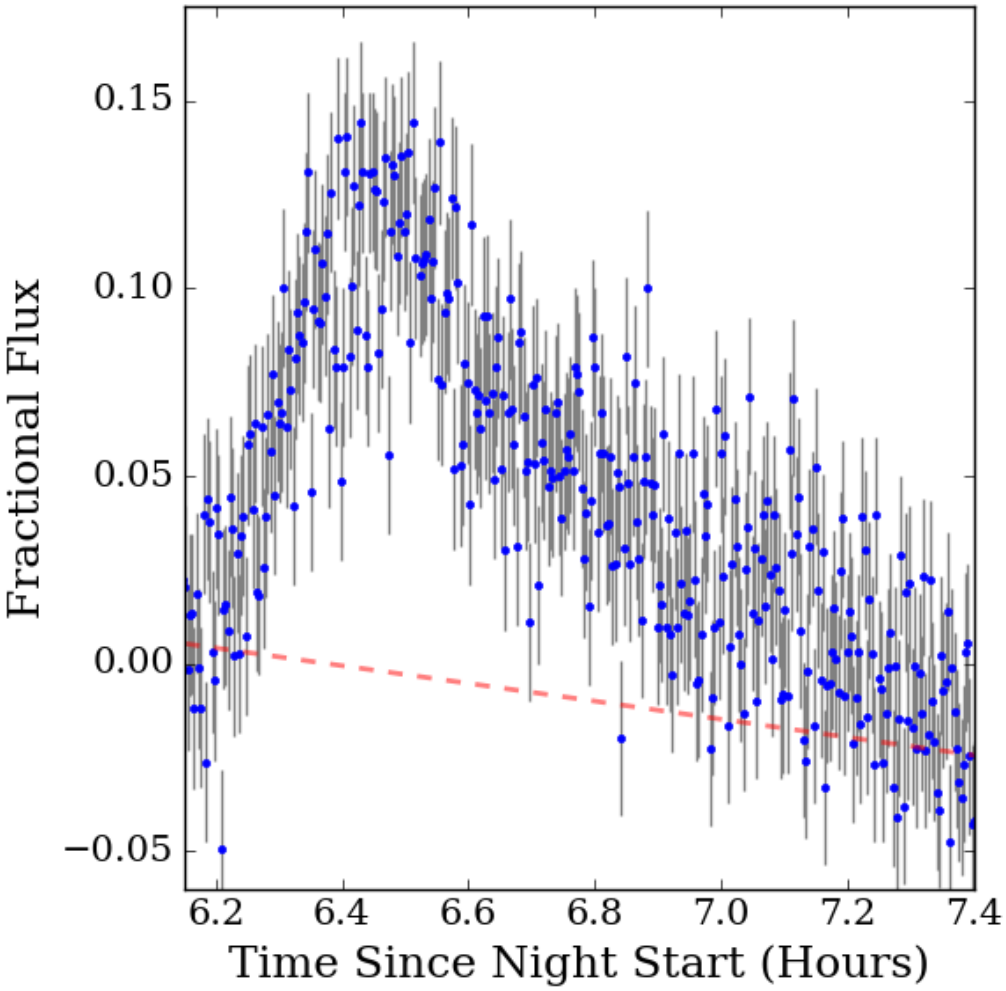

Figure 7.1: The lowest amplitude flare detected in our sample. The red dashed line is an example of the baseline used when calculating flare energies, as discussed in Sect. 7.2.3

.

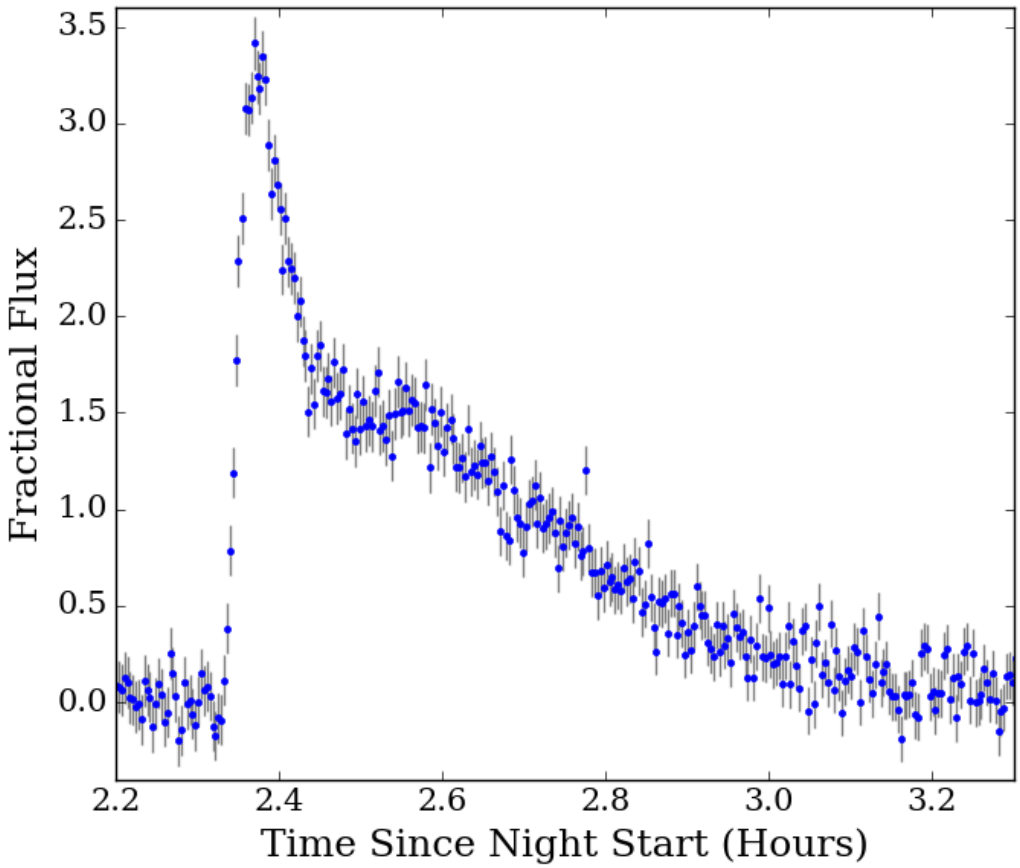

Figure 7.2: The highest amplitude flare detected in our sample.

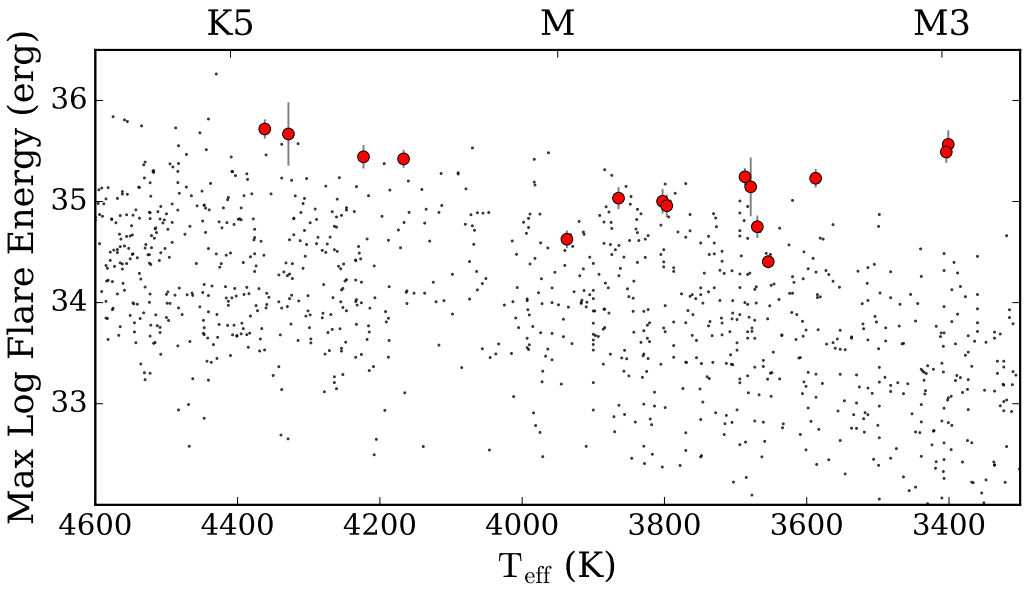

Figure 7.3: Maximum observed bolometric flare energy against effective temperature for our detected flaring stars. The red circles are the stars observed with NGTS. The underlying black points represent stars from Yang and Liu (2019), using *a posteriori* corrected long cadence *Kepler* observations. Note how the young Orion-associated sources appear to flare with the highest observed energies.

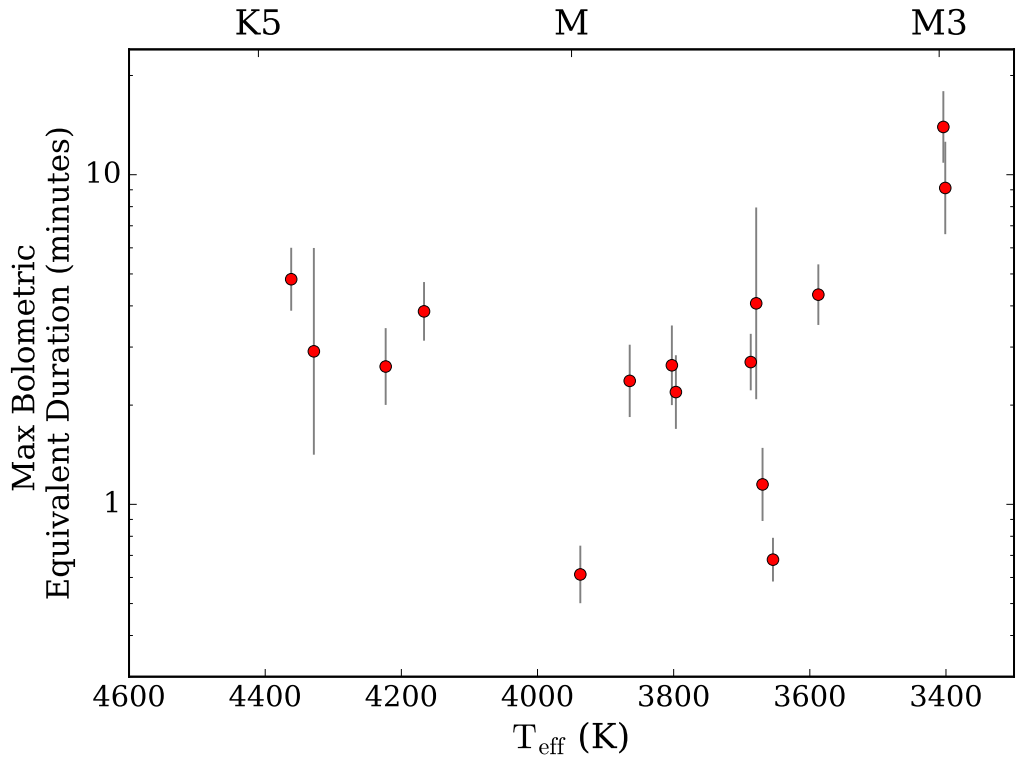

Figure 7.4: Maximum observed equivalent duration (in minutes) against effective temperature for our detected flaring stars. We have calculated this using our measured bolometric energies and dereddened SEDs from Sect. 7.2.2.

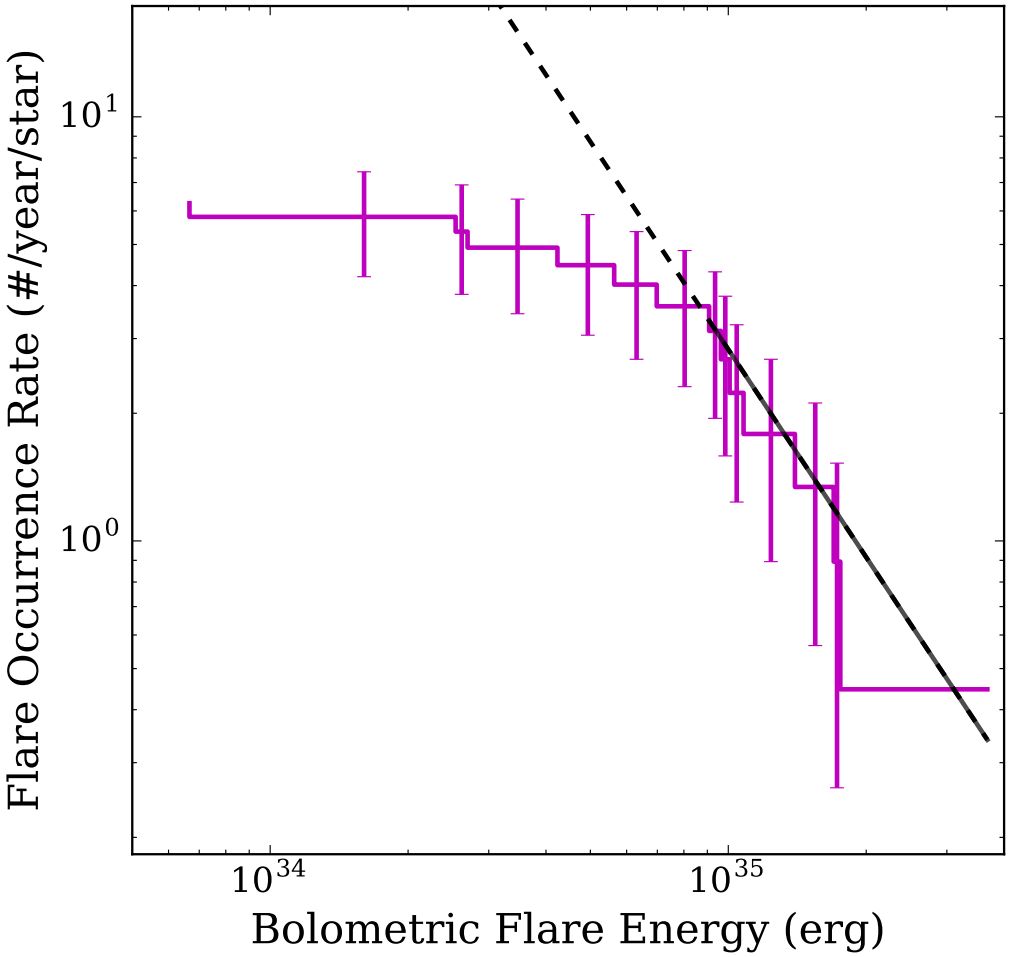

Figure 7.5: Flare occurrence rate with energy for 4.0 ± 0.2 Myr M stars associated with Orion. These stars were selected to have effective temperatures between 3400 and 3940K, approximately equivalent to M0-M3. The black solid line indicates the best fitting power law in our fitting range, while the dashed line is this fit extrapolated over our measured energy range. The best fitting parameters are $\alpha = 2.63 \pm 0.62$ ($\beta = -1.63 \pm 0.62$) and $C = 57.4 \pm 21.9$.

2MASS Source ID	Gaia DR2 Source ID	SpT	SpT Source	Energy (erg)	Amplitude	$t_{1/2}$ Duration (minutes)
2MASS J05354229-0701538	3016493834224711552	G3*	SED		0.16	49.50
2MASS J05331830-0701552	3016526991372177664	K6.5	SED	$2.77^{+0.85}_{-0.65} \times 10^{35}$	0.52	26.13
2MASS J05331830-0701552	3016526991372177664	K6.5	SED	$1.87^{+0.58}_{-0.44} \times 10^{35}$	0.35	8.28
2MASS J05265619-0706548	3016662403101758720	M0.5	SED	$9.64^{+3.44}_{-2.53} \times 10^{34}$	0.59	15.35
2MASS J05265619-0706548	3016662403101758720	M0.5	SED	$1.01^{+0.32}_{-0.24} \times 10^{35}$	0.84	10.87
2MASS J05312392-0709304	3016615055382512768	M0	SED	$4.24^{+0.94}_{-0.77} \times 10^{34}$	0.61	4.62
2MASS J05313541-0710550	3016614402547478784	M1.5	SED	$1.76^{+0.38}_{-0.31} \times 10^{35}$	0.46	21.63
2MASS J05314319-0717409	3016424736790884736	M1.5	SED	$1.40^{+1.33}_{-0.68} \times 10^{35}$	1.23	61.00
2MASS J05340216-0717390	3016505963212457088	M3.5	SED	$2.70^{+1.02}_{-0.74} \times 10^{34}$	0.71	1.70
2MASS J05340216-0717390	3016505963212457088	M3.5	SED	$6.98^{+2.51}_{-1.85} \times 10^{34}$	0.80	23.65
2MASS J05340216-0717390	3016505963212457088	M3.5	SED	$3.68^{+1.40}_{-1.01} \times 10^{35}$	1.10	48.87
2MASS J05362219-0716064	3016469060853517824	M1.5	K18		0.44[ll]	23.95
2MASS J05350988-0718045	3016457000585375872	M2	SED	$1.70^{+0.40}_{-0.32} \times 10^{35}$	1.03	8.55
2MASS J05351113-0719063	3016456210311395456	M1	SED	$9.08^{+2.66}_{-2.06} \times 10^{34}$	1.16	4.42
2MASS J05304799-0731323	3016413501156518400	K6	SED	$4.66^{+4.93}_{-2.40} \times 10^{35}$	0.30	21.80
2MASS J05304799-0731323	3016413501156518400	K6	SED	$2.12^{+1.86}_{-0.99} \times 10^{35}$	0.14	25.32
2MASS J05295834-0738069	3016388315468339200	K7	SED	$3.29^{+0.76}_{-0.62} \times 10^{34}$	0.27	2.52
2MASS J05295834-0738069	3016388315468339200	K7	SED	$2.64^{+0.60}_{-0.49} \times 10^{35}$	0.89	60.55

2MASS J05273635-0744059	3015081163645266304	M1.5	SED	$5.64^{+1.64}_{-1.27} \times 10^{34}$	0.38	8.60
2MASS J05295183-0750306	3016374743371710592	K5.5	SED	$5.22^{+1.28}_{-1.03} \times 10^{35}$	0.41	24.97
2MASS J05295183-0750306	3016374743371710592	K5.5	SED	$3.51^{+0.83}_{-0.67} \times 10^{35}$	0.25	19.45
2MASS J05295183-0750306	3016374743371710592	K5.5	SED	$9.93^{+2.64}_{-2.09} \times 10^{34}$	0.30	12.35
2MASS J05350942-0749194	3015674698061271936	M3.5	SED	$3.09^{+0.88}_{-0.68} \times 10^{35}$	3.47	7.68
2MASS J05293055-0754194	3014873669481488896	M1.5	SED	$2.54^{+0.42}_{-0.36} \times 10^{34}$	0.40	8.22
2MASS J05340890-0912415	3013742546894832384	M0.5	SED	$6.66^{+1.91}_{-1.49} \times 10^{33}$	0.56	1.28
2MASS J05340890-0912415	3013742546894832384	M0.5	SED	$1.08^{+0.31}_{-0.24} \times 10^{35}$	0.46	22.40

Table 7.2: Detected flares and their measured properties. The SpT Source column indicates the method used to obtain the spectral type for this source. 2MASS J05362219-0716064 was marked in our analysis as a blended source, so does not have a measured flare energy and its amplitude is marked as a lower limit (^{ll}). The spectral type of 2MASS J05354229-0701538 is marked with an asterisk for reasons discussed in Sect. 7.3. K18 indicates the spectral type is taken from Kounkel et al. (2018).

7.2 Observations

As described in Chapter 2, NGTS is a ground-based wide-field exoplanet survey located at the Paranal observatory in Chile. It consists of twelve 20 cm aperture telescopes with a total instantaneous field of view of 96 square degrees (Wheatley et al., 2018). These telescopes obtain full frame images with a 13 second cadence. During this work we noted that one field overlapped with the southern edge of the Orion complex. This serendipitous overlap provided an opportunity to measure the white-light flaring behaviour of some of the youngest stars on the sky. This field was NG0531-0826, which is centered on 05:31:24.5, -08:25:0.5. This field was observed with NGTS between the dates of 2015 Sept 23 and 2016 Apr 20, with a total of 138 nights of observation.

To search for flares we followed the two step method described in Sec. 2.2.

7.2.1 Association

To identify which stars are associated with groups within Orion we crossmatched all NGTS sources in the Orion-overlapping field with the catalogue of Kounkel et al. (2018). Using *Gaia* DR2 and APOGEE data, Kounkel et al. (2018) have mapped distinct groups within the Orion complex and their catalogue provides designations for Orion-associated stars and field stars. From this matching we identified 83 Orion-associated stars which fell within our field of view. Of these, 19 flared at least once during our observations. The smallest and largest amplitude detected flares are shown in Fig. 7.1 and Fig. 7.2. The groups and ages of the stars in our sample are shown in Tab. 7.1. We can see in Tab. 7.1 that these groups have similar ages. Consequently, we have considered them as a single group of pre-main sequence stars with an average age of 4.0 ± 0.2 Myr for the rest of this analysis. We calculate this age using the $\mathrm{Age_{CMD}}$ values from Kounkel et al. (2018), measured using colour-magnitude diagrams. These colour-magnitude diagrams used APOGEE and *Gaia* DR2 colours with PARSEC models to obtain absolute magnitudes for all young stars in their sample, including for young stellar objects without reliable parallaxes. The $\mathrm{Age_{HR}}$ values listed in Tab. 7.1 used the *Gaia* parallaxes and APOGEE measured effective temperatures to obtain luminosities, which were compared with PARSEC models to infer ages. The dependence on the effective temperature results in a small sample having $\mathrm{Age_{HR}}$ values, as seen in Tab. 7.1.

7.2.2 Stellar Properties

Eight sources in our sample had effective temperatures and angular sizes measured by Kounkel et al. (2018) from APOGEE spectra. We obtained the stellar radius for these sources by combining the angular sizes with their measured distances from the Bailer-Jones et al. (2018) catalogue, using parallaxes from *Gaia* DR2 (Gaia Collaboration et al., 2016a, 2018b).

For the rest of our sources we performed Spectral Energy Distribution (SED) fitting using the PHOENIX v2 spectral library (Allard et al., 2012). Each source was crossmatched with *Gaia* DR2, 2MASS (Skrutskie et al., 2006), APASS (Henden and Munari, 2014), SDSS (Aguado et al., 2019) and ALLWISE (Cutri and et al., 2014) to obtain broadband photometry. Distance information was obtained from the catalogue of Bailer-Jones et al. (2018). To account for the effects of reddening and extinction we fit for the extinction in magnitudes in the V band A_V, with $R_V = 3.1$ (Cardelli et al., 1989). R_V is the ratio of the total to selective extinction. We applied a Gaussian prior on the reddening based on the values measured from APOGEE spectra for the groups in Tab. 7.1 by Kounkel et al. (2018). The prior on the extinction A_V was 1.0 ± 0.6. This was chosen over existing *bayestars* dust maps of Green et al. (2019). We analysed the Green et al. (2019) *bayestars* dust maps for the stars in our sample and and many had poor likelihoods in their fits for the reddening and extinction. 63% had minimum χ^2 above 3 and 50% were above 5, the value used by Green et al. (2019) to rule out poor fits. We confirmed the poor fits in the reddening through comparison of the Green et al. (2019) maps with stars from the Kounkel et al. (2018) sample which had individually measured values of A_V from APOGEE spectra. Over half of the *bayestars* extinction values were twice that measured from APOGEE spectra and as such we did not use these maps.

To avoid the effects of blending between close neighbours influencing our SED fitting, we checked all sources for stars within $15''$ (the radius of an NGTS aperture) which might contribute significant levels of flux. Sources which had nearby neighbours at a distance which could contaminate catalogue photometry were flagged and did not have SED fits generated. Consequently, these stars (flaring and non-flaring) were not used in our analysis.

From our analysis we obtain 10 K type and 49 M type stars in our sample. The rest of the sample either had effective temperatures hotter than K spectral type, or did not have a reliable SED fit. Of the 19 flare stars, 3 were flagged as being blended with a nearby source and were not used to calculate energies. One of these 3 did however have an effective temperature available from Kounkel et al. (2018) and so the flare amplitude and duration are presented in Tab. 7.2.

7.2.3 Flare Properties

To calculate flare energies we follow an adjusted version of the method from Shibayama et al. (2013). The original method uses the observed flare amplitude to normalise an assumed 9000±500 K flare blackbody (e.g. Hawley and Fisher, 1992) relative to the quiescent stellar spectrum within the observed bandpass. The bolometric flare energy is measured by integrating over the renormalised 9000 K flare spectrum at each observed time. We have modified this method in our analysis to account for the effects of reddening on the observed flare and stellar spectrum (e.g. Paudel et al., 2018a), using the fitted values of A_V from Sect. 7.2.2. We used the average Milky Way extinction model from Cardelli et al. (1989) in this method.

When applying this method we assume the underlying quiescent stellar flux can be modelled with a linear baseline between the start and end of the flare. For the stellar properties and extinction we use the radii, effective temperatures and extinction values from Sect. 7.2.2.

We calculated the $t_{1/2}$ duration and amplitude for all flares, which are listed in Tab. 7.2. The $t_{1/2}$ duration is a commonly used measure of flare duration (e.g. Davenport et al., 2014) and is defined as the time spent above half of the flare amplitude. We calculated the amplitude following the method from Hawley et al. (2014) using $\frac{\Delta F}{F} = \frac{F-F_o}{F_o}$ where F_o is the out-of-flare flux. The value of F_o is calculated from the median of the flux preceding the start of the flare. As these parameters are independent of spectral type we have listed both $t_{1/2}$ and the amplitude for all flares in Tab. 7.2.

7.3 Results and Discussion

From an analysis of 83 stars associated with the Orion complex which were observed with NGTS we detected 25 flares from 19 stars. 16 of these 19 flare stars had effective temperatures from our SED fits or the Kounkel et al. (2018) sample, which corresponded to spectral types between G3 and M3. Nine stars were M spectral type and five were K. The observed flares had energies ranging between 6.7×10^{33} and 5.2×10^{35} ergs.

The presence of a flare from a G3 star in our sample is interesting due to the rarer nature of flares from these stars. However, investigating this source further shows it has previously been classified as K4 from low-resolution spectra by Pravdo and Angelini (1995) and as G8 from spectroscopic observations by Strom et al. (1990). Based on these observations it is likely this source is later in spectral type than our SED fitting suggests, however without an exact classification we have

chosen to leave it out from our energy analysis.

7.3.1 Maximum Flare Energy

In Fig. 7.3 we have compared the maximum flare energy of the Orion-associated stars to main sequence stars observed with *Kepler* from Yang and Liu (2019). The Orion-associated stars reside at the top of the energy envelope with maximum flare energies between 2.5×10^{34} and 5.2×10^{35} erg. These energies are similar to those observed by Flaccomio et al. (2018) from simultaneous mIR, optical and X-ray observations of pre-main sequence stars in the $\sim$3 Myr old NGC 2264 star forming region. Adopting the ratio between optical and X-ray energies (0.5-8.0 keV) from Flaccomio et al. (2018) we estimate that our maximum X-ray flare energies are between 1.4×10^{33} and 7.7×10^{34} erg.

Our measured bolometric flare energies, while similar to the Flaccomio et al. (2018) sample, reside towards the lower end of their measured energies. This is possibly due the Flaccomio et al. (2018) sample observing more stars in their study, approximately 500 stars for 60 days with *CoRoT*. Consequently this suggests that while our flares have high energies, they are not at the maximum limit of flare energies for these young stars. Further observations are therefore required to reach the maximum flare energy limit for 4 Myr old stars.

We have also measured the bolometric equivalent durations (EDs) for each flare in our sample, using the bolometric flare energies and our SED fits from Sect. 7.2.2. The ED is the amount of time required for the quiescent luminosity of the star to emit an energy equal to an observed flare (e.g. Hawley et al., 2014). We calculated our EDs by dividing the bolometric flare energies by the stellar bolometric luminosity. We calculated the bolometric luminosity by integrating in wavelength over our best fitting SED fits (after removing the effect of extinction) and multiplying by $4\pi d^2$ where d is the distance. Figure 7.4 shows the maximum bolometric ED for each star in our sample, showing that the equivalent durations have values up to 15 minutes, however the majority seem to have values of a few minutes. These values are lower than those reported for rare extreme flare events from other pre-main sequence stars (e.g. Paudel et al., 2018b; Jackman et al., 2019a, also Chapter 4) which can stretch to hours (although the ED is often reported for a single filter, which can change measured values, e.g. Hawley et al., 2014). This again suggests that our sample, while exhibiting high flare energies, has not reached the maximum flare energy limit for these young stars, something which will be probed in future studies with both NGTS and other surveys (e.g. *TESS*).

7.3.2 Flare Occurrence Rate of M stars

As discussed in Sect. 1.2.4, previous studies (e.g. Lacy et al., 1976; Hilton, 2011; Hawley et al., 2014) have shown that flares occur with a power law distribution in energy. This is typically written as

$$dN(E) \propto E^{-\alpha} dE \tag{7.1}$$

where E is the flare energy and α is the power law index. From this, a linear relation for the cumulative flare frequency distribution (CFFD) can be written as

$$\log \nu = C + \beta \log E \tag{7.2}$$

where ν is the cumulative flare frequency, C is a normalisation constant and $\beta = 1 - \alpha$ (Hawley et al., 2014).

In Fig. 7.5 we have plotted the average flare occurrence rate for stars in our Orion-associated sample. This was done for stars with effective temperatures between 3400 and 3940 K, representative of early-M (M0-M3) in spectral type (e.g. Pecaut and Mamajek, 2013). To fit the power law shown in Fig. 7.5 we have used the Python POWERLAW package (Alstott et al., 2014). POWERLAW is designed for fitting to heavy-tailed distributions and has been used previously for analysis of flare occurrence rates (e.g. Lin et al., 2019).

To make sure our sample is complete in terms of the detected flare energies we performed flare injection and retrieval tests, following a similar methodology to those employed by Davenport (2016) and Ilin et al. (2019). We first injected 1000 artificial flares into the lightcurves of every star in the 3400-3940 K sample. These flares were generated using the Davenport et al. (2014) empirical flare model. The amplitude of each flare was chosen randomly to have a value from between 0.01 and 4 times the median of an object's lightcurve. The $t_{1/2}$ timescale for each flare was chosen randomly from between 30 seconds and 70 minutes, to encompass the full range of detected flares. The automated detection method outlined in Sect. 7.2 was then run for each object on every night with an injected flare. We calculated the energies of each injected flare on a star-by-star basis, applying the energy calculation from Sect. 7.2.3 to the artificially generated flare. Injected flares were given a flag of 1 if they were automatically detected, 0 if not. The fraction of recovered flares as a function of energy was then calculated for each lightcurve.

The fraction of recovered flares was calculated as a function of energy for each star, using 20 bins in energy. Following Davenport (2016), the recovery fraction was

smoothed using a Wiener filter of three bins, to smooth any jumps and drops between bins. For each star we measured the flare energy at which at least 68 per cent of flares were retrieved, which was recorded for each star, as in Davenport (2016).

To ensure a complete sample when calculating the flare occurrence rate and when fitting the associated power law, an energy limit was used. For a given energy limit, only stars with a 68 per cent recovery fraction energy below this limit were used in calculating the average flare occurrence rate. This applied whether or not a star had any detected flares within its NGTS lightcurve. The power law itself, as seen in Fig. 7.5, was fit only to flares (from stars within this complete sample) with energies above the chosen energy limit. To select an energy limit, we tested a series of values to maximise the number of flares used in our power law fitting, without compromising the total number of stars used. Low energy limit values would exclude most stars (and their flares) from use in the flare occurrence rate fitting. Very high energy limit values, while including all stars in the sample, would have very few flares to fit the power law to. We found a value of 9×10^{34} erg best satisfied this compromise and was thus used as our energy limit.

29 stars in our 3400-3940 K sample (40 stars in total) had 68 per cent recovery fraction energies below our limit of 9×10^{34} erg, and were used in our occurrence rate analysis. 10 of these stars had a detected flare. 8 flares (from 7 stars) had energies above the 9×10^{34} erg, to which we fitted a power law distribution. 6 flares (from 5 stars) had energies below this threshold and were not used in our power law fitting. Some stars in our sample flared more than once, with energies above and below 9×10^{34} erg.

From fitting our sample above this threshold we measured $\alpha = 2.63 \pm 0.62$ ($\beta = -1.63 \pm 0.62$) and $C = 57.4 \pm 21.9$. An α value greater than 2 indicates that lower energy flares dominate the total flare energy distribution.$\alpha > 2$ has also been noted in previous works as a requirement for low energy flares to heat Solar and stellar coronas (e.g. Doyle and Butler, 1985; Parker, 1988; Güdel et al., 2003). With our sample we are not able to confidently rule out high energy flares dominating the distribution, although we note the possibility that flares may be a significant contributor to the quiescent magnetic environment of young M stars. This value is also consistent with the value of $\alpha = 2.2 \pm 0.2$ measured by Caramazza et al. (2007) for X-ray flares from Orion associated 0.1-0.3 $M_{\odot}$ stars.

From our power law fit in Fig. 7.5 we estimate that the average M0-M3 star in the Orion complex flares with an energy above 10^{35} erg once every 130 days. This is almost 1000 times the rate measured by Lin et al. (2019) for main-sequence M dwarfs using *K2* observations, highlighting how active these pre-main sequence

sources are.

Previous studies have noted there may be a break off and steepening in the power law towards the highest flare energies (e.g. Chang et al., 2015). We note the possibility that this is the regime we have measured and that α at lower energies may be less than what we have measured. More observations of white-light flares from Orion-associated stars will allow us to further constrain α at the highest energies, by increasing the number of stars and rare high energy flares observed.

Comparison with other clusters

Ilin et al. (2019) found from *K2* observations that between the 125 Myr Pleiades (M44) and 630 Myr Praesepe (M45) open clusters the average flare occurrence rate (for bolometric energies above 3.4×10^{33} erg) of early-M stars decreases quicker than the Skumanich $t^{-1/2}$ law. They found that the activity of hotter stars drops the quickest, tying in with previous observations of hotter stars spinning down more quickly than their cooler counterparts (e.g. Amard et al., 2019). The rate of this decrease, if it tracks with the change in surface rotation, is also expected to be variable at young ages (e.g. Barnes, 2010). We can use our sample to try and extend this work for the highest energy flares down to stars of 4 Myr in age.

To measure the change in the flare rate for energies above 1×10^{35} erg we have split our sample into the 3500-3750 K and 3750-4000 K groups from Ilin et al. (2019). In each subset we have measured the rates directly by linearly interpolating the measured average occurrence rates to the value at 1×10^{35} erg. To calculate the rates for the Pleiades and Praesepe we first multiplied the *Kepler* bandpass occurrence rates measured by Ilin et al. (2019) by 3.1 to convert them to bolometric energies, using the conversion factor from Paudel et al. (2018b). We then extrapolated these power laws to 1×10^{35} erg. These values are presented in Tab. 7.3.

For the 3500-3750 K sample the the measured average occurrence rate of flares above 1×10^{35} ergs changes from 2.0 to 7.3×10^{-2} and then to 6.5×10^{-2} from Orion, through the Pleiades, to Praesepe. The change in this measured rate consequently changes from -1.6×10^{-2} to -1.73×10^{-5} flares/year/Myr. For the 3750-4000 K sample the rate of flares above 1×10^{35} ergs changes from 2.3 to 2.5×10^{-1} and then to 3.5×10^{-2}. The change in this measured rate consequently changes from -1.7×10^{-2} to -4.22×10^{-4} flares/year/Myr. We can see from Tab. 7.3 that at the youngest ages the hotter stars appear to be more active than their cooler counterparts throughout the first 125 Myr. However, we can also see that, from the change in the measured occurrence rate between open clusters, the observed activity of hotter stars (above 1×10^{35} ergs) is dropping at a faster rate in the first 600 Myr

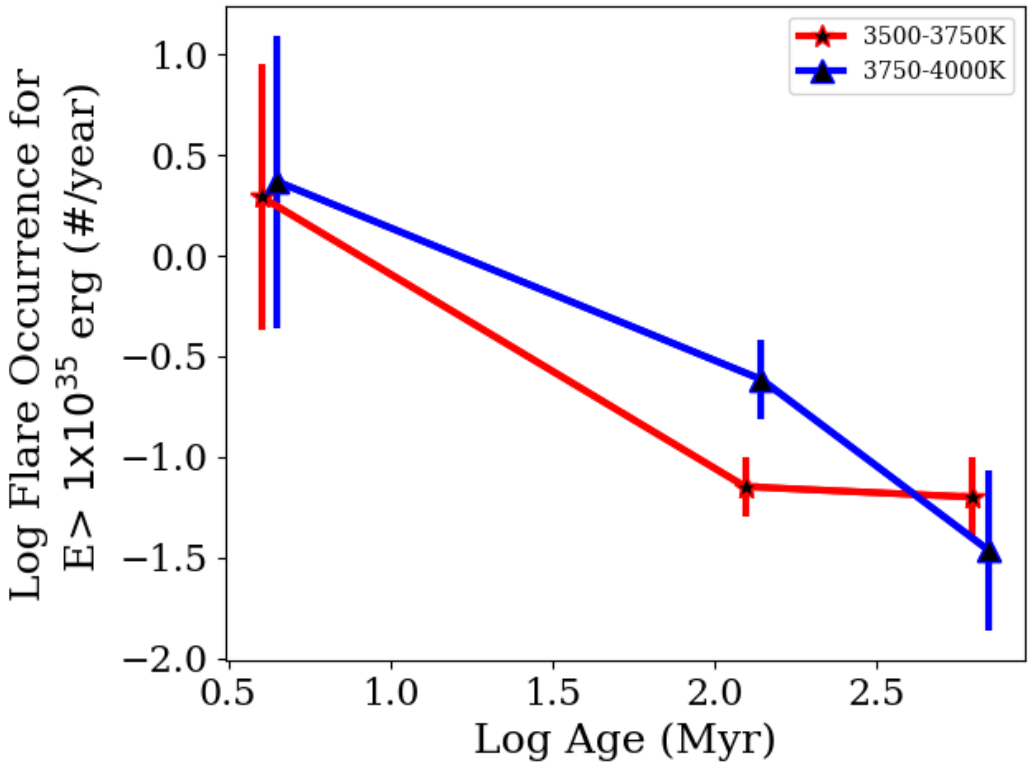

Figure 7.6: Change in the average flare occurrence rate above 1×10^{35} erg with age. We have offset the 3750-4000 K sample by 0.1 for clarity. Note the log-log scaling of the plot and the changing gradient with age, in contrast to that predicted by Davenport et al. (2019).

than cooler, lower mass, stars. We also note that the change of occurrence rate of flares above 1×10^{35} ergs is not linear in log-log space, in disagreement with the model derived by Davenport et al. (2019), in particular for the 3500-3750 K sample. This is shown in Fig. 7.6. However, as noted in Sect. 7.3.2 flaring behaviour may change at the energies we are probing. These changes (e.g. breaks in power laws; Chang et al., 2015) were not included in the Davenport et al. (2019) model and as such a strict comparison may not be valid. We also note that the number of flares in our 3500-3750 K and 3750-4000 K Orion subsets are 5 and 6 respectively. The small sample size in these subsets combined with the extrapolation of the Ilin et al. (2019) occurrence rates means the values in Tab. 7.3 should be used with caution.

By combining these datasets together and linearly interpolating in age we can predict limits of the average flare rates for M stars in other clusters and associations. Some predictions for nearby young clusters are given in Tab. 7.3 for E>1×10^{35} ergs. We find that up to 70 Myr both samples can flare up to once a year with an energy

Cluster	Age (Myr)	3500-3750 K (#/year)	n_{flares}	3750-4000 K (#/year)	n_{flares}
Orion*	4	2.0	5	2.3	6
Beta Pic	24	1.7	5, e	2.0	6, e
Carina	45	1.3	5, e	1.6	6, e
Pleiades ‡	125	7.3×10^{-2}	e	2.5×10^{-1}	e
AB Doradus	149	7.3×10^{-2}	e	2.4×10^{-1}	e
Praesepe ‡	630	6.5×10^{-2}	e	3.5×10^{-2}	e

Table 7.3: Predictions of the average flare occurrence rate for some nearby young associations, for flare energies above 1×10^{35} erg. We have calculated these by combining our measured occurrence rates with those extrapolated from Ilin et al. (2019). For intermediate age clusters we linearly interpolated between measured samples. The * indicates these are our measured values for Orion. The ‡ indicates these are the Ilin et al. (2019) extrapolated values for Pleiades and Praesepe, again shown for reference. Also shown are the number of flares from our NGTS analysis used in the estimates of the flare rate. "e" indicates an estimate uses the extrapolated Ilin et al. (2019) occurrence rates. Quoted ages for groups other than Orion, Pleiades and Praesepe come from Bell et al. (2015).

above 1×10^{35} ergs.

Formation of the radiative zone

With an age of 4 Myr, the pre-main sequence early M stars in Orion are fully convective. The magnetic fields of pre-main sequence early-M stars have previously been characterised as being large scale and axisymmetric. As these early M stars evolve they will contract and spin up, something which seems counter-intuitive to a decrease in flare rates. However, during this process they begin to form an inner radiative zone which is separated from the outer convective regions by a tachocline. From the Baraffe et al. (2015) models this radiative zone reaches its maximum size at roughly 100 Myr. The formation of the radiative zone is expected to be accompanied by a change in the stellar magnetic topology and has previously been linked to observed decreases in the coronal X-ray luminosity (Gregory et al., 2016), which is often used as a tracer of magnetic activity (e.g. Wright et al., 2011). The transition between fully and partially convective interiors for main sequence stars may also be linked to a decrease in the magnetic field strength, something previously noted by Mullan et al. (2018) (see Fig. 14 of Moutou et al., 2017). It may be that the formation of a radiative zone for early M stars causes a drop in flare energies

and rates between 4 and 125 Myr. After 125 Myr the average flare behaviour would more closely follow the decay of stellar rotation. Further observations of stars in Orion to confirm our measured occurrence rates along with further observations of open clusters or moving groups with intermediate ages will be needed to test this hypothesis for early M stars (e.g. the 30-40 Myr Octans group; Murphy and Lawson, 2015) and other spectral types.

7.4 Conclusions

In this chapter we have presented the detection of high energy white-light stellar flares from 4.0 ± 0.2 Myr pre-main sequence stars associated with the Orion Complex. These are some of the youngest stars to have a measured white-light flare occurrence rate. By combining our measured occurrence rates with those in the literature we identified that the rate of change in the average flare occurrence rate above 1×10^{35} ergs for M dwarfs is variable with time, changing rapidly during the 100 Myr before slowing. This result is similar to findings for surface rotation. We have used these rates to predict the flare occurrence rates for nearby moving groups.

Chapter 8

Conclusions and Future Work

"Exit, pursued by a flare."

William Shakespeare, *A Winter's Tale*
(adapted by J. A. G. Jackman)

In this thesis I have presented the results of searching for stellar flares in data from the Next Generation Transit Survey. These detections showed how ground based photometry can rival that available from space and push our understanding of stellar activity. These detections also led to the discovery of an ultra-short period transiting brown dwarf, NGTS-7Ab.

In Chapter 3, I described the detection of two superflares from a G star. This was the first time G star superflares had been detected from the ground using a CCD. The 13 second cadence of NGTS was used to fit a new empirical flare model incorporating a Gaussian heating pulse with a two-timescale exponential decay. The continuous model made use of the flare rise, a region usually ignored in flare studies due to the difficulty in resolving it. The flare had a rise timescale of 2.5 minutes and an energy of $2.5^{+0.3}_{-0.2} \times 10^{35}$ erg. The star itself was measured to have a rotation period of 59 hours, with changing starspot modulation.

In Chapter 4, I presented the detection of a giant stellar flare from a pre-main sequence M star. This flare was one of the most energetic ever seen from an M star, with an energy of above $3.2^{+0.4}_{-0.3} \times 10^{36}$ erg. In the flare peak we identified multi-mode quasi-periodic pulsations formed of two statistically significant periods of approximately 320 and 660 seconds. This flare is one of the largest amplitude events to exhibit such pulsations. The shorter period mode is observed to start after a short-lived spike in flux lasting around 30 seconds, which would not have been resolved in the short cadence modes of either *Kepler* or *TESS*. This work made use of Solar techniques to analyse the detected pulsations, showing how such

methods can be used in stellar cases to identify the possible MHD modes at work.

In Chapter 5, I presented the first detection of a white-light flare from an L2.5 dwarf. This flare was detected from a targeted search for stellar flares from faint low mass stars in the NGTS full frame images. This search focused on red stars which were too faint to be detected in quiescence with NGTS, however they became detectable while flaring. This flare had an energy of $3.4^{+0.9}_{-0.7} \times 10^{33}$ erg, making it an order of magnitude more energetic than the Carrington event. The flare had an amplitude of Δm_{NGTS}= -6, corresponding to an inferred amplitude of ΔV $\sim$-10. With a spectral type of L2.5 this star was also the coolest star to show a white-light flare to date, pushing the regime of known flaring stars. This event also showed that magnetic activity as traced by stellar flares continues down to this spectral type, despite previous studies showing that these stars have weak or diminished chromospheres. Estimating the emitting area of the visible disc of the star showed approximately 35-40 per cent was dominated by flare emission. The flare had an equivalent duration of 1.8 hours. This work showed how full frame images in exoplanet surveys can be used to detect the highest energy flares from low mass stars, despite the stars themselves being extremely faint in quiescence.

In Chapter 6, I presented the detection of NGTS-7Ab, a high mass brown dwarf transiting an M dwarf with a period of 16.2 hours. This is the shortest period transiting brown dwarf around a main or pre-main sequence star to date and the fifth transiting an M star host. The system was initially noted for multiple flares within the NGTS lightcurve, after which transits on a 16.2 hour period were noticed. The M star host (NGTS-7A) has an age of roughly 50 Myr and is in a state of spin-orbit synchronisation, which we attribute to tidal interaction with the brown dwarf acting to spin up the star. The host star also has an M star companion (NGTS-7B) at a separation of 1.13 arcseconds with very similar proper motion and systemic velocity, suggesting the NGTS-7 system is a hierarchical triple. The combination of tidal synchronisation and magnetic braking is expected to drive ongoing decay of the brown dwarf orbit. We estimated that NGTS-7Ab has a remaining lifetime of 5-10 Myr in its current state, after which the inspiral of the brown dwarf is not able to replace the angular momentum lost through magnetic braking and it falls inwards.

In Chapter 7, I presented a study of white-light flares detected from pre-main sequence stars associated with the Orion complex. I was able to show that the maximum flare energies observed were greater than those observed for main sequence stars, consistent with expectations of young stars being more magnetically active than their older counterparts. However, from comparison with previous studies of

pre-main sequence stars (both in and out of Orion) it was likely that we had not observed the absolute upper limit of flare energies. I used the NGTS observations of flaring and non-flaring Orion-associated stars to measure the average flare occurrence rate for 4 Myr M0-M3 stars. Combining this occurrence rate with those measured by Ilin et al. (2019) for the Pleiades and Praesepe open clusters I was able to show a non-linear decrease with age for the occurrence rate of flares above 1×10^{35} erg. I was also able to show that flares above 1×10^{35} erg may occur more than once per year up to ages of 70 Myr. I also noted that the formation of the radiative zone in young stars may act to reduce their flaring activity during the first 100 Myr of their evolution, something to be tested in future works.

8.1 Future Work

All the results presented in this thesis have arisen from searching for stellar flares in the NGTS datasets. Each result has emerged from a larger survey and drawn attention to itself, demanding further investigation. I intend to focus on the larger survey in the immediate future, using the methods outlined in Chapter 2. I will probe how flare parameters such as energy, amplitude and duration vary with stellar properties. One aspect I am particularly interested in is how the average flare occurrence rates vary with spectral type for main sequence stars. This analysis will use the methods from Chapter 7 to combine data from both flaring and non-flaring stars. This can then be compared with habitability studies (e.g. Tilley et al., 2017; Rimmer et al., 2018) to see whether stellar flares can help or hinder life on exoplanets around the average main sequence star.

Another aspect of this is how does the maximum flare energy change with spectral type, such as discussed for Orion-associated stars in Chapter 7. An example of this for the full sample is shown in Fig. 8.1, showing an apparent decrease of maximum flare energy with effective temperature. This is consistent with results from previous studies (e.g. Davenport, 2016) and we still find mid-late M stars can flare with energies well above the Carrington event. The bottom left section in Fig. 8.1 is unpopulated due to selection effects related to our sensitivity to low amplitude flares. Lower energy flares typically have lower amplitudes, which may below a certain point will not trigger the automated flare detection thresholds described in Chap. 2. The cut off on the right hand side, at mid-M spectral type, is due to the I=16 magnitude limit imposed on the normal NGTS survey. Low luminosity mid and late-M stars are more likely to fall below this magnitude limit, meaning they are not probed as thoroughly as earlier spectral types in Fig. 8.1. It is unclear whether

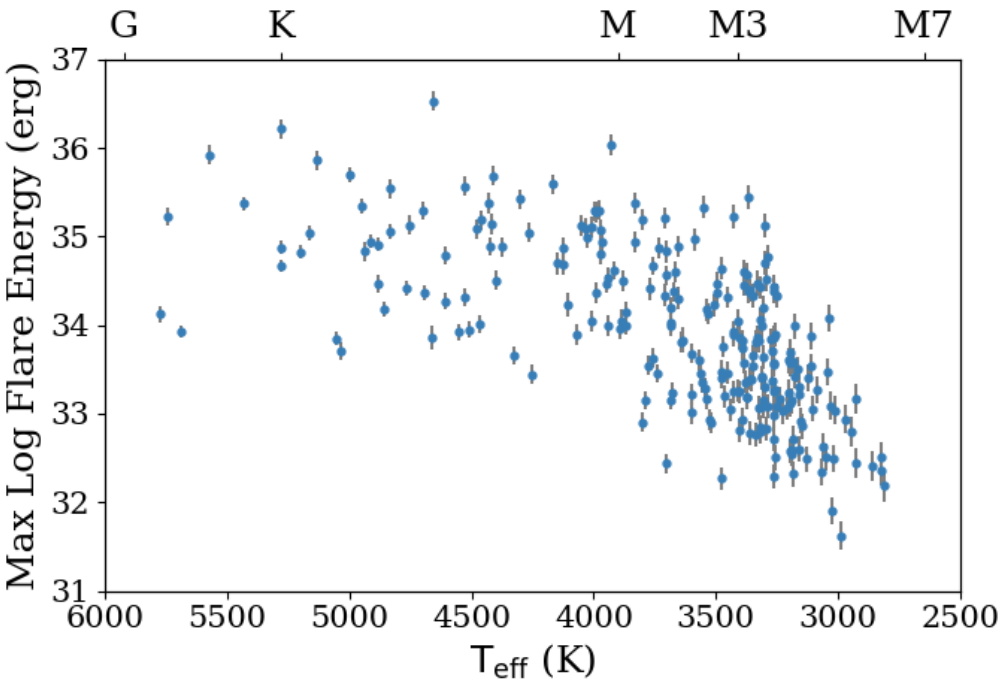

Figure 8.1: Maximum observed flare energy against effective temperature for flaring stars detected with NGTS.

we have reached a maximum energy cut off in Fig. 8.1 (e.g. Wu et al., 2015). By combining measured flare occurrence rates with the total NGTS observing duration we can study this and confirm both whether this maximum energy cut off and whether the observed decrease in the maximum flare energy in the upper envelope is real.

Along with these aspects I will study how flare occurrence relates to starspot phase for a larger sample, similar to the work performed in Chapters 3 and 6. This will be compared with similar studies from *Kepler* (Roettenbacher and Vida, 2018), *K2* (Doyle et al., 2018) and *TESS* (Doyle et al., 2019). I am interested to see whether any other systems show a starspot-flare relation similar to NGTS-7Ab, or whether flares occur uniformly with starspot phase, similar to the mentioned previous studies.

Further along in the future I intend to revisit the NGTS-7 system. The purpose of this will be to improve the constraints on the system parameters. The first way of doing this will be to constrain the dayside temperature of NGTS-7Ab further through follow-up observations of the secondary eclipse. In Sect. 6.3.6 I was able to use our fitted NGTS eclipse to limit the brown dwarf temperature to a value

below 3200 K (assuming a geometric albedo of 0). Targeted follow-up observations of the secondary eclipse will hopefully reveal changes in depth with wavelength which can be used to constrain the dayside temperature further. By more precisely measuring the dayside temperature of NGTS-7Ab (in turn measuring a luminosity), and combining it with the measured radius and mass, we will be able to better compare this object to brown dwarf evolutionary models (e.g. Baraffe et al., 2015). These models are currently untested by mass, radii and temperature observations between 10 Myr and 3 Gyr. We will be able to use NGTS-7Ab to try and better constrain these models at $\approx$ 50 Myr. If NGTS-7Ab is not well explained by these models, then we will be able to test the level of discrepancy, such as was performed for the transiting brown dwarf CWW 89Ab, which was found to be 16 times more luminous than models suggested (Beatty et al., 2018).

As the secondary eclipse is shallow (the depth is on the order of millimag), detecting the eclipse from observations of single events will be challenging. Telescopes with large collecting areas will be required to maximise any chance of detecting the eclipse. As we know that NGTS-7Ab emits more flux towards longer wavelengths, another way of maximising our chance of detecting the eclipse is to observe using near-infrared filters (e.g. J, H, K). The predicted eclipse depths for NGTS-7Ab in the J, H and K filters are shown in Fig. 8.2. These values were calculated using the PHOENIX v2 models for NGTS-7A and NGTS-7B, and the BT-Settl models for NGTS-7Ab. Predicting the eclipse depth for the two geometric albedos considered in Sect. 6.3.6 (A_g=0, 0.5) we can see the minimum eclipse depth would be about 0.15 per cent, assuming dilution from NGTS-7B. An undiluted version of Fig. 8.2 is available in Fig. 8.3, showing the minimum eclipse depth increases to 0.26 per cent. From Fig. 8.2 we can also see that the measured eclipse depth between filters changes, due to the changing brown dwarf temperature associated with the changing albedo along with the changing flux from NGTS-7A itself. It is possible that these eclipse depths could be measured using SOFI on the ESO 3.6m New Technology Telescope (NTT) at La Silla (Moorwood et al., 1998), or SPARTAN on the 4.1m SOAR telescope at Cerro Pachon (Loh et al., 2012). If near-infrared observations are not available, an alternative way of distinguishing between the two scenarios would be to try in different optical filters. Simulated eclipse depths in u', g', r', i' and z' filters are shown in Fig. 8.4. An undiluted version is shown in Fig. 8.5. While the eclipse depths for these filters are generally less than or similar to that observed with NGTS (with the exception of z'), they may still be possible with dedicated follow up using an instrument such as ULTRACAM on the NTT (Marsh and Dhillon, 2006).

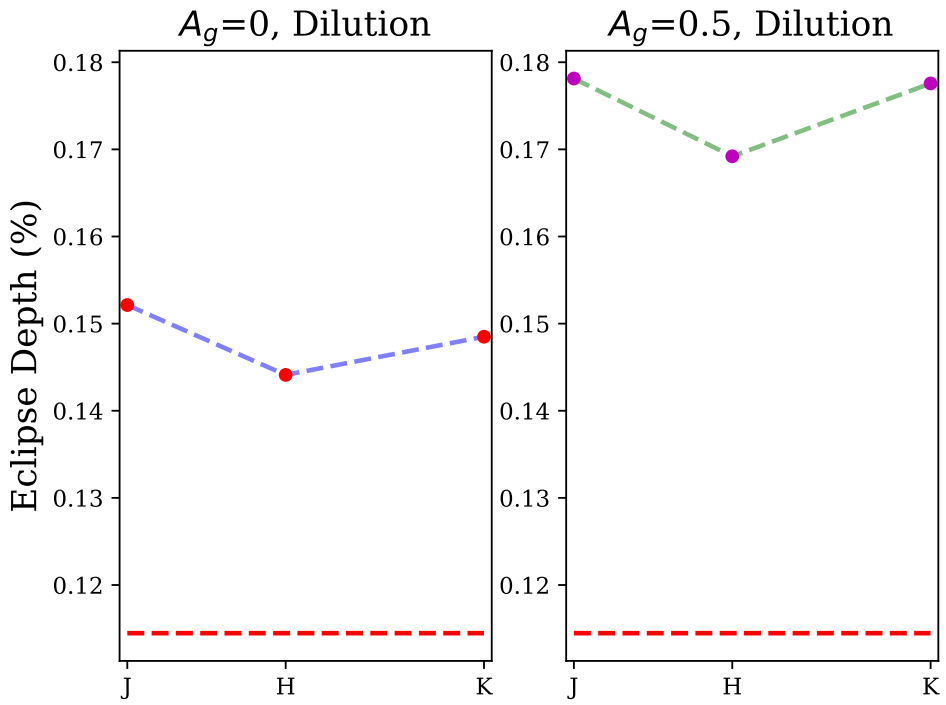

Figure 8.2: Predicted NGTS-7Ab eclipse depths in the J, H and K_s bands, assuming photometry includes flux from both NGTS-7A and NGTS-7B. The left and right hand panels are for the A_g=0 and A_g=0.5 respectively. The dashed red line is the value in the NGTS filter, taken from our fitted model in Chapter 6.

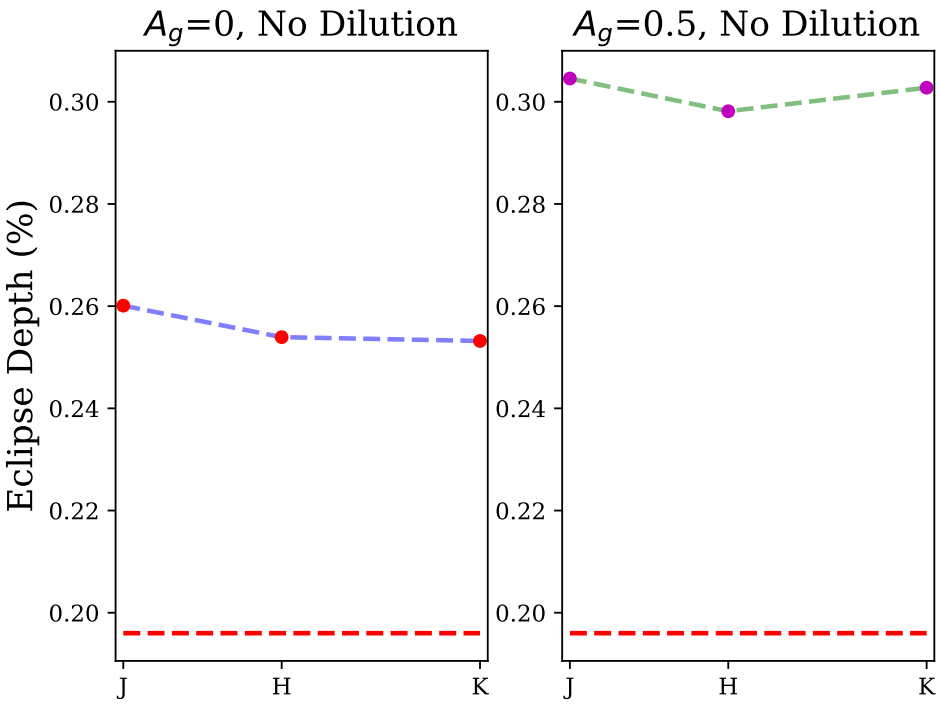

Figure 8.3: Predicted NGTS-7Ab eclipse depths in the J, H and K_s bands, assuming photometry includes flux from just NGTS-7A. The left and right hand panels are for the A_g=0 and A_g=0.5 respectively. The dashed red line is the value in the NGTS filter, taken from our fitted model in Chapter 6.

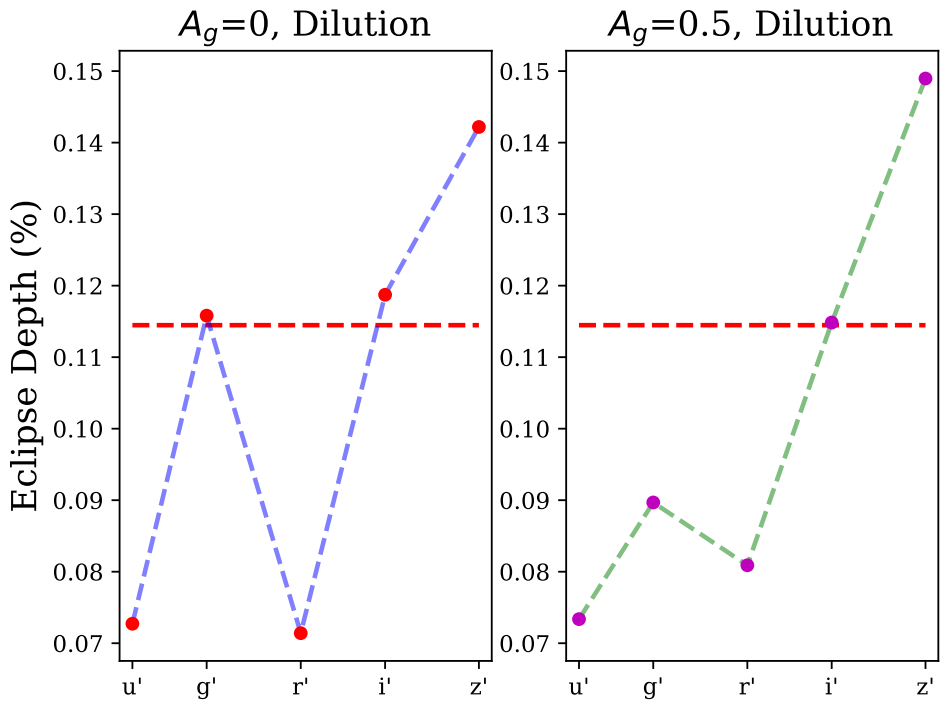

Figure 8.4: Predicted NGTS-7Ab eclipse depths in the u', g', r', i' and z' bands, assuming photometry includes flux from both NGTS-7A and NGTS-7B. The left and right hand panels are for the A_g=0 and A_g=0.5 respectively. The dashed red line is the value in the NGTS filter, taken from our fitted model in Chapter 6.

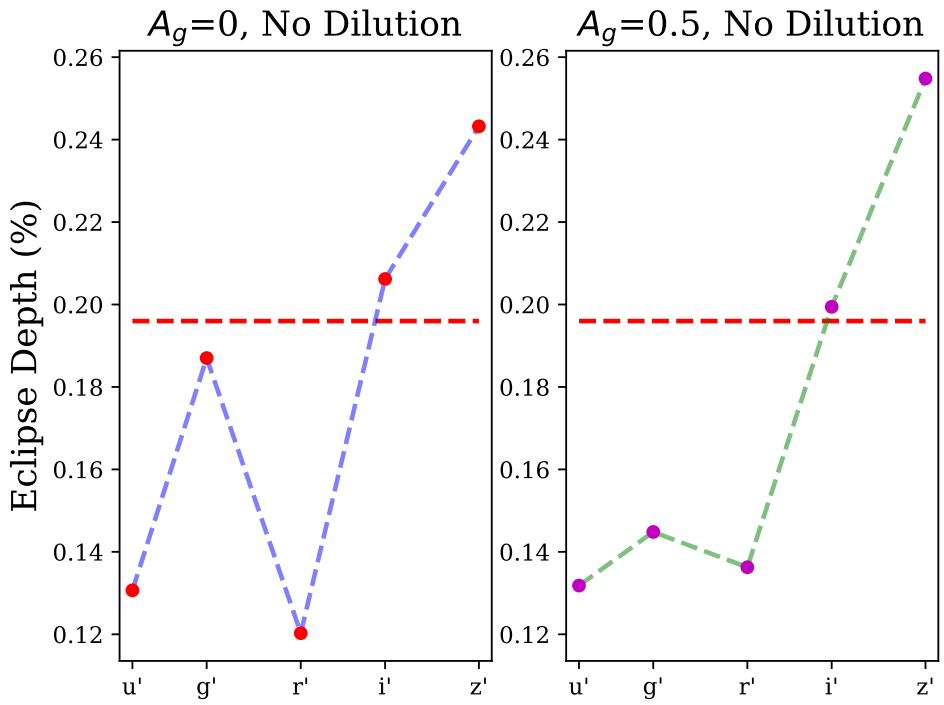

Figure 8.5: Predicted NGTS-7Ab eclipse depths in the u', g', r', i' and z' bands, assuming photometry includes flux from just NGTS-7A. The left and right hand panels are for the A_g=0 and A_g=0.5 respectively. The dashed red line is the value in the NGTS filter, taken from our fitted model in Chapter 6.

In late 2020 improved astrometry and photometry for NGTS-7A and NGTS-7B will available from *Gaia* EDR3. One of the main ambiguities currently in our understanding of the NGTS-7 system is whether NGTS-7A and NGTS-7B are truly at the same distance. *Gaia* astrometry showed that NGTS-7A failed the recommended quality checks due to significant astrometric excess noise, while NGTS-7B passed but with non-zero astrometric excess noise. High astrometric excess noise is a sign that the single source astrometric solution in *Gaia* DR2 has failed. We noted in Chapter 6 that this may be due to the close (1.13 $''$) proximity of NGTS-7A and NGTS-7B may have resulted in confusion between their respective photocentres. Along with this, the majority of scans (over 75 per cent) were taken along the position angle separating NGTS-7A and NGTS-7B, which may have contributed to the confusion between photocentres. *Gaia* EDR3 will contain 34 months of data (*Gaia* DR2 had 22 months) and as such will have both more scans and scan angles for the NGTS-7 system. When these data become available I intend to use the improved astrometry to further constrain the distances of NGTS-7A and NGTS-7B and confirm whether or not they are at the same distance and associated. Assuming the astrometry from *Gaia* EDR3 for both stars passes any recommended astrometric filters, I will use both distances as priors in new SED fitting to obtain accurate radius measurements for both stars. The new SED fits will in turn be used to update the properties of the NGTS-7 system, in particular the system age and stellar masses.

If the *Gaia* EDR3 astrometry does not pass recommended quality checks, then one option will be to wait for the full *Gaia* DR3 release (currently anticipated in the second half of 2021). *Gaia* DR3 will contain the astrometry and photometry from *Gaia* EDR3, however will also contain information on non-single stars, which may highlight remaining underlying issues with the *Gaia* astrometry. Of course, failing this I can hopefully wait until the full 60 months of data from *Gaia* DR4!

8.2 Looking forward

For both white-light flares and transiting brown dwarfs there is currently a wealth of data coming in from both the ground and from space which will be used to push this research area further. As mentioned in Chapter 1 and hopefully proven in this thesis, ground-based wide-field surveys such as NGTS and EvryScope are able to detect flares in high cadence full frame images. These surveys will continue to detect many more flares in their data. To date, NGTS has been taking data for five years and has 100 fields (and counting) that can be searched for flares and transiting brown dwarfs. For stars brighter than $I = 16$, I have looked at 24 of these

fields so far to search for flares. Each field contains approximately ten thousand stars brighter than $I = 16$, which can be seen in quiescence and used to measure occurrence rates, study flare-starspot relations and test existing and new empirical flare models. Along with these, hopefully more examples of substructure, such as those discussed in thesis, will be detected.

On top (or rather below) these "bright" sources there are tens of thousands of faint red stars per field which can be used to study the maximum flare energies for faint ultracool dwarfs, similar to that presented in Chapter 5. I have looked at 22 fields so far for these faint star flares.

TESS has recently been approved for its extended mission, which will begin in July 2020 (Ricker et al., 2015). The *TESS* data has already been proven as useful for stellar flare studies (e.g. Doyle et al., 2019), however there is currently a lot of data that has not been analysed. I intend to utilise *TESS* data to push the open cluster flare work presented in Chapter 7 further, by studying a greater number of open clusters. This will hopefully expand our understanding of flare evolution to a greater range of ages, along with pushing to a wider range of spectral types (e.g. mid-K to mid-M). Along with this, there is the possibility of studying common proper motion white dwarfs and M dwarfs to constrain flare energies and occurrence rates at older ages. By studying how the flare activity changes as a function of time across a wide range of ages constraints can be placed on the time-integrated energy output of flares, something which will be of use for studies of exoplanet habitability and their atmospheres. The extended mission will change the full frame image cadence to 10 minutes, an improvement on the 30 minute cadence used in the nominal mission. The improved cadence mode means that a greater number of flares can be detected. Along with this, those that are detected will be subject to less smearing than at a 30 minute cadence. This in turn should improve the accuracy of resultant flare amplitude, duration and energy measurements. However, while the 10 minute cadence will be an improvement relative to the nominal mission, it may not be enough to detect flares from the faintest stars (such as in Chapter 5), which may only be visible to *TESS* for durations of 10-20 minutes. For flares from the coolest stars, studies using *TESS* may still be limited to the nearest sources.

The nominal mission of *TESS* has already turned out multiple transiting brown dwarfs on a range of spectral types (Šubjak et al., 2019; Carmichael et al., 2020). The extended mission will be an asset in discovering these systems. For known systems the extra transits at a long baseline will provide improved measured ephemerides. For candidate systems, the extra transit signals will help improve their signal-to-noise and the confidence of detection. Along with this, further observations

can help to constrain any present out-of-transit modulation and its evolution in time (e.g. changing spot modulation).

Looking further ahead, in this decade the Vera C. Rubin telescope is expected to come online and begin taking data for the Legacy Survey of Space and Time (LSST) (Ivezić et al., 2019). This 10-year survey, expected to begin in 2023, is estimated to cover 25,000 deg^2 of the southern sky. The telescope will have an effective aperture of 6.7m and will take observations in six broad optical filters (*ugrizy*). 18,000 deg^2 of the sky coverage will be through the main survey. The main survey will take back-to-back pairs of 15 second exposures in each visit of a field, before moving onto a neighbouring field. Two visits are planned in a night which according to Ivezić et al. (2019) should be separated by 15-60 minutes, with each field being revisited on average every three nights. The wide sky coverage and the magnitude depth of LSST in the main survey means it will be well positioned to detect large numbers of extremely rare high energy flares, particularly on ultracool dwarfs. Flares which are detected in the main LSST program will likely be similar in temporal resolution to those currently being detected by ASASSN, namely having sparse time cadence. This is contrast to the *TESS* extended mission which will have a better time cadence, but on much fewer stars. The limited LSST cadence will limit various aspects of analysis, however previous studies using ASASSN data (Schmidt et al., 2019) have already shown how the use of empirical flare models can recover some of the information.

The remainder of the 25,000 deg^2 will be allocated to dedicated programs. One dedicated program of note for flare studies will be the proposed "mini-surveys" and "deep drilling fields" (DDF). The exact makeup of these min-surveys and DDFs are currently under debate, so their exact impact on flaring is currently unknown. However, depending on the chosen strategy, the chosen mini-surveys and DDFs may offer improved shorter exposure times and improved cadences for carefully selected patches of sky. An increased number of visits will mean we will be more likely to detect a flare from any given ultracool star within the mini-survey. In addition, any detected flares in the mini-survey may be better characterised than from the main survey alone, due to an improved cadence. Single fields targeted for a series of exposures on a single night may also be able to detect faint transiting or eclipsing systems, although if these systems are faint the prospect for follow up is limited.

Looking *even further* ahead in time, the *PLATO* telescope is expected to be launched in 2026 (Rauer et al., 2014). With a field of view of approximately 2200 deg^2 and a 25 second cadence for all targeted stars means that *PLATO* will be of use to stellar flare and transiting brown dwarf research. *PLATO* observations

will allow for large scale studies of flare substructure such as the QPPs shown in Chapter 4. Importantly as well, the 25 second cadence will allow us to measure flare properties such as energy, amplitude and duration without worrying about smearing effects. The cadence and precison of the *PLATO* lightcurves will allow us to study both the highest energy events (in exquisite detail) and the more common low energy flares. This in turn will hopefully result in some of the most accurately measured flare occurrence rates, for both single stars and entire spectral types. In the time between now and when *PLATO* launches it is likely laboratory experiments designed to constrain the effects of flares on habitability will have yielded important new results, which flare studies will be able to build on. Along with this, for G and K type stars *PLATO* will observe starspot modulation and Solar-like oscillations, which will be used for asteroseismic studies. These observations will help push forward studies on how flares of different energy correlate with other signs of stellar activity. However, due to limitations in telemetry, *PLATO* is not expected to provide full frame mages. This will limit the use of *PLATO* in studying the largest flares from faint ultracool dwarfs.

It should also go without saying that *PLATO* will likely discover many more transiting brown dwarfs on all sorts of stars. These discoveries will range from ultra-short period objects, similar to NGTS-7Ab, to longer period ($\approx$ 100 days) objects. These discoveries, when combined with those expected from *TESS* (e.g. Carmichael et al., 2020), will be pivotal in studying brown dwarf formation and evolution pathways.

Between now and the launch of *PLATO* I expect there to be many more spectroscopic studies of flares performed, to better understand the mechanisms at work. As discussed in Chap. 1, the current use of a 9000 K blackbody for calculating the energies is, while useful and rooted in observation, an assumption that needs improving. By obtaining spectra of a greater number of flares, we will be able to improve our understanding of the flare physics and how we calculate flare energies from single-filter photometry (e.g. from *PLATO*). Spectra of flares from ultracool dwarfs should also be obtained, so that we can test whether the standard flare model holds down towards the brown dwarf boundary and better understand ultracool dwarf activity. This is work I intend to pursue in the near future, by targeting late M stars with both multi-colour photometry and spectroscopy. One of the difficulties to date in such studies is the unpredictability of flares. Known active stars have to be chosen and repeatedly observed in the hopes of obtaining flare spectra (e.g. Kowalski et al., 2013), limiting the sample of stars with such measurements. Alerts from surveys such as LSST (and even NGTS) may be able to overcome this, by

providing notification of high amplitude flare events in progress that can be rapidly targeted for follow up. Multi-colour flare photometry can also be used to follow up these alerts. Follow up spectroscopy and photometry will both help us to better understand the changing flare temperatures (and physics in general) at work, along with how these high energy events compare to those we see on the Sun.

One of the advantages of NGTS compared to other surveys has been its high cadence. With it we have been able to detect short duration flares and resolve the flare rise and substructure (Chap. 3 and 4), helping to pioneer new empirical flare models and study the local magnetic environments of flares. To be able to fully resolve flares and push forward our understanding of the mechanisms at work, high cadence observations are a necessity. Without high cadence observations, flare phases become blurred together. This may result in composite spectra (or multi-colour photometry) of the impulsive rise and gradual decay, making it difficult to identify the full range of flare temperatures. In future photometric studies high cadences are required to accurately measure flare durations and amplitudes, along with capturing lower energy events. Along with this, future studies of substructure such as quasi-periodic pulsations will benefit from high cadence studies.

Stellar flares and transiting brown dwarfs are both fast moving fields of research. New discoveries and detections are being published all the time, using a wide range of different telescopes, instruments and techniques. Current and upcoming missions and surveys are unlikely to let this pace slack in the future. It's a field I've been lucky to be a part of/ stumble in to and one I hope to remain part of for the foreseeable future.

Bibliography

1997. *The HIPPARCOS and TYCHO catalogues. Astrometric and photometric star catalogues derived from the ESA HIPPARCOS Space Astrometry Mission*, volume 1200 of *ESA Special Publication*.

Abrevaya X.C. et al., 2020. *MNRAS*, 494(1):L69–L74.

Aguado D.S. et al., 2019. *ApJS*, 240(2):23.

Allard F., 2016. In C. Reylé, J. Richard, L. Cambrésy, M. Deleuil, E. Pécontal, L. Tresse, and I. Vauglin, editors, *SF2A-2016: Proceedings of the Annual meeting of the French Society of Astronomy and Astrophysics*, 223–227.

Allard F. and Hauschildt P.H., 1995. *ApJ*, 445:433.

Allard F., Homeier D., and Freytag B., 2012. *Philosophical Transactions of the Royal Society of London Series A*, 370:2765–2777.

Allred J.C. et al., 2006. *ApJ*, 644(1):484–496.

Alstott J., Bullmore E., and Plenz D., 2014. *PLoS ONE*, 9(1):e85777.

Amard L. et al., 2019. *A&A*, 631:A77.

Andrews J.J., Chanamé J., and Agüeros M.A., 2017. *MNRAS*, 472:675–699.

Andrews J.J., Chanamé J., and Agüeros M.A., 2018. *Research Notes of the American Astronomical Society*, 2:29.

Andrews S.M. et al., 2013. *ApJ*, 771:129.

Anfinogentov S. et al., 2013. *ApJ*, 773:156.

Anglada-Escudé G. et al., 2016. *Nature*, 536:437–440.

Ansdell M. et al., 2016. *ApJ*, 816(2):69.

Ansdell M. et al., 2017. *AJ*, 153:240.

Antonucci E. and Dennis B.R., 1983. *Sol. Phys.*, 86(1-2):67–77.

Arenou F. et al., 2018. *A&A*, 616:A17.

Armitage P.J. and Bonnell I.A., 2002. *MNRAS*, 330(1):L11–L14.

Armstrong D.J. et al., 2016. *Nature Astronomy*, 1:0004.

Aschwanden M., 2006. *Physics of the solar corona: an introduction with problems and solutions*. Springer Science & Business Media.

Aschwanden M.J., Dennis B.R., and Benz A.O., 1998. *ApJ*, 497:972–993.

Aschwanden M.J., Xu Y., and Jing J., 2014. *ApJ*, 797:50.

Aschwanden M.J. et al., 2000. *ApJ*, 535:1047–1065.

Asplund M. et al., 2009. *ARA&A*, 47:481–522.

Astropy Collaboration et al., 2013. *A&A*, 558:A33.

Auchère F. et al., 2016. *ApJ*, 825:110.

Ayres T.R., 2019. In O. Engvold, J.C. Vial, and A. Skumanich, editors, *The Sun as a Guide to Stellar Physics*, 27 – 57. Elsevier. ISBN 978-0-12-814334-6.

Babcock H.W., 1961. *ApJ*, 133:572.

Bailer-Jones C.A.L. et al., 2018. *AJ*, 156:58.

Bakos G. et al., 2004. *PASP*, 116(817):266–277.

Bakos G.Á. et al., 2002. *PASP*, 114(799):974–987.

Balona L.A., 2012. *MNRAS*, 423:3420–3429.

Balona L.A., 2015. *MNRAS*, 447:2714–2725.

Balona L.A., 2019. *MNRAS*, 490(2):2112–2116.

Balona L.A. et al., 2015. *MNRAS*, 450:956–966.

Balthasar H. and Woehl H., 1980. *A&A*, 92(1-2):111–116.

Baluev R.V., 2008. *MNRAS*, 385:1279–1285.

Baraffe I. et al., 2003. *A&A*, 402:701–712.

Baraffe I. et al., 2015. *A&A*, 577:A42.

Barker A.J. and Ogilvie G.I., 2009. *MNRAS*, 395:2268–2287.

Barnes S.A., 2010. *ApJ*, 722(1):222–234.

Basri G., Marcy G.W., and Graham J.R., 1996. *ApJ*, 458:600.

Bayliss D. et al., 2017. *AJ*, 153:15.

Bayliss D. et al., 2018. *MNRAS*, 475:4467–4475.

Beatty T.G. et al., 2018. *AJ*, 156(4):168.

Becklin E.E. and Zuckerman B., 1988. *Nature*, 336(6200):656–658.

Bell C.P.M., Mamajek E.E., and Naylor T., 2015. *MNRAS*, 454(1):593–614.

Bell C.P.M. et al., 2013. *MNRAS*, 434:806–831.

Benedict G.F. et al., 2016. *AJ*, 152:141.

Benz A.O. and Güdel M., 2010. *Annual Review of Astronomy and Astrophysics*, 48:241–287.

Bessell M.S. and Brett J.M., 1988. *PASP*, 100:1134–1151.

Bessell M.S., Castelli F., and Plez B., 1998. *A&A*, 333:231–250.

Boller T. et al., 2016. *A&A*, 588:A103.

Bolmont E. et al., 2012. *A&A*, 544:A124.

Bonomo A.S. and Lanza A.F., 2012. *A&A*, 547:A37.

Borucki W. et al., 2009. In F. Pont, D. Sasselov, and M.J. Holman, editors, *Transiting Planets*, volume 253 of *IAU Symposium*, 289–299.

Borucki W.J. et al., 2010. *Science*, 327:977.

Boteler D.H., 2019. *Space Weather*, 17(10):1427–1441.

Bouchy F. et al., 2011. *A&A*, 525:A68.

Boyajian T.S. et al., 2012. *ApJ*, 757:112.

Boyajian T.S. et al., 2017. *ApJ*, 845:178.

Bradshaw S.J. and Hartigan P., 2014. *ApJ*, 795:79.

Bramich D.M. et al., 2008. *MNRAS*, 386:887–902.

Bressan A. et al., 2012. *MNRAS*, 427:127–145.

Brown D.J.A. et al., 2011. *MNRAS*, 415:605–618.

Bryson S.T. et al., 2013. *PASP*, 125:889.

Buccino A.P., Lemarchand G.A., and Mauas P.J.D., 2007. *Icarus*, 192:582–587.

Burgasser A.J. et al., 2015. *The Astrophysical Journal Supplement Series*, 220:18.

Candelaresi S. et al., 2014. *ApJ*, 792:67.

Canfield R.C. et al., 1987. *Nature*, 326(6109):165–166.

Cannon A.J. and Pickering E.C., 1901. *Annals of Harvard College Observatory*, 28:129–P.6.

Cantat-Gaudin T. and Anders F., 2020. *A&A*, 633:A99.

Caramazza M. et al., 2007. *A&A*, 471:645–654.

Cardelli J.A., Clayton G.C., and Mathis J.S., 1989. *ApJ*, 345:245.

Carmichael H., 1964. *A Process for Flares*, volume 50, 451.

Carmichael T.W., Latham D.W., and Vand erburg A.M., 2019. *AJ*, 158(1):38.

Carmichael T.W. et al., 2020. *arXiv e-prints*, arXiv:2002.01943.

Carrington R.C., 1859. *MNRAS*, 20:13–15.

Casewell S.L. et al., 2018. *MNRAS*, 481(2):1897–1907.

Cassak P.A. and Shay M.A., 2007. *Physics of Plasmas*, 14(10):102114.

Castenholz R.W. and Garcia-Pichel F., 2012. In *Ecology of Cyanobacteria II*, 481–499. Springer.

Chabrier G. and Baraffe I., 1997. *A&A*, 327:1039–1053.

Chabrier G. and Baraffe I., 2000. *ARA&A*, 38:337–377.

Chabrier G., Baraffe I., and Plez B., 1996. *ApJ*, 459:L91.

Chabrier G. and Küker M., 2006. *A&A*, 446(3):1027–1037.

Chabrier G. et al., 2000. *ApJ*, 542(1):464–472.

Chang S.W., Byun Y.I., and Hartman J.D., 2015. *ApJ*, 814:35.

Charbonneau D. et al., 2005. *ApJ*, 626(1):523–529.

Charbonneau P., 2010. *Living Reviews in Solar Physics*, 7(1):3.

Cho I.H. et al., 2016. *ApJ*, 830:110.

Choi J. et al., 2016. *ApJ*, 823:102.

Chrimes A.A., Stanway E.R., and Eldridge J.J., 2020. *MNRAS*, 491(3):3479–3495.

Chromey F.R., 2010. *Place, time, and motion*, 6097. Cambridge University Press.

Chubb T.A. et al., 1957. *Nature*, 179(4565):861–862.

Claret A., 2000. *A&A*, 363:1081–1190.

Cody A.M. et al., 2014. *AJ*, 147(4):82.

Colombo S. et al., 2019. *A&A*, 624:A50.

Colón K.D., Morehead R.C., and Ford E.B., 2015. *MNRAS*, 452(3):3001–3009.

Coppejans R. et al., 2013. *Publications of the Astronomical Society of the Pacific*, 125:976.

Crause L.A. et al., 2016. In *Ground-based and Airborne Instrumentation for Astronomy VI*, volume 9908 of *Society of Photo-Optical Instrumentation Engineers (SPIE) Conference Series*, 990827.

Crosby N.B., Aschwanden M.J., and Dennis B.R., 1993. *Sol. Phys.*, 143:275–299.

Cutri R.M. and et al., 2014. *VizieR Online Data Catalog*, 2328.

Damiani C. and Díaz R.F., 2016. *A&A*, 589:A55.

Damiani C. and Lanza A.F., 2015. *A&A*, 574:A39.

Davenport J.R.A., 2016. *ApJ*, 829:23.

Davenport J.R.A., Hebb L., and Hawley S.L., 2015. *ApJ*, 806:212.

Davenport J.R.A. et al., 2012. *ApJ*, 748(1):58.

Davenport J.R.A. et al., 2014. *ApJ*, 797(2):122.

Davenport J.R.A. et al., 2019. *ApJ*, 871(2):241.

David T.J. et al., 2019. *ApJ*, 872(2):161.

Dawson K.S. et al., 2013. *AJ*, 145:10.

de la Reza R. and Pinzón G., 2004. *AJ*, 128:1812–1824.

De Luca A. et al., 2020. *A&A*, 634:L13.

Deleuil M. et al., 2008. *A&A*, 491(3):889–897.

Dickey J.M. and Lockman F.J., 1990. *ARA&A*, 28:215–261.

Dobbs-Dixon I., Lin D.N.C., and Mardling R.A., 2004. *ApJ*, 610(1):464–476.

Dolla L. et al., 2012. *ApJ*, 749:L16.

Dopita M. et al., 2007. *Ap&SS*, 310:255–268.

Dotter A., 2016. *ApJS*, 222:8.

Douglas S.T. et al., 2017. *ApJ*, 842:83.

Douglas S.T. et al., 2019. *ApJ*, 879(2):100.

Doyle J.G. and Butler C.J., 1985. *Nature*, 313(6001):378–380.

Doyle L. et al., 2018. *MNRAS*, 480:2153–2164.

Doyle L. et al., 2019. *MNRAS*, 2115.

Drake A.J., 2003. *ApJ*, 589(2):1020–1026.

Dupuy T.J. and Liu M.C., 2012. *The Astrophysical Journal Supplement Series*, 201:19.

Edwin P.M. and Roberts B., 1983. *Sol. Phys.*, 88:179–191.

Ehrenreich D. et al., 2015. *Nature*, 522(7557):459–461.

Eigmüller P. et al., 2018. *MNRAS*, 480:3864–3870.

Eisenstein D.J. et al., 2011. *AJ*, 142(3):72.

Emslie A.G. et al., 2012. *ApJ*, 759(1):71.

Epstein C.R. and Pinsonneault M.H., 2014. *ApJ*, 780(2):159.

Escude G.A., 2018. *Journal of the American Association of Variable Star Observers (JAAVSO)*, 46(2):191.

Esteves L.J., De Mooij E.J.W., and Jayawardhana R., 2015. *ApJ*, 804:150.

Estrela R. and Valio A., 2018. *Astrobiology*, 18(11):1414–1424.

Evans D.W. et al., 2018. *A&A*, 616:A4.

Fabricius C. et al., 2016. *A&A*, 595:A3.

Favata F. et al., 2005. *ApJS*, 160:469–502.

Feigelson E.D., 2010. *Proceedings of the National Academy of Science*, 107:7153–7157.

Fisher G.H., 1989. *ApJ*, 346:1019.

Fitzpatrick E.L., 1999. *PASP*, 111(755):63–75.

Flaccomio E. et al., 2018. *A&A*, 620:A55.

Fleming T.A. et al., 1995. *ApJS*, 99:701.

Fletcher L. and Hudson H.S., 2008. *ApJ*, 675(2):1645–1655.

Fontanive C. et al., 2019. *MNRAS*, 641.

Fontenla J.M. et al., 2016. *ApJ*, 830(2):154.

Foreman-Mackey D. et al., 2013. *PASP*, 125:306.

Foukal P.V., 2007. *The Chromosphere and Corona*, chapter 9, 277–317. John Wiley Sons, Ltd. ISBN 9783527602551.

Foullon C. et al., 2005. *A&A*, 440(2):L59–L62.

Gagné J. et al., 2018. *ApJ*, 856:23.

Gaia Collaboration et al., 2016a. *A&A*, 595:A2.

Gaia Collaboration et al., 2016b. *A&A*, 595:A1.

Gaia Collaboration et al., 2018a. *A&A*, 616:A10.

Gaia Collaboration et al., 2018b. *A&A*, 616:A1.

Gaia Collaboration et al., 2019. *A&A*, 623:A110.

Garcia H.A., 1994. *Sol. Phys.*, 154(2):275–308.

Ge J. et al., 2008. *The Multi-object APO Radial-Velocity Exoplanet Large-area Survey (MARVELS)*, volume 398 of *Astronomical Society of the Pacific Conference Series*, 449.

Giles H.A.C., Collier Cameron A., and Haywood R.D., 2017. *MNRAS*, 472:1618–1627.

Gillen E. et al., 2017. *ApJ*, 849:11.

Gilliland R.L. et al., 2010. *ApJ*, 713:L160–L163.

Gillon M. et al., 2017. *Nature*, 542:456–460.

Girardi L. et al., 2004. *A&A*, 422:205–215.

Gizis J.E. et al., 2013. *ApJ*, 779:172.

Gizis J.E. et al., 2015. *ApJ*, 813:104.

Gizis J.E. et al., 2017a. *ApJ*, 838:22.

Gizis J.E. et al., 2017b. *ApJ*, 845:33.

Goddard C.R. et al., 2016. *A&A*, 585:A137.

Golden L.M., 2013. *Experiment 17 Blackbody Radiation*, 473–498. Springer New York, New York, NY. ISBN 978-1-4614-3311-8.

Gonzalez W. and Parker E., 2016. *Astrophysics and Space Science Library*, 427:10–1007.

Gray D.F., 2005. *The Observation and Analysis of Stellar Photospheres*. Cambridge University Press, 3 edition.

Green G.M. et al., 2019. *arXiv e-prints*, arXiv:1905.02734.

Gregory S.G., Adams F.C., and Davies C.L., 2016. *MNRAS*, 457(4):3836–3858.

Grether D. and Lineweaver C.H., 2006. *ApJ*, 640:1051–1062.

Grieves N. et al., 2017. *MNRAS*, 467:4264–4281.

Gruber D. et al., 2011. *A&A*, 533:A61.

Gryciuk M. et al., 2017. *Sol. Phys.*, 292:77.

Güdel M. et al., 2003. *ApJ*, 582(1):423–442.

Guillot T. et al., 2014. In *EAS Publications Series*, volume 65, 327–336.

Günther M.N. et al., 2017. *MNRAS*, 472:295–307.

Günther M.N. et al., 2018. *MNRAS*, 478:4720–4737.

Günther M.N. et al., 2020. *AJ*, 159(2):60.

Guo Z. et al., 2018. *ApJ*, 852(1):56.

Haisch B.M., 1983. *X-ray observations of stellar flares*, volume 102 of *Astrophysics and Space Science Library*, 255–268.

Halbwachs J.L. et al., 2000. *A&A*, 355:581–594.

Hale G.E. et al., 1919. *ApJ*, 49:153.

Hansen C.J. and Kawaler S.D., 1994. *Stellar Interiors. Physical Principles, Structure, and Evolution.*

Hanser F.A. and Sellers F.B., 1996. *Design and calibration of the GOES-8 solar x-ray sensor: the XRS*, volume 2812 of *Society of Photo-Optical Instrumentation Engineers (SPIE) Conference Series*, 344–352.

Hartman Z.D. and Lépine S., 2020. *ApJS*, 247(2):66.

Hastings W.K., 1970.

Hatzes A.P. and Rauer H., 2015. *ApJ*, 810(2):L25.

Hawley S.L. and Fisher G.H., 1992. *ApJS*, 78:565–598.

Hawley S.L. et al., 2003. *ApJ*, 597:535–554.

Hawley S.L. et al., 2014. *ApJ*, 797:121.

Hayashi C., 1961. *PASJ*, 13:450–452.

Heinzel P. and Shibata K., 2018. *ApJ*, 859(2):143.

Heinzel P. et al., 2017. *ApJ*, 847(1):48.

Henden A. and Munari U., 2014. *Contributions of the Astronomical Observatory Skalnate Pleso*, 43:518–522.

Hennebelle P. and Chabrier G., 2013. *ApJ*, 770(2):150.

Henyey L.G., Lelevier R., and Levée R.D., 1955. *PASP*, 67(396):154.

Hertzsprung E., 1911. *Publikationen des Astrophysikalischen Observatoriums zu Potsdam*, 22:A1–A40.1.

Heyner D., Glassmeier K.H., and Schmitt D., 2012. *ApJ*, 750:133.

Hilton E.J., 2011. *The Galactic M Dwarf Flare Rate*. Ph.D. thesis, University of Washington.

Hirayama T., 1974. *Sol. Phys.*, 34(2):323–338.

Hodgson R., 1859. *MNRAS*, 20:15–16.

Hodžić V. et al., 2018. *MNRAS*, 481:5091–5097.

Hoeg E. et al., 1997. *A&A*, 323:L57–L60.

Høg E. et al., 2000. *A&A*, 355:L27–L30.

Houdebine E.R. et al., 2017. *ApJ*, 837:96.

Howard W.S. et al., 2019a. *ApJ*, 881(1):9.

Howard W.S. et al., 2019b. *arXiv e-prints*, arXiv:1907.10735.

Howell S.B. et al., 2014. *Publications of the Astronomical Society of the Pacific*, 126:398.

Howell S.B. et al., 2016. *ApJ*, 831(1):27.

Hudson H.S., Wolfson C.J., and Metcalf T.R., 2006. *Sol. Phys.*, 234(1):79–93.

Huensch M., Schmitt J.H.M.M., and Voges W., 1998. *A&AS*, 132:155–171.

Hunt-Walker N.M. et al., 2012. *PASP*, 124:545.

Husser T.O. et al., 2013. *A&A*, 553:A6.

Ilgner M. and Nelson R.P., 2006. *A&A*, 455:731–740.

Ilin E. et al., 2019. *A&A*, 622:A133.

Inglis A.R. and Nakariakov V.M., 2009. *A&A*, 493:259–266.

Inglis A.R. et al., 2016. *ApJ*, 833:284.

Irwin J. et al., 2009. In F. Pont, D. Sasselov, and M.J. Holman, editors, *Transiting Planets*, volume 253 of *IAU Symposium*, 37–43.

Irwin J. et al., 2010. *ApJ*, 718:1353–1366.

Irwin J.M. et al., 2018. *AJ*, 156(4):140.

Ishikawa S.n. et al., 2017. *Nature Astronomy*, 1:771–774.

Ivezić Ž. et al., 2019. *ApJ*, 873:111.

Jackman J.A.G. et al., 2018. *MNRAS*, 477:4655–4664.

Jackman J.A.G. et al., 2019a. *MNRAS*, 482(4):5553–5566.

Jackman J.A.G. et al., 2019b. *MNRAS*, 485(1):L136–L140.

Jackman J.A.G. et al., 2019c. *MNRAS*, 489(4):5146–5164.

Jackson A.P., Davis T.A., and Wheatley P.J., 2012. *MNRAS*, 422(3):2024–2043.

Jackson R.J. and Jeffries R.D., 2014. *MNRAS*, 441:2111–2123.

Janes K. and Adler D., 1982. *ApJS*, 49:425–446.

Jansen F. et al., 2001. *A&A*, 365:L1–L6.

Jeffries R.D., 2014. In *EAS Publications Series*, volume 65 of *EAS Publications Series*, 289–325.

Jeffries R.D. and Oliveira J.M., 2005. *MNRAS*, 358(1):13–29.

Jehin E. et al., 2011. *The Messenger*, 145:2–6.

Jiang Y. et al., 2012. *ApJ*, 744(1):50.

Jing J. et al., 2016. *Scientific Reports*, 6:24319.

Johnson J.A. et al., 2011. *ApJ*, 730:79.

Johnstone C.P. and Güdel M., 2015. *A&A*, 578:A129.

Johnstone C.P. et al., 2012. *MNRAS*, 419:29–38.

Jordi C. et al., 2010. *A&A*, 523:A48.

Kalberla P.M.W. et al., 2005. *A&A*, 440:775–782.

Kao M.M. et al., 2018. *The Astrophysical Journal Supplement Series*, 237:25.

Kay C., Opher M., and Kornbleuth M., 2016. *ApJ*, 826:195.

Kerr G.S. and Fletcher L., 2014. *ApJ*, 783(2):98.

Kim Y.C. and Demarque P., 1996. *ApJ*, 457:340.

Kippenhahn R., Weigert A., and Weiss A., 1990. *Stellar structure and evolution*, volume 192. Springer.

Kippenhahn R., Weigert A., and Weiss A., 2012. *Transport of Energy by Radiation and Conduction*, 37–46. Springer Berlin Heidelberg, Berlin, Heidelberg. ISBN 978-3-642-30304-3.

Kirk J. et al., 2019. *AJ*, 158(4):144.

Kirkpatrick J.D., Henry T.J., and Liebert J., 1993. *ApJ*, 406:701.

Kirkpatrick J.D. et al., 1999. *ApJ*, 519(2):834–843.

Kiseleva L.G., Eggleton P.P., and Mikkola S., 1998. *MNRAS*, 300(1):292–302.

Klimchuk J.A., 2006. *Sol. Phys.*, 234(1):41–77.

Knutson H.A. et al., 2012. *ApJ*, 754(1):22.

Kochanek C.S. et al., 2017. *PASP*, 129(980):104502.

Kolotkov D.Y., Anfinogentov S.A., and Nakariakov V.M., 2016. *A&A*, 592:A153.

Kolotkov D.Y. et al., 2015. *A&A*, 574:A53.

Kopp R.A. and Pneuman G.W., 1976. *Sol. Phys.*, 50(1):85–98.

Kopparapu R.K. et al., 2013. *ApJ*, 765:131.

Kounkel M. et al., 2018. *AJ*, 156(3):84.

Kowalski A.F., Mathioudakis M., and Hawley S.L., 2018. In *20th Cambridge Workshop on Cool Stars, Stellar Systems and the Sun*, Cambridge Workshop on Cool Stars, Stellar Systems, and the Sun, 42.

Kowalski A.F. et al., 2009. *AJ*, 138(2):633–648.

Kowalski A.F. et al., 2010. *ApJ*, 714:L98–L102.

Kowalski A.F. et al., 2011. In C. Johns-Krull, M.K. Browning, and A.A. West, editors, *16th Cambridge Workshop on Cool Stars, Stellar Systems, and the Sun*, volume 448 of *Astronomical Society of the Pacific Conference Series*, 1157.

Kowalski A.F. et al., 2013. *ApJS*, 207:15.

Kowalski A.F. et al., 2015. *Sol. Phys.*, 290(12):3487–3523.

Kowalski A.F. et al., 2016. *ApJ*, 820(2):95.

Kowalski A.F. et al., 2017. *ApJ*, 836(1):12.

Kozai Y., 1962. *AJ*, 67:591.

Kretzschmar M., 2011. *A&A*, 530:A84.

Krucker S. et al., 2015. *ApJ*, 802(1):19.

Kumar P., Nakariakov V.M., and Cho K.S., 2017. *ApJ*, 836:121.

Kundu M.R., 1961. *J. Geophys. Res.*, 66(12):4308–4312.

Kupriyanova E.G. et al., 2010. *Sol. Phys.*, 267:329–342.

Kurucz R.L., 1979. *ApJS*, 40:1–340.

Lacy C.H., Moffett T.J., and Evans D.S., 1976. *The Astrophysical Journal Supplement Series*, 30:85–96.

Lambert J.H., 1760. *JH Lambert,... Photometria, sive de Mensura et gradibus luminis, colorum et umbrae*. sumptibus viduae E. Klett.

Laming J.M., 2015. *Living Reviews in Solar Physics*, 12:2.

Lammer H. et al., 2007. *Astrobiology*, 7:185–207.

Landin N.R., Mendes L.T.S., and Vaz L.P.R., 2010. *A&A*, 510:A46.

Lawrence A. et al., 2007. *MNRAS*, 379:1599–1617.

Lendl M. et al., 2012. *A&A*, 544:A72.

Lépine S. and Gaidos E., 2011. *AJ*, 142(4):138.

Li D., Li L., and Ning Z., 2018. *MNRAS*, 479(2):2382–2388.

Lidov M.L., 1962. *Planetary and Space Science*, 9:719–759.

Liebert J. et al., 2003. *AJ*, 125:343–347.

Lin C.L. et al., 2019. *ApJ*, 873(1):97.

Lindegren L. et al., 2018. *A&A*, 616:A2.

Lingam M. and Loeb A., 2017. *ApJ*, 848:41.

Lloyd's, 2013. *Solar storm risk to the North American electric grid.*

Loh E.D. et al., 2012. *PASP*, 124(914):343.

López-Santiago J. et al., 2010. *ApJ*, 712:78–87.

Loyd R.O.P. et al., 2018. *ApJ*, 867(1):71.

Lucy L.B. and Sweeney M.A., 1971. *AJ*, 76:544–556.

Lurie J.C. et al., 2017. *AJ*, (6):250.

Ma B. and Ge J., 2014. *MNRAS*, 439:2781–2789.

Mace G.N. et al., 2018. *ApJ*, 854:145.

Maciel W.J., 2015. *Introduction to stellar structure.* Springer.

Maehara H. et al., 2012. *Nature*, 485:478–481.

Maehara H. et al., 2015. *Earth, Planets, and Space*, 67:59.

Maehara H. et al., 2017. *PASJ*, 69(3):41.

Mann A.W. et al., 2015. *ApJ*, 804:64.

Mann A.W. et al., 2019. *ApJ*, 871(1):63.

Marcy G.W. and Butler R.P., 2000. *PASP*, 112(768):137–140.

Marsh T.R. and Dhillon V.S., 2006. In N. Solomos, editor, *Recent Advances in Astronomy and Astrophysics*, volume 848 of *American Institute of Physics Conference Series*, 808–809.

Martin D.C. et al., 2005. *ApJ*, 619:L1–L6.

Martín E.L. et al., 1999. *AJ*, 118(5):2466–2482.

Martínez Oliveros J.C. et al., 2012. *ApJ*, 753(2):L26.

Mason H.E. et al., 1986. *ApJ*, 309:435.

Mathioudakis M. et al., 2003. *A&A*, 403:1101–1104.

Matt S.P. et al., 2015. *ApJ*, 799(2):L23.

Maxted P.F.L., 2016. *A&A*, 591:A111.

Mayor M. and Queloz D., 1995. *Nature*, 378(6555):355–359.

Mayor M., Queloz D., and Udry S., 1998. *Mass Function and Orbital Distributions of Substellar Companions (invited review)*, volume 134 of *Astronomical Society of the Pacific Conference Series*, 140.

Mayor M. et al., 2003. *The Messenger*, 114:20–24.

Mazeh T., Tamuz O., and Zucker S., 2007. In C. Afonso, D. Weldrake, and T. Henning, editors, *Transiting Extrapolar Planets Workshop*, volume 366 of *Astronomical Society of the Pacific Conference Series*, 119.

McCormac J. et al., 2013. *PASP*, 125:548.

McCormac J. et al., 2020. *MNRAS*, 493(1):126–140.

McLaughlin J.A., Thurgood J.O., and MacTaggart D., 2012. *A&A*, 548:A98.

McLaughlin J.A. et al., 2018. *Space Sci. Rev.*, 214.

Metropolis N. et al., 1953. *J. Chem. Phys.*, 21(6):1087–1092.

Miles-Páez P.A. et al., 2017. *ApJ*, 840:83.

Mitra-Kraev U. et al., 2005. *A&A*, 436:1041–1047.

Moffett T.J., 1974. *The Astrophysical Journal Supplement Series*, 29:1–42.

Monet D.G. and Dahn C.C., 1983. *AJ*, 88:1489–1507.

Monet D.G. et al., 1992. *AJ*, 103:638.

Moon Y.J. et al., 2002. *ApJ*, 574:434–439.

Moorwood A., Cuby J.G., and Lidman C., 1998. *The Messenger*, 91:9–13.

Moran E.C. et al., 1996. *ApJ*, 461:127.

Morgan W.W., Keenan P.C., and Kellman E., 1943. *An atlas of stellar spectra, with an outline of spectral classification.*

Morris B.M., 2020. *arXiv e-prints*, arXiv:2002.09135.

Moutou C. et al., 2017. *MNRAS*, 472(4):4563–4586.

Muirhead P.S. et al., 2018. *AJ*, 155:180.

Mulkidjanian A.Y., Cherepanov D.A., and Galperin M.Y., 2003. *BMC evolutionary biology*, 3(1):12.

Mullan D.J. et al., 2006. *ApJS*, 164:173–201.

Mullan D.J. et al., 2018. *ApJ*, 869(2):149.

Müller D.A.N. et al., 2001. *Sol. Phys.*, 203(2):211–232.

Murphy S.J. and Lawson W.A., 2015. *MNRAS*, 447:1267–1281.

Murphy S.J., Mamajek E.E., and Bell C.P.M., 2018. *MNRAS*, 476(3):3290–3302.

Murray M.J., van Driel-Gesztelyi L., and Baker D., 2009. *A&A*, 494:329–337.

Nakajima T. et al., 1995. *Nature*, 378(6556):463–465.

Nakamoto T. et al., 2005. In *Chondrites and the Protoplanetary Disk*, volume 341, 883.

Nakariakov V.M. and Melnikov V.F., 2009. *Space Sci. Rev.*, 149:119–151.

Nakariakov V.M. and Ofman L., 2001. *A&A*, 372:L53–L56.

Nakariakov V.M. et al., 2004. *MNRAS*, 349:705–709.

Nakariakov V.M. et al., 2006. *A&A*, 452:343–346.

Nakariakov V.M. et al., 2016. *Space Sci. Rev.*, 200:75–203.

Namekata K. et al., 2017. *ApJ*, 851(2):91.

Newton H.W. and Nunn M.L., 1951. *MNRAS*, 111:413.

Nisticò G., Pascoe D.J., and Nakariakov V.M., 2014. *A&A*, 569:A12.

Notsu Y. et al., 2013. *ApJ*, 771:127.

Notsu Y. et al., 2019. *ApJ*, 876(1):58.

Núñez A. and Agüeros M.A., 2016. *ApJ*, 830(1):44.

Ofman L. and Wang T., 2002. *ApJ*, 580:L85–L88.

Ofman L. and Wang T.J., 2008. *A&A*, 482:L9–L12.

Ogilvie G.I., 2014. *Annual Review of Astronomy and Astrophysics*, 52:171–210.

Olson E.C., 1980. *Information Bulletin on Variable Stars*, 1825:1.

Orlando S. et al., 2011. *MNRAS*, 415:3380–3392.

Osborn J. et al., 2015. *MNRAS*, 452:1707–1716.

Osten R. et al., 2013. *ApJ*, 765:L44.

Osten R.A. and Wolk S.J., 2015. *ApJ*, 809:79.

Osten R.A. et al., 2010. *ApJ*, 721:785–801.

Oughton E.J. et al., 2017. *Space Weather*, 15(1):65–83.

Pandey J.C. and Srivastava A.K., 2009. *ApJ*, 697:L153–L157.

Parker E.N., 1955. *ApJ*, 122:293.

Parker E.N., 1988. *ApJ*, 330:474.

Parnell C.E. and Jupp P.E., 2000. *ApJ*, 529:554–569.

Parviainen H. and Aigrain S., 2015. *MNRAS*, 453:3821–3826.

Pätzold M. and Rauer H., 2002. *ApJ*, 568(2):L117–L120.

Paudel R.R. et al., 2018a. *ApJ*, 861(2):76.

Paudel R.R. et al., 2018b. *ApJ*, 858:55.

Paudel R.R. et al., 2020. *MNRAS*, 494(4):5751–5760.

Payne C.H., 1925. *Stellar Atmospheres; a Contribution to the Observational Study of High Temperature in the Reversing Layers of Stars.* Ph.D. thesis, RADCLIFFE COLLEGE.

Pecaut M.J. and Mamajek E.E., 2013. *The Astrophysical Journal Supplement Series*, 208:9.

Pecaut M.J. and Mamajek E.E., 2016. *MNRAS*, 461:794–815.

Pepper J. et al., 2007. *PASP*, 119(858):923–935.

Pepper J. et al., 2012. *PASP*, 124(913):230.

Perdelwitz V. et al., 2018. *A&A*, 616:A161.

Pérez-Garrido A., Lodieu N., and Rebolo R., 2017. *A&A*, 599:A78.

Perryman M., 2018. *The Exoplanet Handbook*.

Perryman M.A.C. et al., 1997. *A&A*, 500:501–504.

Peterson L. and Winckler J.R., 1958. *Phys. Rev. Lett.*, 1(6):205–206.

Peterson L.E. and Winckler J.R., 1959. *J. Geophys. Res.*, 64(7):697–707.

Pineda J.S., Hallinan G., and Kao M.M., 2017. *ApJ*, 846:75.

Pizzolato N. et al., 2003. *A&A*, 397:147–157.

Poletto G., 1989. *Sol. Phys.*, 121:313–322.

Pollacco D.L. et al., 2006. *PASP*, 118(848):1407–1418.

Pollum M. et al., 2016. *Journal of the American Chemical Society*, 138(36):11457–11460.

Pravdo S.H. and Angelini L., 1995. *ApJ*, 447:342.

Prescott G.B., 1860. *The North American Review*, 91(189):564. ISSN 00292397.

Pugh C.E., Broomhall A.M., and Nakariakov V.M., 2017. *A&A*, 602:A47.

Pugh C.E., Nakariakov V.M., and Broomhall A.M., 2015. *ApJ*, 813:L5.

Pugh C.E. et al., 2016. *MNRAS*, 459:3659–3676.

Racine É. et al., 2011. *ApJ*, 735(1):46.

Rackham B.V., Apai D., and Giampapa M.S., 2018. *ApJ*, 853:122.

Raghavan D. et al., 2010. *The Astrophysical Journal Supplement Series*, 190:1–42.

Ramsay G. and Doyle J.G., 2015. *MNRAS*, 449:3015–3020.

Ramsay G. et al., 2013. *MNRAS*, 434:2451–2457.

Ranjan S., Wordsworth R., and Sasselov D.D., 2017. *ApJ*, 843:110.

Rauer H. et al., 2014. *Experimental Astronomy*, 38:249–330.

Raynard L. et al., 2018. *MNRAS*, 481:4960–4970.

Rebolo R., Zapatero Osorio M.R., and Martín E.L., 1995. *Nature*, 377(6545):129–131.

Reid I.N. and Walkowicz L.M., 2006. *PASP*, 118(843):671–677.

Reid N., Hawley S.L., and Mateo M., 1995. *MNRAS*, 272(4):828–842.

Ricker G.R. et al., 2014. In *Space Telescopes and Instrumentation 2014: Optical, Infrared, and Millimeter Wave*, volume 9143, 914320.

Ricker G.R. et al., 2015. *Journal of Astronomical Telescopes, Instruments, and Systems*, 1:014003.

Riello M. et al., 2018. *A&A*, 616:A3.

Rimmer P.B. et al., 2018. *ArXiv e-prints*.

Roberts B., Edwin P.M., and Benz A.O., 1984. *ApJ*, 279:857–865.

Roettenbacher R.M. and Vida K., 2018. *ApJ*, 868(1):3.

Roettenbacher R.M. et al., 2013. *ApJ*, 767:60.

Roettenbacher R.M. et al., 2016. *ApJ*, 832(2):207.

Rugheimer S. et al., 2015. *ApJ*, 806(1):137.

Russell H.N., 1914. *Popular Astronomy*, 22:275–294.

Sadeghi Ardestani L., Guillot T., and Morel P., 2017. *MNRAS*, 472:2590–2607.

Salaris M. and Cassisi S., 2005. *Evolution of stars and stellar populations*, volume 400. Wiley Online Library.

Sarker P.K. et al., 2013. *Advances in Space Research*, 51(12):2235–2240.

Schaefer B.E., 1989. *ApJ*, 337:927–933.

Schaefer B.E., King J.R., and Deliyannis C.P., 2000. *ApJ*, 529:1026–1030.

Schmidt S.J. et al., 2010. *AJ*, 139:1808–1821.

Schmidt S.J. et al., 2015. *AJ*, 149:158.

Schmidt S.J. et al., 2016. *ApJ*, 828:L22.

Schmidt S.J. et al., 2019. *ApJ*, 876(2):115.

Schmitt J.H.M.M., Fleming T.A., and Giampapa M.S., 1995. *ApJ*, 450:392.

Segura A. et al., 2010. *Astrobiology*, 10:751–771.

Selwa M., Murawski K., and Solanki S.K., 2005. *A&A*, 436:701–709.

Serio S. et al., 1991. *A&A*, 241(1):197–202.

Severino G., 2017. *The Structure and Evolution of the Sun*.

Shibata K. et al., 1995. *ApJ*, 451:L83.

Shibata K. et al., 2013. *PASJ*, 65:49.

Shibayama T. et al., 2013. *The Astrophysical Journal Supplement Series*, 209:5.

Shimizu T., 1995. *Publications of the Astronomical Society of Japan*, 47:251–263.

Shu F.H. et al., 2001. *ApJ*, 548:1029–1050.

Shulyak D. et al., 2017. *Nature Astronomy*, 1:0184.

Shulyak D. et al., 2019. *A&A*, 626:A86.

Silva-Valio A. and Lanza A.F., 2011. *A&A*, 529:A36.

Simões P.J.A., Hudson H.S., and Fletcher L., 2015. *Sol. Phys.*, 290:3625–3639.

Skrutskie M.F. et al., 2006. *AJ*, 131:1163–1183.

Skrzypek N., Warren S.J., and Faherty J.K., 2016. *A&A*, 589:A49.

Skrzypek N. et al., 2015. *A&A*, 574:A78.

Skumanich A., 1972. *ApJ*, 171:565.

Smith A.M.S. et al., 2018. *MNRAS*, 474:5523–5533.

Smith R.K. et al., 2001. *ApJ*, 556:L91–L95.

Solanki S.K., 2003. *A&ARv*, 11:153–286.

Solanki S.K., 2009. *Photospheric Magnetic Field: Quiet Sun*, volume 405 of *Astronomical Society of the Pacific Conference Series*, 135.

Somers G. and Pinsonneault M.H., 2016. In J.H. Kastner, B. Stelzer, and S.A. Metchev, editors, *Young Stars & Planets Near the Sun*, volume 314, 91–94.

Spiegel E.A. and Zahn J.P., 1992. *A&A*, 265:106–114.

Stamatellos D. and Whitworth A.P., 2009. *MNRAS*, 392(1):413–427.

Stassun K.G. et al., 2004. *AJ*, 127:3537–3552.

Stassun K.G. et al., 2012. *ApJ*, 756:47.

Stauffer J. et al., 2016. *AJ*, 152:115.

Stelzer B. et al., 2006. *A&A*, 460:L35–L38.

Stelzer B. et al., 2007. *A&A*, 468:463–475.

Stephens D.C. et al., 2009. *ApJ*, 702:154–170.

Strom K.M. et al., 1990. *ApJ*, 362:168.

Sturrock P.A., 1966. *Nature*, 211(5050):695–697.

Svestka Z. and Cliver E.W., 1992. *History and Basic Characteristics of Eruptive Flares*, volume 399, 1.

Telleschi A. et al., 2005. *ApJ*, 622:653–679.

Thomas J.H. and Weiss N.O., 2008. *Sunspots and starspots*, volume 46. Cambridge University Press Cambridge.

Thurgood J.O., Pontin D.I., and McLaughlin J.A., 2017. *ApJ*, 844:2.

Tilley M.A. et al., 2017. *arXiv e-prints*, arXiv:1711.08484.

Török T. et al., 2011. *ApJ*, 739(2):L63.

Troup N.W. et al., 2016. *AJ*, 151:85.

Tsang B.T.H. et al., 2012. *ApJ*, 754:107.

Tsurutani B.T. et al., 2003. *Journal of Geophysical Research: Space Physics*, 108(A7):n/a–n/a. ISSN 2156-2202. 1268.

Van Doorsselaere T., Kupriyanova E.G., and Yuan D., 2016. *Sol. Phys.*, 291:3143–3164.

Van Doorsselaere T., Shariati H., and Debosscher J., 2017. *The Astrophysical Journal Supplement Series*, 232:26.

Van Doorsselaere T. et al., 2011. *ApJ*, 740:90.

VanderPlas J.T., 2018. *The Astrophysical Journal Supplement Series*, 236:16.

Vaughan S., 2005. *A&A*, 431:391–403.

Venot O. et al., 2016. *ApJ*, 830:77.

Vernet J. et al., 2011. *A&A*, 536:A105.

Vida K. et al., 2017. *ApJ*, 841:124.

Šubjak J. et al., 2019. *arXiv e-prints*, arXiv:1909.07984.

Walkowicz L.M. and Hawley S.L., 2009. *AJ*, 137(2):3297–3313.

Wang T., 2011. *Space Sci. Rev.*, 158:397–419.

Warell J., 2004. *Icarus*, 167(2):271–286.

Watanabe K. et al., 2010. *ApJ*, 715(1):651–655.

Watanabe K. et al., 2013. *ApJ*, 776(2):123.

Wdowiak T.J. and Clifton K.S., 1985. *ApJ*, 295:171–174.

Weber E.J. and Davis Leverett J., 1967. *ApJ*, 148:217–227.

Welsh B.Y. et al., 2006. *A&A*, 458:921–930.

Welsh W.F. et al., 2010. *ApJ*, 713:L145–L149.

West A.A. et al., 2015. *ApJ*, 812(1):3.

West R.G. et al., 2019. *MNRAS*, 486(4):5094–5103.

Wheatley P.J., 1998. *MNRAS*, 297(4):1145–1150.

Wheatley P.J. et al., 2018. *MNRAS*, 475:4476–4493.

White S.M. et al., 2011. *Space Sci. Rev.*, 159(1-4):225–261.

Wilms J., Allen A., and McCray R., 2000. *ApJ*, 542:914–924.

Wolf C. et al., 2018. *Publications of the Astronomical Society of Australia*, 35:e010.

Wood B.E., Laming J.M., and Karovska M., 2012. *ApJ*, 753:76.

Wood B.E. and Linsky J.L., 2010. *ApJ*, 717:1279–1290.

Wright E.L. et al., 2010. *AJ*, 140:1868–1881.

Wright N.J. et al., 2011. *ApJ*, 743:48.

Wright N.J. et al., 2018. *MNRAS*, 479:2351–2360.

Wu C.J., Ip W.H., and Huang L.C., 2015. *ApJ*, 798:92.

Xu Y. et al., 2014. *ApJ*, 787(1):7.

Yabuki K. et al., 2017. In M. Serino, M. Shidatsu, W. Iwakiri, and T. Mihara, editors, *7 years of MAXI: monitoring X-ray Transients, held 5-7 December 2016 at RIKEN. Online at ¡A href="https://indico2.riken.jp/indico/conferenceDisplay.py?confId=2357"¿ https://indico2.riken.jp/indico/conferenceDisplay.py?confId=2357¡/A¿, p.187*, 187.

Yan X.L. et al., 2018. *ApJ*, 856(1):79.

Yang H. and Liu J., 2019. *The Astrophysical Journal Supplement Series*, 241(2):29.

Yang H. et al., 2017. *ApJ*, 849:36.

Yang H. et al., 2018. *ApJ*, 859:87.

Yashiro S. and Gopalswamy N., 2009. In N. Gopalswamy and D.F. Webb, editors, *Universal Heliophysical Processes*, volume 257 of *IAU Symposium*, 233–243.

York D.G. et al., 2000. *AJ*, 120:1579–1587.

Young A.T., 1967. *AJ*, 72:747.

Zacharias N., Finch C., and Frouard J., 2017. *AJ*, 153:166.

Zaitsev V.V. and Stepanov A.V., 1982. *Soviet Astronomy Letters*, 8:132–134.

Zaitsev V.V. and Stepanov A.V., 2008. *Physics Uspekhi*, 51:1123–1160.

Zaitsev V.V. et al., 2004. *Astronomy Letters*, 30:319–324.

Zari E. et al., 2018. *A&A*, 620:A172.

Zeilik M. et al., 1990. *ApJ*, 363:647.

Zhilyaev B.E. et al., 2000. *A&A*, 364:641–645.

Zimovets I.V. and Nakariakov V.M., 2015. *A&A*, 577:A4.

Zirin H. and Liggett M.A., 1987. *Sol. Phys.*, 113(1-2):267–283.

Zuckerman B. and Becklin E.E., 1992. *ApJ*, 386:260.

Zuckerman B. and Song I., 2004. *ARA&A*, 42(1):685–721.

Zwaan C., 1978. *Sol. Phys.*, 60(2):213–240.